Title
Experimental Mapping of Elastoplastic Surfaces for Sand and Cyclic Failure of Low-Plasticity Fine-Grained Soils

Permalink
https://escholarship.org/uc/item/9zw0g81m

Author
Eslami, Mohammad

Publication Date
2017

UNIVERSITY OF CALIFORNIA
Los Angeles

Experimental Mapping of Elastoplastic Surfaces for Sand and Cyclic Failure of Low-Plasticity Fine-Grained Soils

A dissertation submitted in partial satisfaction of the
requirements for the degree Doctor of Philosophy
in Civil Engineering

by

Mohammad Eslami

2017

ABSTRACT OF THE DISSERTATION

Experimental Mapping of Elastoplastic Surfaces for Sand and Cyclic Failure of Low-Plasticity Fine-Grained Soils

by

Mohammad Eslami
Doctor of Philosophy in Civil Engineering
University of California, Los Angeles, 2017
Professor Scott Joseph Brandenberg, Chair

Part I of this dissertation describes a simple experimental technique that can be used to obtain the slopes of the plastic potential and yield functions during shear based on the deformation theory of plasticity. The method imposes small perturbations in the direction of the stress increment by closing the drainage valve, thereby abruptly switching from drained to undrained loading conditions during plastic loading. Elastoplastic moduli are obtained immediately before and after the perturbation from the measured deviatoric stress, mean effective stress, deviatoric strains, and volumetric strains for the stress paths immediately before and after closing the drain valve. During drained shear, samples were sheared while the mean effective stress was maintained constant.

Combining tests performed at several confining stresses, the proposed method can map yield and plastic potential surfaces and predict their evolution for a wide range of stresses.

Part II of the dissertation focuses on providing insights into the effects of changes in clay mineralogy and pore-fluid chemistry on cyclic behavior of low-plasticity fine-grained soils. A series of cyclic and monotonic direct simple shear experiments was conducted on three low-plasticity fine-grained mixtures of non-plastic silt with either bentonite or kaolinite clay minerals blended with fresh deionized water or saline water. The clay fractions were adjusted to achieve a plasticity index of PI = 9 for all three mixtures to study differences or similarities in their behavior and to examine the effectiveness of index properties in identifying the observed differences in lab results.

Even though all three blends have the same plasticity index, significant differences in their cyclic response were observed. Results indicate that plasticity index is an insufficient indicator of the cyclic behavior of low-plasticity fine-grained soils, and corrections for pore fluid chemistry and clay minerology may be needed for future liquefaction susceptibility and cyclic softening assessment procedures. Site-specific cyclic and monotonic testing for important projects remains to be the recommended approach for properly characterizing the seismic behavior of such soils with the current level of understating of their complex behavior.

The collected experimental data, visualization and post-processing tools, as well as documented experimental procedures of Part I are curated and published for public access on http: www.DesignSafe-ci.org. The data from Part II is being curated and will be published online in the near future.

The dissertation of Mohammad Eslami is approved.

Jonathan Paul Stewart

Ertugrul Taciroglu

Anne Lemnitzer

Daniel Pradel

Scott Joseph Brandenberg, Committee Chair

University of California, Los Angeles

2017

It was tried to take a step toward advancement of our profession by the work in this dissertation; it is dedicated to all researchers and practitioners who strive to make safer infrastructure around the world.

TABLE OF CONTENTS

LIST OF FIGURES

LIST OF TABLES

ACKNOWLEDGMENTS

I am Deeply indebted to Professor Scott Brandenberg for his mentorship, guidance, and support during my time as a PhD student. Through my studies at UCLA, his challenge, patience, and thoughtful insights helped me become a much better engineer. Troubled times during research projects are no exception to any graduate student, thanks Scott for believing in me and making my experience joyful as your PhD student!

I would like to warmly thank Professor Daniel Pradel for teaching me how to run high quality triaxial laboratory tests – by Japanese standards! Support with testing, as well as thoughtful insights and comments on Part I of the dissertation are much appreciated. Thanks to Professor Jonathan Stewart for serving on my PhD defense committee, providing insights in Part II of this dissertation, and teaching a fantastic “geotechnical earthquake engineering” course. It was certainly the favorite of all courses during my time as a student. Also, I feel lucky to have been your TA for foundation engineering, it was a great experience. Thanks to Professors Taciroglu and Lemnitzer for serving on my defense committee, their valuable comments, and friendship.

Greatest appreciation goes to my parents and brother who have endlessly supported me throughout this journey from day one! Especially, my father who has always provided the most thoughtful insights and encouragement throughout my academic career, and life in general. Thanks to uncle Zavosh and his wife Chris, and my grandmother for helping me out when I first came to the U.S. and keep supporting me. I thank my best friend Dr. Sepehr Rejai for his support and true friendship during the four years we were roommates in Los Angeles.

Part I of this dissertation was funded through TA-ships at UCLA. Thanks to all great students at UCLA who made these experiences one of a kind; making me want to continue research

and teaching as my profession. Part II of the dissertation was sponsored by the National Science Foundation (NSF) under award number 1563638, where committee chair Professor Scott J. Brandenberg and committee member Jonathan P. Stewart were principal investigator and co-principal investigators. This support is gratefully acknowledged.

I am grateful to undergraduate and high school students who had assisted in Atterberg limits and consolidation laboratory testing and creating data visualization tools; Ariel Siegel, Mike Liu, Soheil Kashani, Joanna Sanchez, Brandon David, and Claire Zeller – thank you all for your help. I truly appreciate the help from Ai Zhong in creating Jupyter notebooks on DesignSafe for lab data visualization, and Maria Esteva for the assistance in curating and publishing our datasets. Guidance with using and maintenance of the simple shear device from Dr. Ali Shafiee and Ravi Venugopal is greatly appreciated. Thanks to the SIMS Lab at UCLA Department of Earth, Planetary and Space Sciences and especially Elizabeth Bell for her assistance with using the SEM. I thank Dr. Karina Dahl for providing data from her thesis, and the staff at UCLA in the Civil and Environmental Engineering department, especially Jesse and Reba who helped me with all administrative processes during these years.

Finally, thanks to my lab mates and the good friends that I made at UCLA for their support, humor, friendship, creating a great working environment, and for keeping me sane during the last five years; Sean Ahdi, Benjamin Turner, Samuel Yniesta, Dong Youp Kwak, Yi Tyan Tsai, Paolo Zimmaro, and Margo Durante. I have enjoyed the time that we have spent, and thank you all for tolerating the noise from the simple shear testing. I am thankful to Kioumars Afshari for our valuable technical and non-technical discussions over these years which I learned a lot from, and Victor Contreras for being a great racquetball coach and opponent!

VITA

Education

M.S., (December 2013), Geotechnical Engineering, University of California, Los Angeles

M.S., (October 2011), Structural Engineering, Sharif University of Technology

B.S., (August 2009), Civil Engineering, Azad University, Central Tehran Branch

Professional Experience

Teaching Assistant, Dept. of Civil & Env. Engineering, UCLA (2013-2015)

Graduate Student Researcher, Dept. of Civil & Env. Engineering, UCLA (2015-2017)

Research Engineer, ImageCat Inc. (summer 2013)

Selected Publications

Eslami, M., Pradel, D., Brandenberg, S. J. (201x). “Experimental Mapping of Elastoplastic Surfaces for Sand Using Undrained Perturbations.” *Soils and Foundations*, Elsevier, Accepted for publication (September 2017).

Eslami, M., Brandenberg, S. J., Zhong, A., Pradel, D. (2017). “Triaxial Tests on Sand for Yield Surface Mapping.” DesignSafe-CI [publisher], Dataset, DOI: https://doi.org/10.17603/DS23T00

Eslami, M., Esteva, M., Brandenberg, S.J. (2017). “Direct Simple Shear Test Analysis Using Jupyter Notebooks on DesignSafe-CI.” American Geophysical Union (AGU) Fall Meeting, New Orleans, Louisiana. Accepted for publication (October 2017).

Eslami, M., Pradel, D., Brandenberg, S. J. (2017). “Mapping of Yield and Plastic Potential Surfaces Using Undrained Perturbations in Triaxial Compression.” ASCE Engineering Mechanics Institute Conference (EMI 2017), MS 63 Minisymposia on “Recent Advances in Constitutive Modeling for Geotechnical Engineering”, San Diego, California, USA.

Esteva, M., Brandenberg, S.J., Eslami, M., Adair, A., Kulasekaaran, S.A. (2016). “Modelling Natural Hazards Engineering Data to Cyberinfrastructure.” SciDataCon 2016 at International Data Week, Advancing the Frontiers of Data in Research, paper No. 282, Denver, Colorado, USA. http://www.scidatacon.org/2016/sessions/104/paper/282/

1 Introduction to Dissertation

This dissertation contains two separate sections; Part I, and Part II. Below is a brief description of each section.

Part I:

Using numerical simulations to predict permanent deformations caused by surcharges, excavations, and other similar geotechnical loading mechanisms, requires constitutive models that successfully estimate the anticipated level of irrecoverable strains. This practice is crucial especially in large infrastructure projects such as dams, tunnels, highway embankments, and for deep excavations next to existing buildings.

Commonly used constitutive models exhibit significant differences in the treatment of their main constituents; the yield and plastic potential surfaces. The shape of the yield and plastic potential surfaces used in constitutive models are rarely directly based on experimental measurements due to the requirement of numerous complex laboratory tests that require careful interpretation. Rather, basic parameters such as elastic constants and hardening variables are based on experimental measurements and several modeling parameters are adjusted to provide a reasonable match between predictions and experimental observations. Counter-balancing errors, between hardening moduli and the yield and plastic potential equations may result in a good match to experimental data for a particular stress path, even if the underlying assumptions of the yield and plastic potential surfaces are incorrect.

Part I of this dissertation describes a simple experimental method developed to directly measure the plastic modulus, and slopes of the plastic potential and yield surfaces for loose sand during monotonic shear in triaxial compression. The measurements are then compared with some models that are commonly used by practicing engineers, and similarities or differences are discussed. The experimental technique can be implemented without specialized laboratory equipment, and constitutes a departure from the typical practice of calibrating constitutive models to match experimental data, and can be useful to develop new and more accurate elastoplastic constitutive models for sands.

Part II:

The essential first step in characterizing seismic soil behavior whether assessment of liquefaction susceptibility, or sand-like versus clay-like behavior, is commonly based on soil index properties such as liquid limit (LL), plasticity index (PI), and particle size. Also, several procedures have been developed for estimating cyclic strengths of soils when considered prone to liquefaction or cyclic softening. Similarly, such procedures are also quite often based on soil index properties, especially in clay-like soils where the cyclic strength is related to effective confining stress or undrained shear strength, based on plasticity level. Some recent studies however, criticize the effectiveness of soil index properties solely, being sufficient indicators for adequately capturing variations in cyclic behavior of fine grained soils and suggests that factors such as clay mineralogy, clay content, and pore-fluid chemistry should be considered for satisfactory engineering judgement and practice under seismic conditions.

Part II of this dissertation focuses on providing insights into the effects of changes in clay mineralogy and pore-fluid chemistry on cyclic behavior of low-plasticity fine-grained soils. An extensive laboratory study has been performed on low-plasticity silty clay mixtures with varying compositions, but at equal plasticity levels, to study differences or similarities in their behavior and to examine the effectiveness of index properties in identifying the observed differences in lab results. The results indicate that plasticity index is an insufficient indicator of the cyclic behavior of low-plasticity fine-grained soils, and corrections for pore fluid chemistry and clay minerology may be needed for future liquefaction susceptibility and cyclic softening assessment procedures.

PART I: EXPERIMENTAL MAPPING OF ELASTOPLASTIC SURFACES FOR SAND

How accurate are the yield surfaces of soil constitutive models available for geotechnical engineering practice – that are proved to be able to capture soil behavior well?

2 Introduction and Background to Part I

2.1 OVERVIEW

Solution of soil mechanics problems requires statements of equilibrium, kinematics, and the relation between stress and strain changes, namely the constitutive model. Constitutive models are used as tools in geotechnical engineering design software that predicts soil behavior, assisting practicing engineers in designing new projects, or mitigating existing infrastructure. In important projects, usually the use of more rigorous constitutive models is considered. For example, in sites located in seismically active regions prone to liquefaction during earthquakes, finding the most practical, yet optimized mitigation strategy is goal, which can be done efficiently through numerical analysis and models that mimic true soil behavior. It is important however, for these models to be based on the right ingredients. Basic constituents of a constitutive model include the elastic constants, plastic modulus, yield surfaces, and the flow rule (often described by a plastic potential surface).

Being able to predict behavior of soil has been a leading motivation for numerous efforts put into developing constitutive models which began in the early 1960's by researchers at the University of Cambridge. To date, numerous other efforts have been put together having the same goal; to predict soil behavior in the most realistic fashion. These efforts though having the same objective, consist of major differences in how the problem and its solution is approached. Research in the field of predicting soil behavior mainly consists of two schools of thought:

(1) Purely theoretical and mathematical approaches for main ingredients of constitutive models (yield surface, plastic potential surfaces, etc.) based on plasticity theory, where several equations are developed and calibrated to match laboratory test data and model predictions,

(2) Very few approaches that have directly tried to capture the nature of yield and plastic potential surfaces of plasticity-based constitutive models through numerous, complex, and careful laboratory testing.

Either school of thought, leaving unanswered questions in one's mind; for example, how accurate are the assumptions for the models based on approach (1)? How feasible is it to perform new practices similar to approach (2)? Part I of this dissertation focuses on making direct measurements of the yield and plastic potential surfaces [approach (2)] by using a unique experimental method involving triaxial laboratory tests on sand.

2.2 OBJECTIVES AND STRUCTURE

Based on approach (1) mentioned above, functional forms are assumed for the yield surface and plastic potential, then the modeling constants and parameters are adjusted so that the model matches available laboratory test data. The yield surface and plastic potential surfaces have not been measured directly using approach (2) in very many studies to date and therefore, this field remains a poorly understood aspect of sand behavior.

Focus of Part I of this dissertation is on implementing a quite unique laboratory testing method to directly measure yielding parameters for a uniformly graded sand in the laboratory by means of standard traditional triaxial compression testing without the need for specialized equipment, which makes the method attractive for routine use. Specific steps of the simple method are explained below.

A simple plastic hardening stress-strain relationship has been chosen for sand based on the assumption of non-associative plasticity. A series of triaxial compression tests are conducted on saturated loose sand samples under drained conditions while the effective confining pressure is held constant. Additionally, at intervals the test is switched from drained to undrained mode where volumetric strains are not free to develop. Using the experiment outcomes, the stress-strain equations are solved, and moduli as well as slopes of the yield surface and plastic potential are measured. The shape of the yield surface, and direction of plastic flow is inferred based on the measured slopes through different approaches. The obtained shapes of the yield surface are compared with existing models commonly used in practice or given in the literature, where criticism and fundamental variations are provided.

The remaining sections of this Chapter provides the historical development of constitutive modelling for soils; more specifically for sands, including general frameworks of plasticity theory which serves as basis of most, if not all, constitutive models. Major differences between approaches and methods are discussed. The chapter is followed by a section on fewer available experimental mapping studies on direct measurement of elastoplastic surfaces for sands.

Chapter 3 concentrates on the proposed methodology of the current study. The incremental stress-strain formulation has been described thoroughly. Moreover, the mechanisms for solving the mathematical equations are presented. Details of the testing program, procedures, and the triaxial apparatus are provided in Chapter 3 as well.

Chapter 4 presents results of the experiments performed in the geotechnical laboratory combined with interpretation of the yielding characteristics based on the collected data which is followed by discussion and comparison with currently available models.

Finally, Chapter 5 provides a summary along with main conclusions that are drawn from Part I of the dissertation, and provides insights on possible future work that can be done in this field of research.

This chapter contains an overview of soil plasticity theory and some basic definitions that will be used in the Part I, followed by a detailed section on the topic of constitutive modeling in sands and its evolution over time. Examples of more recent advancements in soil constitutive modeling research have been introduced in addition to discussing fundamental variations in the proposed approaches.

2.3 DEFINITIONS

Definitions of parameters that are used in Part I of this dissertation are explained to familiarize the reader with the notation utilized in the document.

The experimental program in Part I consists of triaxial compression laboratory tests and usage of plasticity formulations, which are based on stress and strain invariants. Definitions of deviatoric (shear) and mean effective stress invariants are presented in equations (2.1) and (2.2), respectively. Note that simplified version of these invariants (i.e. $\sigma_2 = \sigma_3$) are also presented in the equations. Radial stresses (σ_2 and σ_3) are controlled by the cell pressure applied to the soil sample through the cell. Axial or shear stress (σ_1) to the sample is applied through a vertical rod. Note that the "prime" superscript is an indication of *effective* stresses.

$$q=\sqrt{\frac{1}{2}\left[\left(\sigma_1-\sigma_2\right)^2+\left(\sigma_1-\sigma_3\right)^2+\left(\sigma_2-\sigma_3\right)^2\right]}\xrightarrow{in\ triaxial\ space}q=\sigma_1-\sigma_3 \tag{2.1}$$

$$p'=\frac{1}{3}\left(\sigma_1^{'}+\sigma_2^{'}+\sigma_3^{'}\right)\xrightarrow{in\ triaxial\ space}p'=\frac{1}{3}\left(\sigma_1^{'}+2\sigma_3^{'}\right) \tag{2.2}$$

Similarly, deviator and volumetric strains are defined as in equations (2.3) and (2.4). Where ε_1 and ε_3 (and ε_2) are increments of axial and radial strains, respectively. Simplified versions of these invariants for triaxial space are also presented in these equations.

$$\varepsilon_q=\frac{2}{3}\sqrt{\frac{1}{2}\left[\left(\varepsilon_1-\varepsilon_2\right)^2+\left(\varepsilon_1-\varepsilon_3\right)^2+\left(\varepsilon_2-\varepsilon_3\right)^2\right]}\xrightarrow{in\ triaxial\ space}\varepsilon_q=\frac{2}{3}\left(\varepsilon_1-\varepsilon_3\right) \tag{2.3}$$

$$\varepsilon_v=\varepsilon_1+\varepsilon_2+\varepsilon_3\xrightarrow{in\ triaxial\ space}\varepsilon_v=\varepsilon_1+2\varepsilon_3 \tag{2.4}$$

Elastic deviatoric and volumetric and strains can be computed using *G* and *K*, the elastic shear and bulk moduli using equations (2.5) and (2.6), respectively. Note that the superscript *e* denotes elastic strains.

$$d\varepsilon_q^e=\frac{dq}{3G} \tag{2.5}$$

$$d\varepsilon_v^e=\frac{dp'}{K} \tag{2.6}$$

The deformation theory of plasticity (e.g., Jones, 2009 and Wood, 1990) postulates that strains can be decomposed into elastic (fully recoverable) and plastic (irrecoverable) components. For a time-independent material this postulate is expressed incrementally in equation (2.7). Where superscripts *e* and *p* denote elastic and plastic, respectively.

$$d\varepsilon_{ij} = d\varepsilon_{ij}^{e} + d\varepsilon_{ij}^{p} \tag{2.7}$$

In process of loading and unloading a soil sample, the departure from the elastic response that occurs as the reloading proceeds beyond the past maximum load may be called *yielding*, and the past maximum load becomes a current *yield* point (Wood, 1991). A series of yielding points would define a *yield surface*. For stress conditions inside a yield surface, the response of soil is elastic. As soon as a stress change engages a current yield surface, the soil behavior would be a combination of elastic and plastic responses.

An important factor in predicting soil behavior is to determine the mechanism of plastic deformation. This can be done using a flow rule and using plastic potential surfaces. As mentioned previously, yielding is associated with both plastic volumetric strains and plastic shear (deviator) strains. By plotting the magnitudes of these strains at a yield point, a plastic strain increment can be produced, which is orthogonal to the plastic potential surface.

It is important to note that if the yield surface and the plastic potential surfaces for a given material coincide, the material is assumed to obey the postulate of *normality*. In other words, the material is said to follow a law of *associated flow*. In this case, the plastic deformations (flow) in the material, is associated with the yield surface of that material. For many materials, the plastic potentials and yield surfaces are not identical and the differences should be considered for purposes of developing a constitutive model. The flow rule describes the evolution of the plastic strains and the hardening law describes the evolution of the hardening variables.

A constitute model is based on (Simo and Hughes, 1998):

- A yielding criterion, or yield surface, which defines the state of stress that yielding occurs
- A flow rule, describing the evolution of plastic strains when the material is yielding
- A hardening law, defining the strain hardening of the material when plastic strains evolve
- Kuhn-Tucker loading-unloading conditions and consistency equations, which are used to derive mathematical formulations to find relations between stresses and strains.

Given the brief introduction on theory of plasticity fundamentals, the following section concentrates on some commonly used models that are used for predicting behavior of sands.

2.4 HISTORICAL DEVELOPMENT OF SOIL CONSTITUTIVE MODELING

Perhaps one of the early stages before the development of plastic stress-strain relationships for soils was based on the limit equilibrium concept used by Coulomb in the 18th century for solving geotechnical stability problems of retaining walls and earth pressures. The limit equilibrium method assumes that the soil is at a state of failure along a prescribed surface, and therefore inherently assumes rigid-perfectly plastic constitutive behavior. Two yield surfaces commonly utilized to define failure in limit equilibrium methods are the Mohr-Coulomb and Drucker-Prager models. These models are presented first, followed by other advancements in constitutive modeling which considering nonlinearity and are capable of predicting more realistic behavior of soils.

2.4.1 Mohr-Coulomb Model

Perhaps the oldest proposition for failure criterion for cohesionless soils would be that of Coulomb's in the 18th century which we know today of the Mohr-Coulomb model, and is shown in Figure 2.1 Equation (2.8) is the most common statement of the Mohr-Coulomb failure criterion, suggests that yielding occurs when the shear stresses and the normal stresses satisfy this equation. Where τ and σ are the shear and normal stresses respectively, c and ϕ are the cohesion and internal friction angle of the soil. The functional form of the yield surface of the Mohr-Coulomb criterion is expressed in equation (2.9).

$$\tau = c + \sigma \tan\phi \tag{2.8}$$

$$f = \sigma_1 - \sigma_3 - \left(\sigma_1 + \sigma_3\right)\sin\phi - 2c\cos\phi = 0 \tag{2.9}$$

The Mohr-Coulomb model only consists of a yield surface and lacks assumptions for plastic modulus, and a flow rule or the plastic potential surface. The plastic potential usually takes the same form as the yield surface function (i.e. associated flow rule). Alternatively, to account for dilatancy in cohesionless material, by assumption of a dilation angle (distinct of the friction angle and smaller than the friction angle) a non-associated flow rule can be considered for the Mohr-Coulomb model. The dilatancy angle can be estimated by recommended relationships between the dilation and the friction angle such as given by Bolton (1986), where they are related through the friction angle at critical state.

A limitation to the Mohr-Coulomb model aside from its elastic-perfectly plastic assumption, is the corners and pointed tips, in other words discontinuities of the yield surfaces, which makes it disadvantageous from a computational point of view and return mapping algorithms. Moreover, the Mohr-Coulomb model only takes account the major and minor principal stresses, and does not incorporate effects of the intermediate principal stresses.

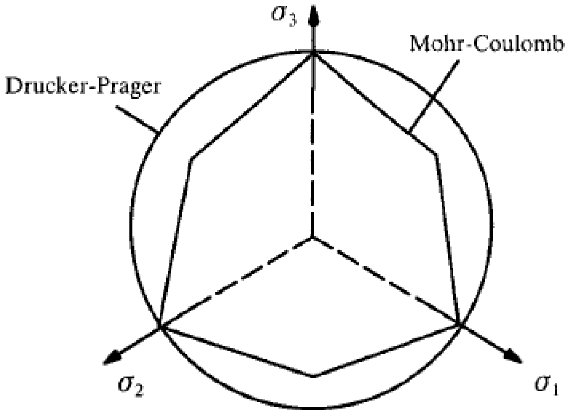

Figure 2.1. Mohr-Coulomb and Drucker-Prager yield surfaces on deviatoric plane (Yu, 2006)

2.4.2 Drucker-Prager Model

The Drucker-Prager model has a circular shape in the deviatoric plane (Figure 2.1) and avoids the discontinuities such as those of the Mohr-Coulomb model. Drucker and Prager (1952) proposed a yield criterion with two material constants considering all principal stresses and the yield function having a mean pressure dependent term. The functional form of the Drucker-Prager yield surface is shown in equation (2.10); first the general form of the yield surface is presented in terms of stress invariants J_2 and I_1, followed by the simplified form of the yield surface in triaxial space. Note that J_2 and I_1 are quite similar to stress invariants q and p' defined previously in this chapter.

To obtain the material constants, the Drucker-Prager yield surface is matched with the Mohr-Coulomb yield surface. These constants are presented at the end of equation (2.10).

$$\begin{gathered}
f=\sqrt{J_2}-aI_1-k=0 \\
\textit{where, }\; J_2=\frac{1}{6}\left[\left(\sigma_1-\sigma_2\right)^2+\left(\sigma_2-\sigma_3\right)^2+\left(\sigma_1-\sigma_3\right)^2\right],\; \textit{and }\; I_1=\sigma_1+\sigma_2+\sigma_3 \\
\textit{simplified form in Triaxial space}: f=\sqrt{\frac{1}{3}}\left(\sigma_1-\sigma_3\right)-a\left(\sigma_1+2\sigma_3\right)-k=0 \\
a=\frac{2\sin\phi}{\sqrt{3}\left(3-\sin\phi\right)}\;\; \textit{and},\; k=\frac{6c\cdot\cos\phi}{\sqrt{3}\left(3-\sin\phi\right)}
\end{gathered} \tag{2.10}$$

The Drucker-Prager yield surface for a cohesionless material with friction angle of 32° is sketched in Figure 2.2. The yield surface is a straight line in *q-p′* space, similar to the Mohr-Coulomb yield surface type. The model has been used quite widely for numerical modeling in geotechnical engineering because of its simplicity. Some studies have shown that the circular shape of its yield surface in the deviatoric plane does not agree well with experimental data and therefore, its use should be considered with caution for important analyses (Yu, 2006). Other than the simplistic yield surface of the Drucker-Prager model, its usage faces some other issues as well. For example, considering an associative flow rule, the plastic potential would have the same shape as the yield surface sketched in Figure 2.2. It can be inferred that at failure, the plastic potential would result in a negative direction for the plastic strain increment vector, indicating volume increase or dilation at failure, which contradicts typical loose sand behavior, which contracts during shear.

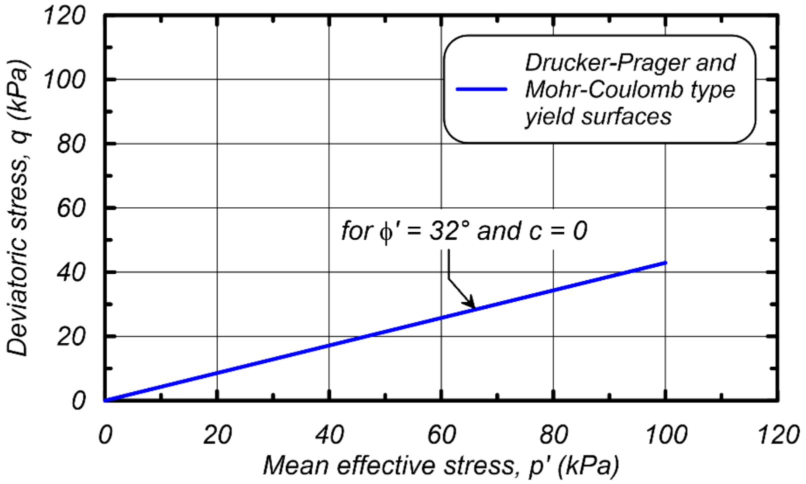

Figure 2.2. Drucker-Prager and Mohr-Coulomb type yield surfaces for ϕ′ = 32° in *q-p′* space

Models such as the Mohr-Coulomb and Drucker-Prager neglect many fundamental features of soil behavior, including plastic volumetric flow under isotropic loading conditions (i.e., do not generate irrecoverable strains in isotropic consolidation), small-strain yielding, and critical state soil mechanics.

2.4.3 Duncan and Chang (1970)

The realistic behavior of soil is nonlinear and not elastic-perfectly plastic, considered by earlier models such as Mohr-Coulomb and Drucker-Prager. To capture more realistic behavior, various functions were adopted and compared for the stress-strain relationships observed from soils, and hyperbolic functions seemed suitable. The Duncan and Chang (1970) model has 6 model parameters, two of which are the Mohr-Coulomb model strength parameters, c and ϕ for the yielding criterion, and the remaining parameters are essentially introduced for the plastic modulus and flow rule. The parameters can all be found by performing a series of triaxial compression tests involving loading, unloading, and reloading. A main limitation of this model is that in the early versions no attempt had been made to relate the volumetric strains to shear strains, similar to the

Mohr-Coulomb and Drucker-Prager models. It is well known that under triaxial conditions, sand dilates and/or contracts under shear, yet the model is merely able to predict shear strains, therefore dilation and contraction could not be captured.

Motivation for capturing the volumetric behavior of cohesionless material in addition to shear yielding, and considering strain hardening or softening, led to the development of the *cap* models, which include these features. Particularly, to capture the volumetric strains during isotropic consolidation, which are plastic irrecoverable strains. The idea came from the Cam-clay and the modified Cam-clay models developed for cohesive soil types by Roscoe and Schofield (1963) and Roscoe and Burland (1968), respectively, where Critical State Soil Mechanics (CSSM) concept was first introduced.

2.4.4 Cam-clay and Modified Cam-clay Models

Though the focus of this chapter is to demonstrate advancements in constitutive modeling for sands, yet the Cam-clay models are introduced herein which were developed for cohesive materials. These models are widely used in practice, and are also compared with the experimental results from Part I of the dissertation in subsequent chapters.

The Cam-clay model [Roscoe and Schofield (1963)] was developed based on the concept of critical state soil mechanics. The critical state in soil is when shear deformation continues for constant stress and zero volumetric strain rate. Alternatively, it can be inferred that at critical state, the plastic volumetric strain increments are zero due to the constant stress conditions. This suggests that at critical state the shear stress invariant is equal to a constant function of the mean principal stress, or in other words, $q = M \cdot p'$, where M is the slope of the critical state line and function of the soil's friction angle. The functional form of the yield surface of the Cam-clay model in triaxial space is presented in equation (2.11). Where p_o is the consolidation pressure.

$$f = q + Mp' \cdot \ln\left(\frac{p'}{p_0}\right) = 0 \qquad (2.11)$$

$$where,\ M = \frac{6\sin\phi'}{3-\sin\phi'}$$

The Cam-clay yield surface (and plastic potential due to associated flow rule) is sketched in Figure 2.1 for M = 1.4. It can be inferred that at low stress ratios ($\eta = q/p'$), the Cam-clay model would predict significant plastic shear strains. For instance, under isotropic consolidation conditions where soil only experiences volumetric plastic strains, the Cam-clay model (due to the direction of plastic flow at $\eta = 0$) would predict significant shear strains which are unrealistic. To overcome this issue, the model was refined and re-presented as the modified Cam-clay model by Roscoe and Burland (1968). The functional forms of the modified Cam-clay yield surface are presented in equation (2.12), and the elliptic yield surface is sketched in Figure 2.3 for M = 1.4. The elliptic shape of the yield surface eliminates deviatoric strains under isotropic loading conditions.

$$f = q^2 - M^2\left[p'\left(p_0 - p'\right)\right] = 0 \qquad (2.12)$$

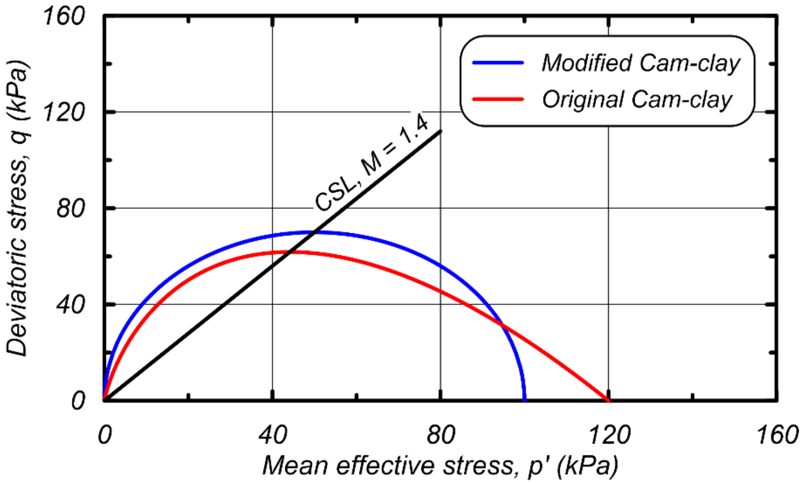

Figure 2.3. The Original and Modified Cam-clay models for M = 1.4

Since the formulation of these yield surfaces is isotropic (the size of the yield surface changes during plastic shearing), their elastic region is quite large after significant yielding, making them not quite suitable for predictions for different stress increment directions such as reverse or cyclic loading conditions. To more accurately model cyclic behavior, Mróz et al. (1979) proposed a modeling technique based on kinematic hardening, where the yield surface translates and rotates during shearing, generally within the context of a larger bounding surface that exhibits isotropic and/or kinematic hardening. Examples include the Cam-clay bubble model developed by Al-Tabbaa and Muir Wood (1989) for clays in which a small "bubble" yield surface moves inside of an isotropic bounding surface (Figure 2.4). Both the yield and bounding surfaces have the shape of the modified Cam-clay model.

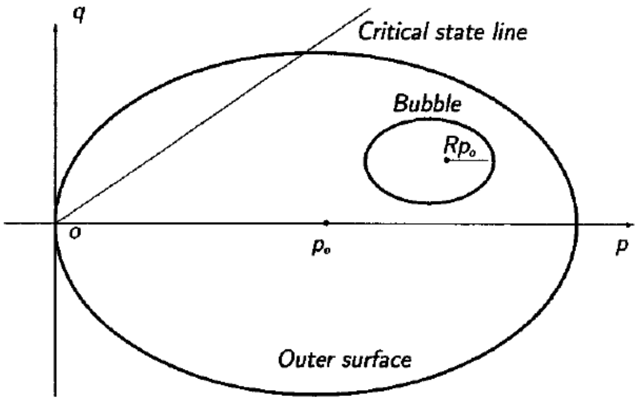

Figure 2.4. Kinematic hardening Cam-clay bubble model by Al-Tabbaa and Muir Wood (1989)

2.4.5 DiMaggio-Sandler Cap Model (1971)

DiMaggio and Sandler (1971) is one of the first *capped* constitutive models adopted for granular material. These models consist of two yield surfaces; the first yield surface (i.e. the failure surface) is fixed, and has the form of a Drucker-Prager criterion, and a second elliptic yield surface (cap) which can evolve during yielding. The cap intersects the first yield surface with an angle that creates no volumetric strain component at the intersection of the two yield surfaces, following the CSSM concept at failure.

The main difference between the cap models and the Cam-clay models is that in the cap models, both the moving cap and the fixed failure surface contribute in defining the yielding process, whereas in the Cam-clay model the cap has the main role in defining yielding and the fixed yield surface is to define the critical state (Khoei, 2005). Perhaps a limitation of such models aside from the fact that they are based on associative flow rule, is that they are not capable of adequately modeling stress-induced soil anisotropy, and that they are also not applicable to cyclic loading conditions, whereas the modeling formulation does not allow cyclic loading.

2.4.6 Lade’s double hardening model (1977)

In the model proposed by Lade (1977), to capture the dilatant behavior of cohesionless material as well as contractive, it is assumed that the strains are divided into three components; elastic, plastic collapse (collapse of the grain structure resulting in volumetric contraction), and a plastic expansive. The elastic strains are computed using Hooke’s law, the plastic collapse component of strains are found from consolidation data using a caped yield surface, and the plastic expansive strains by a second conical yield surface with apex at the origin in the stress space. The two yield surfaces of this double hardening model are presented in Figure 2.5. Note that this figure also contains a “single yield surface in new model” sketch, which is from a single hardening model developed by Lade and Kim (1988) which will be subsequently described in section 2.4.8.

It is important to note that because of equality of the strains in the three principal directions during isotropic consolidation, the strain increment vector coincides with the hydrostatic axis and therefore identical to the outward normal to the cap yield surface, resulting in an *associative* flow rule for the plastic collapse strains. Therefore, both the magnitude and the direction of the plastic collapse strains can be found from the cap yield surface. Further, considering that the failure surface is curved for cohesionless material, a curved yield surface is proposed for the expansive component of plastic strains in the model. This yield surface would have an asymmetric bullet shape with apex at the origin, where the yield surface can expand symmetrically as shearing is taking place. Shapes of both plastic potential surfaces (associative and non-associative) are presented in Figure 2.5(b) and (c).

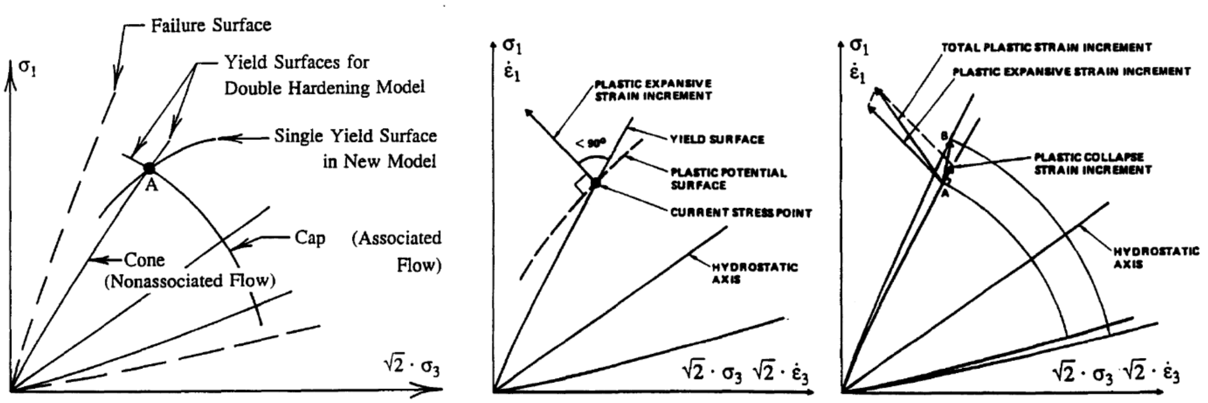

(a) (b) (c)

Figure 2.5. Yield surfaces and plastic potentials in Lade's double hardening model (with revision from Lade and Pradel, 1989)

Poorooshasb et al. (1966), found that an associative flow rule for cohesionless material is inaccurate, and that the plastic potential and the yield surface should not be identical. Therefore, a plastic potential surface was also considered separately. These plastic potential surfaces have a shape similar to the yield surfaces described above, yet with much larger angles at the apex, where they become asymptotic as they get closer to the origin. Moreover, to find the magnitude of the expansive plastic strains, the plastic work has been related to the stresses resulting in a formulation giving the magnitudes of strain. The model has 14 constants in total that can be found from performing isotropic compression and drained triaxial tests.

2.4.7 Vermeer's double hardening model (1978)

To improve predictions for different stress increment directions, Vermeer (1978) developed a double-hardening model for sand consisting of a nonlinear surface for deviatoric yielding (non-associated) and a separate vertical surface (associated) for volumetric yielding The shear yield surface formation is mainly based on experimental findings of Tatsuoka and Ishihara (1974), which will be introduced subsequently in section 2.5.2, where they had observed that the yield surfaces are curved for shear plastic deformation. In addition, they had concluded that varying the stress paths, the shear strains are not altered and that the final stages of stress determine the shear strains. The plastic shear strains are specified by means of a non-associated flow rule also considering dilatancy. Moreover, to capture the purely volumetric plastic strains, a second yield surface perpendicular to the *p* axis in the *q*-*p* plane is adopted, where the volumetric strains are specified using an associated flow rule. A schematic presentation of the shear and volumetric yield surfaces are given in Figure 2.6.

Two major shortcomings of this model are; the pointed tip where the two yield surfaces meet, which creates numerical problems when being solved by a computer. Secondly, the model has fair predictions where the direction of the principal stresses are not changed more than 45 degrees and therefore, is not capable of modeling soil behavior in cyclic compression-extension conditions. Moreover, the formulation in Vermeer's model is isotropic and thus more appropriate for monotonic loading conditions.

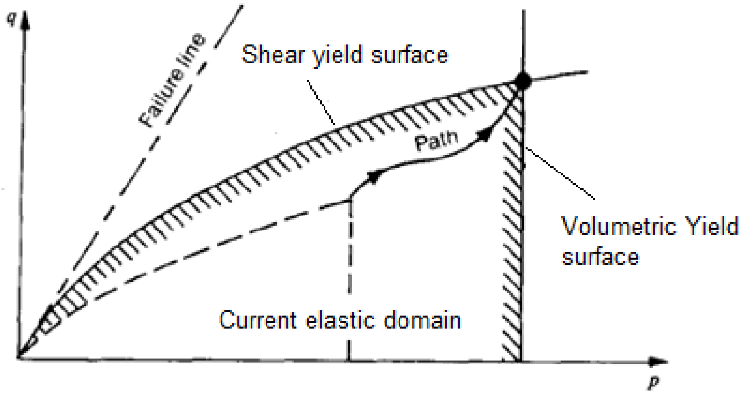

Figure 2.6. Shear and volumetric yield surfaces of Vermeer's double hardening model (with revisions from Vermeer, 1978)

2.4.8 Lade’s Single hardening model (1988)

Having introduced a double hardening model in 1977, Kim and Lade (1988) proposed another model for cohesionless soils, this time considering only one yield surface. The plastic potential surface has the shape of an asymmetric cigar with a smoothly rounded triangular cross section in the triaxial plane as shown in Figure 2.7 (a). The plastic potential is mainly based on the observations from experiments ran by Poorooshasb et al. (1966) and some other laboratory results. These surfaces were adopted with the premise that the plastic potential is independent of the stress path and uniquely developed considering the stress state.

The idea of the shape of the yield surfaces were based on the experimental observations by Tatsuoka and Ishihara (1974) and some experiments ran by the authors. However, in this model the yield surfaces were adopted from equivalent plastic work contours, and have the shape of an asymmetric tear drop in the triaxial plane as shown in Figure 2.7 (b).

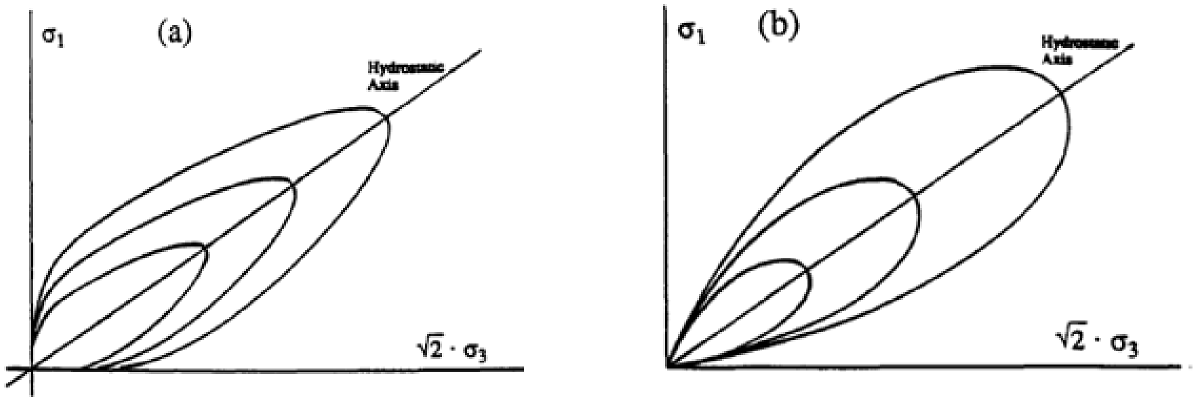

Figure 2.7. (a) Plastic potential surfaces (b) Yield surfaces for single hardening model in triaxial space (with revisions from Kim and Lade, 1988)

Basically, each yield surface would describe a locus that the plastic work is constant, where the yield surface inflates as the plastic work increases until the stress state reaches failure. It is important to note that the model requires twelve material constants which can be obtained by isotropic consolidation and triaxial compression test.

Both the double hardening and single hardening models of Lade (1977) and Kim and Lade (1988) have good accuracy at high stress levels although, the single hardening model is less sensitive to stress path directions. The single hardening model is more computationally efficient than the double hardening model because of having only one yield surface and therefore no discontinuity (Lade and Pradel, 1989).

2.4.9 Multi Surface and Bounding Surface Plasticity Approaches

The described models herein have more or less a good capability of capturing monotonic response of cohesionless soils based on isotropic hardening. Isotropic hardening law considers the size of the yield surface to change during plastic shearing of the material. However, these models face two major shortcomings; (1) they have large elastic regions and fail to capture small-strain nonlinearity preceding failure and (2) they are generally not capable of modeling stress reversals that occur, for example, during cyclic loading (Yu, 2006). To capture the smooth and gradual elastic to plastic transition and to capture the cyclic behavior considering kinematic hardening law, where the center of yield surface is considered to translate in stress space, two main theories were introduced: the multisurface plasticity concept (Mroz, 1967), and the bounding surface plasticity approach (Dafalias, 1986). These approaches account for both isotropic and kinematic hardening, meaning that the yield surface can change in size, and can also move (translate and/or rotate) in a certain direction.

In the multi surface approach (having a series of yield surfaces) and by considering a piecewise linear stress-strain relationship, the most important aspect is to make correct assumptions on how the loading surface is translating in stress space when loaded and/or unloaded. Therefore, different translation rules have been adopted. Prevost (1985) developed a model that can be used for cohesionless material, these models are also known as *nested* models. The yield surface in the Prevost (1985) model has the shape of two straight lines in the *q-p* plane of triaxial similar to the Drucker-Prager model, having a conical shape with apex at the origin (for cohesionless material) in the octahedral plane. The yield surfaces of this model are presented in Figure 2.8 both in the three-dimensional stress space and the triaxial *q-p* space. To find the smooth stress-strain relationship, the stress-strain curves are approximated by linear segments where the secant shear modulus is assumed constant. Therefore, the degree of accuracy by such linearization would be dependent on the number of segments considered (Prevost, 1985).

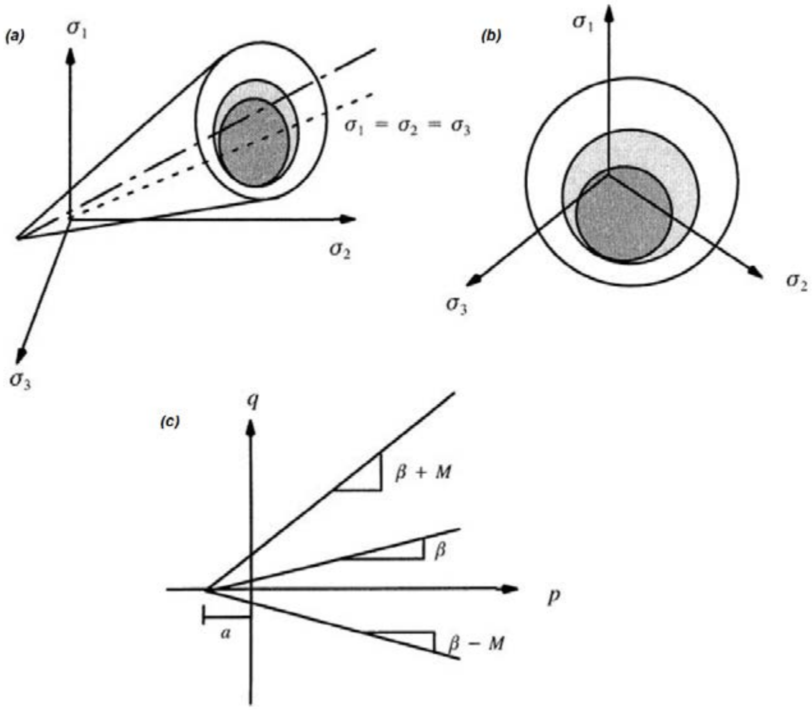

Figure 2.8. Multi yield surfaces of the Prevost (1985) model: (a) and (b) three-dimensional view in stress space, (c) yield surfaces in *q-p* space (figure from Yu,2006)

The consideration of a piecewise linear relationship between stresses and strains makes the multisurface approach incapable of predicting a smooth transition from elastic to plastic behavior in soils. The bounding surface approach on the other hand, having two surfaces namely, the loading surface and the bounding surface, can overcome this limitation. The key aspect of the bounding surface concept is that the hardening of the loading surface is dependent on the distance between a current stress point and an image point on the bounding surface. These models are considerably simpler than the nested models because they consist of much fewer surfaces (Desai, 1984).

Prevost (1982) describes the main pros and cons of two-surface plasticity versus multi surface plasticity theory and reaches to a conclusion that both theories include inherent limitations. The multi surface theory suffering the limitation of storage requirements, having to store all the surfaces, and the two-surface theory having "*a priori* selection of the evolution laws" limitation.

2.4.10 Elgamal et al. (2003) Model

Following the works done by Prevost (1985), Elgamal et al. (2003) propose a model for predicting cyclic mobility and liquefaction of sands using multi-surface plasticity theory. The yield surface has the same as Prevost (1985) but the flow rules and hardening rules have been modified to have more numerical robustness. The (multi) yield surfaces in the octahedral plane can be seen as given in Figure 2.9 having a conical shape. Once more, the shape of the yield surfaces in the *q*-*p* plane would be two lines with different slopes.

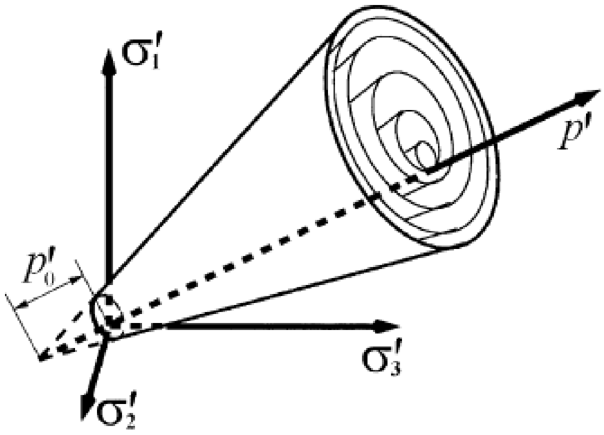

Figure 2.9. Schematic representation of multi yield surfaces in octahedral plane (with revisions from Elgamal et al., 2003)

The yield surfaces are chosen to be open-ended for simplicity without considering a cap. Elgamal et al. (2003) mentions that in the region of interest for geotechncial engineering under normal confining pressures, stress paths usually produce relatively small amounts of strain and therefore, eliminating a cap for the yield surface is considered to be a reasonable simplifacation in this model.

2.4.11 Dafalias and Manzari (2004) Model

The basis of the Dafalias and Manzari (2004) model is bounding surface plasticity accounting for the anisotropy in soil behavior. A more comprehensive definition of bounding surface plasticity is given by Dafalias (1986) as "for any given stress state within or on the bounding surface, a proper mapping rule associates a corresponding "image" stress point on the surface, and a measure of the distance between the actual and image stress points is used to specify the plastic modulus at the actual stress state in terms of a bounding plastic modulus at the "image" stress state". The framework chosen in this model is utilization of general constitutive theories of elastoplasticity combined with the concept of critical state soil mechanics. The authors have showed that the current combination of strategies can be used to construct appropriate soil constitutive models.

To describe the cyclic behavior of soils and pore-water pressure generation under cyclic undrained loading the use of more advanced plasticity modelling concepts such as multisurface plasticity were utilized to capture this type of behavior in soils. Additionally, another important feature that was implemented in those models was the ability to present a singular format of the model for various densities of the sand where previous research work had suggested that the samples of sand would be treated differently when varying in density. To overcome this negative feature, the critical state concept was used to treat sands with different densities with the same constitutive constants. More specifically, the concept of state parameter introduced by Been and Jefferies (1985) was used in the CSSM framework. The state parameter shown by symbol ψ is the difference between the current void ratio (e) of soil in the e-$ln\ p'$ space and the critical state void ratio (e_c). Therefore, when $\psi > 0$, the soil is loose of its critical state, and when $\psi < 0$ the soil is dense of critical relative to the critical state line (CSL). In addition to the critical state line, a dilatancy surface has also been implemented in the Dafalias and Manzari (2004) model, which defines the state that the soil starts dilating. Therefore, at stress conditions above the dilatancy line the soil will dilate, and at conditions beneath the dilatancy line the soil contracts.

The Dafalias and Manzari (2004) model used a narrow open cone type yield surface [equation (2.13)] with apex at the origin obeying rotational hardening of the material. Note that the yield surface is always equal the stress ratio. Figure 2.10 presents a schematic illustration of the yield, critical, dilatancy and bounding lines in the q-p space. Where α is the slope of the bisecting line and called the back stress ratio and ensures kinematic hardening in plasticity, and $2mp$ is the opening of the wedge. Note that η, m, and α are all stress ratio quantities. It is worth noting that the narrowness of the wedge, which is necessary for the cyclic loading simulations and to reduce the elastic region, is controlled by the small value of *m*.

$$f = |\eta - \alpha| - m = 0 \tag{2.13}$$

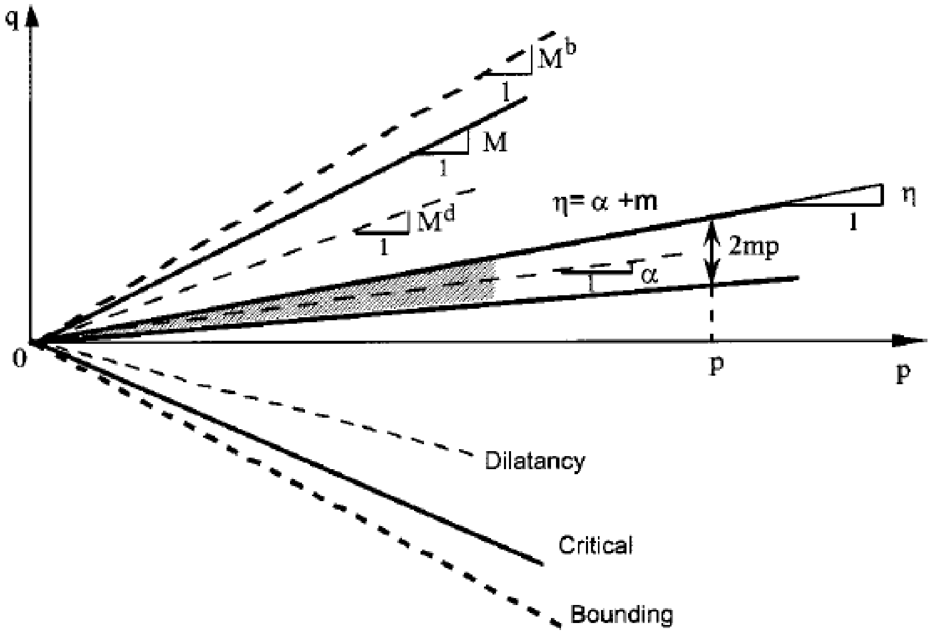

Figure 2.10. Schematic representation of the yield, critical, dilatancy and bounding lines in q-p space (Dafalias and Manzari, 2004)

This model has 11 model constants, divided into the categories of elastic, critical state, state parameter, hardening, and dilatancy that can be calibrated by consolidation and triaxial laboratory experiments. It is important to note that no plastic deformation would be captured by the model, if the stress ratio is held constant; the model only captures plastic strains when the stress ratio is changing. It is evident that in this case the stress path will not cross either of the sides of the yielding wedge shown in Figure 2.10 during constant stress ratio loading, leading to only elastic deformations. An example of η remaining constant is during isotropic and anistropic consolidation, where plastic deformation occur in reality.

2.4.12 SANISAND Model by Taiebat and Dafalias (2008)

To capture the behavior of sand when the stress ratio is held constant, Taiebat and Dafalias (2008) proposed a modified version of the Dafalias and Manzari (2004) model where a closed cap yield surface is introduced. Having the cap, the model would can produce plastic strains even under constant stress ratios. This is important for very loose sand samples with high void ratios under moderate pressures, and for simulation at very high pressures, regardless of density where particle crushing occurs.

It is assumed that the plastic strain rate is decomposed into two parts, the first due to the change in stress ratio and the second, due to loading under constant stress ratio. The closed yield surface can rotate around the origin to capture the reverse loading response of sand and also evolves according to combined isotropic and rotational hardening rules. The functional form of this yield surface is given in equation (2.14).

$$f = (q - p\alpha)^2 - m^2 p^2 \left[1 - \left(\frac{p}{p_0} \right)^n \right] = 0 \tag{2.14}$$

Where again, α denotes the back-stress ratio or the rotational hardening variable of the yield surface, p_0 is the value of p at $\eta = \alpha$ and presents the isotropic hardening, m is the tangent of the half opening angle of the yield surface at the origin which controls the narrowness of the yield surface and is assumed as a very small value. The exponent n is for the closed cap of the yield surface and for instance, can be set to a default value of 20. A schematic representation of this model can be seen in Figure 2.11.

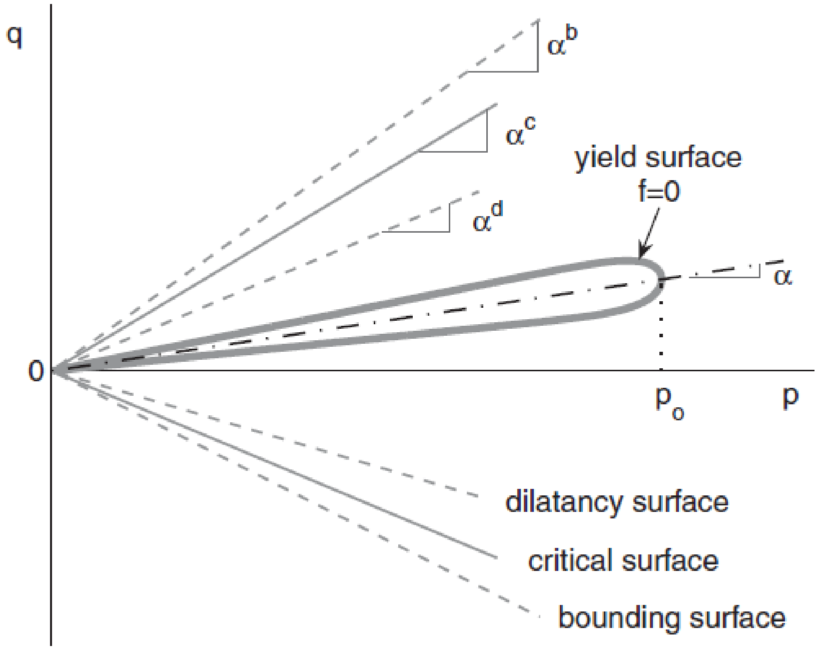

Figure 2.11. Schematic representation of the yield, critical, dilatancy and bounding surfaces in q-p space (Taiebat and Dafalias, 2008)

This model has 16 material constants with the same categorization of the Dafalias and Manzari (2004) model but with the addition of the limiting compression curve (LCC) constants which was itroduced by Pestana and Whittle (1999) suggesting that the LCC and the CSL are approximately parallel at high confining pressures.

As an example, another schematic illustration of rotation and evolution of the yield surface is given in a more sensible fashion in Figure 2.12. It is evident that at first, a change in stess ratio has moved the yield surface rotationally to acertain value which is corresponding to no change in p_0 which in this case is equal to 400 kPa. Following that, when reached to the bounding surface and when a constant stress ratio loading is applied p_0 increases and the yield surface evolves and increases in size.

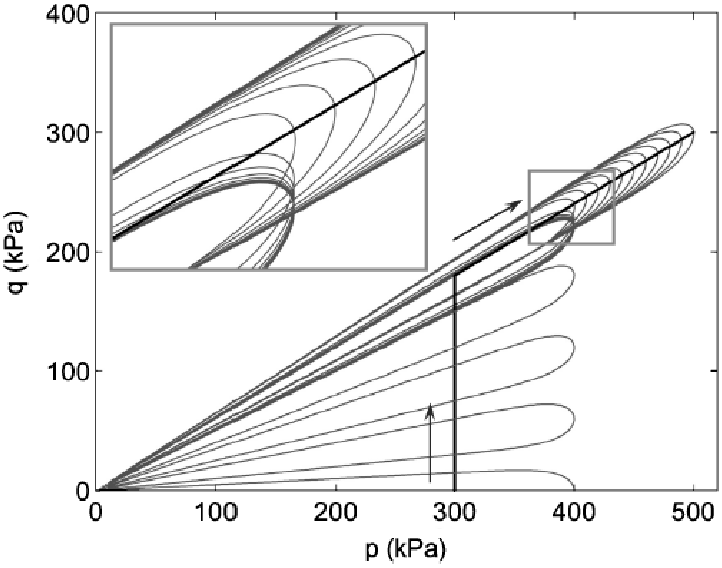

Figure 2.12. Schematic representation of rotation and evolution of yield surface in q-p space during changing stress ratio and constant stress ratio (Taiebat and Dafalias, 2008)

Perhaps the most attractive feature of this model is the cap, which enables the model to capture plastic volumetric strains due to constant stress-ratio loading and also the narrow yield surface, making the model appropriate for cyclic loading conditions. Though implementing the SANISAND model may be more difficult than other simpler models, it can capture features of soil behavior that other models cannot.

2.5 EXPERIMENTAL MAPPING OF YIELD AND PLASTIC POTENTIAL SURFACES

To this point, major contributions in research on soil constitutive modeling has been demonstrated. The following sections focus on experimental studies that have tried to provide insight into the nature of yield and plastic potential surfaces through running complex and very careful laboratory experiments.

2.5.1 Poorooshasb et al. (1966)

One of the first experimental studies on the yielding of cohesionless material was performed by a group of researchers at University of Waterloo, Canada. Poorooshasb et al., (1966, 1967) had combined experimental and theoretical findings of the deformation of Ottawa sand in a triaxial apparatus. In this research, they had more thoroughly adopted the idea that the plastic potentials and yield loci are non-coincidental, contradicting the normality conditions being assumed for cohesive soils such as used in the Drucker-Prager model.

The material tested in the study performed by Poorooshasb et al. (1966), consisted of medium grained and uniform Ottawa sand. Samples were fully saturated and made with initial void ratios of 0.665, 0.555 and 0.465 corresponding to relative densities of 39, 70 and 94 percent, respectively. The six varying stress paths applied to the samples can be seen in Figure 2.13 showing deviatoric stress versus mean effective stress. The inset figure at the top right shows plastic shear strains versus volumetric strains. The correlation between the notation used in Poorooshasb et al. (1966) and the present document has been included in the figure captions. All samples were designed to pass through an arbitrarily chosen mutual point (*a*) to investigate the directions of the increments of strain (volumetric and deviatoric) at this point.

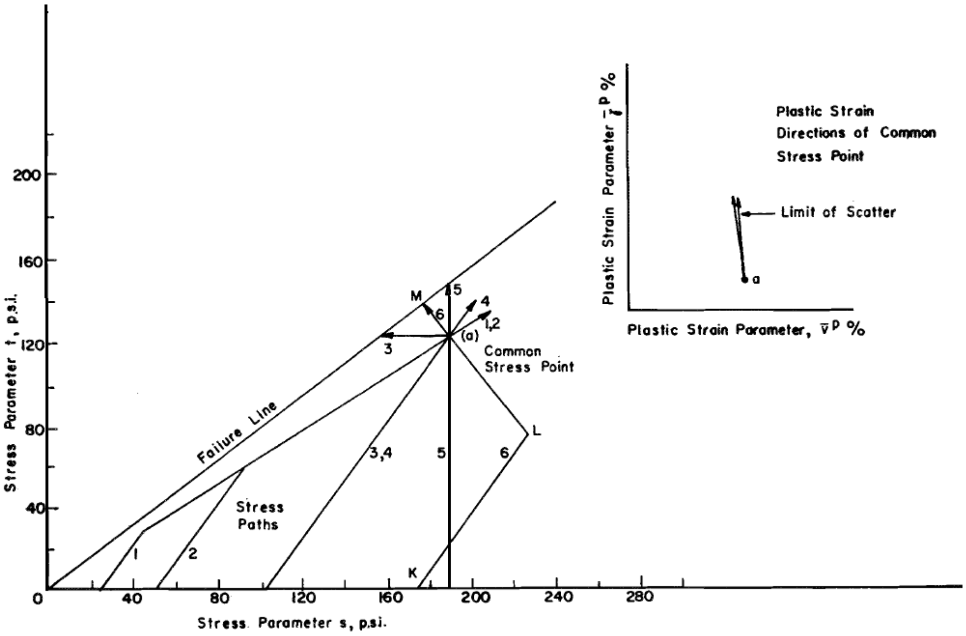

Figure 2.13. Stress paths performed in triaxial apparatus by Poorooshasb et al. (1966) and plastic strain direction, where $t=\sqrt{\frac{2}{3}}q$ and $s=\sqrt{\frac{1}{3}}p'$

The direction of the strain increment which is the resultant of the directions of the volumetric strain and deviatoric strain increment can be seen in the top right plot shown in Figure 2.13. It is evident that no matter which stress path the sample is being tested, the strain increment vector is practically the same at the stress conditions at point (*a*) and unique. Performing the same type of data analysis at different points on the stress paths experiencing various stress conditions, the plastic potential function can be produced.

An example of the set of a family of plastic potentials in the test with initial void ratio of 0.555 can be seen in Figure 2.14, by the dashed curves. The authors have produced these curves considering different values of $\sigma_1/\sigma3$ where it is interesting to note that at the intersection of a specific σ_1/σ_3 line and the plastic potential curves, the strain increment vector is pointing at a unique direction.

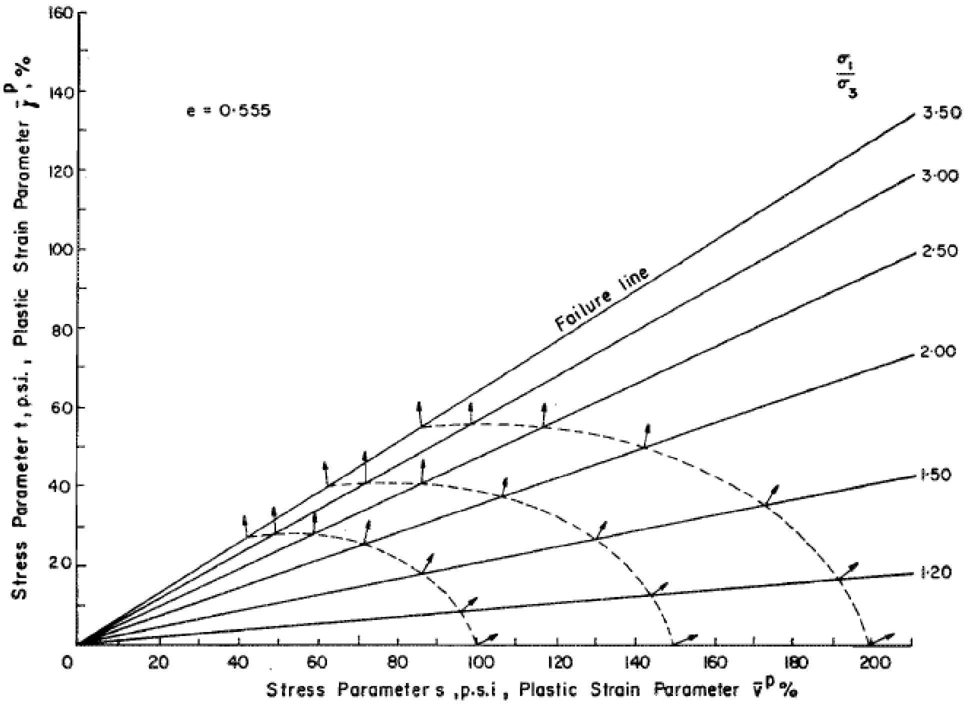

Figure 2.14. Plastic potential curves computed from the inclination of plastic strains (Poorooshasb et al., 1966)

By these experimental findings, Poorooshasb et al. (1966) proved that the plastic potential functions and the yielding surfaces are not identical (i.e. non-associative flow rule in sands). Their work has been continued by studying yielding, the form of the yield loci and the flow rule in the second and third parts of their publication.

The determination of yielding points is done in a manner fairly similar to the procedure of obtaining the maximum stress in an over consolidated clay that has been experienced by the soil in the past. Therefore, by steps of loading, unloading, and reloading, a yield point can be found. The loading, unloading, and yielding points experienced by the samples in the triaxial apparatus are shown in Figure 2.15. These results are presented in the deviator stress vs. axial strain space. Transferring the yield points inferred from Figure 2.15 on the *t-s* plane, Poorooshasb et al. (1967)

suggests that the yield points lay on a straight line and equal to the stress ratio *t/s*. However, later in another publication Poorooshasb (1971) proposed the form of the yield function for the specific sand he had tested in the form of $f = \eta + 0.6 \cdot \ln p$, where, η is the stress ratio (*q/p*). The 0.6 is a calibration constant for the material tested by Poorooshasb (1971).

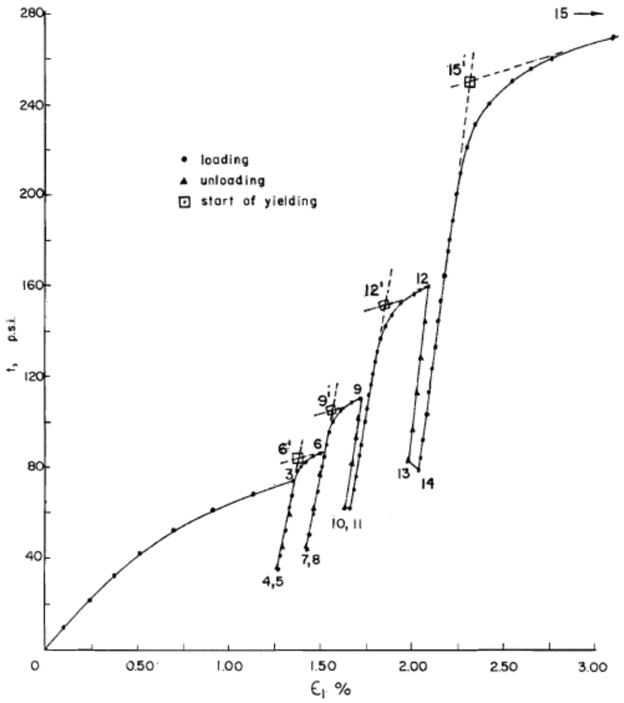

Figure 2.15. Illustration of loading, unloading, reloading, and corresponding yielding points (Poorooshasb et al., 1967)

Perhaps the most important conclusion of this study was to prove that cohesionless material do not obey associative flow rule and therefore, in order to present a model that is able to predict soil behavior more realistically, different sets of equations should be developed for the yield surfaces and plastic potentials. It should also be noted that these yield surfaces were found when the soil was under shear, not representing yielding under consolidation conditions.

2.5.2 Tatsuoka and Ishihara (1974)

Following the study performed by Poorooshasb et al. (1966, 1967), similar research was performed by Tatsuoka and Ishihara (1974). This study was conducted by performing drained triaxial compression tests on fully saturated Fuji River sand at different densities. Again, using the approach of Poorooshasb et al. (1967) by determining the stress states at the points where plastic deformations began to take place, families of yield surfaces were established for various densities of the sand samples. The main motivation to carry this study was that the Poorooshasb et al. (1967) sand samples were prepared in high relative densities (low void ratios). Therefore, Tatsuoka and Ishihara (1974) tried to perform the tests on looser samples of sands to monitor the effect of density.

Maximum and minimum void ratios were reported to be 1.08 and 0.53 respectively. The stress paths used in this investigation are divided into four groups as shown in Figure 2.16, and as it can be seen, type A tests are practically the same as the tests performed by Poorooshasb et al. (1967). Type B tests are similar to type A tests, but the overall mean effective stress is decreasing. A combination of types A and B tests is performed in type C. Tests of type D consisting of more arbitrary stress paths are established to verify the yield loci obtained by test types A, B and C.

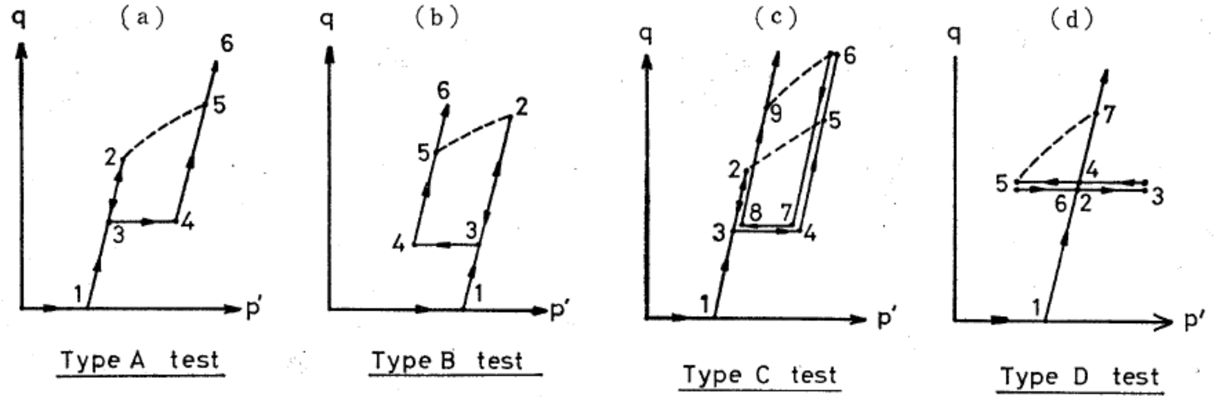

Figure 2.16. Stress paths used in triaxial compression tests performed by Tatsuoka and Ishihara (1974)

It is interesting to note that the stress state at which yielding starts can be defined more clearly in type B tests rather than type A. In order to obtain the yield loci or the yield function, a more elaborate procedure has been used.

It had been mentioned that the samples in the study performed by Tatsuoka and Ishihara (1974) were prepared in various densities. A conclusion that they have made is that the yield loci for loose sand can be uniquely determined irrespective of the stress paths the sample has previously experienced. The presented yield surfaces, are *shear* yield surfaces, used only when the soil is sheared, not considering consolidation conditions. However, the shape of the yield loci in the *q-p* space may vary corresponding to the density of the sand sample being tested. An example of the yield loci obtained from various test types for loose samples are presented in Figure 2.17.

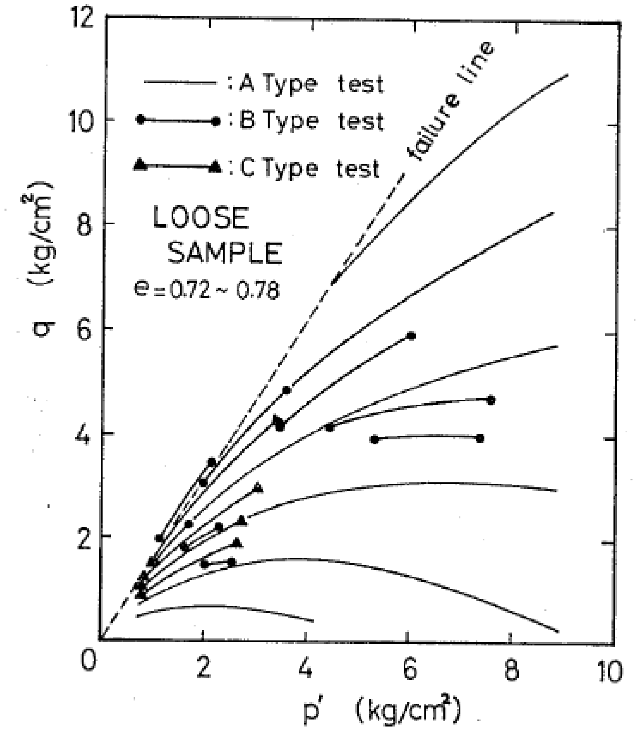

Figure 2.17. Yield surfaces for loose sand samples (figure from Tatsuoka and Ishihara, 1974)

Tatsuoka and Ishihara (1974) have compared their investigation results with that of Poorooshasb (1971). Comparison of results can be seen in Figure 2.18. It is obvious that the yield loci have a curved shape, and also are affected by the densities of the sand samples. It should be noted that all yield loci pass through an arbitrary point (A) in this figure. Figure 2.18 also implies that as the density increases, the curvature of the yield loci will increase, and the slope of the yield surface decreases.

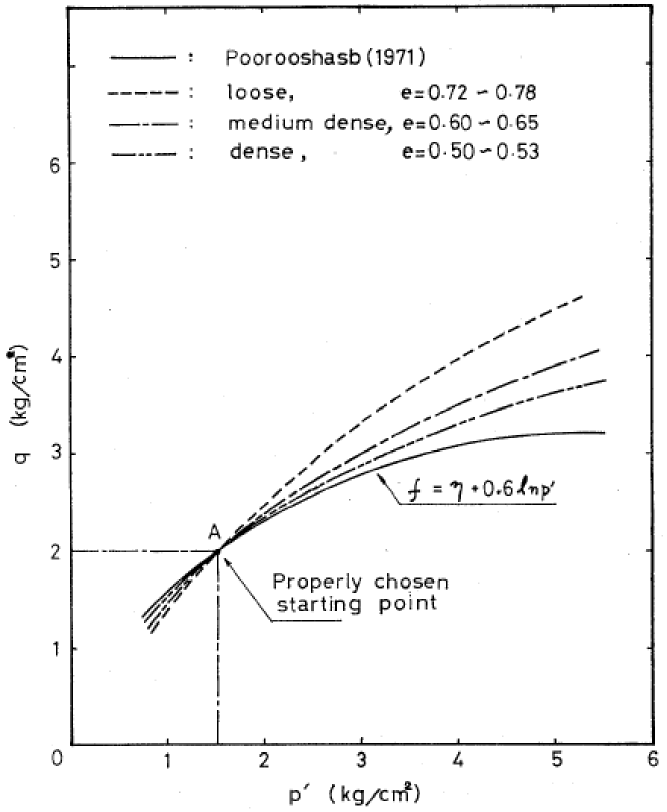

Figure 2.18. Effect of density on shear yield surfaces (from Tatsuoka and Ishihara, 1974)

The authors have also presented another plot comparing their proposed yield surface, with the yield surface of Granta gravel, a yield surface proposed by Schofield and Wroth (1968) which has the same fundamental basis and shape as the Cam-clay model, but for cohesionless material. This can be seen in Figure 2.19, where it is important to notice that during strain hardening in the Granta gravel model, by increase in p' a decrease in q is encountered. However, by test results Tatsuoka and Ishihara (1974) have shown that q is considered to increase as p' increases.

This becomes important when a stress probe AC or AD indicated in Figure 2.19 is applied to the sand sample. Assuming the AC path, Granta gravel would predict yielding in the material whereas the proposed model by Tatsuoka and Ishihara (1974) would result in no yielding of the material. The opposite of this can be seen in stress probe AD where Granta gravel would predict no yielding and Tatsuoka and Ishihara (1974) would predict yielding of the material. In the cases such as stress probe AB, the two models agree on the outcome. Furthermore, by running triaxial tests with stress path type D such as presented in Figure 2.16, Tatsuoka and Ishihara have concluded that the type of yield loci suggested in Granta gravel do not appear to duplicate true soil behavior.

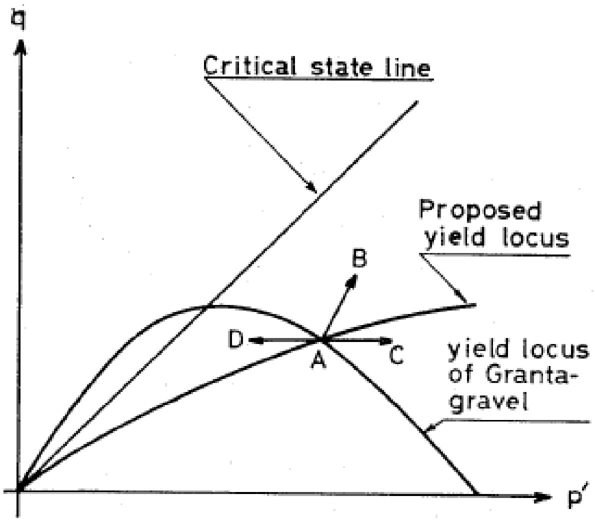

Figure 2.19. Comparison of Granta-Gravel yield surfaces with experimentally obtained yield surfaces (figure from by Tatsuoka and Ishihara, 1974)

2.5.3 Tanimoto and Tanaka (1986)

Perhaps an interesting and also quite different approach was applied by Tanimoto and Tanaka (1986) to observe yielding in sands. Instead of traditional approaches experimentally obtaining yield points from cycles of loading and unloading, they decided to obtain yield points by measuring the acoustic energy released, or in other words acoustic emissions (AE), inside the specimens when plastic deformation occurred. The triaxial tests were performed on decomposed granite at various cell pressures after isotropic consolidation, under two stress paths; constant p', and traditional CD paths.

Results of the yielding points for both the stress paths mentioned in compression and extension can be seen in Figure 2.20. Seemingly, the shape of the yield surface depicted by acoustic emission is qualitatively similar to that of the original Cam-clay model. The study although being interesting in nature, lacks in quantity of the yield points found as shown in the figure, and there are not many observed yield points at lower stress ratios.

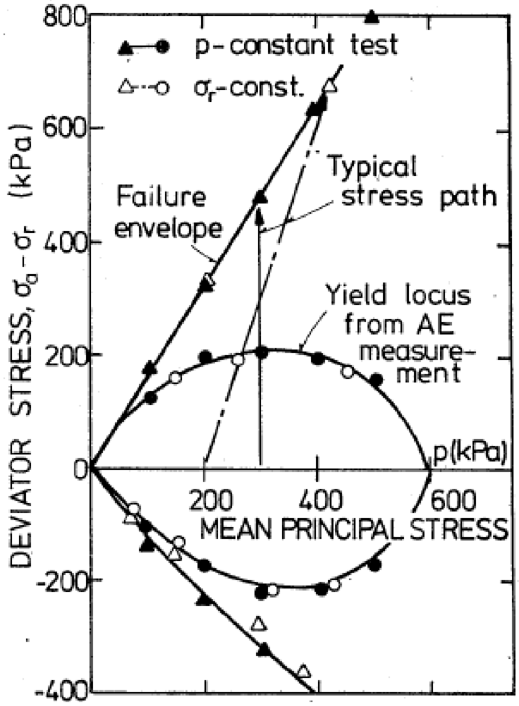

Figure 2.20. Yield surface as determined by Acoustic Emission (AE) (figure by Tanimoto and Tanaka, 1986)

2.5.4 Yasufuku et al. (1991)

Yasufuku et al. (1991) tried to find yield points in over consolidated Aio sand (mostly of quartz and feldspar), both at low (1.5 MPa) and high (25 MPa) cell pressures. The samples were consolidated to point (A) as shown in Figure 2.21, either anisotropically as in Figure 2.21 (a and c), or isotropically as shown in Figure 2.21 (b) and then unloaded to point (B) before shear. After this, the samples were sheared according to the different stress paths shown by the numbers implemented in Figure 2.21.

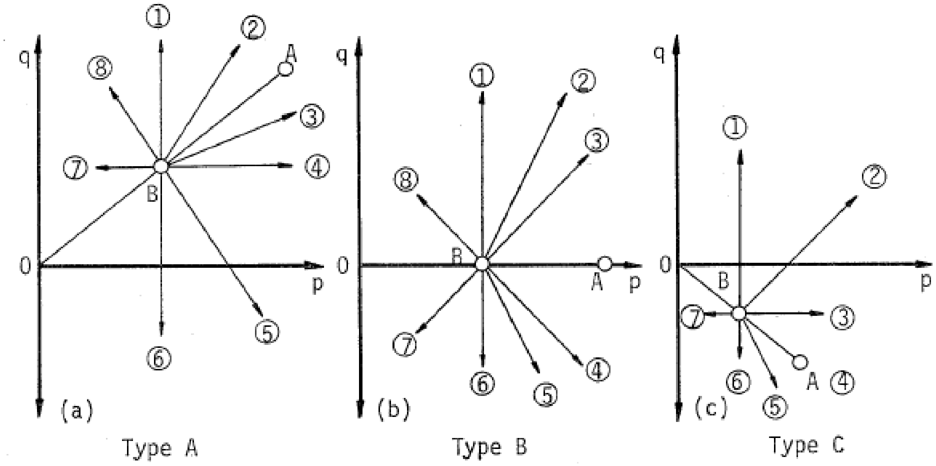

Figure 2.21. Stress paths for determination of yield points corresponding to point (A) (a) anisotropic consolidation or Type A, (b) isotropic consolidation or Type B, (c) anisotropic extension or Type C (figure from Yasufuku et al., 1991)

Following the stress paths, the yield points corresponding to point (A) were then obtained for each stress path, using the stress-strain curves and the procedures similar to Poorooshasb et al. (1967). These yield points were also compared with strain energy dissipations at these points to clearly identify if yielding has occurred. Here, the yield curves obtained for type (A) both for low and high stress levels, and type (B) at low stress levels are demonstrated in Figure 2.22(a) and (b), respectively. Note that the high stress level yield surfaces are drawn on a 0.1 scale so that they can be compared to the yield surfaces at lower stress levels in shape.

From Figure 2.22 it is obvious that the consolidation history of the samples result in different shapes of the yield surface and that neither of the yield surfaces are symmetric with respect to the *p* axis. Another important observation is the strain increment vectors are not perpendicular to the yield surface, an indication of non-associative flow for sands. Moreover, it is interesting to note that at *q=0*, the plastic strain increment vector is pointing downward, indicating an accumulation of plastic shear strain at hydrostatic pressure.

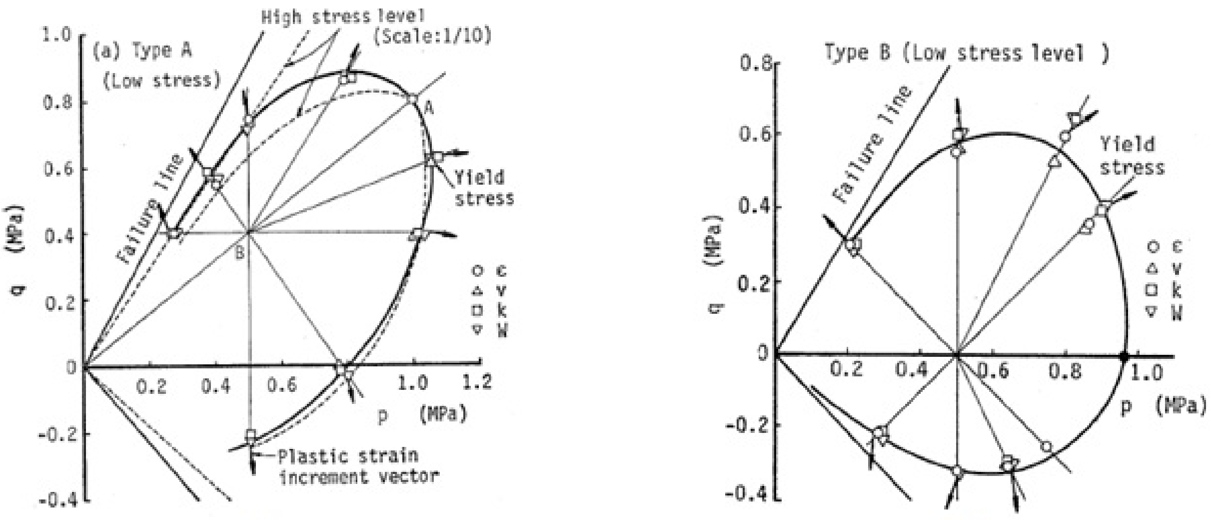

(a) **(b)**

Figure 2.22. Experimental yield curves obtained from (a) Type A tests both at low and high confining pressures, (b) Type B tests at low confining pressures (with revisions from Yasufuku et al., 1991)

To formulate the yield surface in a functional form, the authors have assumed that the slope of the yield surface is proportional to the stress ratio and an internal parameter. Fitting a hyperbolic function relating the stress ratio to the slope of the yield surface, a yield surface function was obtained close to the experimental findings.

2.5.5 Kuwano and Jardine (2007)

Through a number of triaxial experiments, four progressive phases of yielding in sands were identified by Kuwano and Jardine (2007). Lightly overconsolidated as well as normally consolidated specimens in drained and undrained conditions and at various densities where sheared and the direction of the stress paths were changed to map such yield surfaces. The tests were performed in four different configurations. Yielding points and the tentative shape of the yield surfaces as well as the direction of the plastic flow at each yield point is sketched in Figure 2.23 by the dashed lines. A large number of the tests are required for interpretation of the yield surfaces. The Y3 surfaces are analogous to the large-scale shear yield surfaces obtained by previous studies.

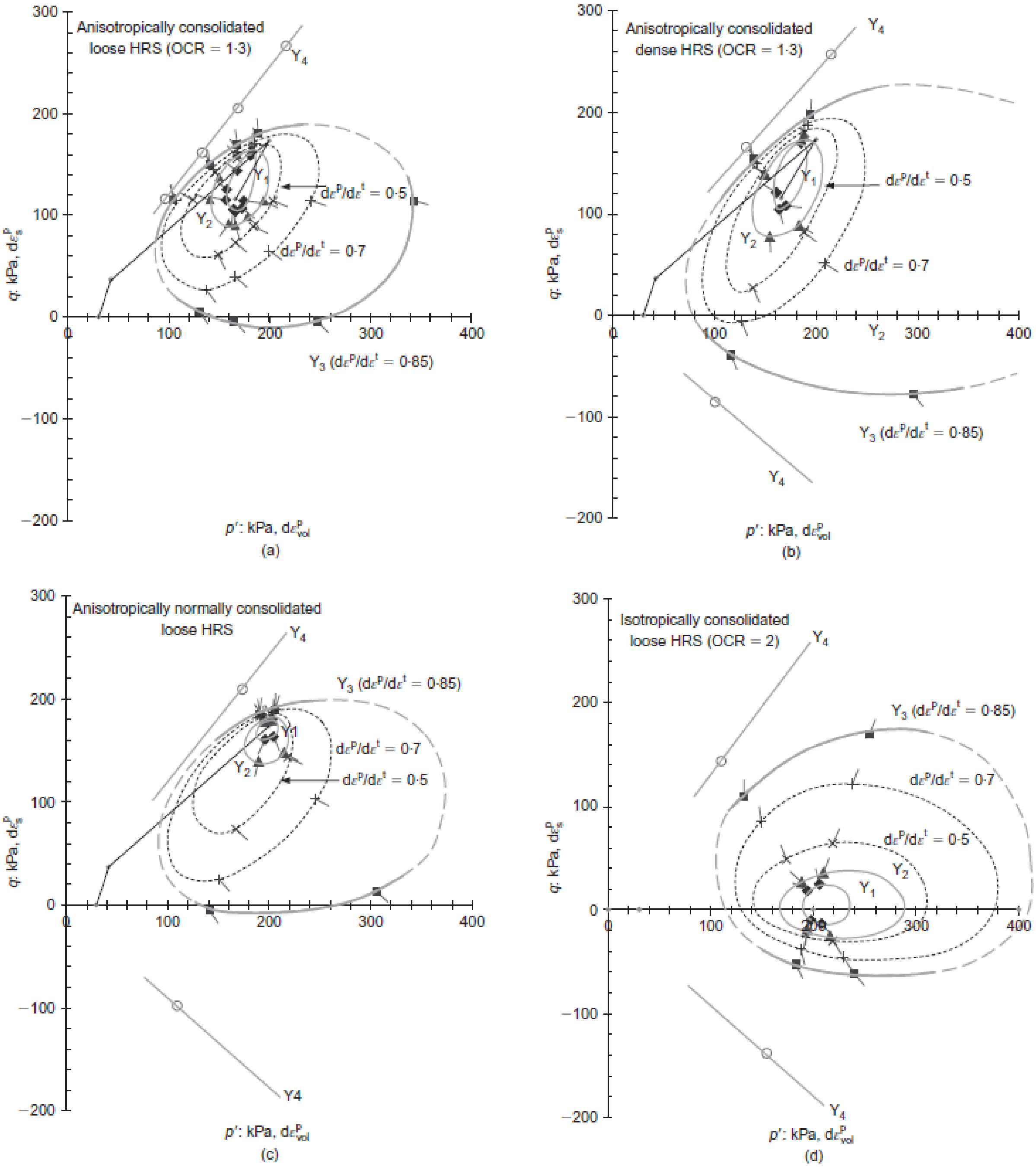

Figure 2.23. Experimental yield curves obtained by Kuwano and Jardine (2007)

3 Methodology, Laboratory Equipment, and Procedures for Part I

Following the historical developments on soil constitutive modelling given in Chapter 2, this chapter mainly focuses on the methodology applied in Part I of the dissertation to directly measure the yield surface and plastic potential slopes for sand. First, the motivation for such research is described, then the incremental formulations and laboratory procedures are explained.

3.1 INTRODUCTION

Illustrated in Figure 3.1 are commonly used models in geotechnical engineering practice, which exhibit significant differences in the treatment of yield surfaces and plastic potential surfaces. These models were introduced in Chapter 2. Interestingly, although the shape of their yield surfaces are notably different, all these models have been shown, by their authors, to produce reasonable predictions for monotonic conventional laboratory tests. It suggests that the input parameters can be tuned to compensate for differences between the experimental and theoretical yield surfaces and flow rules.

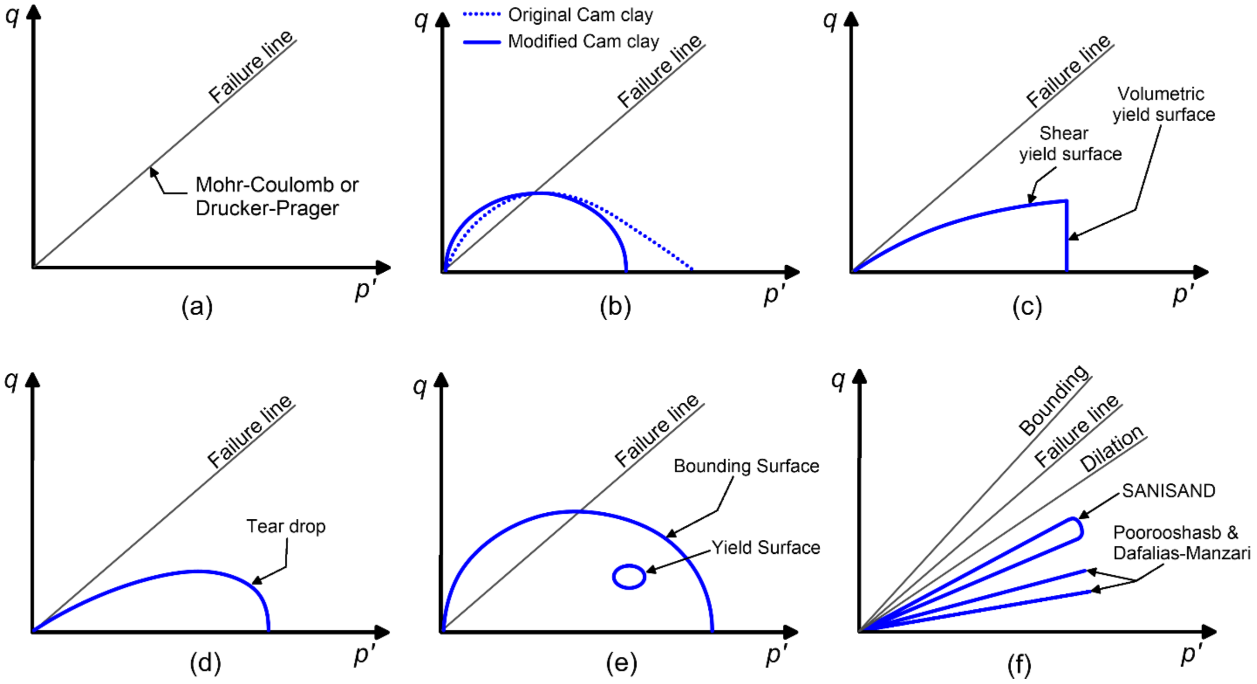

Figure 3.1. Examples of yield surfaces, *f* = *0*, used for geotechnical applications (a) Mohr-Coulomb and Drucker-Prager; (b) Original and modified Cam-clay (Roscoe and Schofield, 1963 and Roscoe and Burland, 1968); (c) Vermeer's Double hardening model (Vermeer, 1978); (d) Tear drop shaped surface from Lade and Kim (1988), (e) Cam-clay bubble model (Al-Tabbaa and Muir Wood (1989), and (f) Drucker-Prager type kinematic hardening surfaces, Poorooshasb and Pietruszczak (1985), Dafalias and Manzari (2004), and SANISAND (Taiebat and Dafalias, 2008)

The appropriateness of the slope of the yield surface is nevertheless very important for the accurate predictions of problems involving more complex stress paths. For instance, if a normally consolidated soil is subject to plastic shear loading followed by a significant increase in pore water pressure under sustained shear, the predicted behavior during the initial stress increment would be:

- ➢ Elastic, according to Cam-clay (Figure 3.1b) and conventional cap models;
- ➢ Plastic, according to double hardening, Dafalias, and Poorooshasb models (Figure 3.1c and f), which would result in irrecoverable strains;

- Elastic or plastic, depending on the stress level according to models having tear-drop shaped surfaces (Figure 3.1d).

Although numerous expressions have been proposed for the yield surface (f = 0) and plastic potential (g = 0) by geotechnical researchers, there are relatively few experimental studies that have attempted to determine their actual shape. Previous experimental studies can be classified according to the following categories, which were discussed in Chapter 2.

- Tests containing cycles of loading, unloading, and reloading (e.g., Poorooshasb et al., 1966 and 1967, Poorooshasb, 1971, Tatsuoka and Ishihara, 1974, Tatsuoka and Molenkamp, 1983, Pradel et al., 1990, Yasufuku et al., 1991, and Nawir et al., 2003), as exemplified in Figure 3.2;
- Acoustic emission tests (Tanimoto et al., 1986);
- Tests in which the strain path is suddenly changed and plastic strains, slopes as well as moduli are calculated (e.g., Pradel and Lade, 1990, Kuwano and Jardine, 2007);

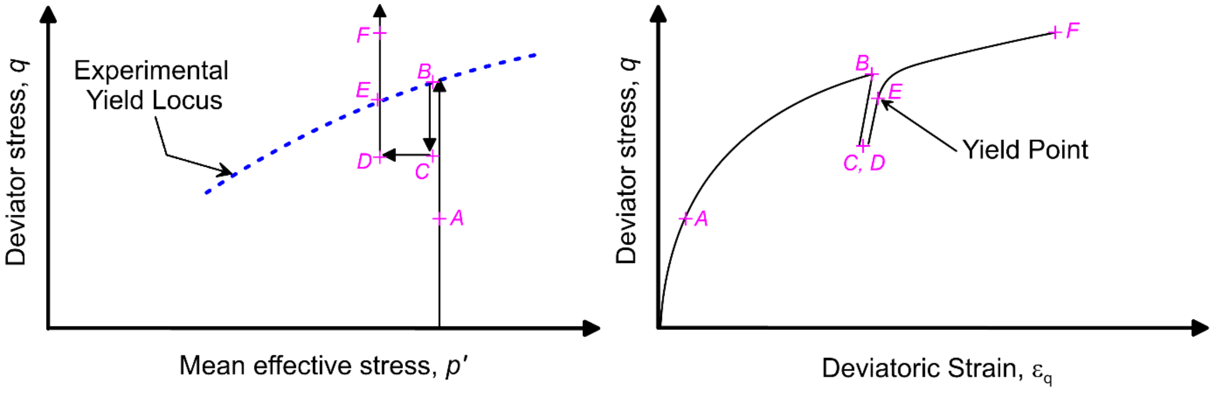

Figure 3.2. Test with cycles of loading and unloading used for the determination of the yield surface

Generally, studies belonging to the first group have been used to investigate what Tatsuoka (2006) describes as “large-scale shear yielding”, and have produced open-type yield surfaces with shapes that are similar to the ones in Figure 3.1 (c and f). Size and mode of shearing can affect the yield surfaces as cautioned in Tatsuoka and Molenkamp (1983). More recent studies by Nawir et al. (2003) have focused on viscous effects by imposing distinct strain rates during cycles of loading and reloading. The method is powerful, however, the tests necessary tends to be numerous, complex, and require careful interpretation. Interpretation can be especially difficult when:

- The mean effective stress, p', increases significantly, which results in both shear and volumetric yielding mechanisms according to double hardening models (Figure 3.1c);
- The unloading cycles produce large loops and irrecoverable strains;
- Yielding occurs near the failure line and mobilizes large strains.

The use of acoustic emissions to determine the shape of the yield surface requires not only specialized equipment (Tanimoto and Tanaka, 1986), but also requires sufficient noise generated by slippage and/or crushing of soil particles to accurately differentiate ambient noise from the acoustic emissions generated by yielding. Hence, the contributions from this methodology have been relatively limited.

The third methodology was used by Kuwano and Jardine (2007) to study kinematic yielding and Pradel and Lade (1990) to study the conditions leading to static liquefaction of saturated and partly saturated sands at a specific state of stress. Both studies involved a large number of tests. For example, Pradel and Lade (1990) used a total of four triaxial tests from which moduli were measured to obtain the slopes of the yield and plastic potential surfaces at a single point in the q - p' plane. Hence, the applicability of these methods to a wide range of stresses is generally not practical.

The main purpose of the present study is to extend the work by Pradel and Lade (1990) to experimentally obtain the slopes of the yield and plastic potential surfaces. This method is based on the incremental formulation of the deformation (or flow) theory of plasticity, and incorporates short undrained perturbations during a drained triaxial test with a vertical stress path. The tests can be performed on a traditional triaxial compression testing device without the need for specialized equipment, which makes the method attractive for routine use.

3.2 THEORETICAL BACKGROUND AND INCREMENTAL FORMULATION

As mentioned in Chapter 2, strains can be decomposed into elastic (fully recoverable) and plastic (irrecoverable) components. For a time-independent material this postulate was expressed incrementally as shown in equation (2.7). The theory of plasticity also postulates that a boundary exists in the stress space between elastic and plastic behavior. This boundary, namely the yield surface, is defined by a mathematical function, *f*, that describes a convex surface in the six-dimensional stress space as $f(\sigma_{ij}) = 0$. During loading (yielding), the direction of the plastic strain increments is perpendicular to a plastic potential surface, defined by a mathematical function, g, as $g(\sigma_{ij}) = 0$. Plastic loading resulting from an effective stress increment, $d\sigma_{ij}$, results in the plastic strain increment given in equation (3.1) by Pradel and Lade (1990). Details of the derivations to arrive at equation (3.1) are provided in Appendix A.

$$d\varepsilon_{ij}^{p} = \frac{1}{h}\frac{\partial g}{\partial \sigma_{ij}^{'}}\frac{\partial f}{\partial \sigma_{kl}^{'}}d\sigma_{kl}^{'} \tag{3.1}$$

Where, *h*, is the plastic hardening modulus (which is a function of hardening variables such as void ratio, previous stress history, stress, and strain invariants).

In most elastoplastic models, the surfaces *f* and *g* are expressed in terms of the deviatoric and mean effective stress invariants, *q* and *p′*, respectively, as defined in equations (2.1) and (2.2) for conventional triaxial space.

The introduction of local linear approximations for the yield surface (e.g., $f = q - \mu . p' - I_f = 0$) and plastic potential (e.g., $g = q - \eta_{pp} . p' - I_g = 0$), adopted from Figure 3.3, into equation (3.1) provides the expressions provided in equations (3.2) and (3.3), for the deviatoric and volumetric strains during plastic loading, respectively. Note that the I_f and I_g are intercepts of the slope of the yield surface and the plastic potential with the y-axis in Figure 3.3, and μ and η_{pp} are the slopes of the yield surface and plastic potential, respectively.

$$d\varepsilon_q^p = \frac{1}{h}\frac{\partial g}{\partial q}\left(\frac{\partial f}{\partial q}dq + \frac{\partial f}{\partial p'}dp'\right) = \frac{1}{h}\left(dq - \mu \cdot dp'\right) \tag{3.2}$$

$$d\varepsilon_v^p = \frac{1}{h}\frac{\partial g}{\partial p'}\left(\frac{\partial f}{\partial q}dq + \frac{\partial f}{\partial p'}dp'\right) = \frac{-\eta_{pp}}{h}\left(dq - \mu \cdot dp'\right) \tag{3.3}$$

Where μ and η_{pp} are tangent slopes of the yield and plastic potential surfaces in the q - p' plane at the current stress point, shown in Figure 3.3. As presented by Pradel and Lade (1990), the total strains are obtained by summing the elastic (defined by equations (2.5) and (2.6)) and plastic strain increments. The summation is provided in matrix form as shown in equation (3.4).

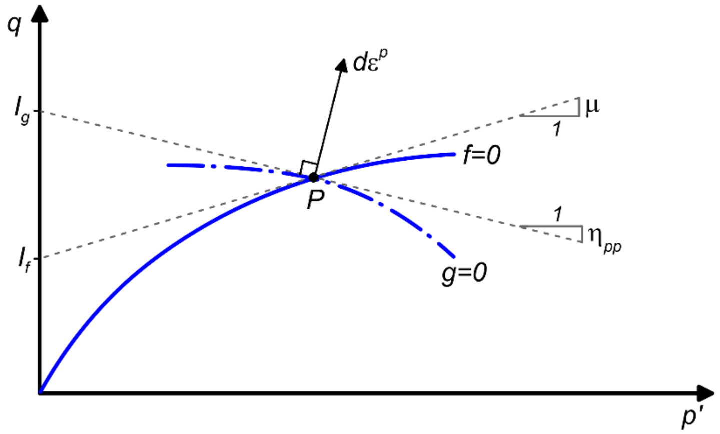

Figure 3.3. Schematic representation of the yield surface, plastic potential and the gradients to these surfaces and the plastic strain increment at point P in the triaxial space

$$\begin{pmatrix} d\varepsilon_q \\ d\varepsilon_v \end{pmatrix} = \begin{pmatrix} \left(\dfrac{1}{3G}+\dfrac{1}{h}\right) & \dfrac{-\mu}{h} \\ \dfrac{-\eta_{pp}}{h} & \left(\dfrac{1}{K}+\dfrac{\mu\cdot\eta_{pp}}{h}\right) \end{pmatrix} \cdot \begin{pmatrix} dq \\ dp' \end{pmatrix} \tag{3.4}$$

Where G and K are the shear and bulk modulus of the soil.

3.3 EXPERIMENTAL APPLICATION OF PROPOSED METHOD

During loading equation (3.4) provides two equations that are derived from the five elastoplastic material properties: G, K, h, μ, and η_{pp}. Though equation (3.4) is strictly applicable at a single point, it is approximately valid for small stress increments within the region where the linearized form is approximately equivalent to the surfaces. To measure these properties, first the elastic moduli, G and K, are measured using small volumetric and deviatoric load paths, or another suitable means such as bender element tests. Because G and K depend on p' for soil, maintaining a constant value of p' is advantageous during shearing. To measure h, μ, and η_{pp}, a triaxial compression test (as illustrated in Figure 3.4) is performed using the following steps:

- A vertical stress path is first applied under drained loading conditions (points A to B in Figure 3.4), and values of $d\varepsilon_q$, $d\varepsilon_v$, and dq are measured;
- The drain valve is closed to provide a small undrained perturbation (e.g., between points B to C in Figure 3.4), and values of $d\varepsilon_q$, dq, and dp' are measured.
- The drain valve is slowly opened (at point C).

The process described above is repeated at multiple points along the stress path.

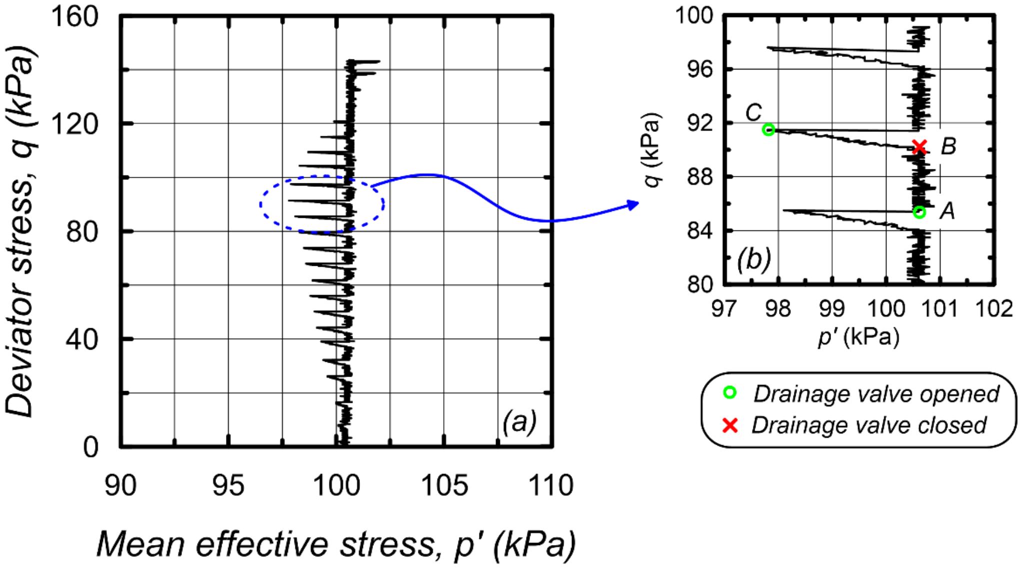

Figure 3.4. Stress path of drained p' constant triaxial test with a short undrained portion (the scale of the horizontal axis has been stretched for illustrative purposes)

During the drained shearing phase, values of h and η_{pp} are computed using equations (3.5) and (3.6), respectively, which are obtained by solving equation (3.4) with $dp' = 0$.

$$h = \frac{1}{\frac{d\varepsilon_q}{dq} - \frac{1}{3G}} \tag{3.5}$$

$$\eta_{pp} = -\frac{d\varepsilon_v}{dq} h \tag{3.6}$$

The value of μ is solved from the undrained loading phase using equation (3.7), obtained after making appropriate substitutions into the portion of equation (3.4) corresponding to $d\varepsilon_q$ (i.e., the top line in the equation), and using the value of *h* found from equation (3.5).

$$\mu = \left[\left(1 + \frac{h}{3G} \right) \frac{dq}{dp'} - \frac{d\varepsilon_q}{dp'} \right] \tag{3.7}$$

Note that $d\varepsilon_v = 0$ for undrained loading (i.e., the bottom line of equation (3.4)) provides an expression for a residual that should equal zero, and therefore provides a means of assessing the quality of the measurements. Equation gives the resulting residual equation (3.8).

$$0 \approx \mathrm{R} = \frac{-\eta_{pp}}{h} dq + \left(\frac{1}{K} + \frac{\mu \cdot \eta_{pp}}{h} \right) dp' \tag{3.8}$$

3.4 TRIAXIAL APPARATUS

A GCTS STX-50 pneumatic triaxial device (Figure 3.5) was utilized to perform the experiments presented herein. The device is equipped with an internal load cell so that friction between the piston and the bushing is not included in the vertical force measurement. Vertical displacements were measured using an LVDT mounted on the piston outside of the cell. Volume change was measured by a differential pressure transducer measuring the difference in pressure between the top and bottom of the burette. The stock burettes that come with the device have a diameter of 17.4 mm, which is rather large. To enhance the accuracy of the volume change measurements, a smaller burette with a diameter of 6.3 mm was installed on the device. Pore pressure was measured using a pressure transducer installed between the bottom of the specimen and the valve on the line coming out of the cell. This position avoids errors in volume change arising from volumetric compliance of the plastic tubes connecting the specimen to the burettes.

Figure 3.5. GCTS STX-050 electro-pneumatic cyclic triaxial device with PCP-200 pressure control panel

The cylindrical specimens had a height of 150mm and a diameter of 71mm. The rubber latex membranes used were 0.5mm thick. The top and bottom platens of the triaxial apparatus were not lubricated, which may contribute to experimental errors due to shear stresses on the top and bottom surfaces. Membrane penetration was not measured, but is expected to be small because the sand is fine relative to the membrane thickness.

The triaxial test configuration utilized herein is fairly standard, and can be replicated in many high-quality testing laboratories. This makes the procedure presented herein approachable for routine application. The influence of measurement errors is quantified by calculating confidence limits on the computed plasticity parameters. The confidence limits include the influence of measurement noise on the computed quantities. More advanced measurement techniques, such as internal displacement or strain measurements, lubricated top and bottom caps, or image analysis of the surface displacement field could improve the data quality, thereby reducing the range of the confidence limits. However, these techniques are available only in very specialized laboratories.

3.5 EXPERIMENTAL PROCEDURES

This section provides explanations on the triaxial testing procedures of Part I of the dissertation.

3.5.1 Tested material, Sample Preparation, and Saturation

The material tested was a clean "Orange County Silica sand-mesh 60", with a mean grain size D_{50}, of 0.3 mm, a coefficient of uniformity $C_u = 2$ and a coefficient of curvature $C_c = 1.24$. This sand classifies as SP according to the Unified Soil Classification System (ASTM D2487). The sand and corresponding grain size distribution curve are shown in Figure 3.6 and Figure 3.7, respectively. The minimum and maximum void ratios for the sand were $e_{min} = 0.792$ and $e_{max} = 0.958$.

Figure 3.6. Orange County Silica sand, mesh 60

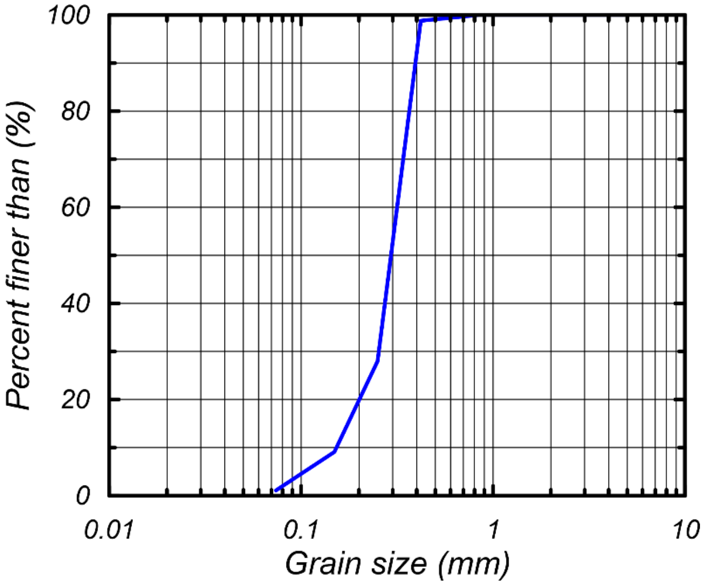

Figure 3.7. Orange County Silica sand grain size distribution curve

The slope of the yield surface depends on the measurement of pore pressure change during small undrained perturbations. To enhance the pore pressure response, the specimens were prepared as loose as possible. A plastic tube with a fine mesh at the bottom was first inserted into the specimen mold with the mesh resting on the bottom porous stone. The outside diameter of the tube was slightly smaller than the inside diameter of the triaxial mold. Dry sand was then placed into the plastic tube, and the tube was raised very slowly so that the sand particles were pluviated at essentially zero drop-height. The average void ratio of the dry samples prior to consolidation was 0.955, which corresponds to a relative density of about 2% prior to testing. The samples were subsequently isotropically consolidated, which caused the relative density to increase slightly but still remain under 10%. Samples were flushed with CO_2 prior to saturation with de-aired water, and back pressure saturation was used to achieve B-values ($B = \Delta u / \Delta \sigma_3 \times 100\%$) larger than 95%. The average saturated unit weight of the samples was 18.1 kN/m^3, and their dry unit weight was on average 13.3 kN/m^3. Steps of preparing the samples are exemplified in Figure 3.8

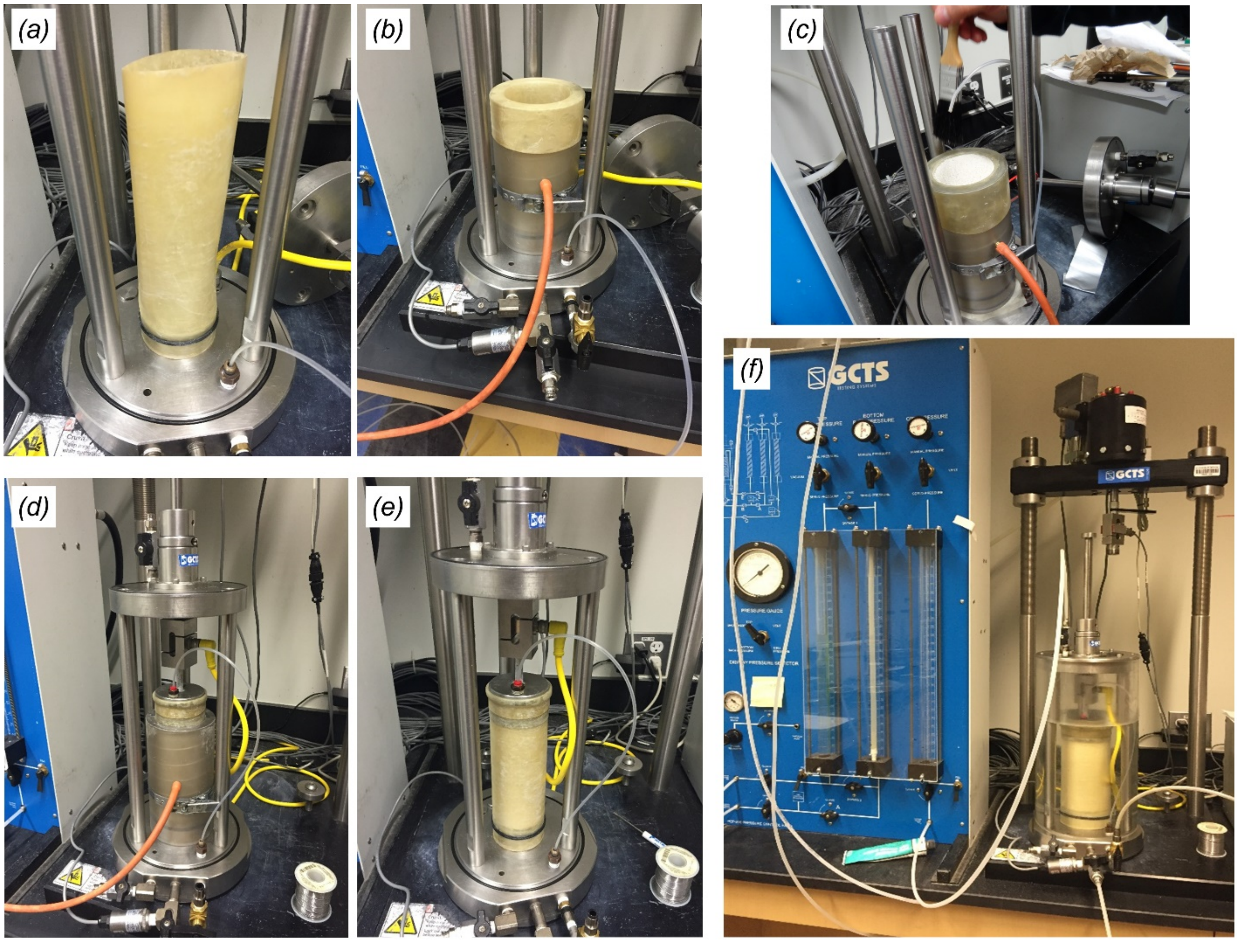

Figure 3.8. Stages of Specimen preparation; (a) assembling the rubber latex membrane and O-ring, (b) assembling the mold and applying vacuum prior to pluviation of the sand, (c) sand slowly pluviated within the mold, trimming the top of the specimen, (d) top platen and loading rod attached to the specimen, (e) mold removed, specimen under vacuum, (f) cell assembled and filled with water, vacuum released and cell pressure applied

3.5.2 Consolidation

Before the shearing stages, the sand sample had to be gradually taken to the required effective stress conditions. This was done by applying cell pressure to the sample while keeping the back pressure of the system constant and allowing free movement of the loading piston on top of the sample. Isotropic compression was manually performed by increasing cell pressure in increments of 20 to 50 kPa. The high permeability of the sand allowed excess pore water pressures to dissipate rapidly and therefore the consolidation process was quick. Before the end of consolidation, an unload – reload step was applied to the specimens for validation of Bulk modulus measurements.

3.5.3 Monotonic Shear

Once the required effective stress condition had been achieved by the consolidation stage, monotonic shear would begin. Testing was conducted for mean effective consolidation stress values of p'= 100, 150, 200, 250, 300, 350 and 400 kPa. Constant mean effective stress conditions (vertical q-p′ stress paths) were obtained using stress-controlled loading and by decreasing the cell pressure as follows: $\Delta\sigma_3 = - q/3$. A computer control system was utilized to achieve the desired stress path.

During drained loading, the drain tap connected to the specimen was periodically closed to impose a small undrained loading perturbation on the specimen. These perturbations manifest as sudden changes in p' as previously presented in Figure 3.4. The drain tap was left closed until adequate pore pressure response had been recorded, and subsequently re-opened very slowly to proceed with drained loading. Approximately 20 to 25 perturbations were imposed on each specimen. The perturbations resulted in a small reduction in p' at low stress ratios where the specimens were contractive. However, the specimens became slightly dilative at higher stress ratios. The tests were continued up to a deviatoric strain of 10%. The undrained conditions were fairly short, usually about 1 minute, avoiding generation of pore water pressures exceeding 10 kPa, and or axial strains more than 0.1%. Yet, if none of the two mentioned criteria were met, then the undrained path would not be applied more than 90 seconds and shearing would be switched back to drained conditions.

Rates of shearing or applied deviator stress to the sample were chosen to be fairly slow and allow for the cell pressure to be reduced sufficiently and the stress path to be kept as vertical as possible. The rates of increasing deviator stress were in the order of 3 to 6 kPa/min where the decrease in cell pressure were between 1 and 2 kPa/min. Shearing to failure required approximately 1.5 to 2 hours, though the tests at higher consolidation stresses took longer time to complete.

4 Experimental Results, and Interpretations of Yield and Plastic Potential Surfaces for Sand

This Chapter provides the results of the triaxial tests performed for Part I of the dissertation as well as interpretations from the laboratory measurements for the elastoplastic surfaces.

Contents of this chapter are formed as a journal article by Eslami, M., Pradel, D., Brandenberg, S.J., entitled “Experimental Mapping of Elastoplastic Surfaces for Sand Using Undrained Perturbations,” accepted for publication in *Soils and Foundations* (201X).

4.1 EXPERIMENTAL RESULTS

4.1.1 Elastic moduli

To measure the elastic bulk modulus, K, a specimen was isotropically consolidated to 100 kPa, and the cell pressure was then cyclically reduced to 80 kPa and increased to 100 kPa while the volume change was recorded using a differential pressure transducer. The bulk modulus was computed using equation (2.6). This process was repeated as the specimen was isotropically consolidated to 200, 300, 400, 300, 200, and 100 kPa. The resulting bulk modulus values at an average effective stress (in the unload-reload cycle applied) found from mean stress-volumetric strain measurements are shown in Figure 4.1.

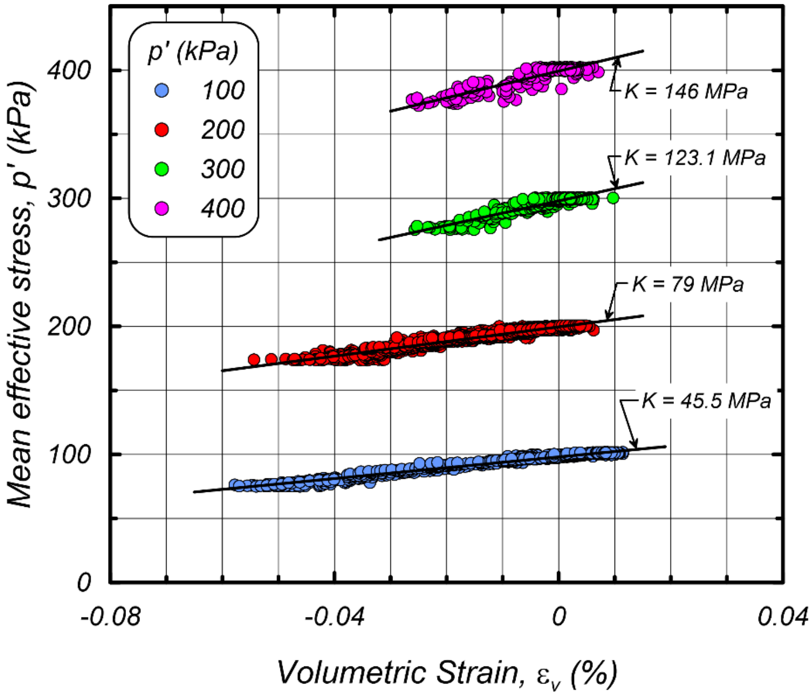

Figure 4.1. Measurements of Bulk modulus at *p′* = 100, 200, 300, and 400 kPa

Based on the measurements shown in Figure 4.1, least-squares regression was performed to relate the bulk modulus to mean effective stress [Figure 4.2(a)], as indicated in equation (4.1), where p_a = 101.325 kPa.

$$K = 50,600kPa\left(\frac{p'}{p_a}\right)^{0.78} \tag{4.1}$$

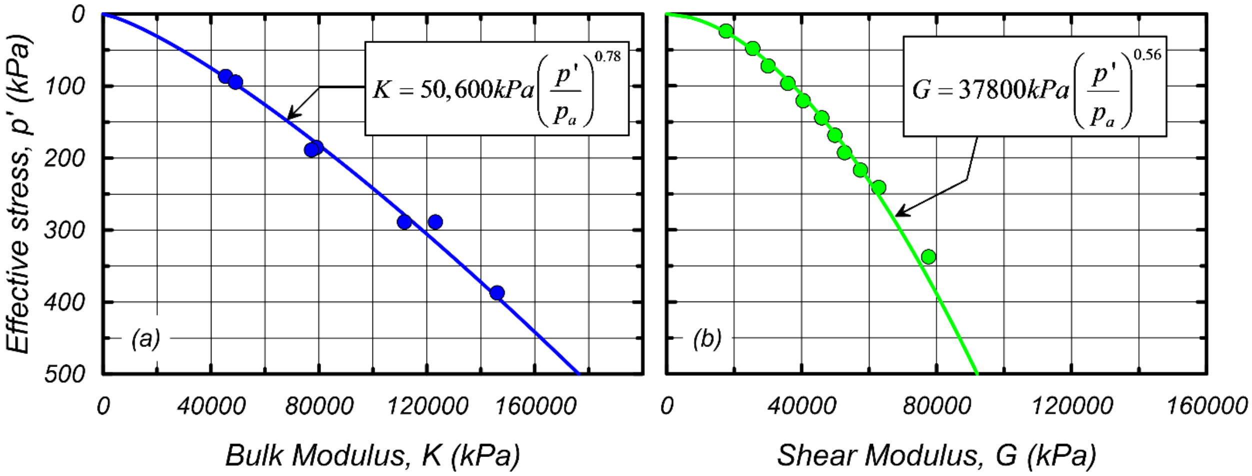

Figure 4.2. Measurements of elastic moduli: (a) bulk modulus measurements and adopted correlation, (b) Shear modulus measurements and correlation

To measure shear modulus, two methods were considered. First, the Young's modulus, *E*, was measured by imposing 0.01% amplitude cyclic axial strain cycles, computing the slope by least squares regression, and subsequently computing shear modulus as $G = 3KE/(9K\text{-}E)$, in accordance with homogeneous isotropic linear elasticity theory, where the measured values of *K* and *E* corresponding to each consolidation pressure were used. This method is not particularly accurate because (1) the cyclic strain amplitude is large enough that the measured response is a combination of elastic and plastic behavior, and separating the two responses requires additional assumptions, and (2) sensor noise contributed significantly to the measurements because 0.01% is close to the resolution limit for the load cell and LVDT. Therefore, the shear modulus was measured using bender elements embedded in the sand using a custom-made consolidation ring (Figure 4.3). Vertical pressures were applied to the sand, the source bender element was excited by a step wave function, and the travel time was selected based on the received signal following procedures outlined by Brandenberg et al. (2008). The bender element excitations are very small strain, and therefore act in the elastic region of the soil. The measurements were then regressed as shown in

Figure 4.2(b), and the functional form of the shear modulus related to mean effective stress is given in equation (4.2).

$$G = 37{,}800kPa\left(\frac{p'}{p_a}\right)^{0.56} \tag{4.2}$$

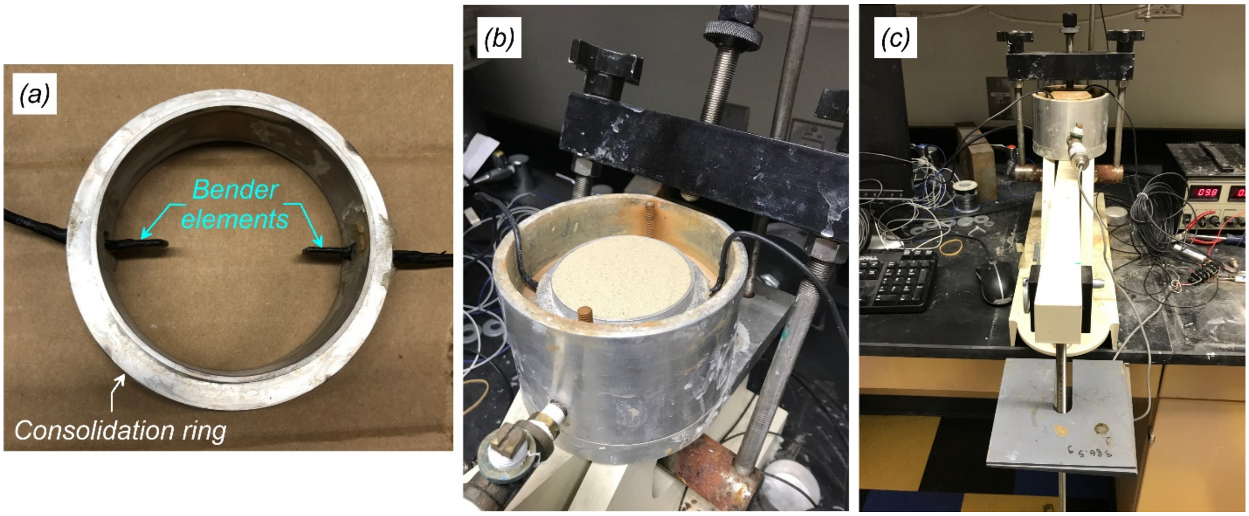

Figure 4.3. (a) custom-made consolidation ring with bender elements, (b) and (c) setup in consolidometer with applied vertical pressure to make shear wave velocity measurements

4.1.2 Monotonic shear response

Testing was conducted for mean effective consolidation stress values of p' = 100, 150, 200, 250, 300, 350 and 400 kPa, and the resulting stress paths and stress-strain curves are plotted in Figure 4.4 (a and b). Constant mean effective stress conditions were obtained using stress-controlled loading and by decreasing the cell pressure as follows: $\Delta\sigma_3 = -q/3$. During drained loading, the drain tap connected to the specimen was periodically closed to impose a small undrained loading perturbation on the specimen. These perturbations manifest as sudden changes in p' apparent in Figure 4.4(a). The drain tap was left closed until adequate pore pressure response had been recorded, and subsequently re-opened very slowly to proceed with drained loading. Approximately

20 to 25 perturbations were imposed on each specimen. The perturbations resulted in a small reduction in p' at low stress ratios where the specimens were contractive. However, the specimens became slightly dilative at stress ratios (q / p') higher than about $M^d = 1.3$ (Figure 4.4a).

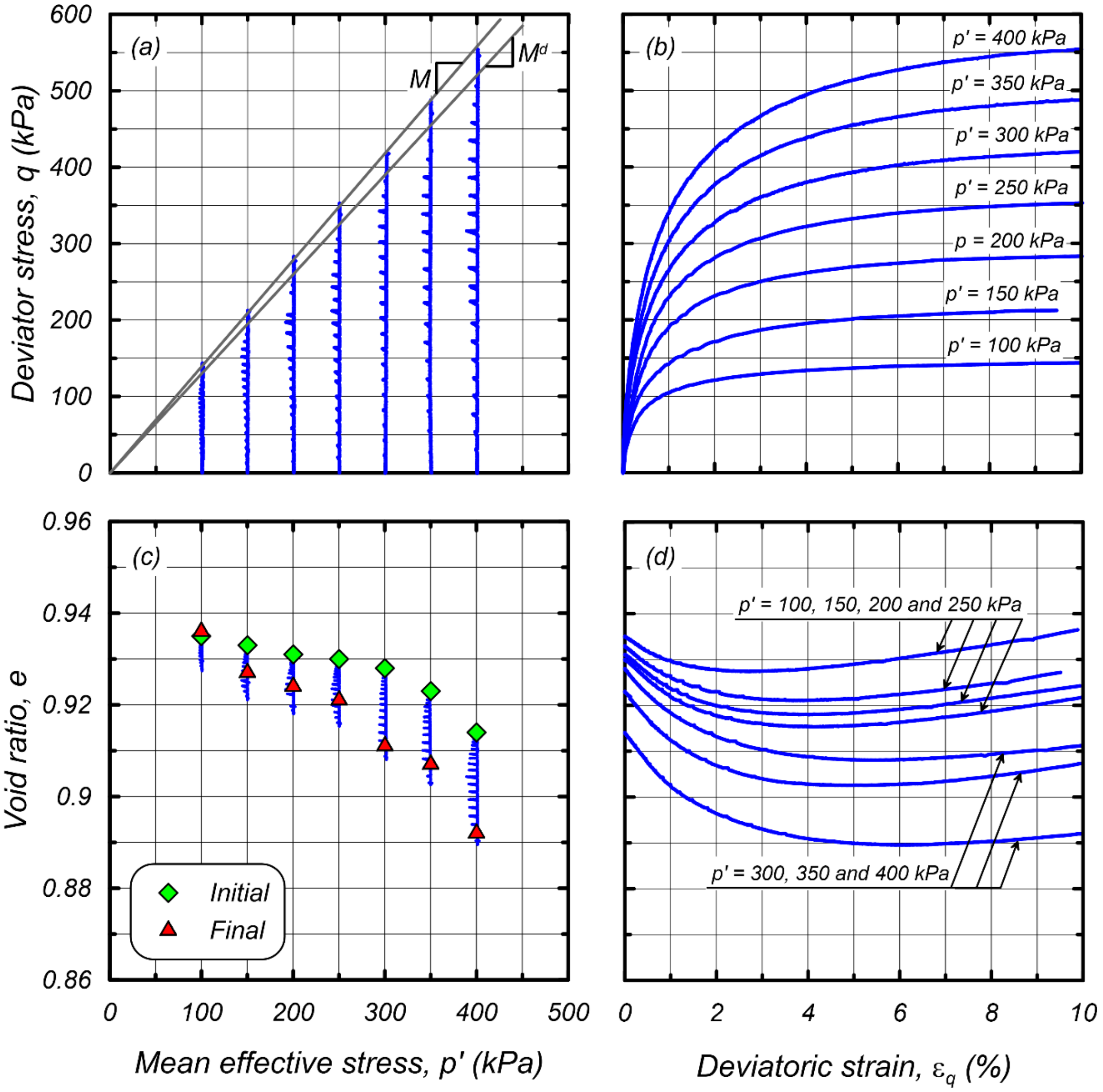

Figure 4.4. General soil behavior of 7 triaxial compression tests: (a) effective stress paths, (b) stress-strain curves, (c) void ratio vs. mean effective stress, (d) void ratio vs. deviatoric strain curves

Note that M^d is the stress ratio at the transition from contractive to dilative behavior, which can also be seen from the change in void ratio as presented in Figure 4.4(d). Initial (after consolidation) and final void ratios (at 10% deviator strain) are shown in Figure 4.4(c). The tests reached deviatoric strains of 10%, at which point the deviatoric stress and void ratio were still changing as deviatoric strain increased, indicating that the specimens did not reach a critical state condition. The stress ratio at a strain of 10% was $M = q / p' = 1.4$, which is associated with a friction angle of $\phi = 34°$, where $M = 6\sin\phi/(3-\sin\phi)$.

The values of dq/dp', $d\varepsilon_q/dp'$, $d\varepsilon_q/dq$, and $d\varepsilon_v/dq$ required to solve for h, η_{pp}, and μ using equations (3.5), (3.6), and (3.7), respectively, were obtained as illustrated in Figure 4.5 for one of the perturbations conducted at a consolidation stress of 400 kPa. The quantities were first plotted versus time, and the rates of change of each quantity were computed using linear least squares regression for the load increment both the drained and undrained portions of loading.

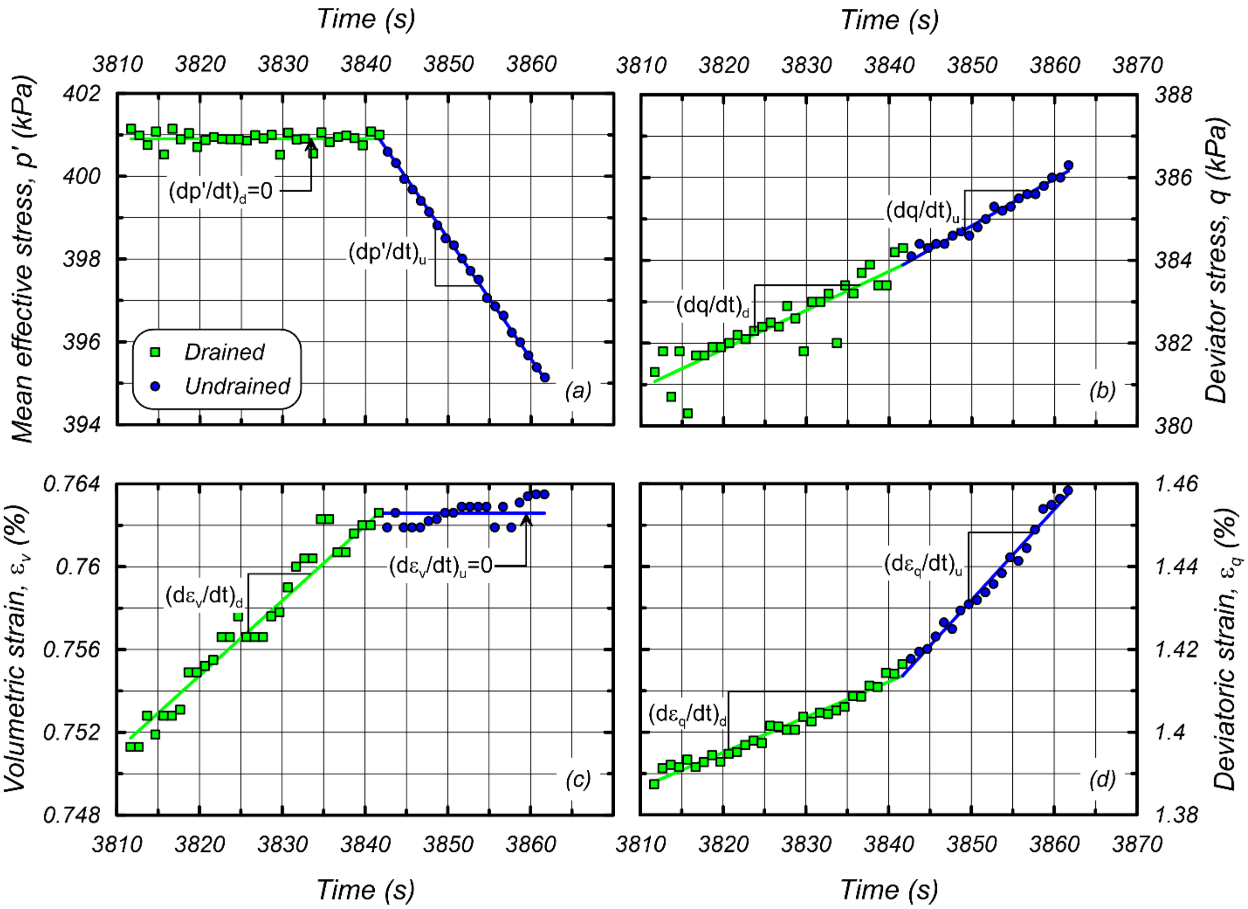

Figure 4.5. Example data during one perturbation for the specimen consolidated at 400 kPa. Data quantities are (a) mean effective stress, (b) deviator stress, (c) volumetric strain, and (d) deviatoric strain.

The rate dp'/dt was set to zero during drained loading and $d\varepsilon_v/dt$ was set to zero for undrained loading. The desired ratios were then computed as the ratio of the rates [e.g., $dq/dp' = (dq/dt)/(dp'/dt)$]. The number of data points extracted for linear least squares regression depended on the amount of nonlinearity in the soil response. Near the beginning of each test (i.e., at low stress ratio) more data points were utilized because the strains evolved more slowly than later in the test. Recall that stress control was required to maintain a vertical stress path, therefore the strain rate tended to increase with time as the soil became softer.

4.1.3 Plastic modulus

A value of plastic modulus was computed from the drained loading stages based on equation (3.5) at each point where an undrained perturbation was imposed on the specimen. The resulting plastic modulus values were subsequently normalized by $3G$, and plotted in Figure 4.6. Plastic modulus is known to depend on shear modulus (e.g., Dafalias and Manzari, 2004), hence normalizing the plastic modulus results in a relationship that is independent of p'. The 95% confidence limits indicate that the measurements were of poorer quality at low stress ratio than at high stress ratio. This is due to the fact that deviatoric strain increments are quite small at low stress ratio, therefore signal noise influences the measurement of h. A weighted least squares regression was performed to arrive at equation (4.3), where weights were assigned to be inversely proportional to the 95% confidence limit range.

$$\frac{h}{3G} = 0.12\frac{1.4-\eta}{\eta} \tag{4.3}$$

The functional form of the expression above, assumes that plastic modulus is inversely proportional to the distance from the current point in q-p' space to the failure line, M. This loosely follows Dafalias and Manzari (2004), with the exception that they compute plastic modulus as a function of distance to the bounding surface, which in turn depends on the state parameter. The constants 1.4 and 0.12 are analogous to the parameters M^b (the bounding or "image" stress ratio on the bounding surface) and b_0 (a parameter that defines the plastic modulus at the initiation of the loading process) in Dafalias and Manzari (2004), respectively.

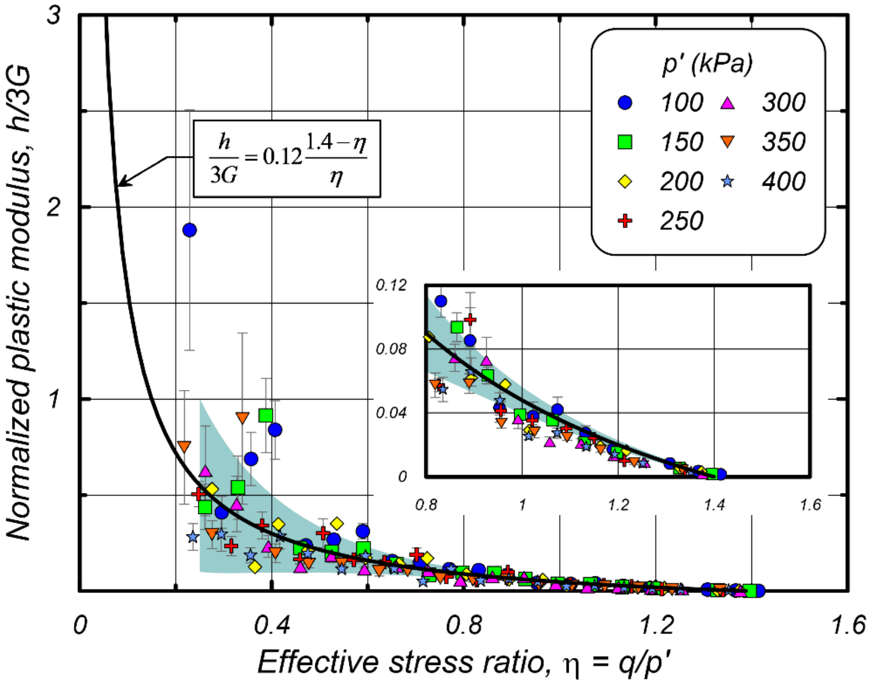

Figure 4.6. Normalized plastic modulus (h/3G) versus stress ratio ($\eta = q / p'$). Vertical bars are 95% confidence limits and shaded region corresponds to ± one standard deviation of the residuals.

4.1.4 Plastic potential slope

The slope of the plastic potential surface, η_{pp}, was computed for each undrained perturbation, and the results are plotted versus the stress ratio $\eta = q/p'$ in Figure 4.7. A negative slope of the plastic potential surface indicates contractive behavior, while a positive slope indicates dilation. The sand is contractive essentially over the full range of loading, and is the most highly contractive at a stress ratio near 0.4.

Superposed on the data are the slopes of the plastic potential surfaces associated with the original and modified Cam-clay models (Schofield and Wroth, 1968, and Roscoe and Burland, 1968). Although the Cam-clay model was formulated for clay and not for sand, the sand tested herein appears to exhibit characteristics that are qualitatively similar to the Cam-clay model. This does not mean that the Cam-clay model is appropriate for sands because the compressibility behavior may in fact be significantly different. The original Cam-clay model has a slope that varies linearly with η, and fits the observed data reasonably well at stress ratios higher than about 0.8, but lies beneath the data at lower stress ratios. The modified Cam-clay model lies significantly below the data. A weighted least squares regression was performed on the data, resulting in the expression given in equation (4.4).

$$\eta_{pp} = -0.177 + 0.599 \cdot \ln(\eta) \quad (4.4).$$

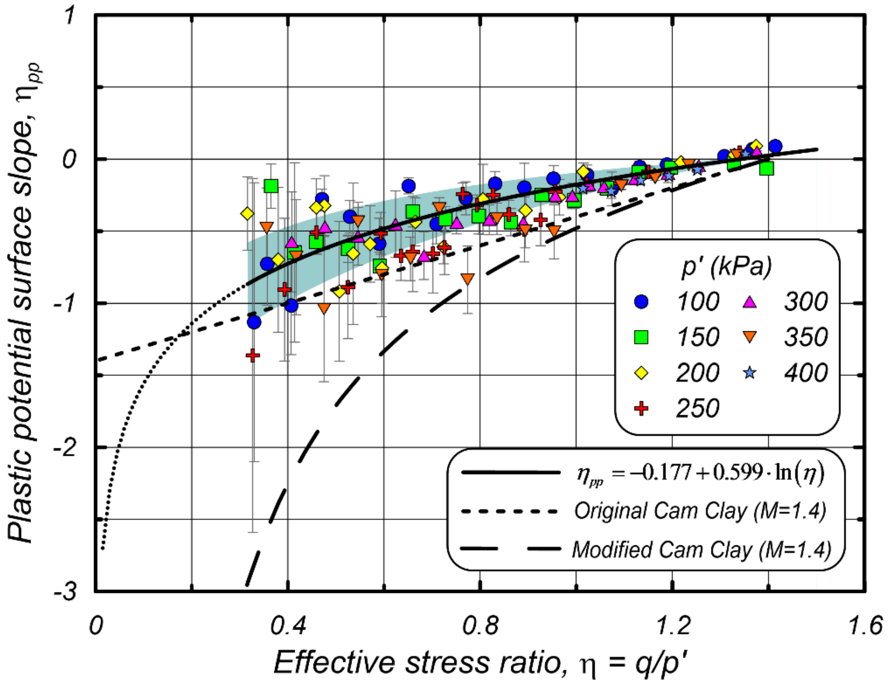

Figure 4.7. Slope of plastic potential surface, η_{pp}, versus effective stress ratio ($\eta = q / p'$). Vertical bars are 95% confidence limits and shaded region corresponds to ± one standard deviation of the residuals.

Flow behavior is known to depend not only on stress ratio, but also on the void ratio relative to the critical state void ratio, which is commonly quantified by the state parameter $\psi = e - e_c$. For example, the tested specimens were more highly contractive at high p' where ψ was largest (Figure 4.4c). To account for the influence of soil state on plastic flow, the plastic potential surface must be a function not only of η, but also ψ. The data were therefore regressed according to the functional form equation (4.5) following Dafalias and Manzari (2004), with the results: $A_d = 0.61$ and $n_d = 11.2$, considering $M = 1.4$. Since the specimens did not reach critical state, the critical state void ratio is unknown. For simplicity, the state parameter was therefore computed as the difference between the current void ratio and final void ratio for the test.

$$\eta_{pp} = -A_d \left[M \cdot \exp\left(n_d \cdot \psi \right) - \eta \right] \tag{4.5}$$

4.1.5 Yield surface slope

The slope of the yield surface is plotted versus stress ratio in Fig. 10. The yield surface is negative at low stress ratio, and increases with stress ratio becoming positive at about $\eta = 1.1$. The 95% confidence limits are larger for the yield surface slope than for the plastic potential slope because the yield surface slope calculation utilizes volumetric strain, which is a comparatively noisy measurement, and carries over measurement errors from h and η_{pp}. A weighted least squares regression results in equation (4.6).

$$\mu = 0.012 + 0.331 \cdot \ln(\eta) \tag{4.6}$$

Equation (4.6) differs from equation (4.5), which indicates that the sand exhibits a non-associated flow rule. For comparison, the Modified Cam-clay (M = 1.4), Original Cam-clay (M = 1.4), and Drucker Prager yield surfaces are provided in Figure 4.8. Note that the slope of the Drucker-Prager yield surface must be equal to the stress ratio for cohesionless material during yielding. None of these yield surfaces provide a particularly suitable match to the experimental data.

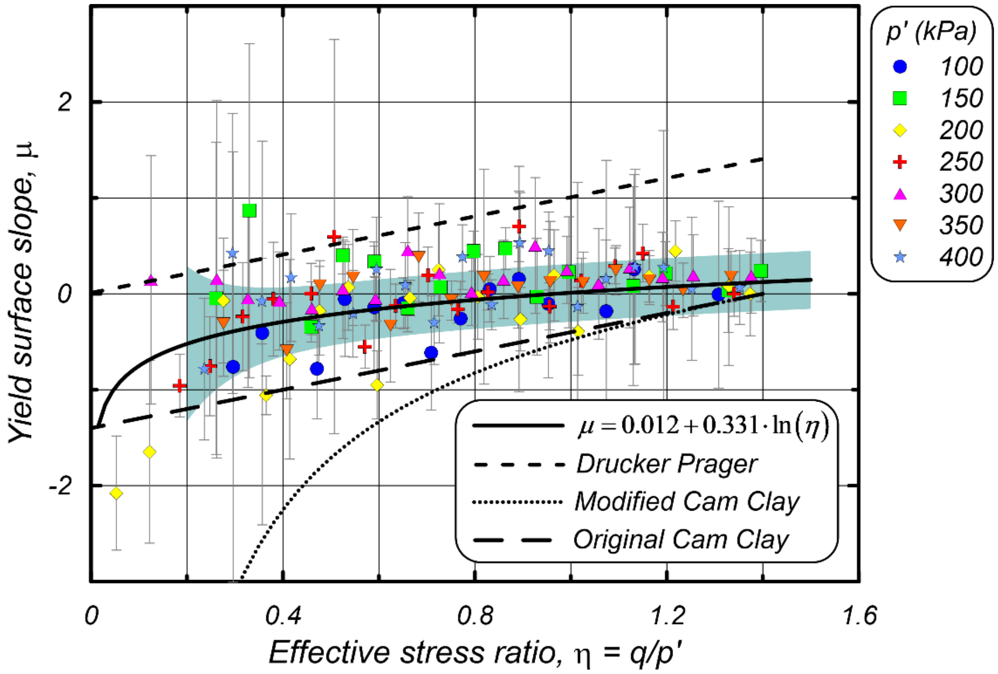

Figure 4.8. Slope of yield surface, μ, versus effective stress ratio ($\eta = q / p'$). Vertical bars are 95% confidence limits and shaded region corresponds to ± one standard deviation of the residuals.

4.1.6 Residuals

Residuals computed using equation (3.8) are plotted in Figure 4.9, and have units of volumetric strain. If the data quantities were measured perfectly, these residual values would be zero. The mean value of the residuals is 8.7e-6, and the standard deviation is 3.3e-5. These numbers are rather small compared with the measurement accuracy of the volume change sensor. For example, the noise amplitude of the volume change sensor is about 2.1e-5, which is close to the standard deviation of the residuals. This is an indication that it has been extracted as much as possible from the data considering the limitations of the measurements. Any systematic errors (e.g., if the soil response were nonlinear within the range of measurements extracted for data processing) would cause these residuals to be higher than the noise levels of the volume change sensor.

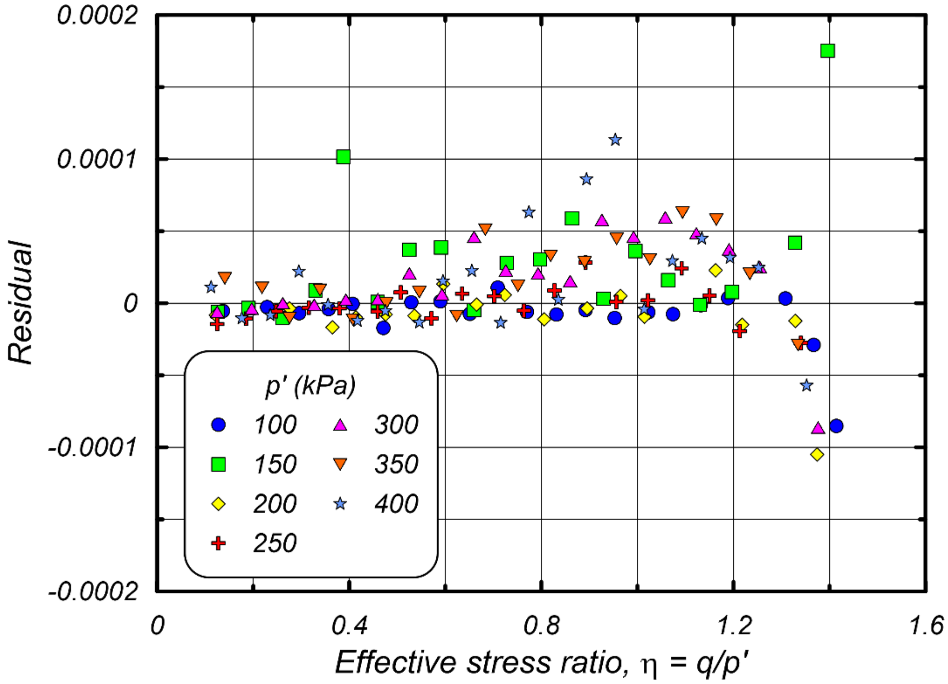

Figure 4.9. Residuals, R, computed using equation (3.8) versus effective stress ratio ($\eta = q/p'$)

4.2 PUBLISHED EXPERIMENTAL DATA ON DESIGNSAFE CYBER INFRASTRUCTURE

Data curation involves activities that lead to publishing datasets that can be reused and enable research validation. These activities include managing, organizing, describing, cleaning, preserving, and archiving data. These processes add value to the data, allowing it to become an integral part of the body of academic knowledge (Beagrie, 2004). In data curation, the notions of understandability and permanence are key. Experimental research, such as the one introduced in this work, involving multiple study paths and tests generates complex and inter-related datasets whose provenance and structure need to be documented for others for reuse.

To publish the dataset derived from this project we used the tools and services available on Design-Safe Cyber Infrastructure (DS-CI), an NSF funded platform for natural hazards research (Rathje et al., 2017), where users can curate, analyze, and publish their data across a research project's lifecycle. To facilitate data curation, DS-CI developed an interactive pipeline that guides researchers to assign their data to categories that represent the main processes of an engineering experiment (Esteva et al., 2016). Part of the researchers' work is deciding how to utilize the categories provided and mapping them to the structure of their research project so every dataset will show a particular configuration. The curation interface provides documentation options such as: selecting specialized terms from a menu, entering free explanatory text, and adding tags to describe the steps, instruments, and data involved in a geotechnical experiment. Our experiment consisted of two types of triaxial events: Elastic Moduli measurements (EM) and Monotonic Shear triaxial (MS), each of which includes varied numbers of stages and corresponding data. As the curation progresses, the GUI generates a tree representing the complex data structure and a data browsing interface showing data in relation to the process that it derives from as provenance.

Next, the publication pipeline steers users into reviewing the accuracy of the tree representation and correcting the entered descriptions, conducts automated verification that the files and information required for data understandability and licensing are in place, and assigns digital object identifiers (DOI) to the published data. Each DOI constitutes a permanent link that will always point to the referenced dataset, regardless if its Web location changes over time. The DOI also generates a reference that is available for ease of data citation. The dataset for the current study can be accessed at Eslami et al. (2017), and is presented in Figure 4.10. To further facilitate reuse, in addition to the collected data, we included in the publication a Jupyter notebook for data visualization and reports on the test procedures.

Having to publish the data stimulated our team to carefully consider the presentation and information required for others to reuse it and consequently to use best practices managing it. We found that curating our data improved the overall research project management and our documentation practices.

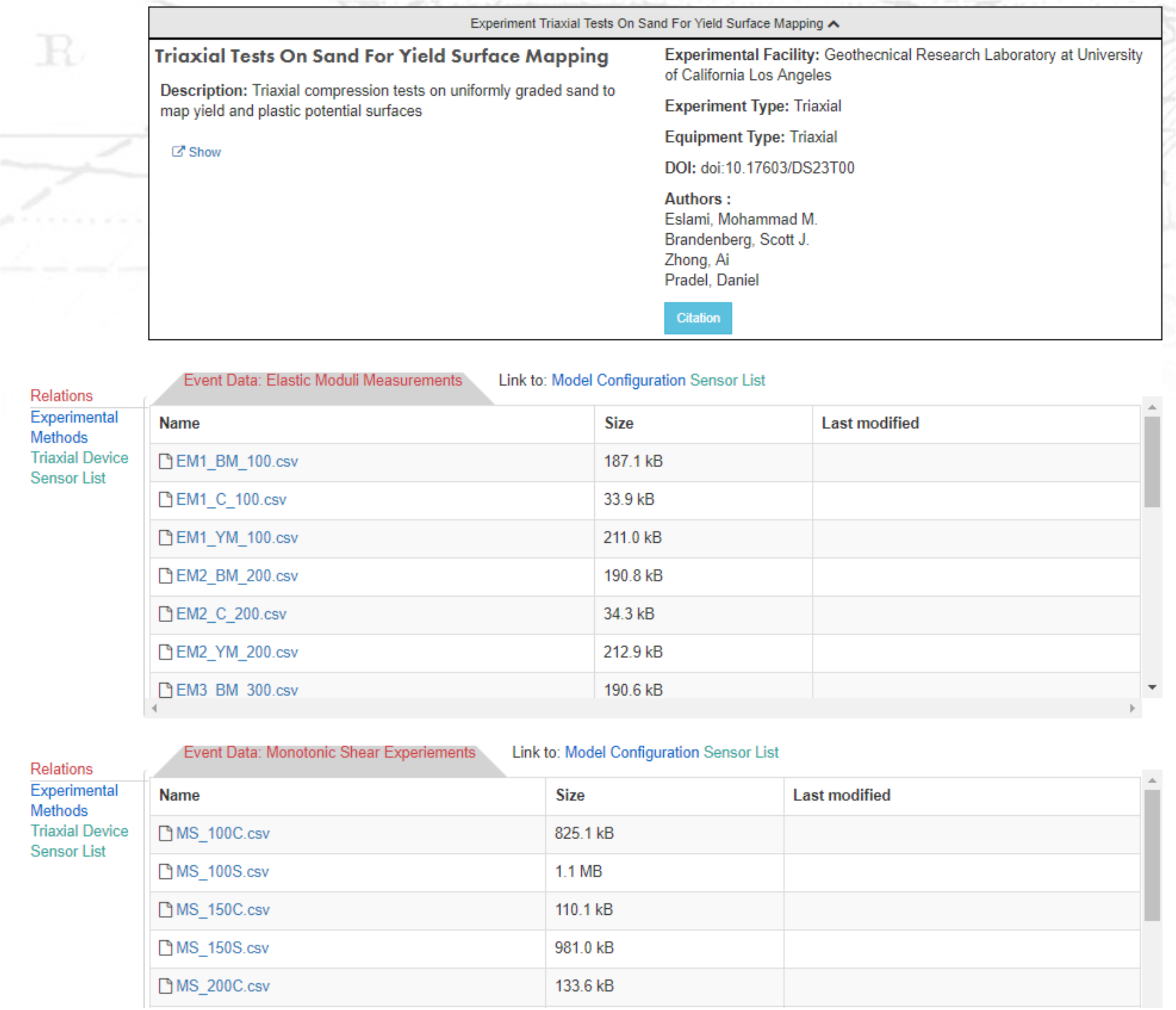

Experiment Triaxial Tests On Sand For Yield Surface Mapping

Triaxial Tests On Sand For Yield Surface Mapping

Description: Triaxial compression tests on uniformly graded sand to map yield and plastic potential surfaces

Experimental Facility: Geothecnical Research Laboratory at University of California Los Angeles

Experiment Type: Triaxial

Equipment Type: Triaxial

DOI: doi:10.17603/DS23T00

Authors :
Eslami, Mohammad M.
Brandenberg, Scott J.
Zhong, Ai
Pradel, Daniel

Event Data: Elastic Moduli Measurements

Link to: Model Configuration Sensor List

Name	Size	Last modified
EM1_BM_100.csv	187.1 kB	
EM1_C_100.csv	33.9 kB	
EM1_YM_100.csv	211.0 kB	
EM2_BM_200.csv	190.8 kB	
EM2_C_200.csv	34.3 kB	
EM2_YM_200.csv	212.9 kB	
EM3 BM 300.csv	190.6 kB	

Event Data: Monotonic Shear Expereiments

Link to: Model Configuration Sensor List

Name	Size	Last modified
MS_100C.csv	825.1 kB	
MS_100S.csv	1.1 MB	
MS_150C.csv	110.1 kB	
MS_150S.csv	981.0 kB	
MS_200C.csv	133.6 kB	

Figure 4.10. Snapshot of published Dataset on DesignSafe-CI

4.3 INTERPRETATION OF DATA

The experimental data provide insights into the slopes of the yield and plastic potential functions. equations (4.4), (4.5), and (4.6) provide these slopes at a particular point in stress space, and assumptions are required to sketch the yield or plastic potential surface.

The simplest approach for interpreting the data is to assign a point in stress space, compute the desired slope at this point, and integrate the slope over a range of stress ratios to sketch the rest of the surface. This inherently assumes that the surfaces enclose an increasingly large elastic region as loading progresses (i.e., isotropic hardening). This assumption is similar to many traditional elastoplastic models such as Cam-clay. An example of this approach is illustrated in Figure 4.11 for a vertical stress path at p' = 200 kPa, where yield surfaces are sketched at three different points along the stress path.

These lines were obtained by numerically integrating equation (4.6). The shape of the surfaces is qualitatively similar to the original Cam-clay model in that the surfaces are curved and skewed to the left. The yield surfaces in Figure 4.11 are drawn only in regions that lie reasonably within the bounds of experimental validation. Vectors indicating the directions of plastic flow that were measured, and computed using equation (4.4) and (4.5) are also shown in Figure 4.11 at the points where the stress path intersects the yield surface. The plastic flow vectors are not perpendicular to the yield surfaces at these points due to the non-associated flow rule.

Traditional isotropic hardening models provide reasonable predictions for monotonic loading, but results in a large elastic region that is inappropriate for cyclic loading. Models that utilize small yield surfaces that exhibit kinematic hardening are better suited to capture inelasticity in the reverse direction. For example, SANISAND (Taiebat and Dafalias, 2008) utilizes a narrow-closed cone-type yield surface given by equation (2.14). This yield surface equation can be calibrated to match the experimental data by setting the parameters n and m, and solving for α and p_0 that provides the desired yield surface slope at a specific point in stress space. Note that α is the rotational hardening backstress ratio, p_0 is the isotropic hardening variable, m is the tangent of half the opening angle of the yield surface, and the exponent *n* introduces the effect of a cap-like shape at the tip of the yield surface. SANISAND yield surfaces are shown in Figure 4.11 for $m = 0.5$ and $n = 20$. These surfaces intersect the isotropic hardening yield surfaces at the same points and with the same slopes, and provide an alternative interpretation that is equally consistent with the experimental data.

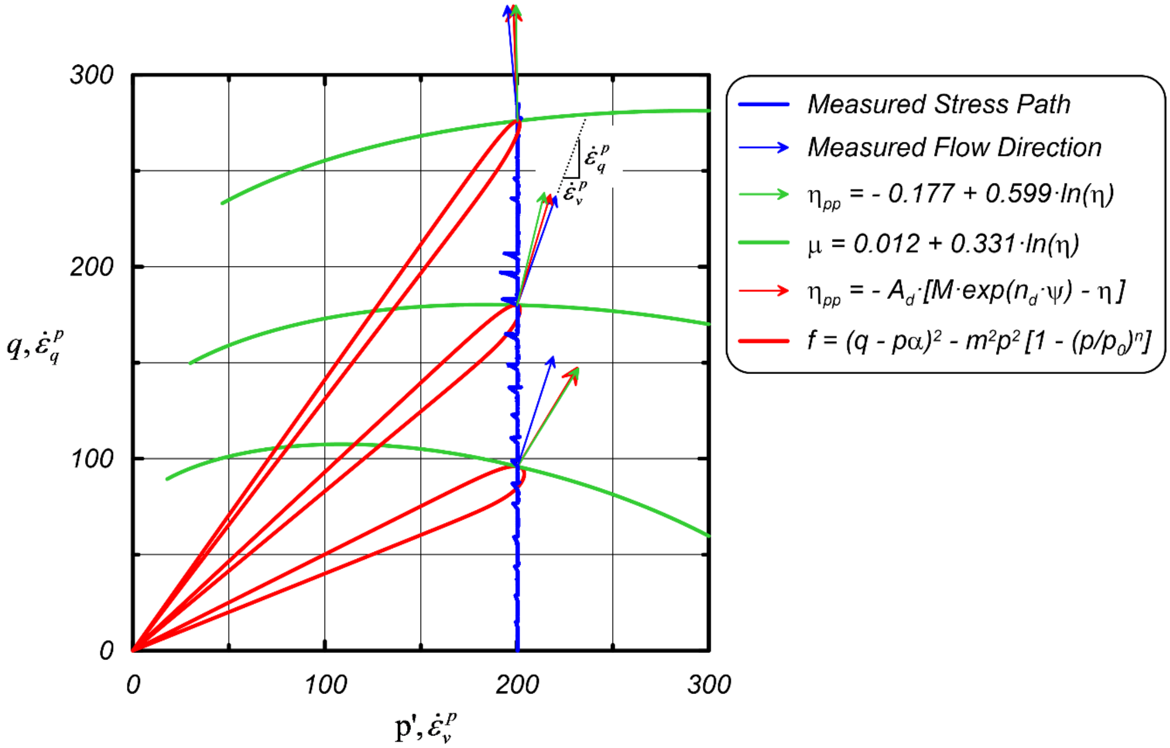

Figure 4.11. Yield and direction of plastic flow consistent with the experimental data for a vertical stress path at $p' = 200$ kPa

5 Summary and Conclusions of Part I

Part I of this dissertation describes a new experimental method based on the deformation (or flow) theory of plasticity. The method was used to determine the plastic modulus, and slopes of the plastic potential and yield surfaces during monotonic shear. The proposed method involves creating, at regular intervals, small undrained perturbations by closing the drainage valve during shear for a short time, and computing slopes and moduli at the locations where these perturbations were imposed. The proposed method was applied to an experimental program consisting of triaxial tests on loose uniformly graded sand.

For ease of interpretation the specimens were sheared while maintaining a constant mean effective stress, p', during shear. Note that constant p' tests are not a necessity for the use of the proposed method, but simplify data interpretation because the elastic properties can be assumed to be constant during shear, and simplifies the analysis described mathematically in equation (3.4).

Results revealed that the plastic potential and yield surfaces are different, indicating non-associated flow. Furthermore, the shape of the plastic potential surfaces was qualitatively similar in shape to the Original Cam-clay model surface (Schofield and Wroth, 1968) in that the surfaces were curved, skewed to the left, and had a zero slope near the ultimate value of the q/p' ratio. Many constitutive models for sand, such as Poorooshasb and Pietruszczak (1985), Dafalias and Manzari (2004), SANISAND (Taiebat and Dafalias, 2008), utilize Drucker-Prager type yield surfaces for which the slope of the yield surface is equal to the stress ratio during yield. The experimental results shown herein, do not support this type of yield surface.

The methods described herein constitutes a departure from the manner in which elastoplastic constitutive models are typically calibrated to match experimental data. Typically, basic parameters such as elastic constants and critical state lines are based on measurements, and other modeling constants are adjusted to provide a reasonable match between predictions and triaxial compression experiments. However, it may not be feasible to adjust the modeling constants to match the experimental data if the underlying assumptions about the yield surface shape and flow rule are incorrect. This may result in significant errors when the stress paths imposed in a simulation differ significantly from the stress paths utilized in the experiments.

The proposed approach provides a simple and expeditious experimental methodology to measure the yield surface and plastic potential surface slopes, thereby enabling identification of errors in the functional form of elastoplastic constitutive models. The method is particularly useful for the calibration of the isotropic elastoplastic models that are commonly used by designers, and for the assessment of kinematic models developed from bounding surface formulations. More importantly, the procedure proves useful for future constitutive model development and refinement.

The experimental data presented herein is curated and publicly available in DesignSafe, the cyberinfrastructure for the Natural Hazards Engineering Research Infrastructure program. Data processing scripts in the form of Jupyter notebooks are stored with the data, and can be run in DesignSafe by anybody with a DesignSafe account. The experimental data and processing scripts have been assigned a DOI, making them citable and ensuring the data will always be available. We believe sharing data in this manner will facilitate research collaborations in the future, and ensure that valuable information is always accessible and never lost to history.

PART II: CYCLIC BEHAVIOR OF LOW-PLASTICITY FINE-GRAINED SOILS WITH VARYING CLAY MINERALOGY AND PORE-FLUID CHEMISTRY

Is plasticity index sufficient for characterizing the cyclic strength loss potential of fine-grained soils? Is it possible that soils with the same plasticity index may exhibit different strength loss behavior? Does pore fluid chemistry play a role?

6 Introduction to Part II and Review on Cyclic Behavior of Fine-Grained Soils

6.1 INTRODUCTION

Events such as the Great Alaska and Niigata, Japan earthquakes in 1964 led to the most dramatic structural damages due to liquefaction in sands and cyclic failure of clays, perhaps initiating formal importance for geotechnical earthquake engineering. Though strength loss and rapid strain generation in sand-like soils is commonly referred to as "liquefaction," large strain accumulation and strength reduction in cohesive (clay-like) soils is addressed as "cyclic softening." Following catastrophic failures during seismic events, geotechnical engineers and researchers have put numerous efforts in trying to better understand seismic soil behavior and provide answers to questions such as:

1) What kinds of soils are *susceptible* to liquefaction or can generally experience significant strength loss and develop large strains under cyclic earthquake loading?

2) If a soil is considered susceptible to liquefaction, *how likely* is it that significant strength loss and large strains would develop during an earthquake?
3) *How much* of the soil's strength would be lost (reduced) during a seismic event or how much strain would develop during and after an earthquake?
4) What are the *consequences* of strength loss and large strain generation?
5) How can the consequences be *mitigated*?

Following these landmark earthquakes, engineers devoted significant effort to understanding liquefaction of sands, resulting in widely adopted engineering evaluation procedures. However, following events such as the Chi-Chi, Taiwan and Kocaeli, Turkey earthquakes in 1999, extensive ground failure and structural damage was observed in presence of clays and plastic silt deposits [e.g. Stewart et al. (2003), and Bray et al. (2004)], that would have widely been considered non-susceptible to liquefaction at the time that the earthquakes occurred. More recent examples of this behavior were observed in the Christchurch, New Zealand and Tohoku, Japan events of 2011 [e.g. Chubrinovski et al. (2011) and Yasuda et al. (2012)]. Failures of fine-grained soils have been less common than liquefaction of sands, therefore seismic behavior of such materials is not fully understood.

The essential first step in characterizing seismic soil behavior is to assess liquefaction susceptibility, where the potential for soil to experience significant reduction in its effective confining stress (associating with strength loss and large deformations) is evaluated based on the soil's composition. Commonly, this practice is based on soil index properties such as liquid limit (LL), plasticity index (PI), and particle size. Although various studies have shown apparent relationships between plasticity and cyclic behavior of soils, significantly divergent recommendations on the levels of plasticity required for a fine-grained soil to be too clay-rich to liquefy can be observed in the literature.

Several procedures have been developed for estimating cyclic strengths of soils, and to assess the likelihood of significant strength reduction or large strain development when a soil is considered liquefiable or can potentially experience cyclic softening. Similar to the susceptibility criteria, such procedures are also quite often based on soil index properties, especially in clay-like soils where the cyclic strength is related to effective confining stress or undrained shear strength, based on plasticity level.

Some recent studies however, criticize the effectiveness of soil index properties solely, being sufficient indicators for adequately capturing variations in behavior of fine grained soils and consequently the available guidelines on evaluating cyclic strengths of clay-like materials. Particularly, in evaluating seismic behavior of low-plasticity intermediate soils where distinguishing between sand-like and clay-like behavior is a rather challenging task. It suggests that factors such as clay mineralogy, clay content, and pore-fluid chemistry should be considered for satisfactory engineering judgement and practice under seismic conditions.

Part II of this dissertation focuses on providing insights into the effects of changes in clay mineralogy and pore-fluid chemistry on cyclic behavior of low-plasticity fine-grained soils. An extensive laboratory study has been performed on low-plasticity silty clay mixtures with varying compositions, but at equal plasticity levels, to study differences or similarities in their behavior and to examine the effectiveness of index properties in identifying the observed differences in lab results. The experimental program consists of Atterberg limits tests, consolidation tests, monotonic and cyclic direct simple shear (DSS) tests, and scanning electron microscope (SEM) imaging.

This Chapter provides a comprehensive review of the literature on developments and currently available guidelines on characterization of seismic behavior of fine-grained soils and procedures commonly used in geotechnical engineering practice (to date) for estimating cyclic strengths of such soils. Examples of extensive ground failure and structural damage in presence of low-plasticity fine-grained soils during the Chi-Chi and Kocaeli earthquakes of Taiwan and Turkey, respectively, are presented to demonstrate the importance of understanding the seismic behavior of such soils. The influence of mineralogy and pore-fluid chemistry is also discussed.

This is followed by technical details of what was hypothesized, the methodology for assessing the hypothesis, explanation of the testing program and procedures for Part II of the dissertation in Chapter 7. Laboratory testing results and discussions on the effects of changes in mineralogy as well as varying the pore-fluid chemistry are presented in Chapter 8. Lastly, the work done in Part II of the dissertation is summarized in Chapter 9, where major conclusions are provided as well as explanations on possible future direction of studies on this topic.

6.2 PROCEDURES FOR EVALUATING STRENGTH LOSS POTENTIAL OF FINE GRAINED SOILS

The essential first step in characterizing seismic soil behavior is to assess liquefaction susceptibility. Once the likelihood of susceptibility is evaluated, or clay-like versus sand-like behavior types have been distinguished, it is common to use liquefaction triggering or cyclic softening procedures to assess whether significant strength loss or large strain development would occur given a specific seismic demand, and to find cyclic strengths of the soil. To assess the cyclic behavior of sands, its cyclic resistance is correlated to several in situ soil properties or resistance measurements such as standard penetration test (SPT) blow counts [e.g. Youd et al. (2001), Idriss and Boulanger (2008)], cone penetration test (CPT) soundings [e.g. Robertson and Wride (1998), Idriss and Boulanger (2008)], and shear wave velocity (V_s) measurements [e.g. Andrus and Stokoe (2000)]. For clays, the cyclic resistance is often quantified as a ratio of the monotonic undrained shear strength (s_u). This section aims to review the currently available and most commonly used procedures in practice.

6.2.1 The "Chinese criteria"

The "Chinese criteria" by Wang (1979) and its modifications by Seed and Idriss (1982) were of the very first liquefaction susceptibility criteria established based on sites that did and did not liquefy during the Haicheng and Tangshan earthquakes in China in 1975 and 1976, respectively. Some authors have used the term "liquefaction" to address cyclic failure of fine-grained soils in the literature, however, the correct notation for soils that went under cyclic failure in the Chinese earthquakes should be "cyclic softening," since they were fine-grained in nature. Hence, the Chinese criteria is essentially a cyclic softening susceptibility criterion.

According to Seed and Idriss (1982), fine-grained soils are susceptible to liquefaction if all three requirements below are met:

- Percent particles finer than 0.005 mm (clay content) < 15%
- Liquid Limit (LL) < 35
- Ratio of natural water content (w_n) to LL > 0.9

Bray and Sancio (2006) present graphs that summarize the data from Wang (1979) of sites that did and did not liquefy as presented in Figure 6.1, where it can be seen that majority of the soils that had liquefied during the earthquakes in China, plot above the A-line on Casagrande's plasticity chart with LL < 35, and also plot below the line of the ratio of water content to liquid limit equal to 0.9. Note that these soils contained less than 15% particles finer than 0.005 mm.

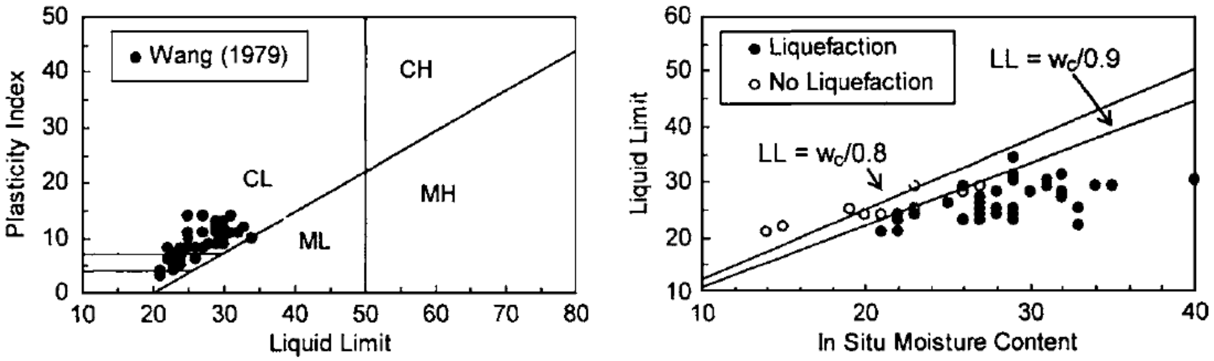

Figure 6.1. Soils that did and did not liquefy during the Haicheng and Tangshan earthquakes in China, which led to the development of the Chinese criteria (Figure from Bray and Sancio, 2006)

Following site reconnaissance of Moss Landing site after the Loma Prieta 1989 earthquake, Boulanger et al. (1998) concluded that silty clay samples collected from subsurface ejecta had a liquid limit of 38, a plasticity index of 17, and contained 24% of particles finer than 0.005 mm. Though the site exhibited 1.3 m of lateral spreading and cyclic triaxial lab tests suggest that this material most likely developed high excess pore pressure ratios, it would have classifieds as non-liquefiable based on the Chinese criteria.

Severe ground failure and structural damage was observed during post-earthquake reconnaissance of the Kocaeli earthquake. Figure 6.2 presents examples of extensive settlement of buildings, structural overturning, and ground destress in presence of low-plasticity fine-grained soils at various locations in Adapazari, Turkey after the Kocaeli event (figures are from Peer website: http://peer.berkeley.edu/publications/turkey/adapazari). Sancio (2003) highlights that building settlements are commonly due to rapidly occurring spread of soil underneath the building towards the sides caused by loss of bearing capacity (Figure 6.2).

Figure 6.2. Examples of structural and ground failure in Adapazari – Turkey during the Kocaeli 1999 earthquake (photos from PEER: http://peer.berkeley.edu/publications/turkey/adapazari/); (a) 1.5 m of settlement of a 5-story building, (b) overturning of a 5-story building, (c) ground destress in between two buildings, and (d) structural settlement and sand ejecta next to a building

Bray et al. (2004) indicate that most soils believed to have liquefied in Adapazari have characteristics that do not meet requirements of the Chinese criteria. Figure 6.3 (a) presents the location of the liquefied soils on a plasticity chart and Figure 6.3 (b) presents a plot of liquid limit of the liquefied soils versus the percent finer than 0.005 mm. The data shows that soils above and below the A-line on Casagrande’s plasticity chart (CL, ML, and CL-ML) with plasticity indices as high as 12 have liquefied, as well as several soils with more than 15% particles finer than 0.005 mm. Nevertheless, Bray et al. (2004) highlight that the ratio of w_n / LL > 0.9, and the low liquid limit elements of the Chinese criteria (LL < 35) are good indicators of liquefaction-type behavior for fine-grained material from Adapazari, yet the percent clay fraction is "not a reliable screening tool."

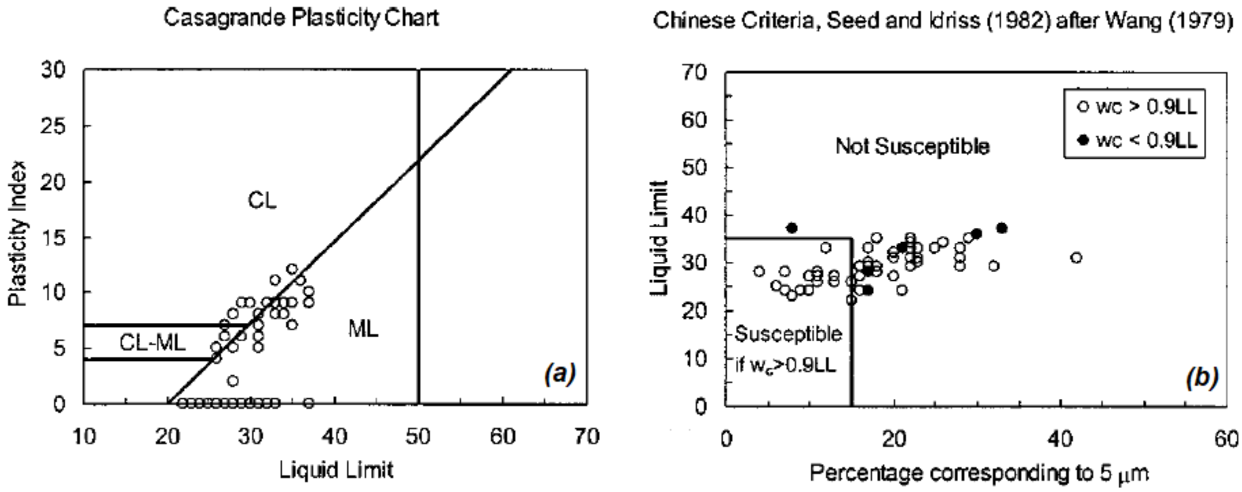

Figure 6.3. Characteristics of liquefied soils from Adapazari, Turkey compared to the Chinese criteria; (a) plasticity chart, and (b) liquid limit versus clay content (modified figure from Bray et al., 2004)

6.2.2 Andrews and Martin (2000)

To refine the Chinese criteria for susceptibility screening of silty material that exhibit liquefaction-type behavior, Andrews and Martin (2000) proposed a criterion for liquefiable vs. non-liquefiable soils based on liquid limit and clay content. The two parameters are considered "key" soil parameters in the seismic characterization of fine-grained soils, as described by the authors.

Reasoning for choosing such parameters as indicators of liquefaction-type behavior was based on reviewing collected data of soil samples from failures during the Northridge 1994 earthquake, ejecta from several seismic events in Japan, and the Saguenay earthquake in Canada 1988, where fine-grained silty material with varying clay contents had exhibited severe strength loss. Andrews and Martin (2000) consider clay content as materials that are finer than 0.002 mm. Further, Koester (1992) compared liquid limits determined by the fall cone penetrometer apparatus versus liquid limits obtained from the Casagrande cup and concluded that a LL = 35 from the fall cone apparatus is equivalent to LL = 32 from the Casagrande cup. Based on this correction to the liquid limits of the Chinese criteria and the percent finer than 0.002 mm particles, Andrews and Martin (2000) suggested the following (Table 6.1) for liquefaction susceptibility.

Table 6.1. Liquefaction susceptibility criteria by Andrews and Martin (2000)

	LL[a] < 32	LL > 32
Clay Content[b] < 10%	Susceptible	Further studies required (considering plastic non-clay sized grains)
Clay Content > 10%	Further studies required (considering non-plastic clay sized grains)	Not susceptible

[a] Liquid Limit determined by Casagrande-type percussion apparatus

[b] Clay defined as grains finer than 0.002 mm

Though the table draws fine lines for susceptible versus not-susceptible materials, it includes a significant range for necessary further studies at higher clay contents and liquid limits. Silts from Adapazari that liquefied during the Kocaeli event fall in the range that has been considered not susceptible by the Andrews and martin (2000) criteria, as presented by Bray et al. (2004). Figure 6.4 indicates that many soils from Adapazari that liquefied, had LL > 32 and more than 10% particles finer than 0.002 mm. Hence, grain size characteristics are not reliable factors in assessing liquefaction susceptibility as cautioned by Bray et al. (2004).

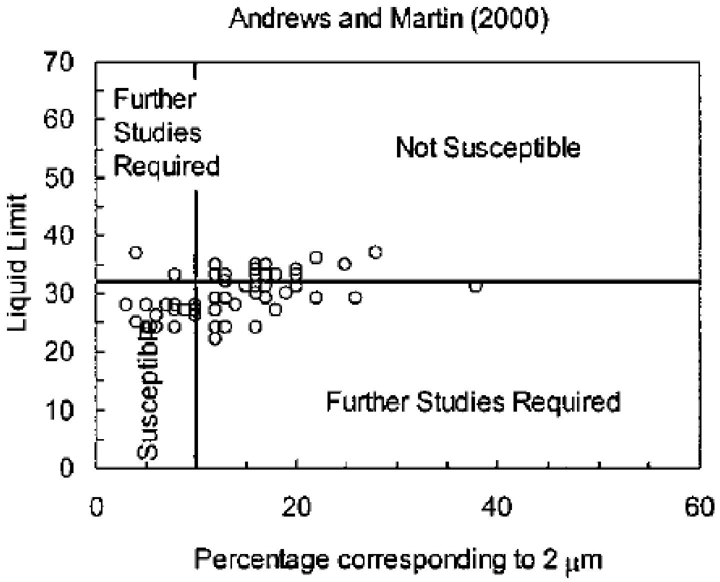

Figure 6.4. Characteristics of liquefiable soils from Adapazari, Turkey compared to the Andrews and Martin (2000) criteria (modified figure from Bray et al., 2004)

6.2.3 Seed et al. (2003)

Severe ground failure was observed in presence of fine-grained soils during the Chi-Chi 1999 earthquake in Taiwan as indicated by post-earthquake reconnaissance reports [e.g. Stewart et al. (2003)]. Figure 6.5 presents example photos (from PEER website: http://peer.berkeley.edu/lifelines/research_projects/3A02/) of lateral spreading, structure tilting, and foundation failures from Wufeng after the Chi-Chi event where many silty clays and sandy silts with interbedded clay and silt with PI < 15 have shown to exhibit liquefaction-type behavior down to depths of about 10 m. Interestingly, such soils had experienced strength reduction and large strain underneath 5 and 6-story buildings as shown in Figure 6.5, yet not in the free field.

Based on collected field and laboratory data from the liquefied sites of events such as Chi Chi and Kocaeli, and the necessity of revising the “Chinese” criteria and Andrews and Martin (2000) criteria due to the misleading “percent clay-size particles” element, Seed et al. (2003)

proposed “interim” recommendations on assessing liquefiable soils with significant fines contents on a plasticity chart (Figure 6.6).

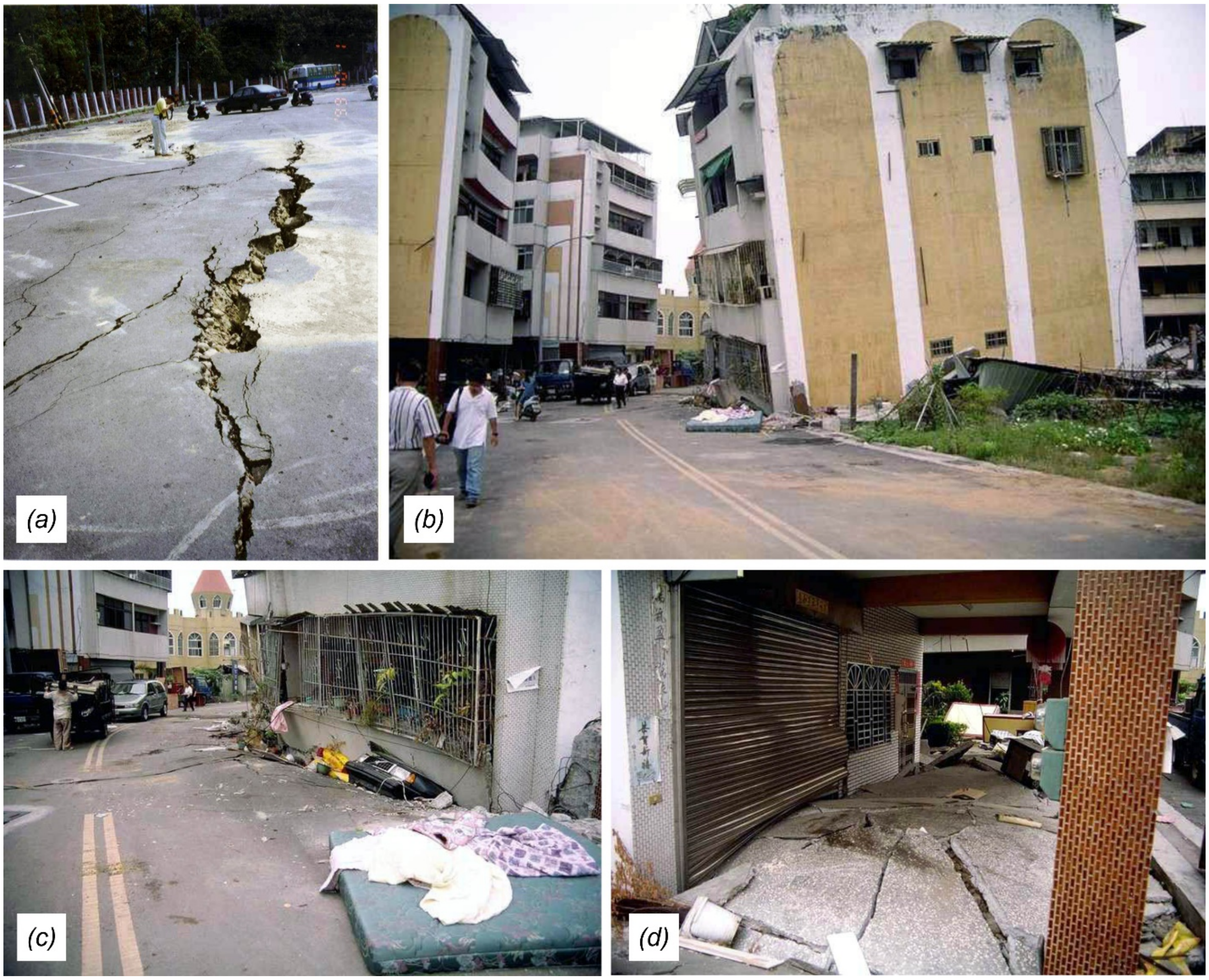

Figure 6.5. Examples of ground and structural failures in Wufeng during the Chi Chi Taiwan 1999 earthquake; (a) lateral spreading, (b) tilted 5-story structure and foundation failure. (c) close-up view of foundation failure of structure on right side of photo (b), and (d) foundation failure beneath a building (photos from PEER website: http://peer.berkeley.edu/lifelines/research_projects/3A02/)

This criteria contains three zones: (1) Zone A soils (potentially susceptible to “classic cyclically induced liquefaction”) if liquid limit is less than 37, PI is less than 12, and natural water content is greater than 80% of the liquid limit; (2) Zone B soils (transitions range) may be liquefiable, and laboratory testing is recommended if water content is greater than 85% of the liquid limit, 37 < LL

< 47 and 12 < PI < 20; and (3) Zone C soils (outside of Zones A and B) are soils that are not generally susceptible to "classic cyclic liquefaction, but should be checked for potential sensitivity" and "may be vulnerable to strength loss with remolding or large shear displacements."

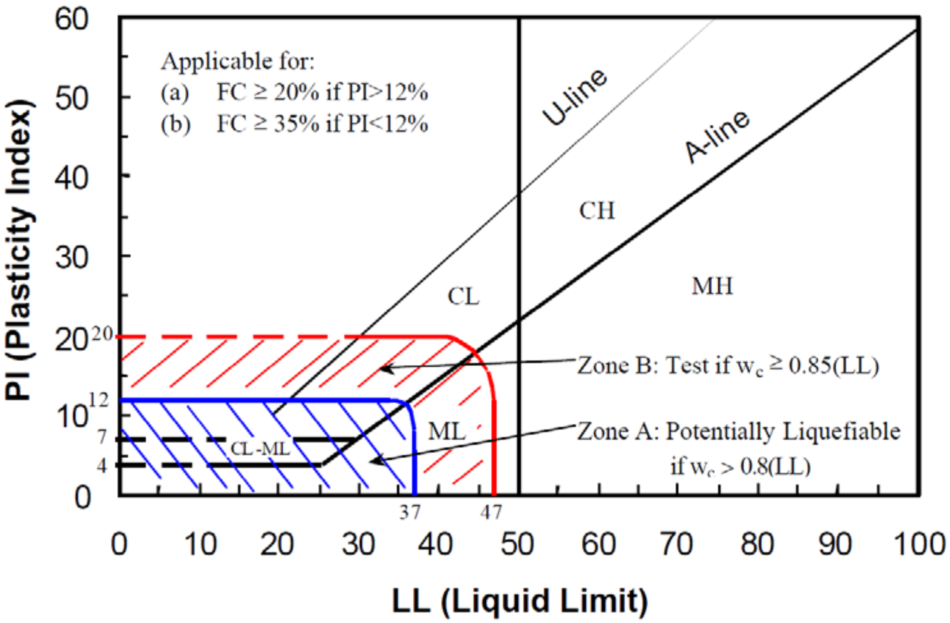

Figure 6.6. Liquefiable soils (with significant fines content) based on recommendations by Seed et al. (2003)

Data from liquefied sites of Adapazari by Bray et al. (2004) do fit in Zone A of the criteria proposed by Seed et al. (2003) and would be considered liquefiable. However, as highlighted by Boulanger and Idriss (2004), it is important to determine the correct engineering procedures for fine-grained soils that have experienced liquefaction-type strength loss and strain development during cyclic earthquake loading.

6.2.4 Boulanger and Idriss (2004)

Major focus had been given on providing guidelines to identify liquefiable fine-grained soil types by criteria such as the Chinese, Andrews and Martin (2000), and Seed et al. (2003)

recommendations. However, better engineering understanding of seismic behavior of low-plasticity fine-grained soils, especially in the range where behavior is believed to transition from materials that behave more similar to sands (sand-like) to materials that have behavior characteristics more similar to clays (clay-like) seemed necessary. More importantly, engineering procedures used for liquefaction (sand-like behavior) triggering and for cyclic softening (clay-like behavior) assessment should be distinct as outlined by Boulanger and Idriss (2004).

Rather than the traditional “liquefiable” versus “non-liquefiable” approach proposed by previous studies (of the time), by detailed review of gathered experimental laboratory results of various fine-grained soils that exhibit clay-like, sand-like, and intermediate types of behavior, Boulanger and Idriss (2004) propose a criterion based solely on soil plasticity index, drawing a line between procedures that are more suitable for estimating cyclic strengths of sand-like and that of clay-like soils, as presented in Figure 6.7. Though in reality, transition from sand-like to clay-like behavior of soils is rather gradual over a range of plasticity indices as shown in the shaded area of Figure 6.7, for practical engineering purposes it is recommended by the authors that fine-grained soils with PI < 7 be considered sand-like, and clay-like if PI ≥ 7.

The proposed criteria does not directly utilize liquid limit, clay fraction, or natural water content as considered by other discussed recommendations. The authors believe that such parameters are misleading and not reliable in distinguishing between sand-like or clay-like behavior for fine-grained soils. Nonetheless, liquidity index $\left(LI = \frac{w_n - PL}{LL - PL}\right)$ and its correlation to the sensitivity (ratio of soils’ peak s_u to fully remolded undrained strength) of clay-like material is recognized to be useful in providing insights in strength loss potential.

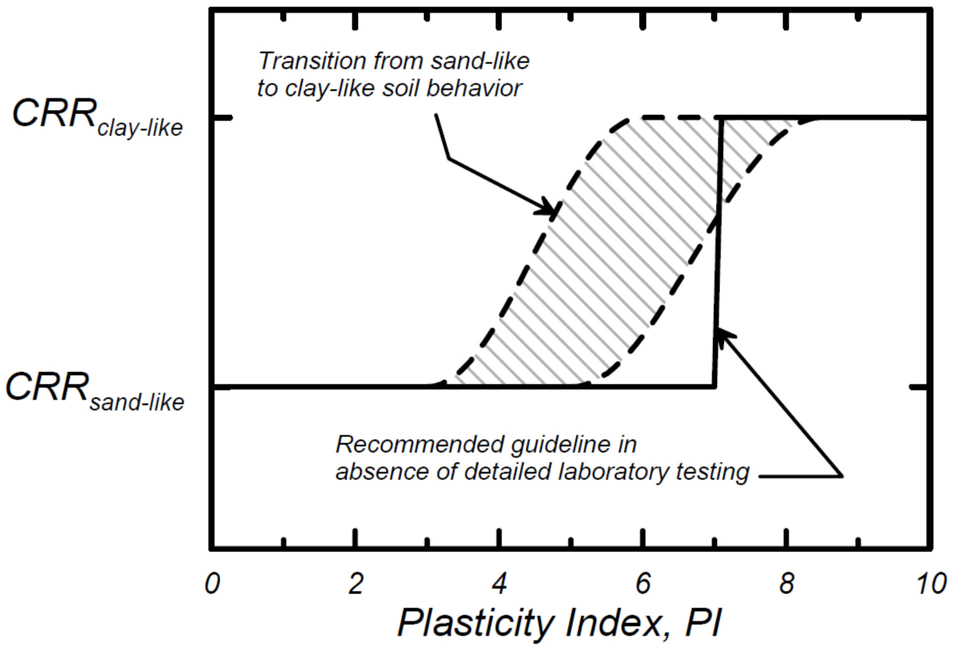

Figure 6.7. Transition from sand-like to clay-like behavior as a function of soil plasticity (figure from Boulanger and Idriss, 2004)

Boulanger and Idriss (2004) propose analytical procedures for evaluating cyclic strengths and consequently assessment of cyclic failure of clay-like soils through a framework quite similar to procedures that are used commonly for sand-like material. Once the cyclic resistance (CRR) of a soil is evaluated, it can be compared to estimates of cyclic stresses (CSR) or demands imposed by an earthquake through a factor of safety $\left(FS = \frac{CSR}{CRR}\right)$. A factor of safety of less than 1 indicates cyclic failure of the material.

Generally, the recommended approach to evaluate cyclic strengths of clay-like soils is to perform cyclic laboratory testing. However, Boulanger and Idriss (2004) provide an alternative approach using empirical factors to estimate cyclic strengths of clay-like soils, if monotonic undrained shear strength (s_u) is known from either laboratory testing or other in situ methods such as vane shear tests or CPT cone tip resistance (which can be correlate to undrained shear strength).

Further, if in situ s_u measurements are not available, the third approach is to estimate the undrained shear strength from guidelines based on the stress history profile of the soil, then use empirical factors to estimate cyclic strengths of the clay-like material.

Figure 6.8 (a) provides the ratios of cyclic strength (τ_{cyc}) to undrained shear strength (s_u) versus plasticity index (PI) for an equivalent number of uniform cycles (N) of 30. Most of the data points on these plots correspond to low and high-plasticity natural silts, mine tailings, and natural clays between plasticity indices of 10 and 27. The plot shows that in this range of plasticity, the τ_{cyc}/s_u ratio for N = 30 is lowest for copper tailings slime and equal to 0.58, and highest for compacted silty clay and (higher than 1). The proposed $(\tau_{cyc}/s_u)_{N = 30}$ ratio for design is considered equal to 0.83 [dashed line in Figure 6.8 (a)] for any clay-like material having PI $\geq$ 7 for direct simple shear loading conditions. Similarly, in Figure 6.8 (b) the ratio of cyclic strength to effective consolidation stress (τ_{cyc}/σ'_{vc}) for the tested material of Figure 6.8 (a) is presented, though the two data points of the compacted clay soils are omitted since the consolidation pressure and overconsolidation ratio (OCR) of these soils were unknown. The proposed ratio of $(\tau_{cyc}/\sigma'_{vc})_{N = 30}$ for design is considered equal 0.183 [dashed line in Figure 6.8 (b)] for normally consolidated clay-like soils that have a plasticity index of 7 or higher under direct simple shear loading conditions.

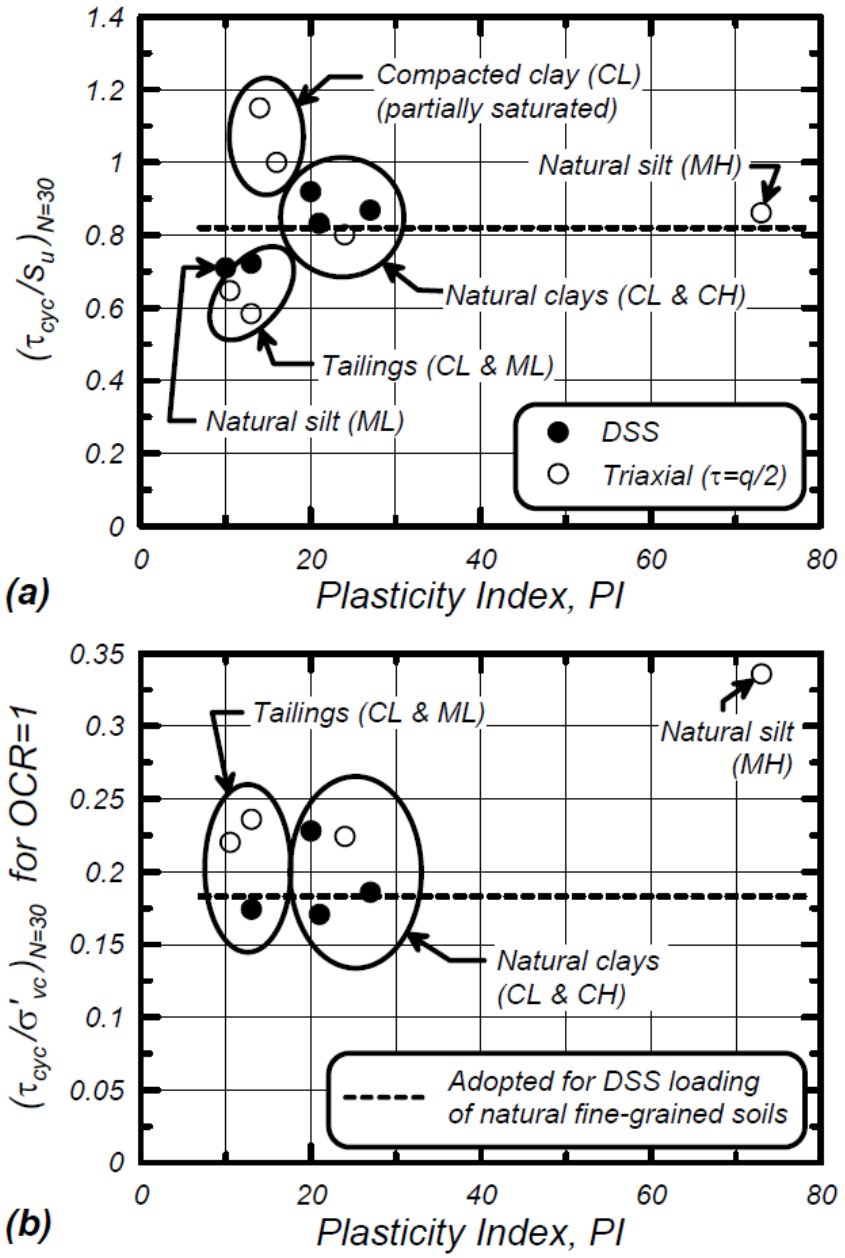

Figure 6.8. Measured cyclic strengths of clay-like soils and proposed relations for design from Boulanger and Idriss (2004)

As outlined by the authors, the number of data points on plots of Figure 6.8 are quite limited. Hence, accumulation of combined laboratory and field test data can lead to refinements of the proposed relations for cyclic strength with more careful considerations for age, PI, soil type, OCR, and test type.

The proposed procedures have been applied to case histories such as the Carrefour shopping center during the 1999 Kocaeli Turkey earthquake and sites in Wufeng during the Chi Chi Taiwan 1999 event in the report by Boulanger and Idriss (2004). Such case studies provide evidence of fine-grained soils that have and have not experienced strength reduction and strain accumulation during the earthquake, making them valuable in assessing the accuracy of the proposed guidelines. The mentioned sites are underlain with low-plasticity silts and clays, some interbedded sand layers that are expected to liquefy, and in some cases higher plasticity clays deeper in the stratum. The recommended procedures can distinguish conditions that lead to ground failure or no ground failure quite consistent with what was observed at these sites. In the case of the Carrefour shopping center, predicted amounts of strain in the clay-like soils (from shaking) from the analysis are known to be slightly higher than that was experienced by the soil as compared with settlement extensometer records instrumented in the field. This suggests that the recommended procedures (exemplified in Figure 6.8) are somewhat conservative, which is argued to be "reasonable given the various uncertainties in some of the analysis parameters" [Boulanger and Idriss (2004)]. During the Chi Chi Taiwan event, large settlements were seen underneath 5- and 6-story structures in Wufeng (Figure 6.5) and relatively little to no ground distress away from the influence of the buildings (in the free field). Recommended procedures by Boulanger and Idriss (2004) have proved to be reliable in identifying such failures and non-failures.

6.2.5 Bray and Sancio (2006)

A comprehensive laboratory program consisting of cyclic triaxial and simple shear testing on silts and clayey soils from Adapazari Turkey (PI typically between 0 and 25) was performed by Sancio (2003). It was concluded that when the PI of the soil is higher than 12, cyclic resistance increases with PI, and that soils with PI > 18 did not generate significant cyclic strains after a high number of loading cycles. Consequently, Bray and Sancio (2006) suggest that soils with plasticity index less than 12 and ratio of water content to LL greater than 0.85 may be susceptible to liquefaction, soils that have 12 < PI < 18 and a ratio of water content to LL greater than 0.8 may be moderately susceptible to liquefaction, and PI > 18 soils are not considered liquefiable at low confinements but can experience significant strength loss and straining when under intense cyclic shear conditions. The authors emphasize that the amount of "clay-size" particles solely, does not govern cyclic behavior of fine-grained soils, but rather the amount and type of clay minerals and their activity are important factors in seismic behavior of such soils. The susceptibility criterion and the soils tested from Adapazari are presented by the authors (Figure 6.9), where laboratory and field observations from Adapazari data is consistent with the proposed criteria. Furthermore, the criteria fits reasonably well for soils that had liquefied during the 1994 Northridge earthquake from Potrero Canyon, data from the Chinese earthquakes [reported by Wang (1979)], and some soils from the 1999 Chi-Chi earthquake.

Similar to cases in Wufeng (in Taiwan), ground failure was observed in areas close to the buildings, but not in the free field in Adapazari during the Kocaeli event. By performing tests at varying effective consolidation stresses, Bray and Sancio (2006) conclude that as the effective consolidation stress (confining stress) decreases, soils with PI < 12 become more resistant to liquefaction and that some soils with PI < 12 may not be susceptible to liquefaction, suggesting that factors such as soils mineralogy, void ratio, overconsolidation ratio, and age may act as contributing elements in liquefaction susceptibility.

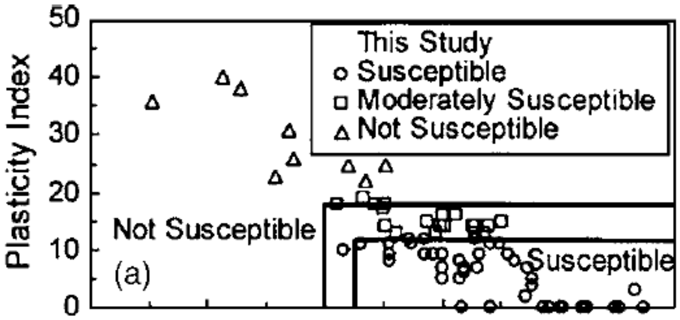

Figure 6.9. Bray and Sancio (2006) susceptibility criteria and liquefied soils from Adapazari during the Kocaeli 1999 event (figure from Bray and Sancio, 2006)

Recently-developed simplified guidelines based on soils index properties for characterization of seismic behavior of silts and clays such as recommendations by Boulanger and Idriss (2004, 2006, and 2007) and Bray and Sancio (2006) are used widely in practice today. However, the amount of laboratory testing data on which these methods are based is limited, and several key questions remain. For example, is plasticity index sufficient for characterizing the cyclic strength loss potential of fine-grained soils? Or is it possible that soils with the same plasticity index may exhibit different strength loss behavior? Does pore fluid chemistry play a role?

6.3 INFLUENCE OF MINERALOGY AND PORE FLUID CHEMISTRY ON PLASTICITY INDEX AND STRENGTH LOSS

Although PI is a convenient index commonly utilized to assess soil plasticity and type of cyclic behavior, it does not capture all factors that influence cyclic strength of soils. A recent study by Jang and Santamarina (2016) highlight that soil plasticity depends on pore-fluid chemistry itself. Several research studies have focused on evaluating the effectiveness of plasticity index in capturing differences in cyclic behavior of soils, seeking trends in fine-grained soil behavior with PI at low- and high-plasticity levels. This section summarizes the finding from such research studies.

6.3.1 Guo and Prakash (1999)

Prakash and Sandoval (1992) performed cyclic triaxial tests on low plasticity silt blended with kaolinite clay. Mixtures had plasticity indices of 1.7, 2.6, and 3.4 corresponding to 0, 5, and 10% kaolinite clay mixed with silt, respectively. All three mixtures reached to excess pore pressure levels equal to the initial consolidation stress ($r_u = 1$). They concluded that in the low-plasticity range ($1.7 < PI < 3.4$), as plasticity increases, the cyclic resistance of the mixtures decreases. This is exemplified in Figure 6.10, where the specimens containing 100% silt lead to the highest relationship of CSR versus number of cycles, followed by the mixtures at PI of 2.6 and lastly 3.4. In other words, for a given CSR, mixtures with PI = 3.4 would require the least number of cycles to reach 2.5% double amplitude axial strains and the pure silt specimens would require the highest number of loading cycles to reach this strain level.

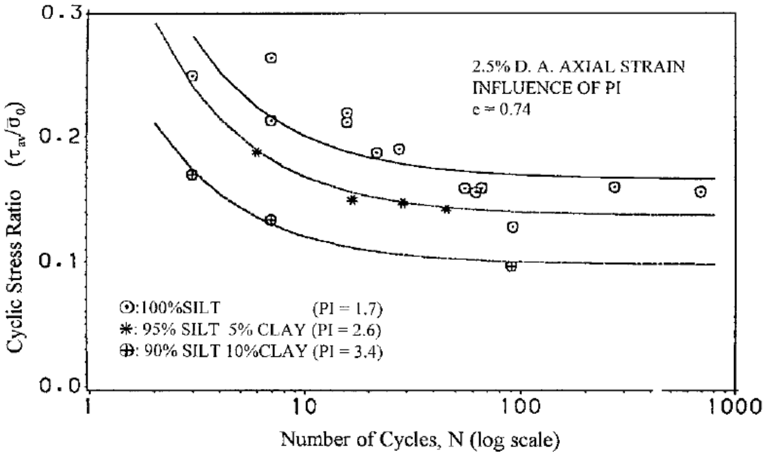

Figure 6.10. Influence of adding varying amounts of Kaolinite clay to silt in the low plasticity range ($1.7 < PI < 3.4$) (figure from Prakash and Sandoval, 1992)

By running cyclic triaxial tests, Puri (1984) showed that in the moderate plasticity range ($10 < PI < 20$), cyclic resistance of silt and silt-clay mixtures increases with plasticity as shown in Figure 6.11. For example, given a CSR value, mixtures with PI = 10 would require the least number of cycles to reach 5% double amplitude axial strains, and mixtures with PI = 20 would require the highest number of cycles to reach this strain level. These specimens do not reach a $r_u = 1$ condition, yet do produce high excess pore pressure ratios. Guo and Prakash (1999) conclude that the mechanism of pore pressure generation in non-plastic silts is the same as sands leading to liquefaction-type behavior. Further, they describe adding high plasticity clays to silts to cause either of two effects:

(1) Adding clay to silt in the low-plasticity range reduces the permeability of the silt-clay mixture and leading to higher excess pore pressure buildup and liquefaction-type behavior (as shown in Figure 6.10).

(2) Adding clay to silt at higher plasticity levels may generate a more cohesive character to the mixtures that leads to an increase in cyclic resistance (as shown in Figure 6.11).

Although (1) may be an important factor for undrained triaxial testing or field conditions, but does not affect constant volume simple shear conditions. These conclusions are illustrated in Figure 6.12 and it is suggested that a critical value of PI (perhaps below 5) exists where transition in behavior (1 and 2 described above) occurs (Guo and Prakash, 1999), and it is emphasized that effects of aging, fabric, and cementation are important factors that influence the pore pressure generation mechanisms of silty soils under cyclic loading and should be recognized in future studies. This suggests that though PI is an important factor in seismic behavior characterization, it may not be adequate to address all variations in cyclic behavior of fine-grained soils.

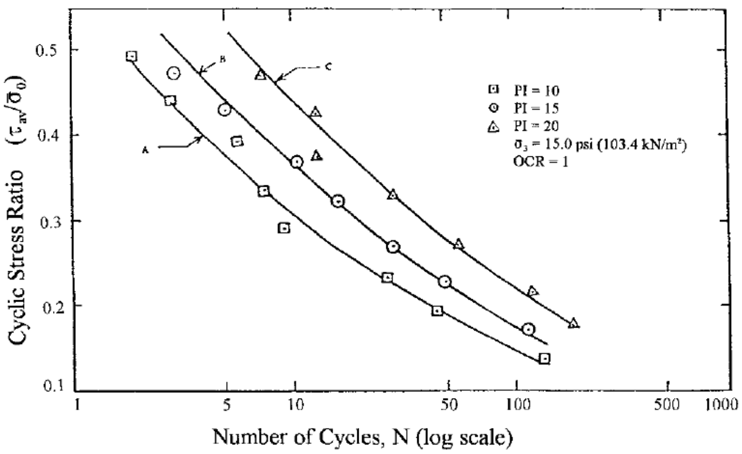

Figure 6.11. Influence of plasticity on cyclic resistance of silt-clay mixtures in moderate plasticity range (10 < PI < 20) (figure from Guo and Prakash, 1999)

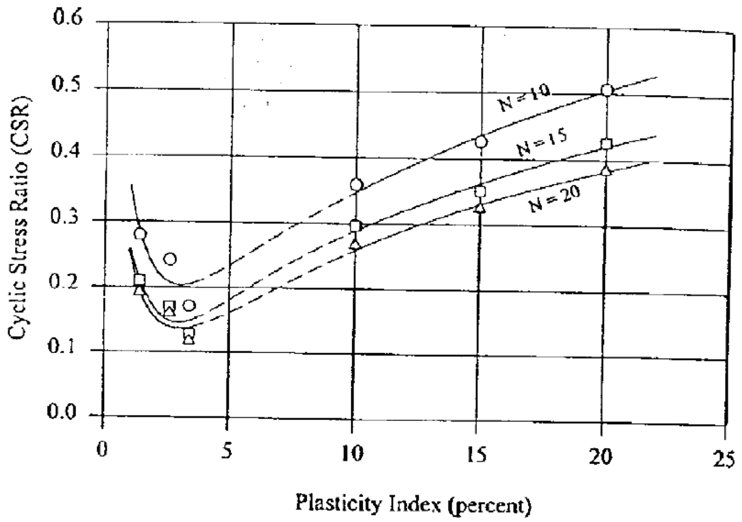

Figure 6.12. Effect of plasticity on cyclic resistance of silt-clay mixtures (figure from Guo and Prakash, 2000)

6.3.2 Gratchev et al. (2006)

Cyclic behavior of soil is shown to be affected by many variables such as fabric, mineralogy, the pore fluid, and pH. Interestingly, all these factors also influence soil plasticity. Gratchev et al. (2006a) performed undrained cyclic stress-controlled ring-shear tests on normally consolidated mixtures of sand with either commercial bentonite, kaolin, or illite at various plasticity levels. Pore fluid in these mixtures varied between solutions of sodium chloride (NaCl), sodium carbonate (Na_2CO_3), sodium hydroxide (NaOH), and calcium carbonate ($CaCO_3$). It was concluded that increase in plasticity strengthens the soil against liquefaction and that bentonite-sand mixtures would not liquefy if PI > 15. Further, it was observed that mixtures of sand with 11% bentonite behaved significantly different when mixed with fresh water versus saline water (containing varying amounts of NaCl), even at same levels of PI. This is demonstrated in Figure 6.13. For example, specimen A with PI = 15.3 showed resistance to liquefaction, whereas sample C (PI = 15.7) liquefied after 5 cycles of loading.

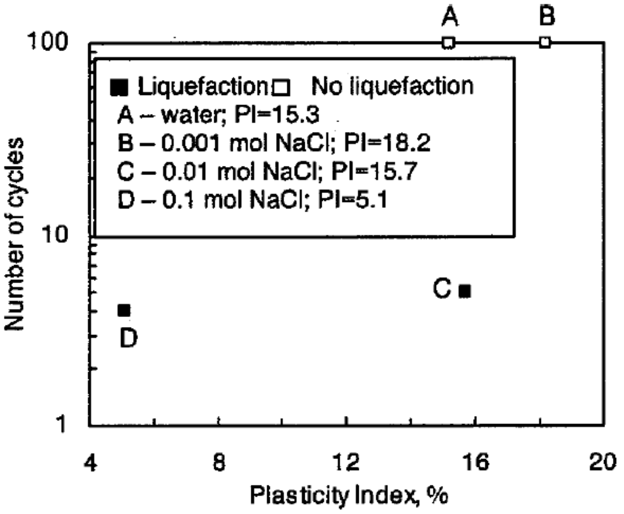

Figure 6.13. Number of cycles to liquefaction versus plasticity index for mixtures of sand with bentonite and varying concentrations of NaCl

To further study the effect of pore-fluid effects on cyclic behavior the sand-bentonite mixtures were treated with varying concentrations of Na_2CO_3, NaOH, and $CaCO_3$. The resulting relationship between number of cycles to liquefaction versus plasticity is presented in Figure 6.14. Interestingly, as PI increases, the number of cycles to liquefaction does not consistently increase. The concentration of the ions in the pore-fluids influences both plasticity, and the number of cycles required to reach a liquefaction state, thereby questioning the effectiveness of PI as a measure for liquefaction potential of clayey soils.

Additionally, more careful studies were performed by Gratchev and Sassa (2009) to observe the effect of pH on cyclic behavior of these mixtures under neutral, acidic, and alkaline environments. It was found that changes in pH can decrease resistance against liquefaction and that susceptibility is significantly dependent on the mineral composition of the clay fraction. Moreover, Gratchev and Sassa (2013) attribute changes in cyclic behavior of soils with varying pore fluids to changes in the diffuse double layer of the clay minerals. It is believed that the thickness of the diffuse double layer decreases as the concentration of acidic or alkaline ions is increased, creating soil structures that are less resistant to cyclic loading.

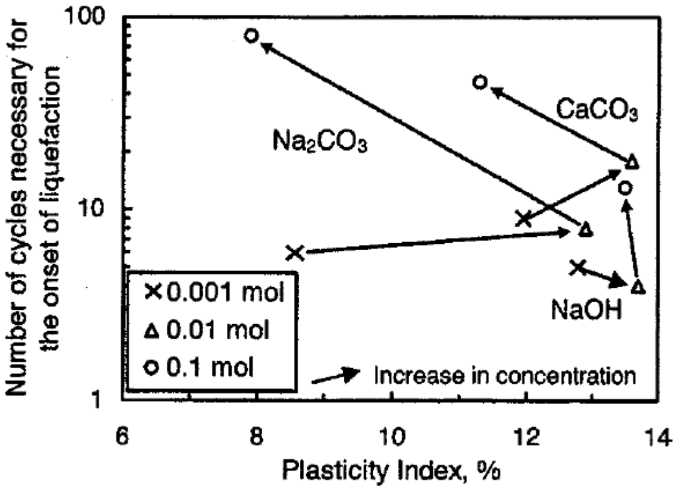

Figure 6.14. Number of cycles to liquefaction versus PI of tested sand-bentonite mixtures with varying pore-fluids

Gratchev et al. (2006b) observed that adding small amounts of bentonite (≤7%) caused rapid liquefaction of the mixture, whereas more amounts of bentonite (≥11%) would significantly strengthen the soil and prevent liquefaction, though still producing high excess pore pressure ratios. It was also found that at the same clay contents, mixtures with bentonite were consistently more resistant to liquefaction in comparison to mixtures with Kaolin or illite, suggesting that the type clay minerals and certain arrangement of particles is what can cause or prevent liquefaction. Mixtures that were resistant to liquefaction consisted of a compact clay matrix that would prevent sand particles to liquefy, and mixtures that liquefied had a more open microfabric with "low-strength clay bridges" that were easily crushed during cyclic loading.

6.3.3 Beroya et al. (2009)

The effect of varying clay minerals in fine-grained silt-clay mixtures on cyclic behavior was investigated by Beroya et al. (2009). Non-plastic silica silt and varying amounts of commercial "kaolinitic, illitic, and montmorillonitic clays" (as described by the authors) have been mixed at different PI values and cyclically tested in the triaxial apparatus at loading frequencies of 1 Hz, where pore pressure measurements are believed to be unreliable. The percent clay minerals were adjusted in the mixtures to ensure that the samples reflect the low-plasticity range; all samples were PI < 7, except for one. Physical properties of the mixtures tested by Beroya et al. (2009) and corresponding CSR against number of cycles to cause cyclic failure are summarized in Figure 6.15.Note that cyclic failure in the mentioned study is defined as the number of cycles that the peak to peak load resistance reaches 10% of the initially applied load. A few major observations can be made from this figure that are described in the following:

(1) Mixtures that contain kaolinitic and illitic clay minerals have lower cyclic strengths compared to pure non-plastic silt. This observation is generally consistent with that of Prakash and Sandoval (1992) described previously.

(2) Mixtures containing very small amounts (even 2.5%) of montmorillonitic clay minerals produce cyclic strengths that are considerable higher than the pure non-plastic silt. Also, CSR increases significantly as the percent montmorillonite increases from 2.5 to 8.45%.

(3) Mixtures Kaolinite 27, Illite 24, and Montmorillonite 3.8 though having fairly equal plasticity indices 6.46, 6.86, and 6.07 respectively, produce cyclic resistance values that differ significantly.

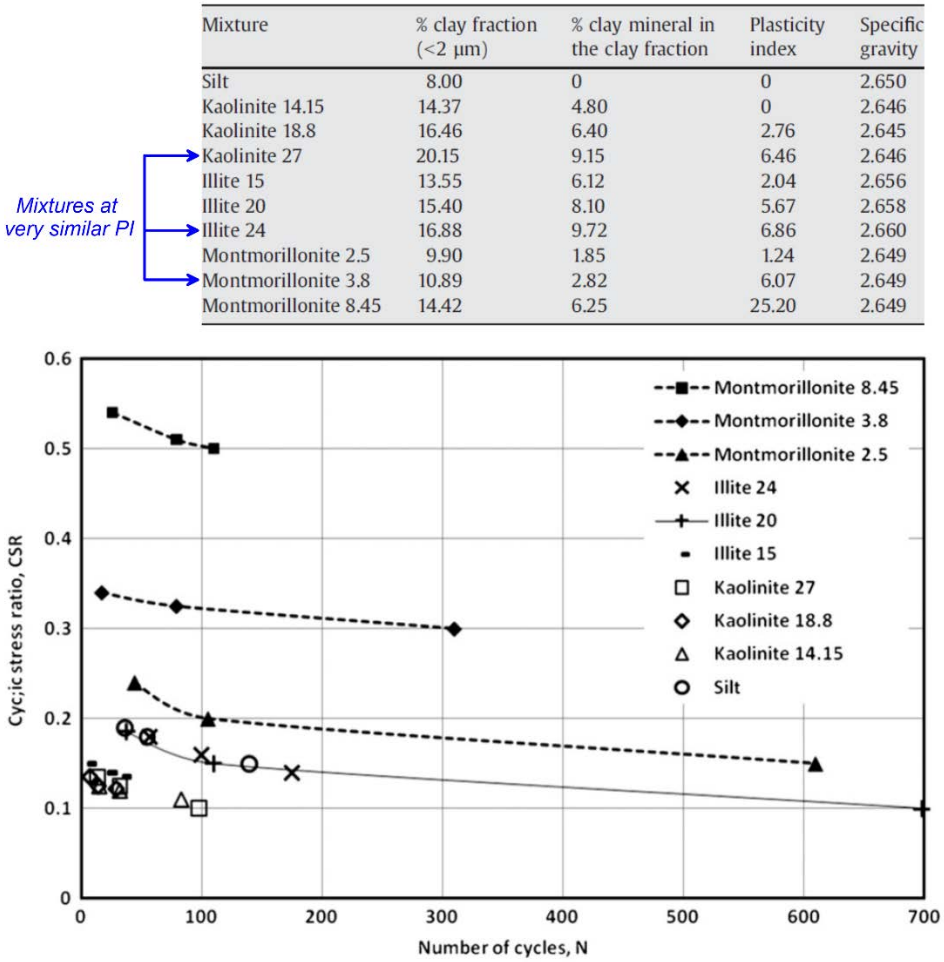

Mixture	% clay fraction (<2 μm)	% clay mineral in the clay fraction	Plasticity index	Specific gravity
Silt	8.00	0	0	2.650
Kaolinite 14.15	14.37	4.80	0	2.646
Kaolinite 18.8	16.46	6.40	2.76	2.645
Kaolinite 27	20.15	9.15	6.46	2.646
Illite 15	13.55	6.12	2.04	2.656
Illite 20	15.40	8.10	5.67	2.658
Illite 24	16.88	9.72	6.86	2.660
Montmorillonite 2.5	9.90	1.85	1.24	2.649
Montmorillonite 3.8	10.89	2.82	6.07	2.649
Montmorillonite 8.45	14.42	6.25	25.20	2.649

Mixtures at very similar PI

Figure 6.15. Mixture properties and CSR versus N curves from Beroya et al. (2009) (Table 2 and Fig 1 of the paper are combined)

The authors emphasize observation (3) by plotting the CSR value at N = 20 versus PI as shown in Figure 6.16. It can be inferred from this figure that the cyclic strength for blend M3.8 is 2.6 times larger than for K27 (PI = 6.07 and 6.46, respectively), which is rather significant. Furthermore, a significant increase of the clay content in the kaolinitic mixtures does not significantly affect cyclic resistance of these mixtures, but adding illitic and montmorillonitic clay minerals leads to sharp increases in cyclic strength. Mixtures containing kaolinitic and illitic clay minerals are believed to have deceased permeabilities compared to the case of pure silt, resulting in development of higher excess pore pressure and lower cyclic strengths, though do not affect simple shear testing. This trend can be seen in mixtures K14.15, K18.8, K27, and I15. However, mixtures I2-, I24, and all mixes containing montmorillonitic clay minerals do not follow this trend. The authors recognize that after a limiting clay fraction (% clay mineral) an adhesive character is developed in the mixtures leading to higher cyclic strengths as compared to the pure silt specimen. The adhesive character seems to act as a bond that holds the silt particles together, reducing excess pore pressure generation, eventually resulting in higher cyclic strengths. Further, differences in cyclic strength of these mixtures is attributed to different mechanisms of adsorbed water on the surface of various clay minerals.

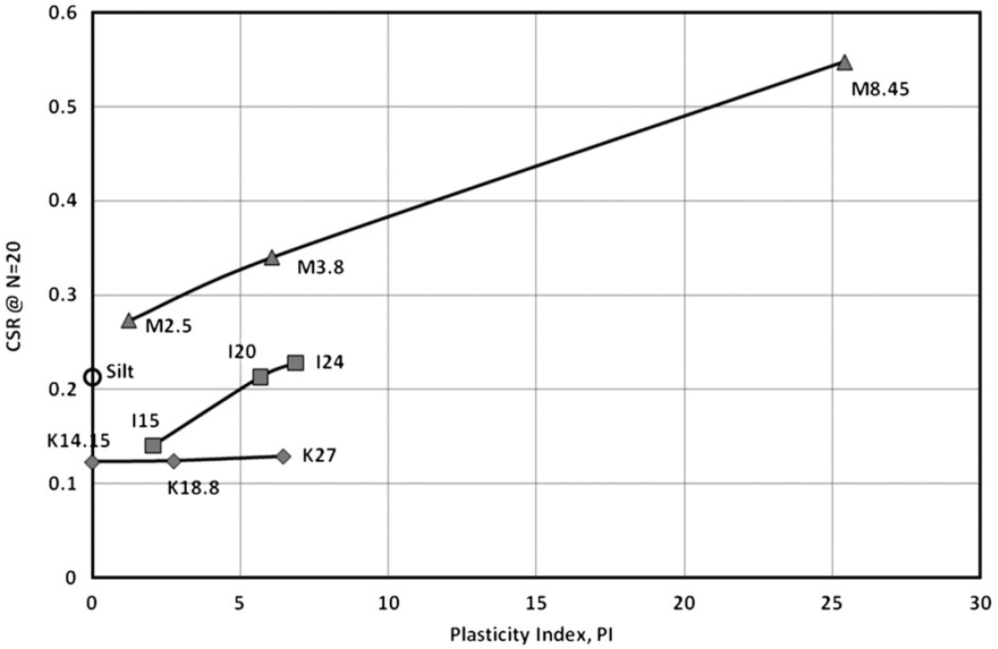

Figure 6.16. CSR at N = 20 against PI for various mixtures (from Beroya et al., 2009)

Beroya et al. (2009) conclude that clay fraction, % clay mineral, and PI are not reliable indicators for evaluation of liquefaction susceptibility in fine-grained mixtures if used soleley, and that type of clay minerals should also be addressed. Addditionally, PI does not capture variations in clay mineralogy, and thereby, cyclic strength of fine-grained soils.

6.3.4 Wang et al. (2015)

Wang et al (2015) studied differences in cyclic and post-cyclic behavior of mixtures of low-plasticity Mississippi River Valley (MRV) silt (PI = 5.8) with varying amounts of bentonite clay through triaxial laboratory testing. Cyclic sinusoidal loading was applied at a frequency of 0.1 Hz and limited to 9% single amplitude axial strain. Specimens with 2.5% and 5% bentonite having PI of 6.2 and 9.4, respectively were tested as well as specimens of pure MRV silt. Figure 6.17 presents CSR versus number of cycles to reach 5% double amplitude axial strain. The results presented in this figure are similar to that of Beroya et al. (2009) where adding small amounts of bentonite seemingly increases cyclic strengths. Although this is seemingly true for CSR values below 0.35, the authors have drawn expected curves for the range of CSR values between 0.25 and 0.35 with dashed lines in this figure. Moreover, it was reported that MRV silt specimens reached r_u value equal to 1 (liquefaction-type behavior)), yet specimens containing bentonite reached r_u value of about 0.8 to 0.9 indicating a cyclic softening type of behavior.

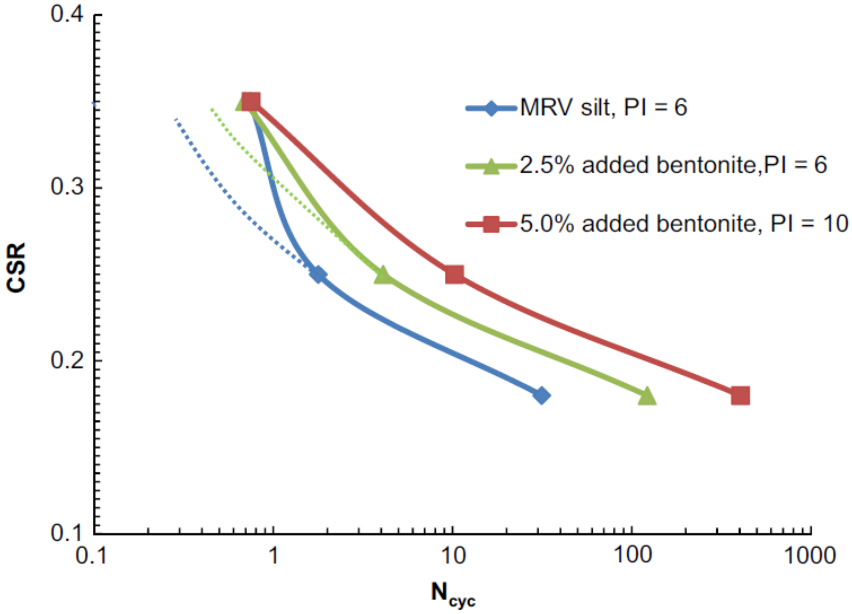

Figure 6.17. CSR versus number of cycles to reach 5% double amplitude axial strain for MRV silt blended with varying amounts of Bentonite (figure by Wang et al., 2015)

Wang et al. (2015) suggests that the transition from sand-like to clay-like behavior occurs at a PI of 6, rather than PI = 7 as recommended by Boulanger and Idriss (2004). The authors emphasize that PI seems to not be an ideal index for identifying changes in seismic behavior of low-plasticity fine-grained soils due to the difficulty of capturing small changes in the plasticity index in engineering practice, and effects of clay mineralogy on cyclic behavior of low-plasticity material should be further investigated. Moreover, by running post-cyclic reconsolidation tests, the authors reached to an interesting conclusion. Interestingly, the authors also found that the compression index during reconsolidation was closer to the virgin compression index rather that the recompression index, suggesting that after cyclic loading, the mixtures behaved more similar to normally consolidated soil, though specimens containing bentonite seemed to have more “memory” of their previous stress history conditions.

6.3.5 Ajmera et al. (2015)

Ajmera et al. (2015) examined the effect of kaolinite and montmorillonite on quartz by constant-volume cyclic simple shear testing. Cyclic loading was applied by sinusoidal stress-controlled loading with a frequency of 0.5 Hz and continued till 10% double amplitude shear strain was reached. Corresponding CSR versus number of cycles to reach 5% double amplitude shear strains are presented in Figure 6.18 and reflect the influence of both clay mineralogy and plasticity. As PI is increasing, cyclic resistance is shown to increase consistently whether the mixture contains kaolinite or montmorillonite. Secondly, samples with varying mineralogy but equal plasticity indices (mixtures SN. 6 kaolinite-quartz and SN. 11 montmorillonite-quartz both at PI = 14) produce significantly different cyclic strength curves. It can be inferred from Figure 6.18 that at N = 30, the resistance of SN.11 is 1.3 times resistance of SN.6 which is quite a significant amount of difference, suggesting that cyclic behavior cannot be solely evaluated based on PI and effects of clay mineralogy should be considered for better understanding cyclic behavior of clay-like soils.

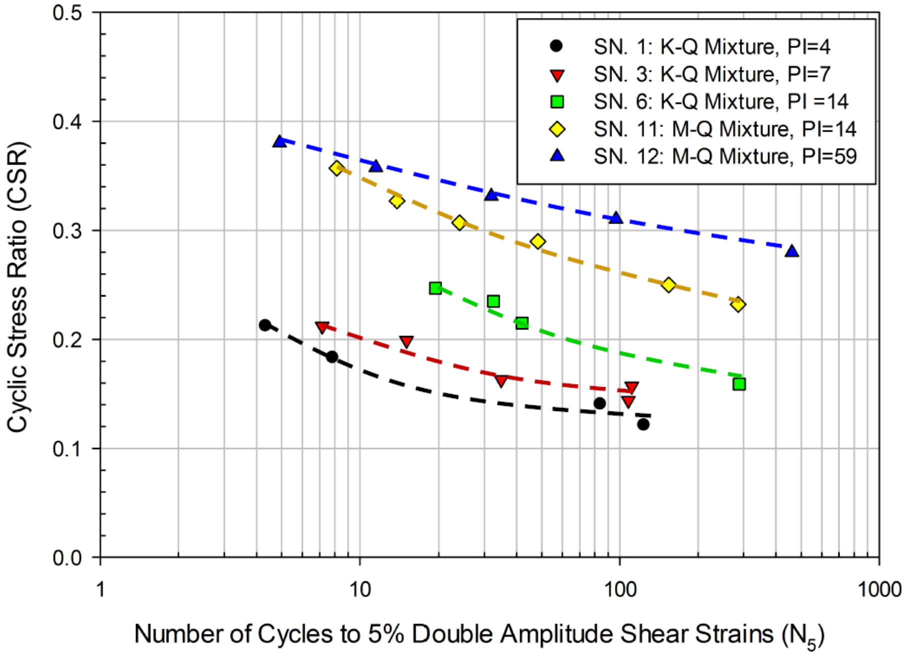

Figure 6.18. Relation of CSR and number of cycles to reach 5% double amplitude shear strain of Kaolinite-Quartz (K-Q) and Montmorillonite-Quartz (M-Q) mixtures at different PI (figure from Ajmera et. al., 2015)

Moreover, comparing CSR versus N curves to reach 2.5, 5, and 10% double amplitude shear strains Ajmera et al. (2016) concluded that the kaolinite-quartz mixtures provide similar cyclic resistance regardless of the amount of shear strain, where in montmorillonite-quartz specimens a significant difference in cyclic resistance was observed at various levels of shear strains.

7 Methodology and Experimental Procedures of Part II

Based on the review of literature in Chapter 6, currently utilized guidelines for characterizing the cyclic strength loss of fine-grained soils are heavily dependent on soil index properties such as liquid limit, plasticity index, and natural water content. These methods are based on limited laboratory testing data (or case studies) and may not be able to adequately represent variations in seismic fine-grained soil behavior. Some parallel studies have shown that factors such as mineralogy and pore-fluid chemistry also effect cyclic behavior of fine-grained soils.

A comprehensive laboratory study was organized to investigate the effectiveness of parameters such as soil's plasticity index in seismic soil characterization and assess the effects of clay minerology and pore fluid salinity on cyclic response of low-plasticity fine-grained mixtures. Additionally, the influence of Soil-Structure Interaction (SSI) on the seismic behavior of these low-plasticity fine-grained mineral blends will be studied through centrifuge testing in another Ph.D. student's dissertation.

Details of the UCLA Bi-directional simple shear device is presented first in this chapter, followed by procedures for specimen preparation, and the descriptions of the laboratory testing program which consisted of Atterberg limits tests, consolidation tests, monotonic and cyclic constant volume direct simple shear tests, and scanning electron microscope (SEM) imaging.

7.1 UCLA BI-DIRECTIONAL BROADBAND SIMPLE SHEAR DEVICE AND TESTING PROCEDURES

For this project, direct simple shear tests were chosen for cyclic and monotonic shearing of the mixtures mainly because the deformations applied to specimens in the simple shear apparatus mimic the vertical one-dimensional shear wave propagation under in situ conditions. The University of California Los Angeles (UCLA) Bi-Directional Broadband Simple Shear (BB-SS) apparatus, a digitally-controlled NGI-type direct simple shear device having capabilities for broadband multidirectional excitations was utilized for this purpose. A schematic of the device is presented in Figure 7.1.

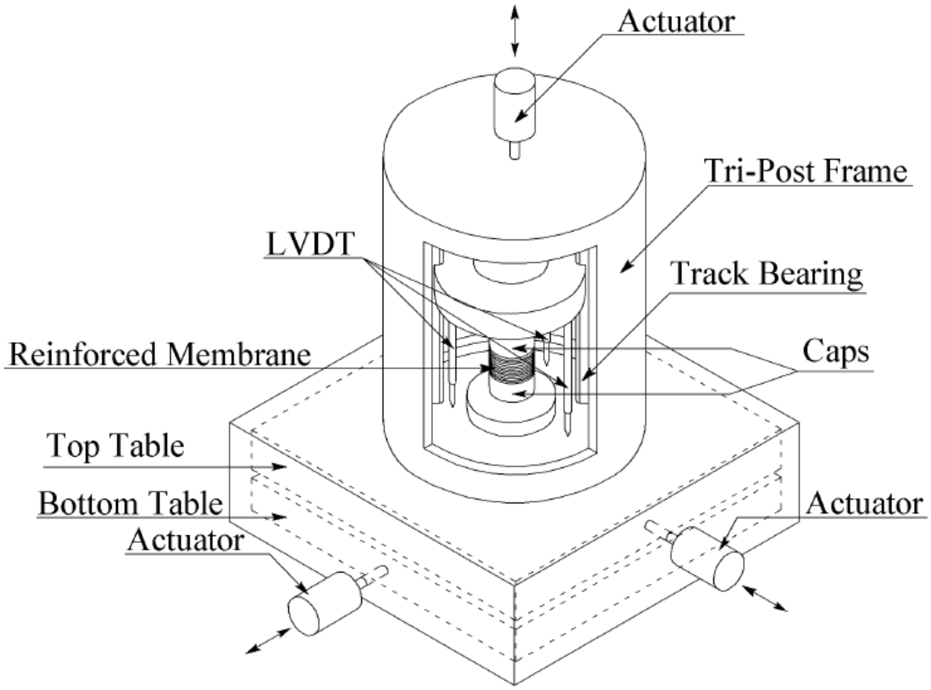

Figure 7.1. Schematic of UCLA Bi-directional Broadband Simple Shear Apparatus

Details of the device are described in Duku et al. (2007) and more recent updates are described by Shafiee et al. (2017). Some unique features of the device are: (1) the device operates with servo-hydraulic actuators that are capable of producing broadband (earthquake-like) excitations with rigorous control; (2) shear can be applied to specimens in two horizontal directions simultaneously for realistically simulating field stress paths; (3) is enhanced with stiff tri-post frame and high-performance track bearing that minimizes (but does not eliminate) system compliance associated with top cap rocking.

Shear is applied through the bottom cap which is fixed vertically, but is free to move horizontally in two perpendicular directions. The top cap cannot be displaced horizontally but can move vertically and can maintain constant vertical loads or constant vertical height. The vertical loads are applied to the top cap by the vertical actuator as shown in Figure 7.1. Cylindrical soil specimens with diameters of 10.2 cm and less can be tested with the UCLA BB-SS device. Specimens are confined with reinforced rubber membranes (Figure 7.2), that prevent (but do not eliminate) lateral deformation, and placed between the relatively rigid top and bottom caps of the device.

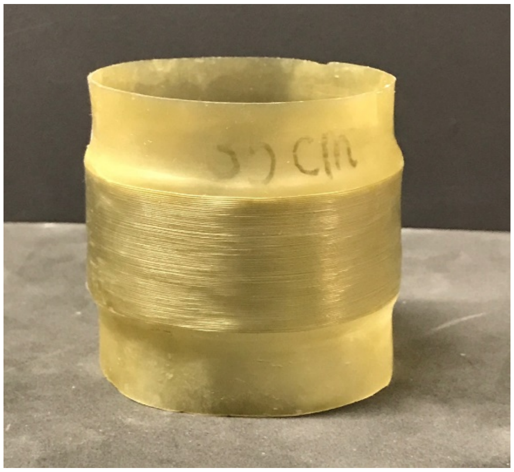

Figure 7.2. Wire-reinforced rubber membranes used for Direct Simple Shear testing

Once a specimen is in place within the two caps, three LVDTs (equally spaced around the specimen) are mounted on the top adaptor plate and fixed to the plate by screws. The device in its original form was designed to test large diameter specimens and to study large-strain applications, seismic compression, and shear strength and under strain-controlled conditions, where cyclic shear strains as low as 0.1% were applicable. Later, Yee et al. (2011) modified the low-strain capabilities of the device to output meaningful shear strains as low as approximately 0.03%.

Shafiee et al. (2017) recently made further modifications to the UCLA BB-SS device to enable constant-height conditions as well as stress-controlled loading. These enhancements were added while maintaining other features of the device and the device is able to operate under either strain- or stress-controlled conditions on all three axes. The current physical form of the device is presented in Figure 7.3

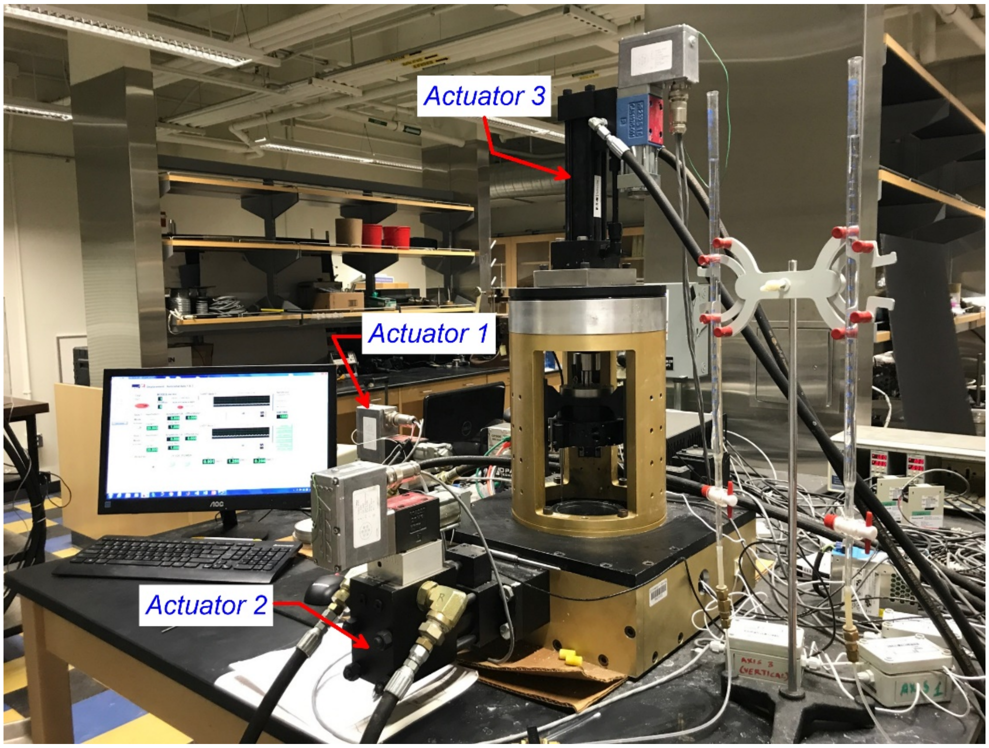

Figure 7.3. Physical presentation of the UCLA BB-SS device in its current form

The constant-height condition is equivalent to undrained testing in a triaxial apparatus where drainage is prevented and the specimen's volume remains constant. The underlying assumption in constant-volume (constant-height) testing in a simple shear device is that changes in the vertical stress required to maintain constant height are equal to changes in excess pore pressure that would have developed in a truly undrained test (Bjerrum and Landva, 1966). The constant height mechanism in the UCLA BB-SS device is made available using a servo-hydraulic vertical actuator by equipping the vertical axis with a servo electric valve, an actuator, and a load cell. By using a closed-loop algorithm, the vertical load is adjusted during the test to maintain constant-height conditions if the feedback from the LVDTs are non-zero values.

The stress-controlled feature is a significant improvement of the device and is applicable for applications in cyclic softening and liquefaction. Both horizontal axes are enhanced with this feature by feedback from the load cells. The horizontal load cells are placed between the actuator and the table, and is capable of measuring soils resistance as well as friction resistance in bearings. Note that the friction resistance is about 2.2 N and rather small because of the usage of high-quality linear trach bearings, as reported by Duku et al. (2007). The mean values of resistance from these bearings are subtracted from the measured loads by the control system. Load control is provided with a PID (Proportional Integral Derivative) controller which was carefully tuned for a range of vertical loads.

Detailed discussions on the performance of the modified device, its precision, and issues such as top cap rocking are provided by Shafiee (2015) and Shafiee et al. (2017). However, since Part II of this dissertation consists of several stress-controlled cyclic tests, important aspects of performance of the device in stress-controlled conditions are summarized herein from Shafiee (2015). Cyclic stress-controlled tests were performed on silica sand at low and high amplitudes. Command and feedback signals from the load cell were plotted and it was observed that at low amplitude loading the mismatch between the two signals is more pronounced. The command and feedback signals are better matched at higher amplitudes of shear force (e.g. 111 N).

To quantify the mismatch, the normalized force root mean square error $\left(\varepsilon_{FRMS} = \sqrt{\frac{\sum_{i=1}^{N}(F_i^f - F_i^c)^2}{\sum_{i=1}^{N}(F_i^c)^2}}\right)$ was computed and plotted for tests at varying CSR and frequency at a consolidation stress of 100 kPa. Note that CSR is constant during each test. The summation occurs over N time steps and F^f and F^c represent the feedback and command force signals, respectively. Figure 7.4 presents values of ε_{FRMS} versus CSR and frequency. The error term ε_{FRMS} decreases with increased frequency and CSR as shown in Figure 7.4(a).

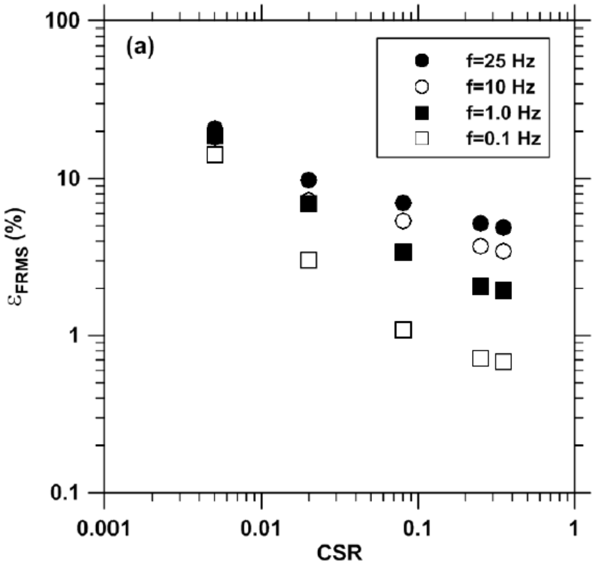

Figure 7.4. Performance of the stress-controlled feature of the UCLA BB-SS device; effect of stress amplitude and frequency on tracking errors (figure from Shafiee, 2015)

To assess the capabilities of the control system to track the command when the horizontal shear stress becomes very close the shear strength of the soil, Silica No. 2 sand prepared at relative density of 40% was tested at CSR = 0.15 and at effective consolidation stress of 100 kPa under different loading frequencies. Figure 7.5(a) presents results of test with a rapid loading frequency of 1 Hz. Tracking errors are time-dependent and are defined as $\varepsilon_F(t) = \left|\frac{F_i^f - F_i^c}{F_i^c}\right|$, where t is the time step. Error term ε_F is plotted against time in Figure 7.5(b), and shows that the feedback signal tracks the command signal quite well up to 6.5 seconds, after which the feedback signal drops and cannot follow the command signal. Large errors occur when the stress path response approaches steady state (initial liquefaction) and high excess pore pressure ratios are developed. At this condition, shear strength drops below the command amplitude and the stress path oscillates near the origin. In ideal conditions, the amplitude of stress should remain constant due to the dilation of the sand, however, the control system is unable to accurately track the command signal (dilation response of the sand) once these conditions are reached at high loading frequencies.

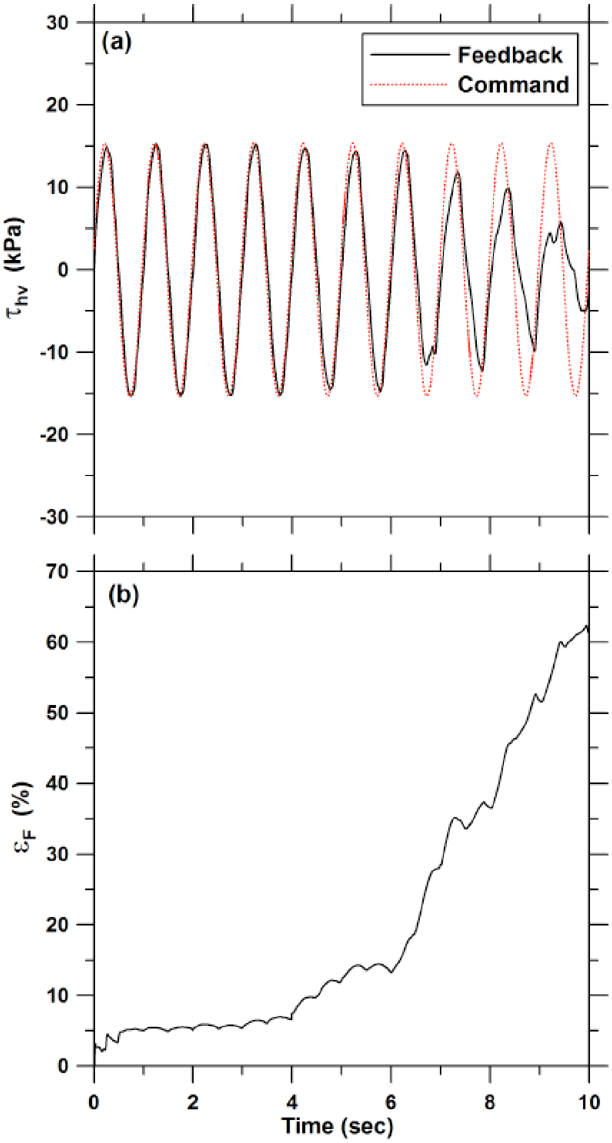

Figure 7.5. Constant volume stress-controlled cyclic test on Silica No. 2 sand at D_r = 40%, σ'_{vc} = 100 kPa, and f = 1 Hz; (a) feedback and command signals for CSR = 0.15, (b) smoothed tracking error (figure from Shafiee, 2015)

Variation of error term ε_F with loading frequency is investigated on similar material and specimens as presented in Figure 7.6. Tracking errors are lowest at a loading frequency of 1 Hz. Moreover, the error term consistently increases after the 4th loading cycle, where initial liquefaction occurs and remains constant for larger number of cycles when a loading frequency of 0.5 Hz or smaller is applied. At loading frequencies larger than 0.5 Hz, the error is seen to increase progressively with more number of cycles after the 4th cycle.

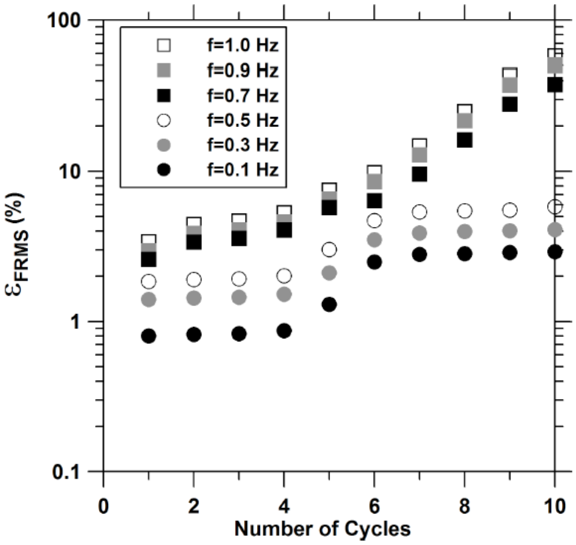

Figure 7.6. Performance of UCLA BB-SS device control system for stress-controlled constant volume tests on sand with varying frequencies (figure from Shafiee, 2015)

Based on these observations, a loading frequency of 0.1 Hz was chosen for cyclic stress-controlled testing of the low-plasticity fine-grained soils of Part II of this dissertation. Validation tests have been performed on Silica sand No. 2 to cross-check with that of Shafiee (2015) prior to starting the laboratory testing program for the current dissertation. Results of the validation tests are not presented in this dissertation however. Stages of the tests performed herein are presented in the following sections.

7.2 MIXTURES USED IN EXPERIMENTAL STUDY AND SPECIMEN PREPARATION

7.2.1 Materials

Three mixtures of commercially available non-plastic silt (Sil-Co-Sil #45 ground silica) and clay minerals were prepared at PI = 9. The mixtures were made at this PI to assess if it's possible that soils with the same plasticity index may exhibit different strength loss behavior. The mixtures contain predominantly silt, mixed with varying amounts of commercially available bentonite or kaolinite clay minerals. To inspect the effects of the pore-fluid chemistry on cyclic behavior, the mixtures were either blended with deionized fresh water or saline water with a concentration of 35g/L of NaCL. Properties of the mixtures as well as their constituent minerals are summarized in Table 7.1, where Atterberg limits are based on methods described in ASTM 4318.

Table 7.1. Properties of mixtures used in experimental study

ID	*% silt*[a]	*% Bentonite*[b]	*% Kaolinite*[c]	*Pore-fluid*	G_s	*LL*	*PL*	*PI*
SBFW	95	5	0	Fresh water	2.64	31.2	22.6	8.6
SBSW	90	10	0	Saline water	2.67	31.9	23.1	8.8
SKFW	78	0	22	Fresh water	2.63	30	21.4	8.6

[a] Sil-Co-Sil #45 ground silica, Non-plastic

[b] *LL* = 455.3, *PL* = 39.6, *PI* = 415.7

[c] *LL* = 66.1, *PL* = 35.8, *PI* = 30.3

Figure 7.7 presents the location of the mixtures prepared in the laboratory on Casagrande's plasticity chart. All three mixtures plot on top of each other and slightly above the A-line, classifying as low-plasticity clay (CL) per the Unified Soil Classification System (USCS). Note from Table 1 that all three mixtures have essentially identical values of LL, PL and PI, and are therefore indistinguishable based on plasticity characteristics, despite their different mineral constituents

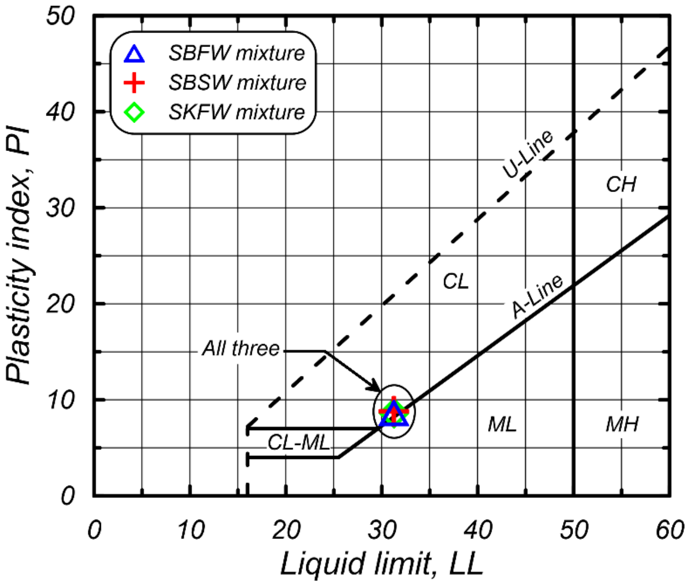

Figure 7.7.Casagrande's plasticity chart showing Atterberg limits of soil mixtures used for laboratory testing

7.2.2 Specimen preparation

Mixtures were first made as a slurry above their liquid limits, then transferred to acrylic tubes with a dimeter of 72.5 mm, which is similar to the consolidation ring used for consolidation testing and slightly larger than the simple shear specimens. The slurries inside the tubes were then consolidated to a vertical stress of 35 kPa by adding weights on an aluminum piston that was placed on top of the slurry and porous stone (Figure 7.8). The pre-consolidation step results in a specimen that is stiff enough to extrude and trim, and subsequently further consolidate in the simple shear device. An alternative would have been to place the slurry directly into the wire reinforced membrane, and consolidate in the simple shear device. This was not feasible for two reasons. First, the amount of time required to consolidate the specimens would be too long to safely operate the hydraulic pump. Second, the vertical displacements that would arise would potentially exceed the range of the vertical LVDTs, which is about 12.5 mm). However, the same procedure did not work for the SKFW blend, which was prone to falling apart after pre-consolidation in the acrylic tubes and could not really be trimmed. In a way, this provides evidence that the materials exhibit different behavior despite their similar plasticity indices. The SKFW mixtures slurries were placed directly into the wire reinforced and consolidated in the simple shear device prior to being sheared.

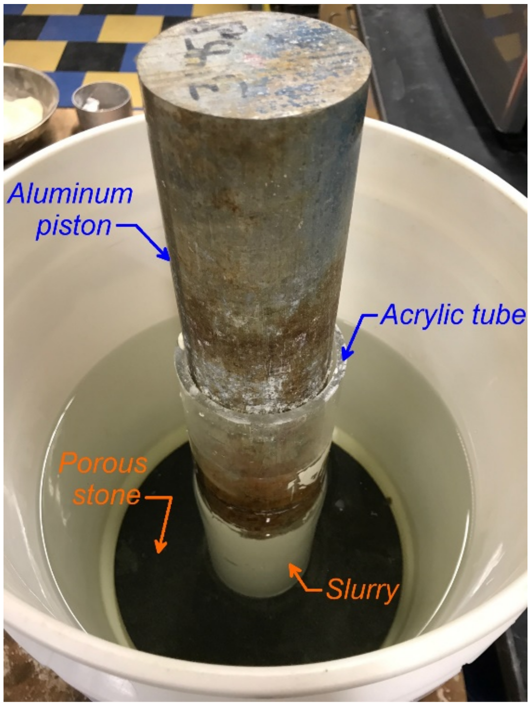

Figure 7.8. Pre-consolidation of slurries inside acrylic tubes

Once the slurries reached to a consolidation stress of about 35 kPa by this manner, they were then extruded from the acrylic tubes to a separate 28 mm tall ring having the same diameter as the acrylic tubes (i.e. 72.4 mm). The sample inside this ring is then cut to the desired height using the ring as a guide [Figure 7.9(a)]. Next, the sample inside the ring is placed on the bottom cap of the simple shear device, which is placed inside a trimming device. The top cap of the trimming device is lowered on the specimen and locked into place, then the ring is pulled up and removed from the specimen. Using a wire saw, the specimen is trimmed to reach a diameter of 66 mm, which is the same as the wire-reinforced rubber membrane. These steps are shown in Figure 7.9.

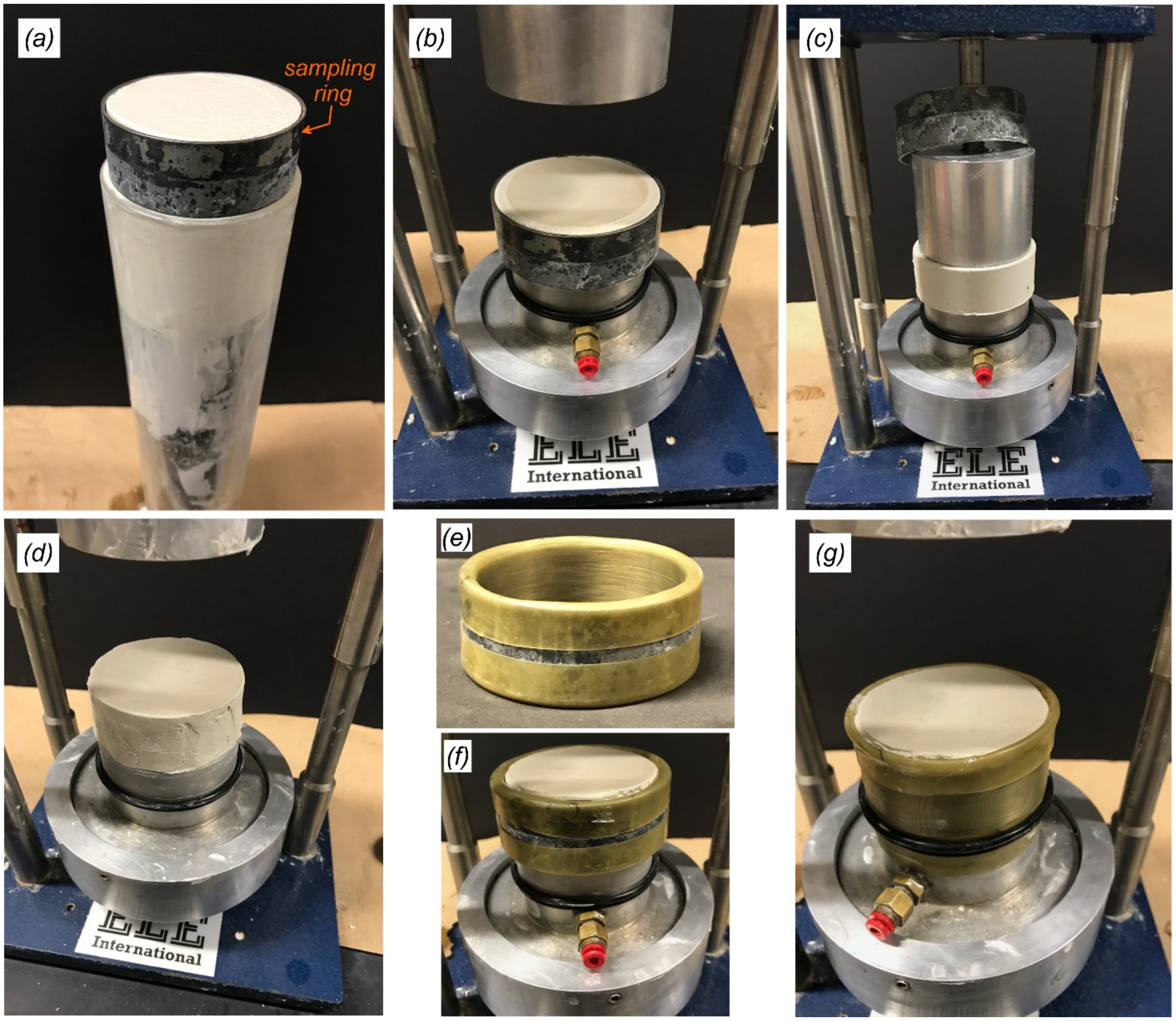

Figure 7.9. Steps for specimen preparation; (a) extruding pre-consolidated mixture to sampling ring, (b) sample inside sampling ring placed on top of the bottom cap of the DSS device and inside the trimming device, (c) top cap of the trimming device lowered and sampling ring removed from specimen, (d) specimen trimmed to diameter of 66 mm, (e) wire-reinforced rubber membrane stretched around a ring, (f) stretched membrane placed on specimen, (g) membrane pulled down around the specimen

The wire-reinforced rubber membrane is stretched around a 68.3 mm diameter ring, and placed on the specimen. The membrane is gently pulled down around the specimen and the non-wired reinforced part of the membrane is unfolded onto the top and bottom caps. at this stage, the ring is removed, and o-ring seals are placed around the top and bottom portions of the membrane. The specimen inside the reinforced rubber membrane is set for testing in the direct simple shear device [Figure 7.9(g)].

7.3 CONSTANT-HEIGHT DIRECT SIMPLE SHEAR TESTING

Each simple shear test performed herein consisted of two stages; consolidation and shear. Procedures within these stages are described in the following sections.

7.3.1 Consolidation

Once the trimmed specimens with diameter of 66 mm and height of 28 mm were prepared, the bottom cap and the soils specimen were placed inside the UCLA Bi-Directional Broadband Simple Shear (BB-SS) device, where the top cap is also placed inside the device maintaining a small gap with the specimen's top surface. The top and bottom caps are connected to drainage lines to help keep the specimens close to fully saturated conditions. The top cap is then lowered until it gently touches the top of the specimen using the servo-hydraulic control of the vertical actuator using a string potentiometer. Following this, the top part of the membrane is attached to the top cap and sealed with o-rings. Next, the vertical LVDTs are mounted and the transducer used for controlling the vertical axis is switched from string potentiometer to the vertical LVDTs, where vertical movement can be controlled.

The device has the capability of performing either strain- or stress-controlled consolidation. Strain-controlled consolidation would be equivalent to a constant rate of strain type of oedometer test. The consolidation stage for the testing program presented herein was performed by stress-controlled conditions until the desired vertical pressure was reached. Pressure was usually applied in increments of 10 kPa and applied once the change in the LVDT measurements were minimal, ensuring that consolidation had finished for the previous loading stage. Sometimes, larger increments of loads were applied to the specimen (larger than 10 kPa) and enough time was given until the sample reached the desired consolidation stress.

To achieve overconsolidated specimens, once consolidation had finished at the desired pressures, vertical pressure was decreased to reach the desired effective confining stresses. Then, the specimen was left to equilibrate for about 5 to 10 minutes, and then shear loading was applied. Depending on the effective stresses and the type of material that was being tested, time to reach end of primary consolidation varied in a manner consistent with results from the oedometer tests that are presented in Chapter 8.

Generally, the normally consolidated and overconsolidated specimens of the present study were tested at an effective consolidation stress of σ'_{vc} = 50 kPa. Some specimens were overconsolidated to a maximum vertical pressure of $\sigma'_{vc,max}$ before being unloaded to σ'_{vc}. The time to reach a consolidation pressure of 50 kPa was in the range of 2 to 3 hours for normally consolidated samples, and longer periods of time were required for the overconsolidated specimens. Secondary compression occurred during consolidation of the soil, rendering an overconsolidation ratio that is larger than the mechanical preload ratio $\sigma'_{vc,max}/\sigma'_{vc}$. Overconsolidation ratio, OCR, was computed based on distance to the normal consolidation line rather than being taken as equal to the preload ratio to account for the influence of secondary compression.

7.3.2 Monotonic and Cyclic Shearing

Once the specimens were consolidated to the desired pressure and OCR, the sample was then ready for constant-height shear. Monotonic shear was applied by strain-controlled conditions with a shear strain rate of 1%/min. Tests at faster strain rates were performed in the initial stages of the project to assess the impact of strain rate on stress-strength behavior. For example, Figure 7.10 presents monotonic shear response of SBSW mixtures at OCR = 4 and σ'_{vc} = 50 kPa of three specimens sheared at 1, 2, and 4% shear strain per minute. The maximum undrained shear strength ratio was measured as 0.601, 0.628, and 0.629 from slowest to fastest strain rates, resulting in small difference. As expected, the fastest test produced the highest undrained shear strength ratio, though the material was not significantly rate-dependent. Consequently, the rate of strain applied for monotonic shear tests was kept at 1%/min for subsequent experiments and to allow pore pressure to redistribute within the specimens.

Monotonic strain-controlled shear was applied up to horizontal displacements of about 5.6 mm (0.22 inch) equivalent to a shear strain of about 20%. Depending on the height of the specimen after consolidation, the amount of ultimate shear strain reached at the end of monotonic shear may vary among different tests and different mixtures.

Cyclic shear testing was performed under stress-controlled conditions with CSRs ranging between 0.1 and 0.3 with a frequency of 0.1 Hz as described in section 7.1.

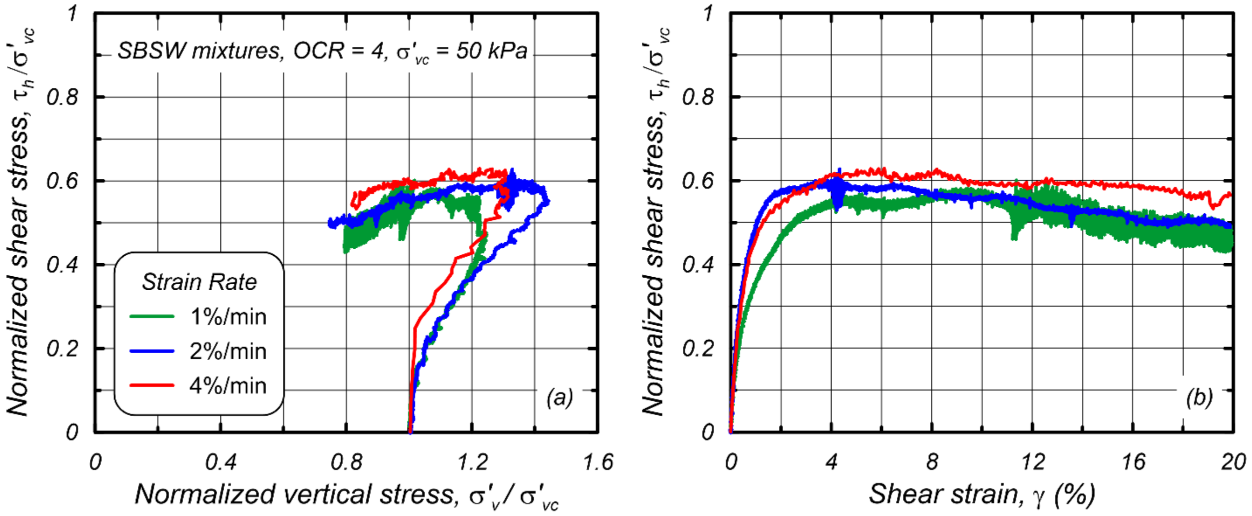

Figure 7.10. Monotonic shear response of SBSW mixtures at various strain rates at OCR = 4 and σ'_{vc} = 50 kPa; (a) stress paths, (b) stress-strain curves

8 Experimental Results and Effectiveness of PI in Seismic Soil Behavior Characterization

This Chapter contains the results of all laboratory experiments that were conducted for Part II of this dissertation including oedometer consolidation tests, monotonic direct simple shear tests, cyclic direct simple shear tests, and images from the Scanning Electron Microscope (SEM). The Chapter also provides synthesis of the results, discusses effects of mineral composition and pore fluid salinity on cyclic response of low-plasticity fine-grained mixtures, and demonstrates comparisons with other published recommendations. Results of the tests are individually presented in Appendices B and C, and are being curated and will be published on DesignSafe Cyber Infrastructure.

The contents of this chapter are formed as a journal article and will be submitted for review by Eslami, M., Brandenberg, S.J., and Stewart, J.P., entitled “Cyclic Behavior of Low-Plasticity Fine-Grained Soils with Varying Clay Mineralogy and Pore Fluid.”

8.1 SCANNING ELECTRON MICROSCOPE IMAGING

To get insights into microscopic differences or similarities of the three mixtures tested in this dissertation, a Tescan Vega-3 XMU variable pressure Scanning Electron Microscope (SEM) was used for imaging and analysis of solid oven dried samples of the mixtures. Samples may be imaged with several detectors that enable topographic and backscattered imaging for compositional variations along with other features. The SEM available at the UCLA SIMS laboratory is shown in Figure 8.1. This SEM accommodates both thin and thick sections, ion probe mounts, pin mounts, and larger samples up to a few centimeters. Samples can be imaged with or without (in low vacuum modes) conductive graphite or gold coating.

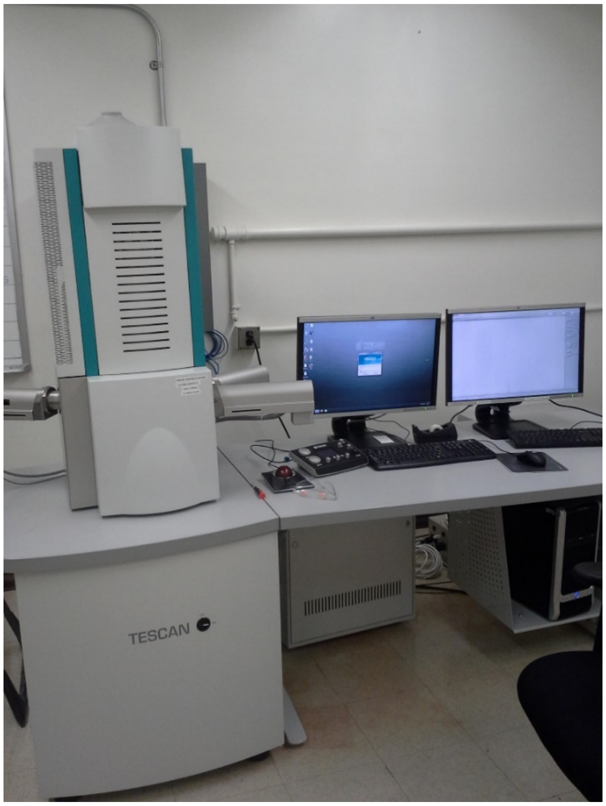

Figure 8.1. Tescan Vega-3 XMU Scanning Electron Microscope available at UCLA SIMS laboratory

Scanning Electron Microscope (SEM) imaging was performed at the SIMS Laboratory at the department of Earth and Space Sciences at UCLA. Images of the three mixtures used for the experimental program in the current dissertation are presented in Figure 8.2. These images show differences in the degree to which the clay minerals adhere to the surface of the silt particles. More clay adheres to the silt particles for the SBSW mixture than for the other two mixtures. This is due to smaller amounts of bentonite in the SBFW mixture, and much larger specific surface area (SSA) of the bentonite compared to kaolinite minerals for the SKFW mix. It is also apparent from Figure 8.2(b) that the NaCl has made differences in the way the clay minerals and silt particles bond with each other when compared to Figure 8.2(a) and (c).

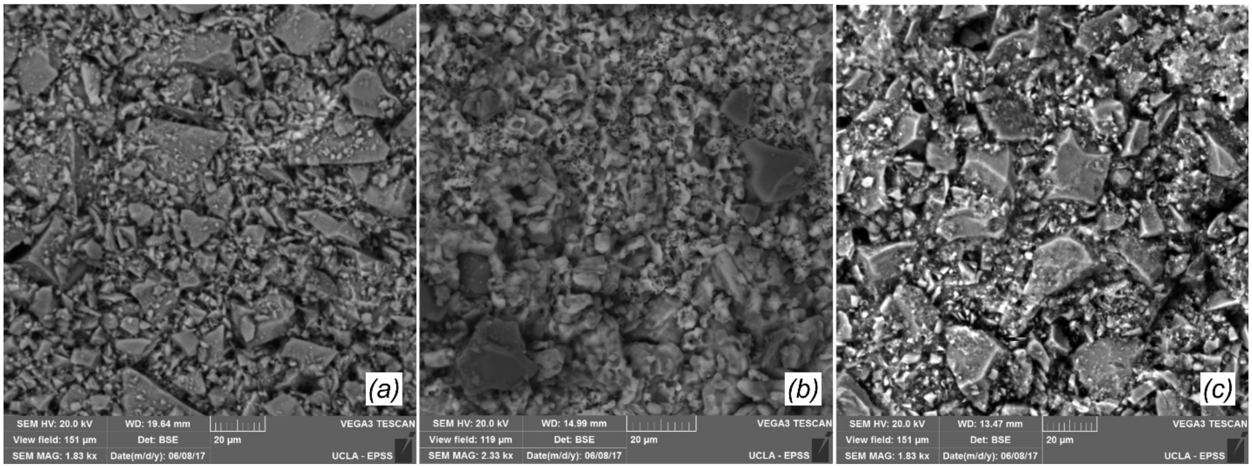

Figure 8.2. Scanning Electron Microscope (SEM) images of the mixtures used for the experimental study: (a) SBFW (b) SBSW, and (c) SKFW

Effects of the various clay minerals other than influencing adhesion and bonding strength between constituent particles, may lead to changes in permeability of the mixtures and therefore, deviations in mechanisms of pore pressure development during shear. Though change in permeability does not affect undrained constant-height simple shear testing, the interplay of these two mechanisms (in field conditions) can lead to an increase or decrease in cyclic resistance as compared to pure silt specimens without any clay minerals, and as outlined by Guo and Prakash (1999) the adhesive character tends to dominate once a limiting amount of plastic clay minerals are exceeded in the mixtures. The adhesive mechanism by forming strong bonds, tends to hold the silt particles from relative movement during cyclic shear, therefore, increasing the mixtures' cyclic resistance by maintaining the effective stress between particles (Beroya et al., 2009).

The adhesive bonding is dependent on the area of the contacts between surfaces of the particles; larger area of contact between particles would result in more adhesion and stronger bonding. This suggests that Specific Surface Area (SSA) of the minerals would affect the bonding strength. Kaolinite minerals have SSA between 10 to 20 m^2/g and bentonite minerals have much larger SSA of about 800 m^2/g (Mitchell and Soga, 2005). The much larger SSA of the bentonite minerals is due to its significantly smaller particles in the form of very thin flakes which would give the coarser silt particles a smooth, regular coating as highlighted by Beroya et al. (2009). This sort of smooth coating seems apparent in the SBSW mixture as shown in Figure 8.2(b). Additionally, mixtures containing kaolinite and silt seem to have a more irregular bonding of particles and larger particles are evident from Figure 8.2(c). Significant difference between the SSA of the two clay minerals may lead to a valid conclusion that small amounts of bentonite, by creating a smooth coating around the silt particles, would result in stronger bonding with the silt as opposed to the mixtures of silt with kaolinite clay minerals.

Another factor that may influence cyclic behavior of these mixtures is the mechanism of the adsorbed water layer. Beroya et al. (2009) elaborates on this aspect in details. In summary, it is expected that (under fully saturated conditions) mixtures containing bentonite would have the highest amount of adsorbed water compared to mixtures containing kaolinite. Similarly, this is a result of the bentonite particles being much smaller than kaolinite, as well as having two basal planes that can orient water molecules as opposed to the single basal plane of the kaolinite minerals. It may be that that mixtures containing kaolinite would contain more free pore water compared to mixtures containing bentonite (where most of the water is strongly held on the surface of the bentonite minerals as adsorbed water), which could result in excess pore pressures that develop easier, or faster. Such variations may play important roles in the differences in monotonic and cyclic response of the three mixtures, which are further discussed in the following sections.

8.2 CONSOLIDATION BEHAVIOR

One dimensional incremental loading consolidation tests were performed on each of the mixtures following the procedures described in ASTM D2435. The consolidometer available at the UCLA geotechnical research laboratory is capable of pore pressure measurement during consolidation that facilitates accurate evaluation of the time for end of primary consolidation. A Schematic of this consolidation apparatus is presented in Figure 8.3. Drainage is allowed through the top of the specimen and pore pressure is measured from the bottom of the sample. A hole through the bottom of the consolidometer is attached to a pore pressure transducer (piezometer) that measures changes in pore pressure as loads are applied to the specimen, simultaneously, as the LVDT records vertical displacement. Usage of the recordings from the pore pressure transducer were especially useful when it was difficult to obtain the time to end of primary consolidation by Casagrande’s log time method.

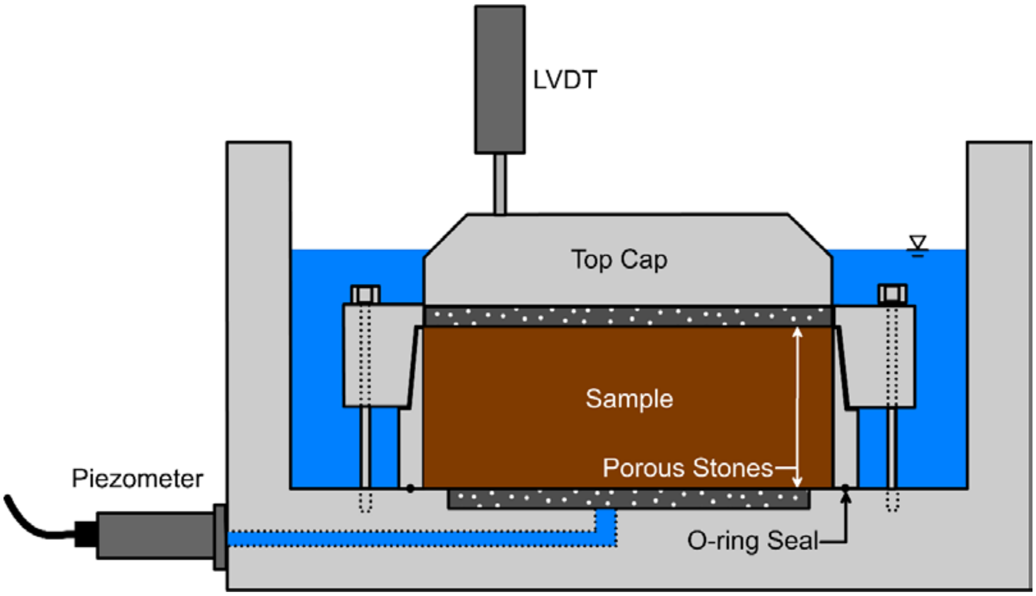

Figure 8.3. Single drainage consolidometer that permits pore pressure measurement (figure from Brandenberg et al., 2016)

Specimens for oedometer testing were extruded from the acrylic tubes, where the mixtures had been pre-consolidated. The dimeter of the acrylic tubes and the consolidation rings were similar and equal to 72.5 mm, enabling direct transfer of the soil from the pre-consolidation tubes to the consolidation ring. The consolidation ring is shown in Figure 8.4.

Figure 8.4. Consolidation ring

Consolidation tests were performed to evaluate compressibility properties such as the compression index (C_c), recompression index (C_r), secondary compression index (C_α), coefficient of consolidation (c_v), and hydraulic conductivity (k). Loading was applied at a load increment ratio equal to 1. Results of the consolidations tests are presented in Figure 8.5 and compression properties of the three mixtures are tabulated in Table 8.1. Values of c_v and k are obtained based on Taylor's square root of time method (Taylor, 1948) and plotted for loading stages. The logarithm of permeability of soil has been observed to be linearly proportional to void ratio, with the slope defined as $C_k = \Delta e/\Delta logk$.

The SBFW and SBSW blends have generally similar compression properties, though the SBSW contains twice the amount of bentonite indicating that the NaCl has an effect in the compressibility behavior of the mixture. In addition, the SKFW and SBSW mixtures show k values that are larger by approximately an order of magnitude compared to the SBFW blend.

Plotted values of c_v and k on plots of Figure 8.5 are during loading stages where a good measurement of the time to end of primary consolidation could be made that would lead to accurate estimations of c_v. Similarly, the values of these parameters during unloading stages of the consolidation test are not plotted since accurate measurements could not be made. However, it was observed that permeability of the SKFW blend remained relatively similar to loading stages if unloaded, whereas permeability of the SBFW and SBSW mixtures were decreased during unloading stages. This may attribute to differences in cyclic behavior of this blend with multiple cycles of loading and unloading during shear.

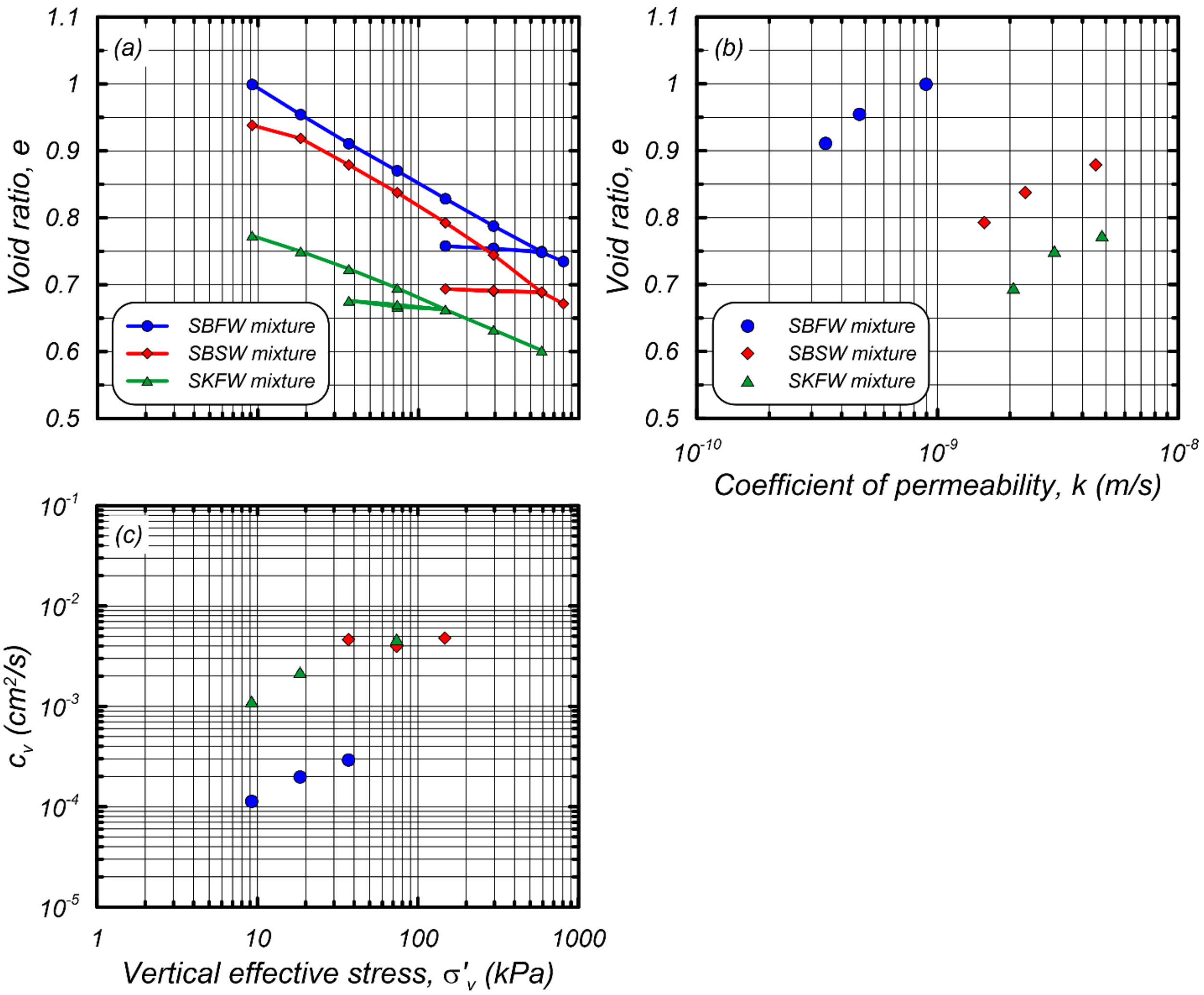

Figure 8.5. Oedometer consolidation test results for soils mixtures SBFW, SBSW, and SKFW; (a) void ratio versus vertical effective stress, (b) void ratio versus coefficient of permeability, and (c) coefficient of consolidation versus vertical effective stress

Table 8.1. Compressibility properties of the three mixtures of silt and clay minerals

Mixture	C_c	C_r	C_k	C_α
SBFW	0.138	0.014	0.089	0.011
SBSW	0.145	0.008	0.079	0.008
SKFW	0.097	0.022	0.091	0.014

8.3 CONSTANT-HEIGHT MONOTONIC SHEAR RESPONSE AND STRENGTH NORMALIZATION WITH STRESS HISTORY

To evaluate the stress-strain response of the three mixtures, constant-height monotonic direct simple shear testing was performed using the UCLA BB-SS apparatus. Details of the apparatus and specimen setup are explained thoroughly in Chapter 7. It was especially important to evaluate whether undrained shear strength (s_u) of these mixtures would exhibit normalization with consolidation stress. For this purpose, monotonic tests were performed at varying overconsolidation ratios. Most tests were performed at an effective consolidation stress of 50 kPa, while a small number of tests were conducted at higher and lower consolidation stresses under normally consolidated conditions to verify strength normalization. A total of 25 monotonic shear test were performed, and Table 8.2 presents the monotonic shearing test matrix for all mixtures. Plots of each individual monotonic shear test are presented in Appendix B.

Constant- height monotonic shear tests were conducted on specimens extruded from pre-consolidated samples from acrylic tubes and trimmed to a diameter of 66 mm and initial height of 28 mm. Specimens were confined by wire-reinforced rubber membranes and consolidated to higher pressures in the simple shear device. Strain-controlled monotonic shear was applied with a strain rate of 1%/min (duration about 24 minutes) to permit excess pore pressures to redistribute within the specimen, and free drainage was allowed during both consolidation and monotonic shear phases of each experiment. During shearing, changes in vertical effective stress that were required to maintain the height of the specimen constant, are assumed equivalent to excess pore pressures that would have developed under undrained loading conditions.

Table 8.2. Constant-height monotonic shear test matrix

Mixture	*Test ID*	σ'_{vc} *(kPa)*	*OCR*	e_c*	$(s_u/\sigma'_{vc})_{pk}$
SBFW	Test26	50	1.4	0.875	0.257
	Test27	50	1.2	0.884	0.277
	Test28	50	1.5	0.87	0.273
	Test50	50	1.9	0.86	0.36
	Test51	50	2.0	0.854	0.353
	Test55	54	3.1	0.839	0.494
	Test85	100	1.0	0.84	0.221
	Test90	30	1	-	0.23
SBSW	Test23	50	1.2	0.853	0.257
	Test24	50	1.4	0.841	0.297
	Test25	50	1.6	0.836	0.324
	Test49	50	1.5	0.837	0.312
	Test52	50	3.6	0.782	0.647
	Test53	50	3.1	0.793	0.565
	Test54	50	4.4	0.77	0.758
	Test87	30	1.0	0.89	0.232
	Test88	95	1.0	0.82	0.232
	Test89	50	1.0	-	0.234
SKFW	Test68	50	1.0	0.706	0.176
	Test71	50	1.0	0.716	0.194
	Test69	50	1.6	0.693	0.291
	Test70	50	5.1	0.648	0.522
	Test81	100	1.5	0.665	0.208
	Test82	200	1.2	0.635	0.225
	Test83	30	1.0	0.722	0.24

*e_c: *post-consolidation void ratio*

$(s_u/\sigma'_{vc})_{pk}$: *peak undrained shear strength ratio*

Representative results of monotonic direct simple shear tests on the three mixtures at various overconsolidation ratios are presented in Figure 8.6, showing normalized effective stress paths (τ_h/σ'_{vc} versus σ'_v/σ'_{vc}) and normalized shear stress (τ_h/σ'_{vc}) versus shear strain (γ). The stress-strain curves are sketched for shear strains up to 20%, however, due to stress-nonuniformities caused in the simple shear apparatus at large strains, the accuracy of the data may be questionable as highlighted by DeGroot et al., 1994)

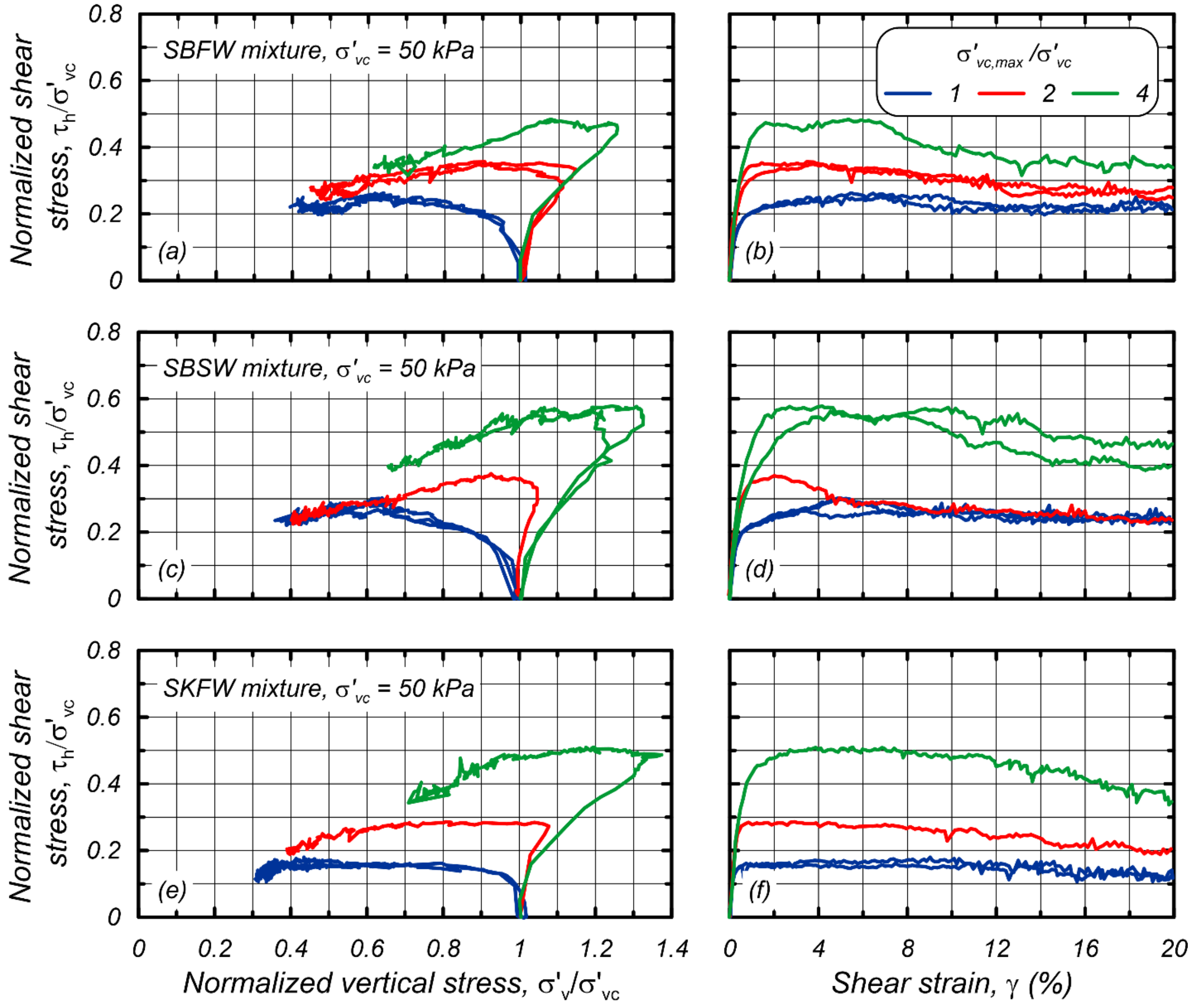

Figure 8.6. Constant-height monotonic DSS response of mixtures. Stress-paths and stress-strain curves; (a) and (b): SBFW, (c) and (d): SBSW, and (e) and (f): SKFW

Normally consolidated specimens of all three mixtures exhibit nearly perfectly plastic ductile behavior and are generally contractive, whereas the overconsolidated specimens show a stress-strain response with some strain softening at higher strains. The overconsolidated specimens exhibit dilative behavior up to a peak shear stress (at about 4 to 5% shear strain) and transition to contractive behavior beyond this level. It is not clear as if this softening is true soil behavior or due to stress non-uniformities in the simple shear apparatus. An alternative hypothesis is that at shear strains larger than 5 to 8%, overconsolidated specimens start to behave more like normally consolidated samples as a result of the soil “losing its memory” of previous maximum pressure or overconsolidation (i.e. history).

The undrained strengths are based on the peak shear resistance of each test, and as can be inferred from Figure 8.6, the SBSW mixture has the highest normalized undrained strength ratios (s_u/σ'_{vc}), followed by the SBFW and SKFW blends, respectively. Higher strengths of the SBSW mixture may be attributed from stronger adhesion within the mixtures due to higher percentage of bentonite minerals in this mixture.

It is known that undrained strength of clay-like soil normalizes with stress history if the critical state line (CSL) and normal consolidation line (NCL) are parallel straight lines in e-logσ'_v space. During monotonic shearing of the specimens, a true critical state was never reached, meaning that the specimens exhibited changes in effective stress (excess pore pressure was generated) while being sheared even at 20% shear strain. Therefore, to assess whether undrained shear strength normalizes with stress history, a Failure State Line (FSL) was considered to check for strength normalization. In other words, combinations of void ratio and vertical effective stress at failure (when the peak undrained shear strength was reached) were plotted for all specimens to draw this line. Void ratios were obtained by measurements of final water content of the specimen after monotonic shearing was finished.

The FSL and NCL for the SBFW, SBSW, and SKFW mixtures are plotted in Figure 8.7 (a), (c), and (e), respectively. The SBFW and SBSW exhibit failure state lines that are parallel with the normal consolidation line [Figure 8.7 (a) and (c)], suggesting that undrained strength should normalize quite well with effective stress and stress history (OCR), and that these mixtures have clay-like behavior. In contrast, the FSL and NCL are less parallel for the SKFW blend in Figure 8.7(e), suggesting that this mixture may exhibit behavior intermediate of clay-like and sand-like types of behavior.

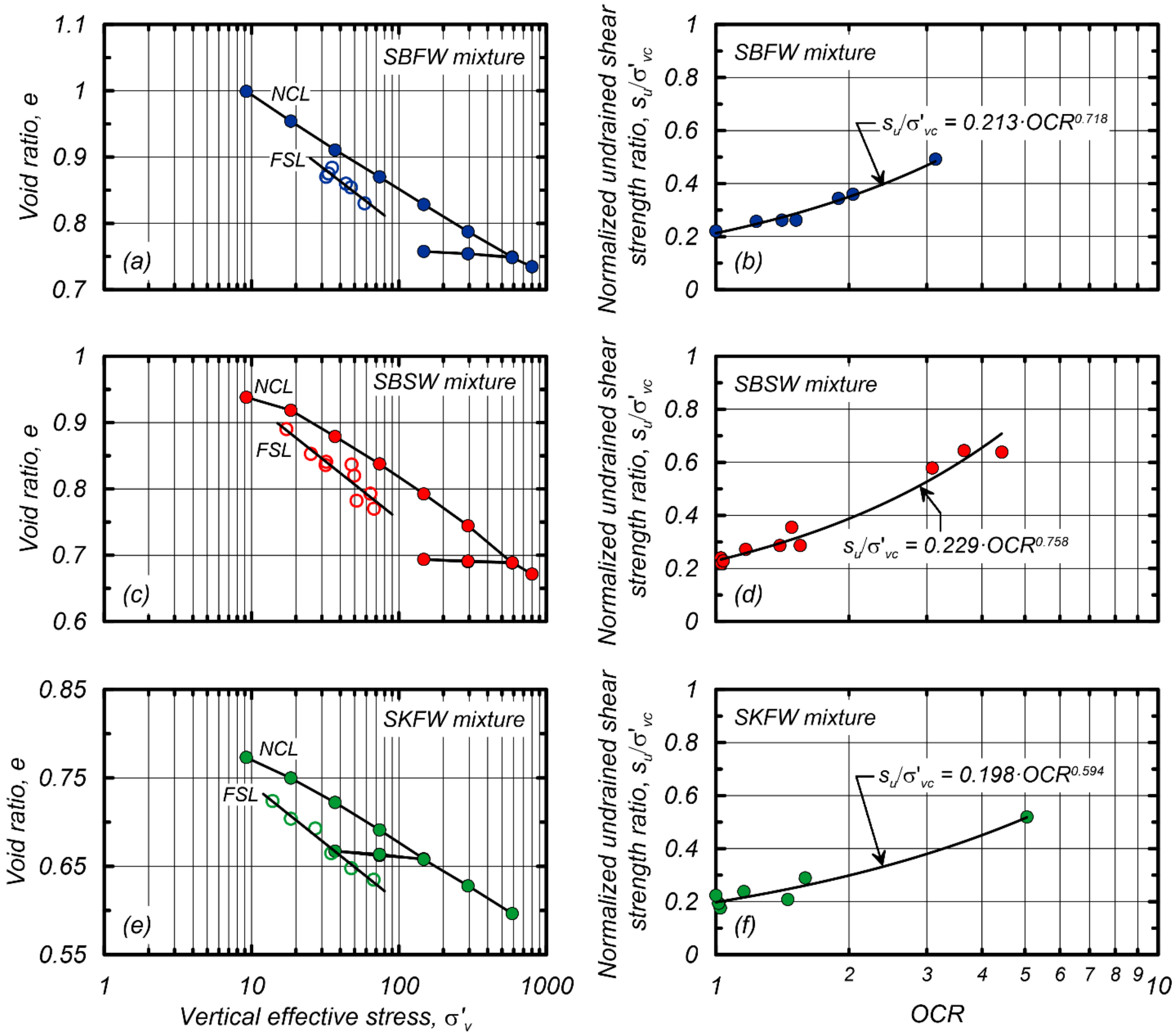

Figure 8.7. Normally Consolidated Lines (NCL) from oedometer tests and Critical State Lines (CSL) at 12% shear strain the three mixtures in e-logσ′v space, and normalized undrained shear strength ratio versus OCR relationships; (a) and (b): SBFW, (c) and (d): SBSW, and (e) and (f): SKFW

However, further testing of normally consolidated specimens of the SKFW mixture proved that undrained strength in fact correlates well with stress history. Hence, it is questionable why the CSL an NCL are less parallel for this mixture. Representative results of monotonic shearing response of the SKFW mixture at OCR = 1 and varying effective consolidation stresses are presented in Figure 8.8, where an average undrained strength ratio of 0.191 was found for this material.

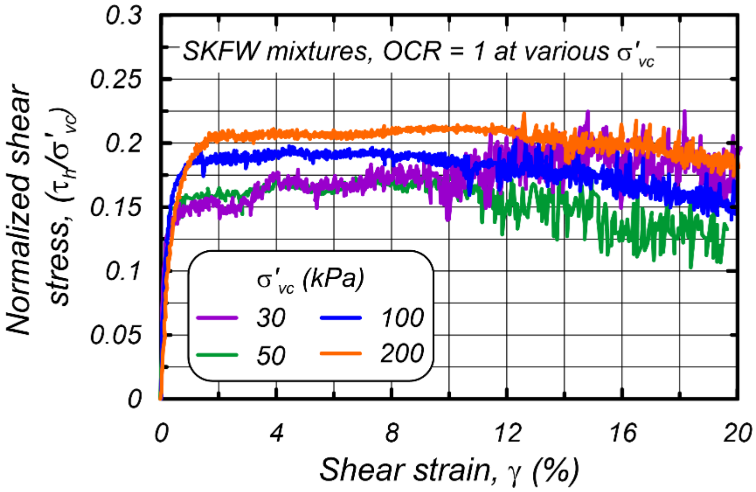

Figure 8.8. Monotonic stress-strain response of SKFW mixtures at OCR = 1 and varying effective consolidation stress

Based on the observation that the FSL and NCL are straight parallel lines, undrained strength ratios of the three mixtures can be expressed by the form proposed by Ladd (1991) and as shown in equation (8.1).

$$\frac{s_u}{\sigma'_{vc}} = S \cdot OCR^m \tag{8.1}$$

Where *S* is the normalized undrained shear strength ratio for a normally consolidated soil, and *m* is the slope of s_u/σ'_{vc} versus OCR in a log-log plot. Fitting this relationship to the data results in *S*

= 0.213 and *m* = 0.718 for SBFW mixtures, *S* = 0.229 and *m* = 0.758 for the SBSW mixtures, and *S* = 0.198 and *m* = 0.594 for SKFW mixtures [Figure 8.7 (b), (d), and (f)]. *S* is in the common range for normally consolidated clays and silts (0.20 to 0.25 for simple shear testing) reported by Ladd (1991), however, *S* is slightly lower for the SKFW mixture. The *m* exponent for most clays is reported about 0.8; though for mixtures SBFW and SBSW this exponent is smaller, it is close to the common range reported in the literature. The SKFW mixture exhibits a lower *m* exponent, implicating that the undrained shear strength of these mixtures are not strongly dependent on OCR.

8.4 CONSTANT-HEIGHT CYCLIC SHEAR RESPONSE

Constant-height undrained direct simple shear tests were performed on the three mixtures with specimens trimmed to dimensions of 66 mm diameter and 28 mm initial height. The height of sheared specimens slightly varies due to differing compressibility properties of the three silt-clay mixtures during the consolidation phase of each test. Shear strains are computed based on the initial height of each specimen after consolidation has finished.

Uniform sinusoidal stress-controlled cyclic tests were performed to compare the measured strengths for the three silt-clay mixtures, as well as comparison with recommended values available in the literature (e.g. Boulanger and Idriss, 2004). A total of 30 constant height cyclic tests with uniform stress amplitudes and varying cyclic stress ratios (CSR) were performed on all three mixtures and at OCRs 1 and 2. The cyclic constant-height simple shear test matrix is presented in Table 8.3. All specimens were cyclically sheared at a loading frequency of 0.1 Hz and at an effective consolidation stress of 50 kPa, similar to the monotonic shear tests. Cyclic loading was continued until the limits assigned to the UCLA BB-SS device was reached (about 25% shear strain. The control system had difficulty maintaining stress-control at high strains, so tests are plotted up to single shear strain amplitudes of about 6% herein, where the command and feedback shear stresses were reasonably compatible.

Table 8.3. Constant-height cyclic simple shear test matrix

Mixture	*Test ID*	σ'_{vc} *(kPa)*	*OCR*	e_c*	*CSR*	*N***	τ_{cyc}/s_u
SBFW	Test36	50	1	0.915	0.149	13.3	0.700
	Test37	50	1	0.904	0.161	8.3	0.756
	Test38	50	1	0.896	0.18	3.6	0.845
	Test39	50	1	0.88	0.186	2.6	0.873
	Test40	50	1	0.875	0.137	17.1	0.643
	Test44	50	1	0.915	0.126	20.8	0.592
	Test45	50	1	0.904	0.115	67.1	0.540
	Test46	50	1	0.889	0.161	4.7	0.756
	Test56	50	2	0.832	0.174	76.7	0.497
	Test61	50	2	0.815	0.185	63.1	0.528
	Test62	50	2	0.801	0.199	33.7	0.568
	Test63	50	2	0.833	0.228	11.8	0.651
SBSW	Test33	50	1	0.85	0.213	3.5	0.930
	Test41	50	1	0.864	0.187	4.6	0.817
	Test42	50	1	0.856	0.161	8.4	0.703
	Test43	50	1	0.84	0.136	51.8	0.594
	Test48	50	1	0.855	0.141	13.1	0.616
	Test57	50	2	0.826	0.219	22.8	0.565
	Test58	50	2	0.83	0.201	33.8	0.519
	Test59	50	2	0.813	0.233	16	0.602
	Test60	50	2	0.794	0.279	3.7	0.720
SKFW	Test64	50	1	0.7	0.116	11.3	0.586
	Test65	50	1	0.682	0.098	38.2	0.495
	Test66	50	1	0.717	0.124	9.8	0.626
	Test67	50	1	0.699	0.141	3.3	0.712
	Test72	50	2	0.674	0.17	51.7	0.569
	Test74	50	2	0.65	0.192	17.3	0.642
	Test75	50	2	0.638	0.214	13.7	0.716
	Test76	50	2	0.628	0.249	7.4	0.833
	Test78	50	2	0.661	0.26	4.1	0.870

e_c: post-consolidation void ratio*

***N: number of uniform cycles to reach 3% peak shear strain*

Typical stress-strain and stress path response of stress-controlled cyclic shear of normally consolidated (OCR = 1) specimens of the three mixtures are presented in Figure 8.9. The applied cyclic stress ratios as well as the number of uniform loading cycles to reach a peak shear strain of 3% are marked inside the plots of Figure 8.9. Generally, the three mixtures produce wide hysteresis loops similar to that of clay-like type of soils and don't reach to a vertical effective stress of zero at high strains. Though the applied CSR (τ_{cyc}/σ'_{vc}) in Figure 8.9(a) and (c) are relatively close, mixture SBSW reaches a peak shear strain of 3% in 52 cycles, whereas the SBFW mixture reaches the same peak shear strain in 21 cycles. This is significant difference between the cyclic response of the two mixtures at the same PI. It is important note that mixtures SBFW and SBSW accumulate small increments of strain during each loading cycle, whereas the SKFW mixture generates shear strains rapidly after the first few cycles of loading.

Maximum equivalent excess pore pressure ratios (r_u) for the three tests shown in Figure 8.9 at 10% shear strain are 0.84, 0.78, and 0.777 for the SBSW, SBFW, and SKFW mixtures respectively, which are quite high for clay-like materials. Though a r_u = 1 condition was never reached for the SKFW mixtures, their strain accumulation mechanism seem more analogous to strain accumulation of sand-like material, however, their hysteresis loops are more similar to clay-like material in that significant dilatancy does not occur.

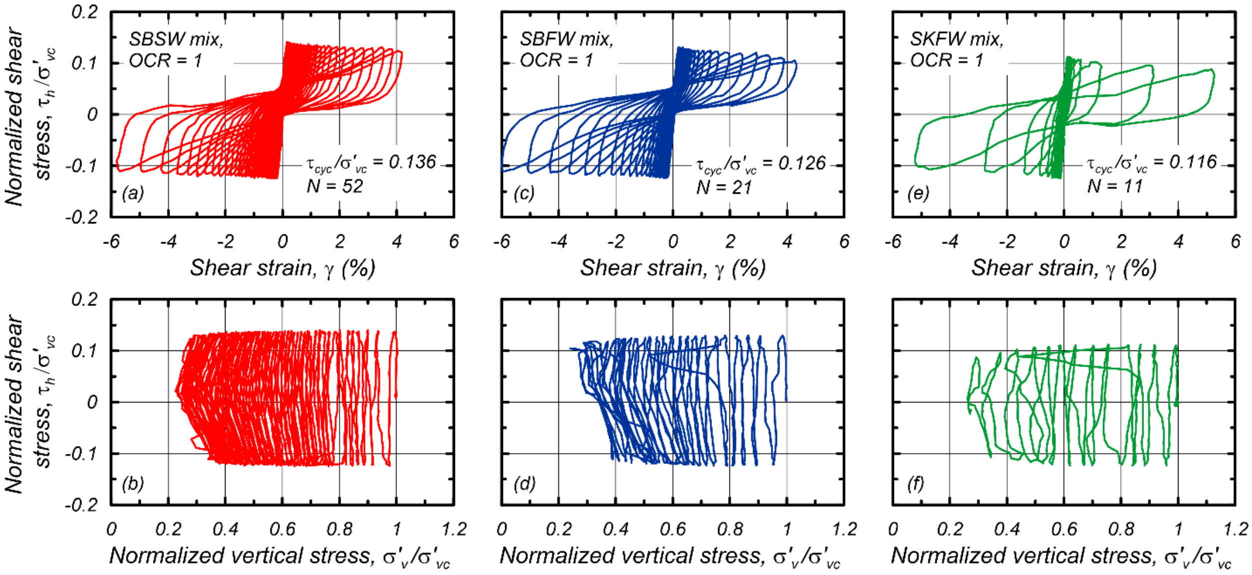

Figure 8.9. Typical stress-strain and stress-path response of constant-height DSS cyclic shear of normally consolidated specimens; (a) and (b): SBSW, (c) and (d): SBFW, (e) and (f): SKFW mixture

Similarly, Figure 8.10 presents representative cyclic response of OCR = 2 specimens of the three mixtures. As mentioned previously, all tests are conducted at an effective consolidation stress of 50 kPa, similar to the monotonic shearing tests for these mixtures. Like normally consolidated specimens, the SKFW mixture tends to accumulate shear strains rapidly in a few number of loading cycles after about 1% shear strain, indicating a behavior more similar to sand-like material, where the SBSW and SBFW specimens tend to generate shear strains with a much slower rate within cycles of loading. Further, the CSR applied to specimens of the SBFW and SKFW mixtures shown in Figure 8.10 (c) and (e) are almost equal, yet the SBFW reaches 3% shear strain in 77 loading cycles, whereas the SKFW mixture reaches the same amount of strain in 52 cycles indicating a significant difference in cyclic resistance of these mixtures, though being at equal values of plasticity. Interestingly, all three tested specimens shown in Figure 8.10 reached excess pore pressure ratios of 0.77 at a single amplitude peak shear strains of 10%.

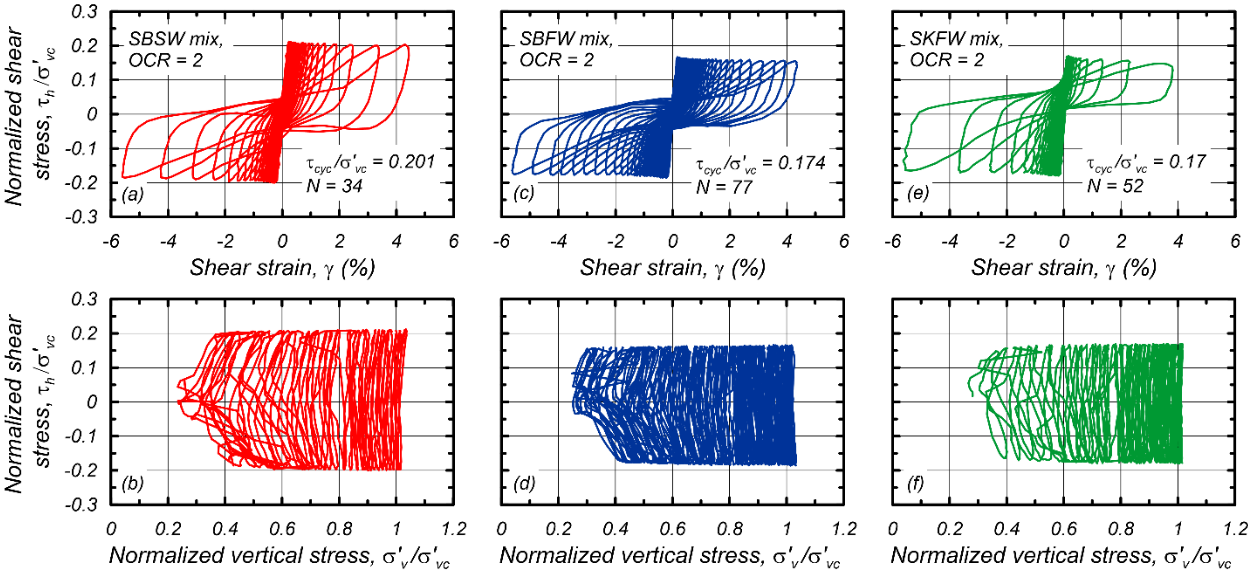

Figure 8.10. Typical stress-strain and stress-path response of constant-height DSS cyclic shear of OCR = 2 specimens; (a) and (b): SBSW, (c) and (d): SBFW, (e) and (f): SKFW mixture

Maximum equivalent excess pore pressure ratios of all cyclic tests at OCRs equal 1 and 2 are plotted against peak values of shear strain in Figure 8.11. The excess pore pressure ratios increase with increasing peak shear strains, yet do not reach unity even at large shear strains.

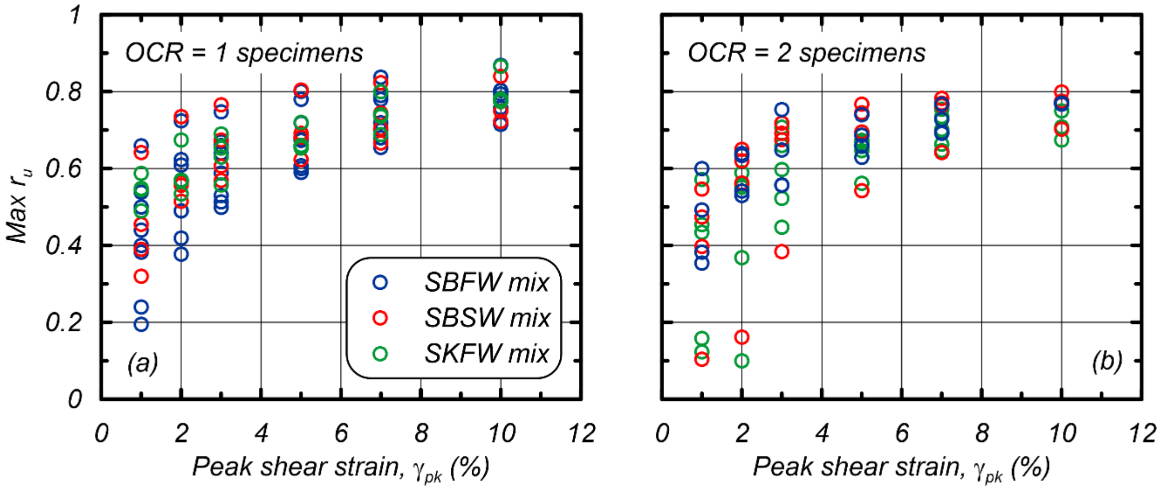

Figure 8.11. Maximum excess pore pressure ratio (r_u) versus peak shear strains for the three mixtures; (a) OCR =1 specimens, (b) OCR = 2 specimens

All three mixtures exhibit similar trends and it is therefore, difficult to conclude whether one blend consistently exhibited larger r_u than another.

8.5 CYCLIC STRENGTHS

Cyclic strengths of the three mixtures tested in this project were normalized by effective consolidation stress, as wells as by the undrained shear strength of these mixtures. The failure criteria assumed is the number of uniforms loading cycles (N) causing a single amplitude peak shear strain of 3%. Comparisons of the measured cyclic strengths with provided recommendations in the literature are presented subsequently.

8.5.1 Cyclic strengths normalized by effective consolidation stress

Figure 8.12 presents cyclic stress normalized with effective consolidation stress (τ_{cyc}/σ'_{vc}) versus number of uniform loading cycles to reach a peak shear strain of 3% for normally consolidated and OCR = 2 specimens of the three mixtures. The plots in Figure 8.12 also consists of least square regressed power functions in the form given in equation (8.2), where the cyclic resistance ratio (CRR) is related to the number of uniform cycles (N) to reach the 3% shear strain failure criteria, where, *a* and *b* are fitting parameters.

$$CRR = a \cdot N^{-b} \tag{8.2}$$

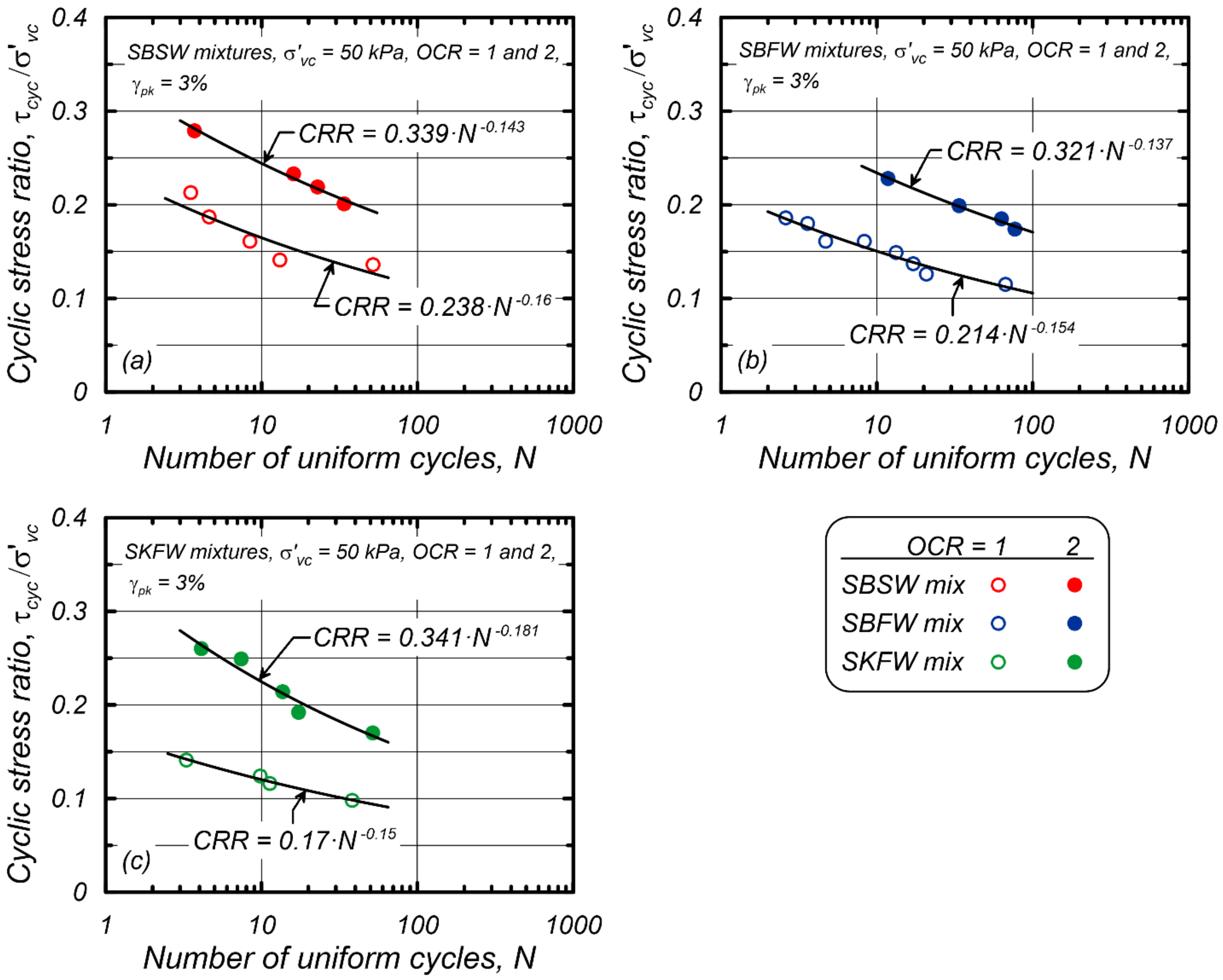

Figure 8.12. Cyclic stress ratio versus number of uniform loading cycles for OCR = 1 and 2 specimens; (a) SBSW mixture, (b) SBFW mixture, (c) SKFW mixture

Fitting parameters, *a* and *b*, are in the common range reported for clay-like soils in the literature [e.g. Boulanger and Idriss (2007) report values for *b* between 0.07 and 0.15]. The SBSW mixtures exhibits the highest resistance for a given number of loading cycle followed by SBFW and SKFW. For example, for normally consolidated specimens at N = 10, the CRR is 0.169, 0.15, and 0.12 for the SBSW, SBFW, and the SKFW mixtures, respectively. This is about a 40% variation in cyclic resistance from the SBSW mix to the SKFW mixture, and it is reasonable to conclude that differences in the CRR versus N relationships for the three mixtures are rather significant.

Moreover, the cyclic resistance of all three specimens show strong influence of OCR, which can be attributed to increase in undrained shear strength with increasing OCR. For instance, at N = 10, the CRR to 3% shear strain for the SBSW mixture and for OCR = 1 is 0.164. whereas at OCR = 2 the CRR for this mixture is equal to 0.244. The increase in CSR with OCR is largest for the SKFW mixture followed by the SBFW, and SBSW mixtures, respectively. Furthermore, the relationship of CRR and N is slightly flatter for OCR = 2 specimens than for normally consolidated specimens for the SBSW and SBFW mixtures (i.e. *b* is smaller for OCR = 2 than for OCR = 1 specimens). In contrast, the CRR versus N relationship for OCR = 1 specimens of the SKFW mixture are flatter that OCR = 2 specimens of this mix.

8.5.2 Cyclic strengths normalized by undrained shear strength

The cyclic response of the three mixtures are further presented in the form of cyclic strength ratio, which is the cyclic stress normalized with undrained shear strength (τ_{cyc}/s_u), versus number of uniform loading cycles (N) to reach 3% peak shear strains. Note that this type of cyclic strength normalization as shown in is suitable for soils that exhibit good stress-normalization and may not be fully be appropriate for the SKFW mix which has less parallel FSL and NCL lines. The normalizations with undrained shear strength is based on relationships that were provided in Figure 8.7 (b), (d), and(f) for the three mixtures.

Results of cyclic strength ratio versus number of uniform loading cycles for normally consolidated and OCR = 2 specimens are presented in Figure 8.13. As expected, the influence of OCR is less pronounced when cyclic strengths are normalized with undrained shear strength, as compared to CSR versus N curves. From Figure 8.13 it can be inferred that the SBSW blend has consistently higher cyclic strength ratios, followed by the SBFW, and SKFW mixtures, respectively. For example, at N = 10 for normally consolidated specimens, the cyclic stress to reach a peak shear strain of 3% is 0.718, 0.705, and 0.606 times the undrained shear strength for the SBSW, SBFW, and the SKFW blends, respectively.

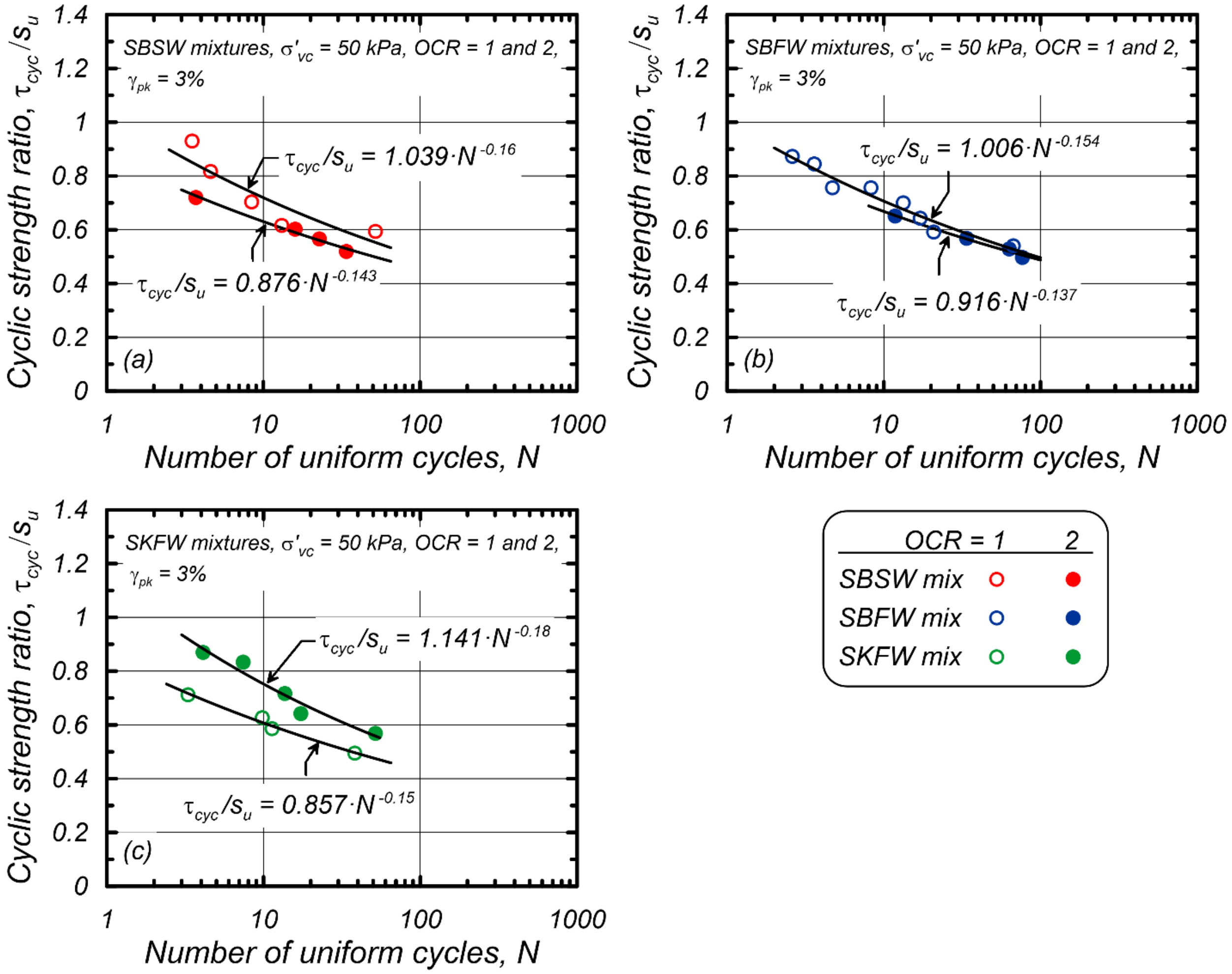

Figure 8.13. Cyclic strength ratio versus number of uniform loading cycles for OCR = 1 and 2 specimens; (a) SKFW mixture, (b) SBFW mixture, (c) SBSW mixture

8.5.3 Comparison of cyclic strengths with proposed recommendations in the literature

Cyclic stress ratios and cyclic strengths of the three mixtures presented in Figure 8.12 and Figure 8.13 can be compared with proposed values and recommendations currently available in the literature. For example, Boulanger and Idriss (2004, 2007) present limited cyclic test results of clay-like materials and propose recommended values for design based on this data. Their recommendations for design include a cyclic resistance ratio (CRR = τ_{cyc}/σ'_{vc}) equal 0.18 for normally consolidated soils, and cyclic strength ratio (τ_{cyc}/s_u) equal 0.83 (independent of OCR) for N = 30 for any clay-like material with PI > 7. These recommendations are replicated in Figure 8.14 up to a PI of 30. From Figure 8.14(a) it can be seen that for normally consolidated conditions, all the cyclic resistance ratios of the three mixtures (ranging from 0.102 to 0.138) fall below the recommended line for design. The average CRR of the three data points (from the three mixtures) for normally consolidated conditions is equal to 0.122, which is quite smaller than the proposed value of 0.18 from Boulanger and Idriss (2007). On the other hand, OCR = 2 specimens of the mixtures (having an average of 0.198) provide a better fit to the recommended line.

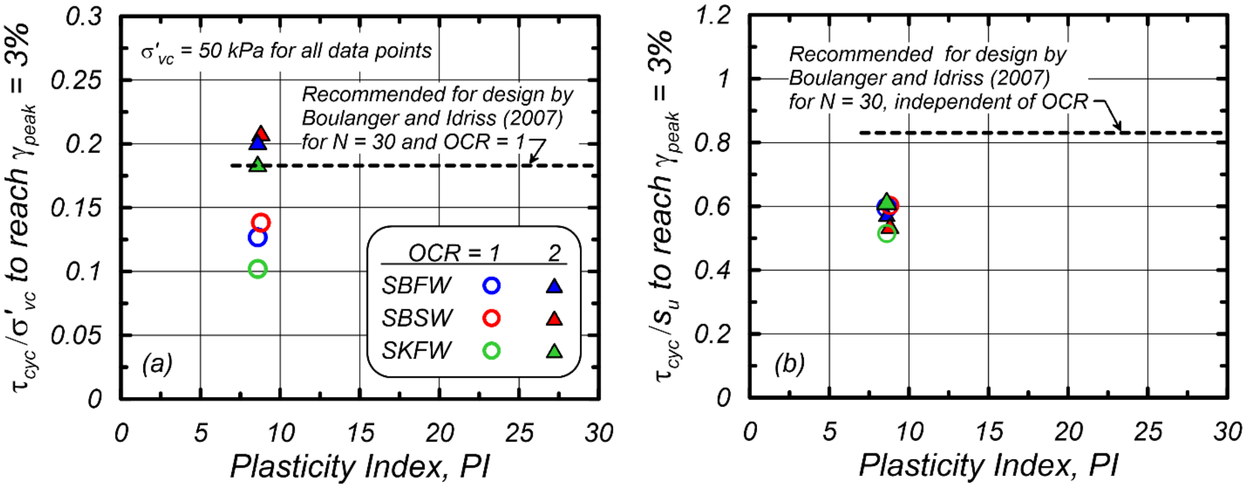

Figure 8.14 Comparison of cyclic strengths of the three mixtures with design recommendations of Boulanger and Idriss (2007): (a) CRR versus PI, and (b) τ_{cyc}/s_u versus PI

Figure 8.14(b) presents cyclic strength ratio versus plasticity index. The τ_{cyc}/s_u values obtained herein fall in a narrower range as compared to CRR values, yet fall below data from Boulanger and Idriss (2007) which had a higher range (from 0.71 to 0.92). The mean of the τ_{cyc}/s_u values for the three mixtures at OCRs 1 and 2 is equal 0.573, which is significantly smaller than 0.83 recommended by Boulanger and Idriss (2007). It is important to note that recommendations of Boulanger and Idriss (2004, 2007) are based on cyclic testing of natural soils. The soil tested herein are mixtures that were made in the laboratory, consolidated within few hours to few days, and are quite “young,” therefore, not replicating effects of aging, fabric, and cementation of natural soil deposits, and perhaps consisting of different minerals.

Interestingly, obtained values for CRR and τ_{cyc}/s_u are comparable to other similar cyclic laboratory testing of low-plasticity fine-grained mixtures by other researchers. For instance, Price et al. (2015) present results of CRR versus N (to 3% peak shear strain) for normally consolidated and OCR = 4 (σ'_{vc} = 100 kPa for both NC and OC specimens) mixtures of non-plastic silica silt with kaolin at PIs of 0, 6, and 20 that are cyclically sheared in a direct simple shear device. A CRR value between 0.1 and 0.15 can be inferred from their data [Figure 8.15(a)] for specimens at PIs of 6 and 20, respectively. Furthermore, Reid and Fourie (2017) present cyclic direct simple shear test results of untreated tailings slurry material (UT) at PI = 9, and Polymer treated (PT) tailings material treated at PI = 24. Their results are presented in Figure 8.15(b). To reach a peak shear strain of 3% for normally consolidated specimens, their results indicate a CRR = 0.12 and τ_{cyc}/s_u = 0.52 for the PI = 9 tailings material at N = 30. These values fall exactly in the range of the mixtures tested herein. Additionally, Soysa and Wijewickreme (2017) present direct simple shear results of natural fine-grained soils (from Fraser River Delta of British Columbia) at PIs 0f 5, 7, and 24. Their produced CRR versus N (to reach peak shear strain of 3.75%) is shown in Figure 8.15(c). These results provide a good match with the obtained data in the current dissertation.

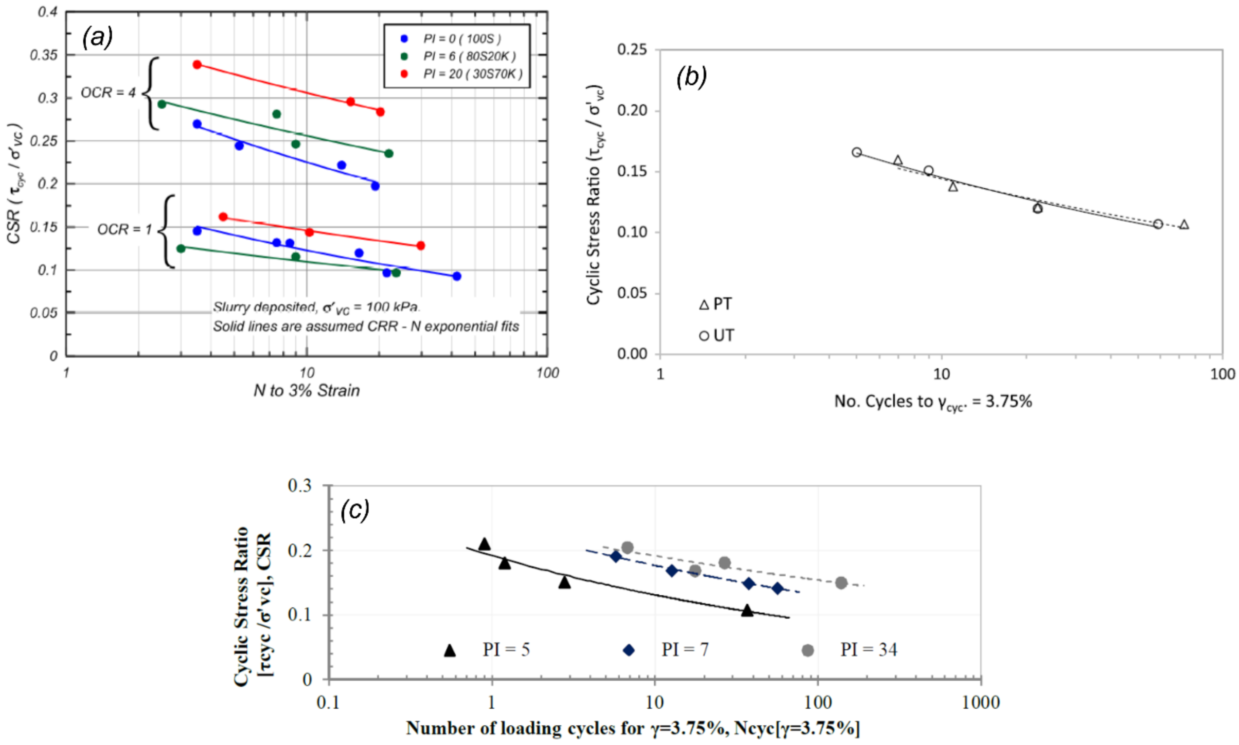

Figure 8.15. Cyclic stress ratios versus N of other studies on fine-grained soils: (a) Price et al. (2015), (b) Reid and Fourie (2017), and (c) Soysa and Wijewickreme (2017)

Dahl et al. (2014) present results of cyclic direct simple shear tests on natural alluvial silt and clay deposits in the plasticity range of 0 to 27. They report CRR = 0.195 for normally consolidated specimens to reach a 3% peak shear strain failure criterion (for N = 30), which is close to the 0.18 recommendation by Boulanger and Idriss (2007), yet the τ_{cyc}/s_u ratio they obtained was equal to 0.71 which is lower than the recommended value of 0.83, but within the range of empirical data reported in Boulanger and Idriss (2007).

Dahl (2011) presents compiled data on cyclic response of clay-like (named Group A) soils within a large range of plasticity including natural soils, tailings, and compacted soils. Natural soils with PI of 6 to 18 are reported to have an average $(\tau_{cyc}/s_u)_{N=30}$ ratio of 0.66. Tailings material with PI of 10.5 to 13 are reported to have $(\tau_{cyc}/s_u)_{N=30}$ equal to 0.584 and compacted soils in with

PI of 10 to 16 are reported to have $(\tau_{cyc}/s_u)_{N=30}$ ratio of 0.723. It is also reported that the τ_{cyc}/s_u ratio generally decreases with decreasing PI in the range of plasticity of 10 to 18, but is relatively similar in the PI ≥ 18 range. Modified versions of the proposed recommendation from Boulanger and Idriss (2007) are provided by Dahl (2011) and presented in Figure 8.16 for N = 10 and 30, where the ratio $(\tau_{cyc}/s_u)_{N=30}$ for PI ≥ 18 is adjusted to 0.8, and decreases linearly to 0.611 at PI of 10. The experimental results found in the current dissertation are inserted onto the plots of Figure 8.16 for comparison. The modified recommendations by Dahl (2011) provide closer values to the data obtained within this dissertation. Further, result from experimental studies on reconstituted samples from Tom (2011) and Reid and Fourie (2017) are also added to this plot. These data points appear to be generally lower than the updated plots from Dahl (2011).

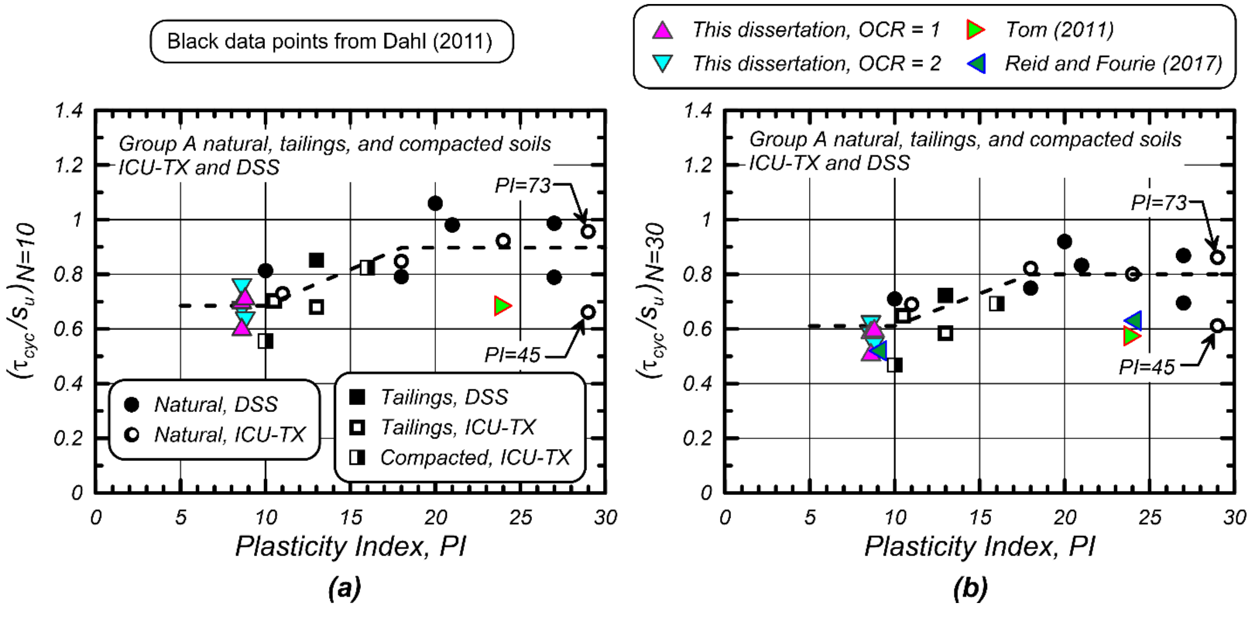

Figure 8.16. Comparison of cyclic strength ratios provided by Dahl (2011) with the data obtained in this dissertation, Tom (2011), and Reid and Fourie (2017); (a) for N = 10, (b) N = 30

Cyclic resistance ratio (CRR) versus plasticity plots for normally consolidated clay-like (group A) and intermediate soils (named Group B) which have in-between sand-like and clay-like behavior from Dahl (2011) are also replicated in Figure 8.17. For N = 30, the original recommendations by Boulanger and Idriss (2007) with CRR = 0.183 provide a good fit to the data at PI ≥ 7, however, a downward trend is proposed at PI < 7 reaching a value of CRR = 0.093 at PI = 0 for N = 30. Data obtained in this dissertation, cyclic testing from Price et al. (2015), Tom (2011), and Reid and Fourie (2017) are also added to Figure 8.17. These data points fall below trendlines from Dahl (2011), suggesting that there is consistent difference in cyclic strengths of reconstituted specimens and mineral blends (and tailings material) with that of natural undisturbed fine-grained soils. It would be interesting to explore in further details the differences between natural undisturbed soils with mineral blends and perhaps reconstituted specimens as part of a future research project.

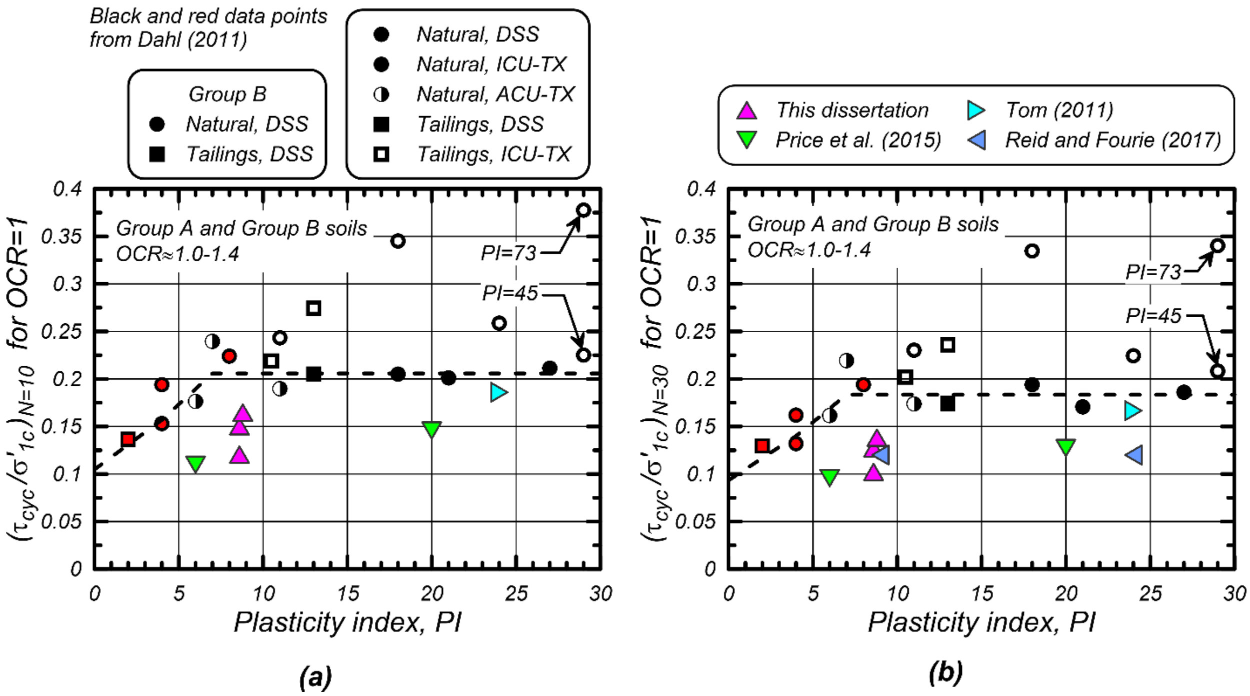

Figure 8.17. Comparison of cyclic resistance ratios provided by Dahl (2011) with data obtained in this dissertation, Price et al (2015), Tom (2011), and Reid and Fourie (2017); (a) for N = 10, (b) for N = 30

8.6 INFLUENCE OF CLAY MINEROLOGY AND PORE FLUID CHEMISTRY

For comparison, CSR versus N and cyclic strength ratio versus N of the three mixtures (previously presented individually for each mixture in Figure 8.12 and Figure 8.13) are plotted together for normally consolidated and OCR = 2 specimens in Figure 8.18 and Figure 8.19, respectively. Although the liquid limit, plastic limit, and the plasticity index of the three mixtures used in this experimental study are equal, significant differences in terms of cyclic strengths of these mixtures at OCRs of 1 and 2 are apparent from these figures. The CSR versus N relationships are consistently highest for the SBSW mixture, followed by the SBFW, and lowest for the SKFW mixtures. The cyclic strengths versus N exhibits a similar trend for normally consolidated specimens, yet an opposite trend for OCR = 2 specimens; highest for the SKFW mixture, followed by the SBFW mix, and lowest for the SBSW blend.

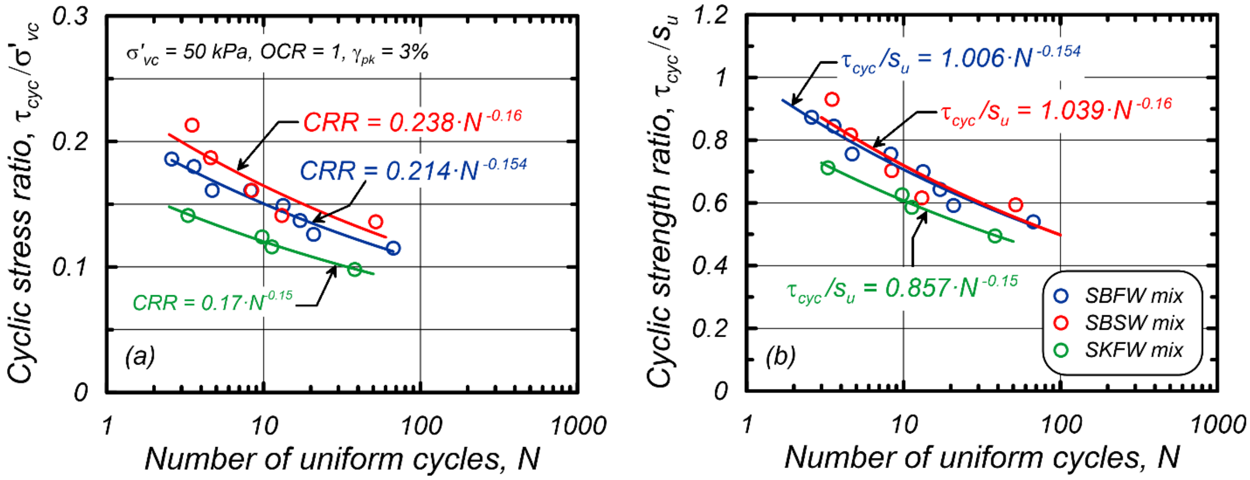

Figure 8.18. Cyclic strengths for OCR = 1 specimens of all three mixtures, (a) cyclic stress ratios versus number of uniform loading cycles, and (b) cyclic strength ratios versus number of uniform loading cycles

The monotonic shear response of the three mixtures exhibited differences in terms of strength normalization as well. Thus, the plasticity index, though being used as a key factor in several liquefaction susceptibility and cyclic softening triggering analyses procedures, seems to be an insufficient parameter to characterize the cyclic behavior of fine-grained soils in general, whether sand-like or clay-like.

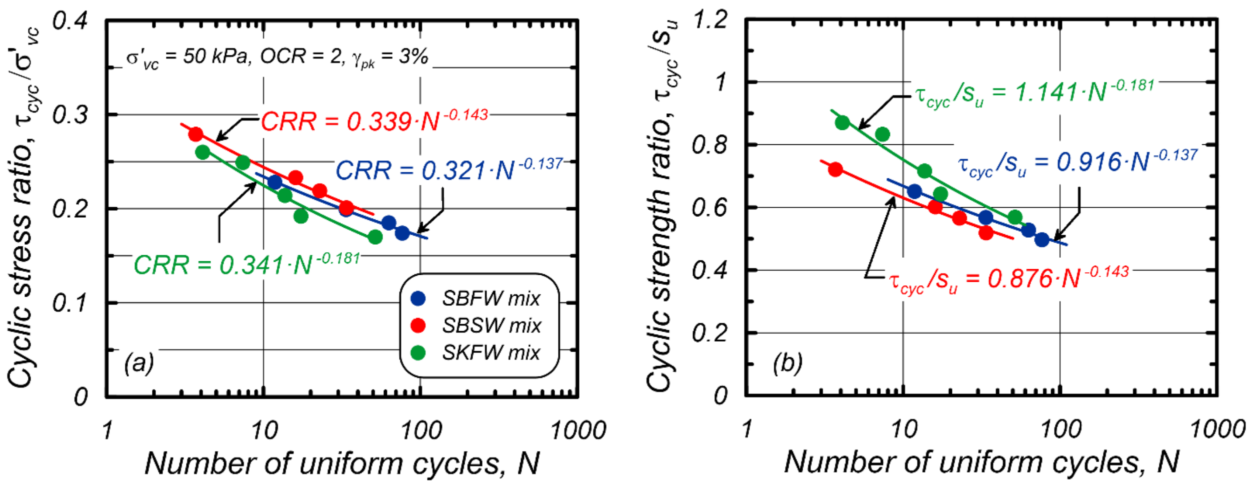

Figure 8.19. Cyclic strengths for OCR = 2 specimens of all three mixtures, (a) cyclic stress ratios versus number of uniform loading cycles, and (b) cyclic strength ratios versus number of uniform loading cycles

It is suggested by Idriss and Boulanger (2008) for engineering practice that for normally consolidated clay-like materials with PI > 7 and for N = 30, $\tau_{cyc}/s_u = 0.83$ and CRR = τ_{cyc}/σ'_{vc} = 0.183. The experimental results provided herein, though being consistent with other experimental studies of other research on mineral mixtures and reconstituted soils [e.g. Price et al. (2015), Reid and Fourie (2017), Tom (2011), and Soysa and Wijewickreme (2017)], not only suggest much lower values, but also present significant differences that are apparent among the three mixtures at the same plasticity.

The results provided herein are from laboratory mixtures that were consolidated in the range of a few hours to a few days and therefore, may not replicate field conditions such as age, fabric, and cementation of natural soils, whereas recommendations in Idriss and Boulanger (2008) are based on experiments on natural materials with much higher age as opposed to mixtures consolidated for just a few days in the laboratory. Hence, it would be interesting to study in more details the differences between minerals blends prepared in the laboratory and natural soils to assess the impact of the observations on plasticity.

It is apparent from Figure 8.18 and Figure 8.19 that cyclic strength is influenced by both pore-fluid chemistry and mineralogy for a given PI. Mixtures SBFW and SBSW show differences in cyclic resistance; the blend containing saline water with 10% bentonite (SBSW) consistently having a higher strength than the blend with fresh deionized water and 5% bentonite clay (SBFW). Additionally, pore-fluid being the same in the case of the SBFW and SKFW mixtures with varying clay minerals (bentonite and kaolinite) and their contents (5% and 22%), cyclic resistance ratios are seen to be distinct, where (for OCR = 1) the mixture with 5% Bentonite requires about 25% more cyclic stress applied to reach 3% shear strain in 10 cycles compared to the mixture with 22% Kaolinite. This difference can be attributed to the differences in the monotonic shear strength of the two mixtures at normally consolidated conditions, the difference becoming less pronounced at higher OCRs.

This difference can significantly influence engineering strategies and practice for important geotechnical engineering projects in presence of seismic activities. It is obvious that the current understanding of low-plasticity fine-grained soils’ behavior is limited and more experimental investigations are essential for better understanding and characterizing these types of soils.

8.7 EXPERIMENTAL DATASET ON DESIGNSAFE-CI.ORG

The experimental data obtained in Part II of this dissertation including results of monotonic and cyclic simple shear tests, as well as data visualization and analysis tools in the form of Jupyter notebooks are being curated and will be published. The dataset will be available on DesignSafe Cyber Infrastructure at http: www.designsafe-ci.org.

The experimental results are grouped into either monotonic or cyclic shear where each test contains two stages; consolidation and shear. Data files include time series of horizontal and vertical loads, displacements and corresponding stresses and strains as well as equivalent excess pore-water pressure. The data has been categorized in this manner to facilitate the use of the visualization notebook, as it provides different plots for the consolidation and shear stages of a test. A simple spreadsheet in the AGS4 format was created to provide descriptive information on the soil specimens that were tested.

Following dataset curation, the GUI generates a tree representing the data structure and a data browsing interface showing data in relation to the process that it derives from as provenance. Two Jupyter notebooks are included; (1) a Data Plotter, aiding users to visualize the collected experimental data, and (2) an analysis notebook creating an environment for the user to combine outcomes of multiple tests, synthesize the data, and enables regression analyses for finding failure state lines, shear strength normalization parameters, and generates CSR vs. N plots for cyclic tests for any arbitrary defined failure criterion (i.e. strain levels can be adjusted to any arbitrary value).

9 Summary and Conclusions of Part II

A series of cyclic and monotonic direct simple shear experiments were conducted on three low-plasticity fine-grained mixtures of non-plastic silt with either bentonite or kaolinite clay minerals blended with fresh deionized water or saline water. The clay fractions were adjusted to achieve a plasticity index of PI = 9 for all three mixtures. Though all three blends have the same plasticity index, significant differences in cyclic and monotonic response were observed leading to valuable insights about the effectiveness of the plasticity index in characterization of low-plasticity fine-grained soils. The collected experimental data, visualization, and post-processing tools as well as documented experimental procedures are being curated and will be published and available publicly on http: www.DesignSafe-ci.org.

The relationship of cyclic stress ratio versus number of cycles was highest for the SBSW mix, followed by SBFW and SKFW, respectively. The ratio of cyclic stress to monotonic undrained strength observed the same trend for normally consolidated specimens, but an opposite trend for OCR = 2 specimens, highest for SKFW, followed by SBFW, and lastly the SBSW mixture, indicating that plasticity index alone is an insufficient indicator of the cyclic behavior of low-plasticity fine-grained soils. The results presented herein indicate that the plasticity index cannot adequately capture differences in clay mineralogy and pore-fluid chemistry. It can be safely concluded that pore-fluid chemistry and clay mineralogy both contribute to cyclic resistance of fine-grained soils.

Common practice for evaluating cyclic strengths of clay-like material is to consider unique relationships between cyclic resistance and the undrained shear strength or effective consolidation stress of the soil. The experimental results of this study, though being in line with other experimental studies on cyclic response of mineral mixtures made in laboratories, do not support such relationships and are generally lower than proposed recommendation in the literature. However, it is important to note that recommendations in the literature such as those by Boulanger and Idriss (2004, 2007) and Idriss and Boulanger (2008) are based on experiments on natural materials with older age and more complex mineral compositions as opposed to mixtures of two minerals consolidated for just a few days in the laboratory.

The relationships of the cyclic resistance to monotonic undrained shear strengths of the mixtures tested herein are closer to the updated relationships for natural soils recommended by Dahl (2011). Hence, it would be interesting to study in more details the differences between mineral blends prepared in the laboratory and natural soils to assess the impact of the observations on plasticity. Gathering all available experimental data on cyclic behavior of fine-grained soils in the literature into a database would be the ideal approach, enabling the generation of such relationships using the most robust possible datasets. This would require developing suitable data models for cyclic strength test data and integration with other databases that are being developed, such as Next Generation liquefaction (NGL) by Stewart et al. (2016).

The differences observed in cyclic strengths can significantly influence engineering strategies or practice for important geotechnical engineering projects in presence of seismic activities. It is obvious that the current understanding of low-plasticity fine-grained soils' behavior is limited and more experimental investigations are essential for better understanding and characterizing these types of soils. The results presented herein suggest a departure from conventionally proposed liquefaction susceptibility and cyclic softening criteria and corresponding procedures for low-plasticity fine-grained soils based solely on plasticity index. It reveals the necessity of corrections for pore fluid chemistry and clay minerology in future guidelines for practicing engineers, though site-specific and detailed cyclic testing for important projects is considered crucial and is generally recommended for accurately characterizing these types of materials.

Appendix A: Derivation of Plastic Flow Incremental Formulation

DERIVATION OF INCREMENTAL STRESS-STRAIN RELATION SHIP

From the elastic stress-strain relationship:

$$\sigma = E\varepsilon^{e} \tag{A.1}$$

Where, E is the Young's modulus, σ and ε^{e} are the stress and elastic strains respectively.

Substituting elastic strains by, total amount of strains (ε) subtracted by the plastic strains (ε^{p}):

$$\sigma = E(\varepsilon - \varepsilon^{p}) \tag{A.2}$$

In terms of stress and strain rates, equation A.2 then becomes:

$$\dot{\sigma} = E(\dot{\varepsilon} - \dot{\varepsilon}^{p}) \tag{A.3}$$

FLOW RULE AND CONSISTENCY CONDITION

Considering non-associated flow rule:

$$\dot{\varepsilon}^{p} = \lambda \cdot \frac{\partial g}{\partial \sigma_{ij}} \tag{A.4}$$

And the consistency condition:

$$f \quad \gamma \geq 0 \rightarrow \dot{f}(\sigma) = 0 \tag{A.5}$$

Where γ is strain.

Assuming $\gamma \geq 0$, then:

$$\dot{f}(\sigma) = \frac{\partial f}{\partial \sigma_{ij}} \cdot \dot{\sigma} \tag{A.6}$$

Substituting equation A.3 into A.6:

$$\dot{f}(\sigma) = \frac{\partial f}{\partial \sigma_{ij}} \cdot E \cdot (\dot{\varepsilon} - \dot{\varepsilon}^{p}) \tag{A.7}$$

Substituting equation A.4 into A.7:

$$\dot{f}(\sigma) = \frac{\partial f}{\partial \sigma_{ij}} \cdot E \cdot (\dot{\varepsilon} - \lambda \cdot \frac{\partial g}{\partial \sigma_{ij}}) \tag{A.8}$$

Using the consistency condition given in equation A.5 and applying to equation A.8:

$$\frac{\partial f}{\partial \sigma_{ij}} \cdot E \cdot \dot{\varepsilon} = \lambda \cdot \frac{\partial f}{\partial \sigma_{ij}} \cdot E \cdot \frac{\partial g}{\partial \sigma_{ij}} \tag{A.9}$$

From A.9 it can be concluded that the hardening variable can be found using A.10:

$$h = \frac{\partial f}{\partial \sigma_{ij}} \cdot E \cdot \frac{\partial g}{\partial \sigma_{ij}} \tag{A.10}$$

Therefore, the magnitude of the plastic strain, λ, can be found using equation A.11:

$$\lambda = \frac{1}{h} \cdot \frac{\partial f}{\partial \sigma_{ij}} \cdot E \cdot \dot{\varepsilon} \rightarrow \ \lambda = \frac{1}{h} \cdot \frac{\partial f}{\partial \sigma_{ij}} \cdot \dot{\sigma} \tag{A.11}$$

By substituting the magnitude of plastic strain, λ, into the non-associated flow rule, one may conclude equation A.12 as the incremental plastic strain formulation, similar to equation (3.1).

$$d\varepsilon^{p}_{ij} = \frac{1}{h} \frac{\partial g}{\partial \sigma'_{ij}} \frac{\partial f}{\partial \sigma'_{kl}} d\sigma'_{kl} \tag{A.12}$$

PLASTIC FLOW INCREMENTAL FORMULATION

Deviatoric strain increment

Given the yield surface and plastic potential surfaces as in equations A.13 and A.14, respectively, and also from equation A.12 one can conclude for plastic shear strains, equation A.15. Note that:

$$f = q - \mu . p' - I_f \tag{A.13}$$

$$g = q - \eta_{pp} . p' - I_g \tag{A.14}$$

$$d\varepsilon^{p}_{q} = \frac{1}{h} \cdot \frac{\partial g}{\partial q} \cdot \frac{\partial f}{\partial \sigma} \cdot d\sigma \rightarrow \ d\varepsilon^{p}_{q} = \frac{1}{h} \cdot \frac{\partial f}{\partial \sigma} \cdot d\sigma \tag{A.15}$$

Moreover, considering that $\frac{\partial f}{\partial \sigma} \cdot d\sigma = \frac{\partial f}{\partial q} \cdot dq + \frac{\partial f}{\partial p} \cdot dp$ and continuing the substitutions, one can reach to equation A.16 for plastic deviator strains (same as equation 3.4).

$$d\varepsilon_q^p = \frac{1}{h}(dq - \mu dp) \tag{A.16}$$

Additionally, for total shear strains, considering the elastic shear strains, $d\varepsilon_q^e = \frac{dq}{3G}$, equation A.17 can be used. A simplified version of the equation can be seen in equation A.18.

$$d\varepsilon_q = \frac{1}{3G} dq + \frac{1}{h} \cdot (dq - \mu dp) \tag{A.17}$$

$$d\varepsilon_q = dq\left(\frac{1}{3G} + \frac{1}{h}\right) + dp\left(\frac{-\mu}{h}\right) \tag{A.18}$$

Where *G* is the elastic Shear modulus.

Volumetric strain increment

Following the same logic as for the plastic shear strains, one can conclude for plastic volumetric strains, equation A.19.

$$d\varepsilon_v^p = \frac{1}{h} \cdot \frac{\partial g}{\partial p} \cdot \frac{\partial f}{\partial \sigma} \cdot d\sigma \rightarrow \ d\varepsilon_v^p = \frac{-\eta_{pp}}{h} \cdot \frac{\partial f}{\partial \sigma} \cdot d\sigma \tag{A.19}$$

Once more, considering that $\frac{\partial f}{\partial \sigma} \cdot d\sigma = \frac{\partial f}{\partial q} \cdot dq + \frac{\partial f}{\partial p} \cdot dp$, and further substitutions, one may conclude equation A.20 for plastic volumetric strains (same as equation 3.5).

$$d\varepsilon_v^p = \frac{-\eta_{pp}}{h}(dq - \mu dp) \tag{A.20}$$

Considering elastic volumetric strains, $d\varepsilon_v^e = \frac{dp}{K}$, one has equation A.21 for total volumetric strains, also given more simplified in equation A.22. Where *K* is the elastic Bulk modulus.

$$d\varepsilon_v = \frac{1}{K}dp + \left(\frac{-\eta_{pp}}{h}(dq - \mu dp)\right) \tag{A.21}$$

$$d\varepsilon_v = dq\left(\frac{-\eta_{pp}}{h}\right) + dp\left(\frac{1}{K} + \frac{\mu\eta_{pp}}{h}\right) \tag{A.22}$$

Stress-strain incremental formulation

Combining equations A.18 and A.22, one can have the matrix format given in equation (3.4), also given here in equation A.23.

$$\begin{pmatrix} d\varepsilon_q \\ d\varepsilon_v \end{pmatrix} = \begin{bmatrix} \left(\frac{1}{3G}\right) + \left(\frac{1}{h}\right) & \left(\frac{-\mu}{h}\right) \\ \left(\frac{-\eta_{pp}}{h}\right) & \left(\frac{1}{K}\right) + \left(\frac{\eta_{pp}\mu}{h}\right) \end{bmatrix} \cdot \begin{pmatrix} dq \\ dp \end{pmatrix} \tag{A.23}$$

Appendix B: Monotonic Direct Simple Shear Test Results

The Table below provides metadata about the strain-controlled constant-height monotonic shear tests that were performed in this dissertation. The following pages in this Appendix provide measurements of stresses and strains for both consolidation and shearing stages of each experiment. The stress-strain curves, stress paths, as well as equivalent excess pore pressure ratio curves are provided for each test. All values are plotted in ratios normalized by the effective consolidation stress.

Note that the test results are presented in the order of the mixtures with SBFW first, followed by SBSW, and lastly SKFW mixtures.

Mixture	*Test ID*	σ'_{vc} *(kPa)*	*OCR*	e_c*	$(s_u/\sigma'_{vc})_{pk}$
SBFW	Test26	50	1.4	0.875	0.257
	Test27	50	1.2	0.884	0.277
	Test28	50	1.5	0.87	0.273
	Test50	50	1.9	0.86	0.36
	Test51	50	2.0	0.854	0.353
	Test55	54	3.1	0.839	0.494
	Test85	100	1.0	0.84	0.221
	Test90	30	1	-	0.23
SBSW	Test23	50	1.2	0.853	0.257
	Test24	50	1.4	0.841	0.297
	Test25	50	1.6	0.836	0.324
	Test49	50	1.5	0.837	0.312
	Test52	50	3.6	0.782	0.647
	Test53	50	3.1	0.793	0.565
	Test54	50	4.4	0.77	0.758
	Test87	30	1.0	0.89	0.232
	Test88	95	1.0	0.82	0.232
	Test89	50	1.0	-	0.234
SKFW	Test68	50	1.0	0.706	0.176
	Test71	50	1.0	0.716	0.194
	Test69	50	1.6	0.693	0.291
	Test70	50	5.1	0.648	0.522
	Test81	100	1.5	0.665	0.208
	Test82	200	1.2	0.635	0.225
	Test83	30	1.0	0.722	0.24

*e_c: *post-consolidation void ratio*

$(s_u/\sigma'_{vc})_{pk}$: *peak undrained shear strength ratio*

SBFW-Test # 26

Stage 1: Consolidation

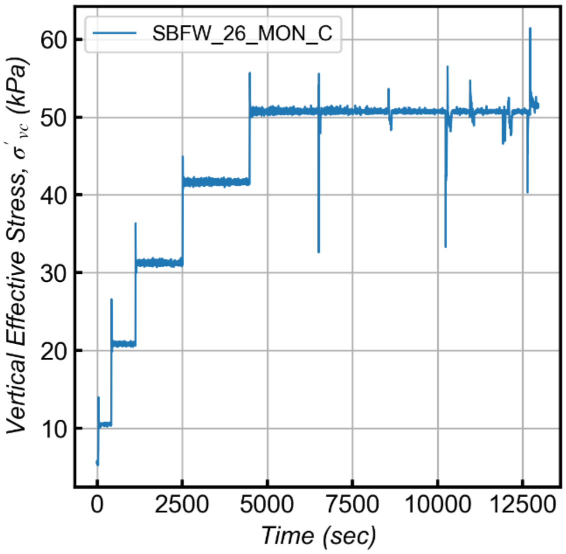

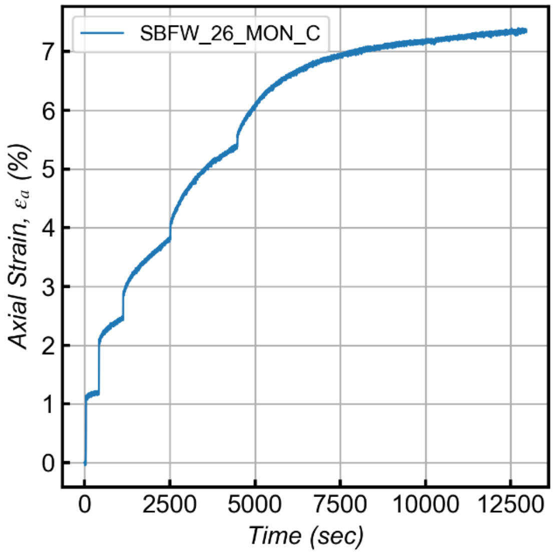

Stage 2: Monotonic Shear

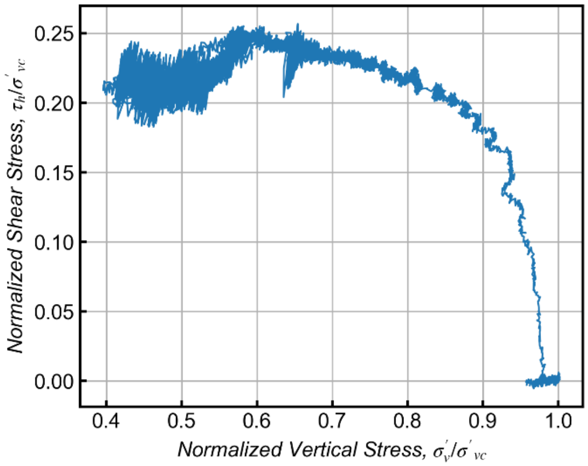

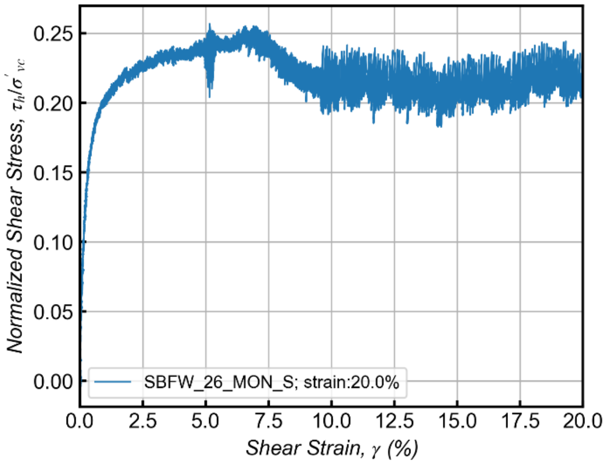

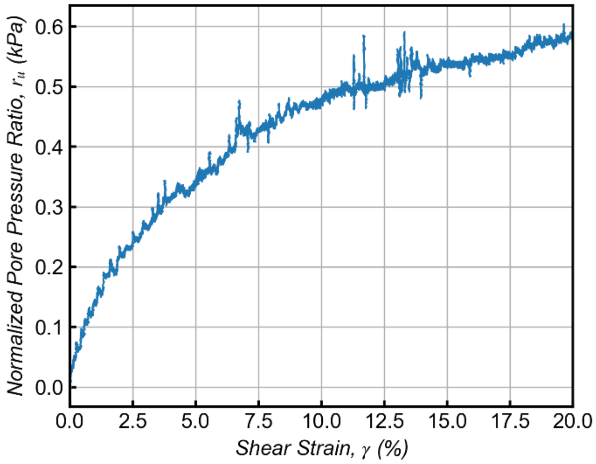

SBFW-Test # 27

Stage 1: Consolidation

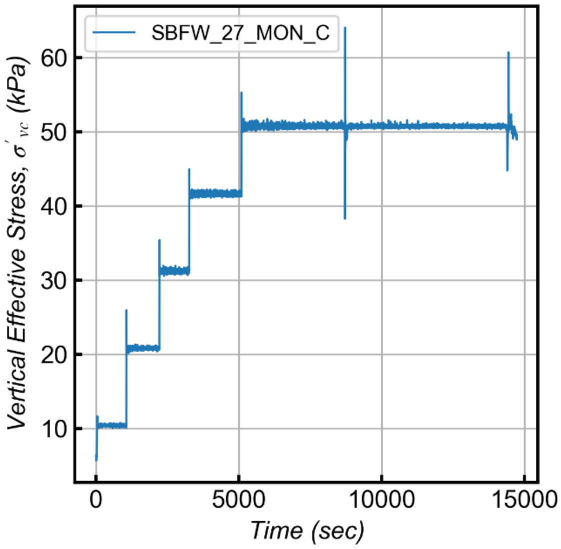

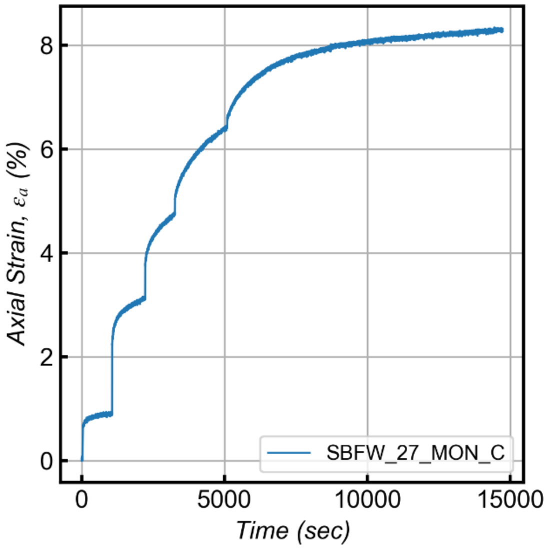

Stage 2: Monotonic Shear

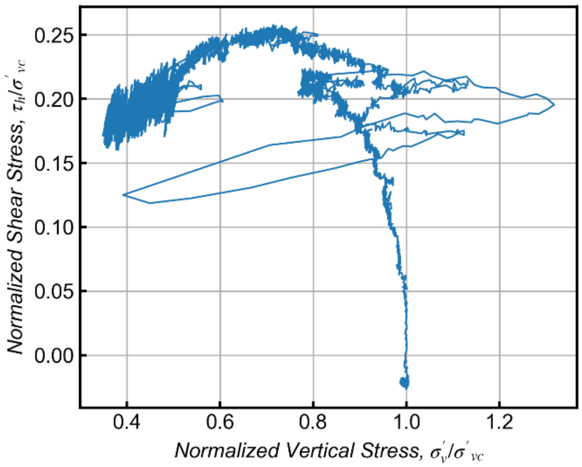

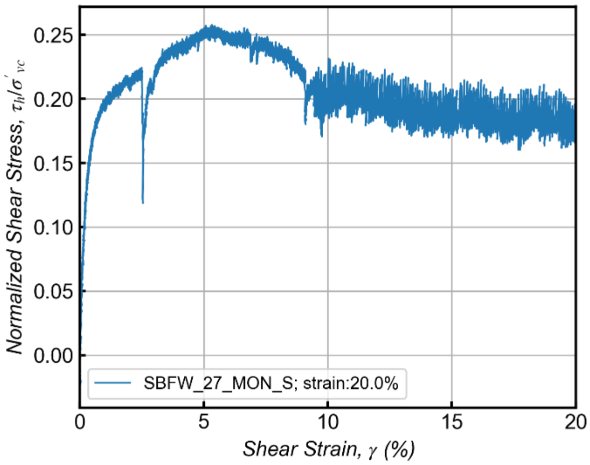

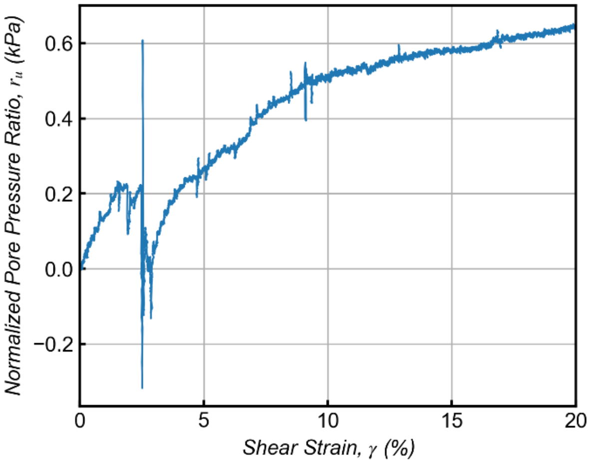

SBFW-Test # 28

Stage 1: Consolidation

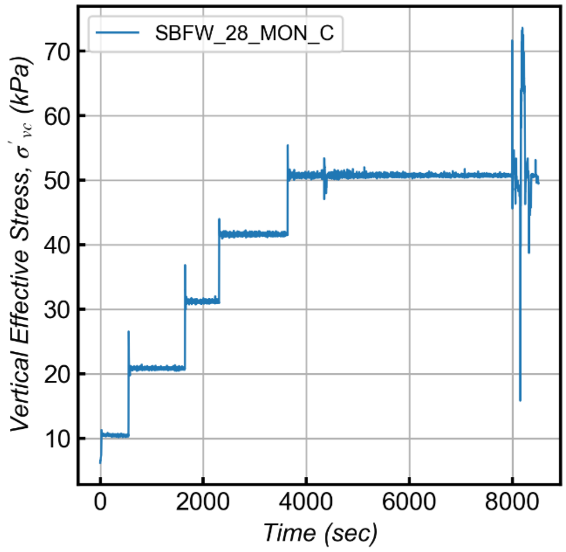

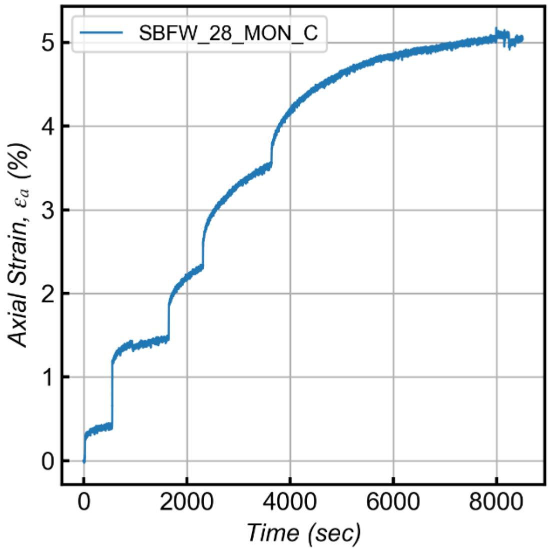

Stage 2: Monotonic Shear

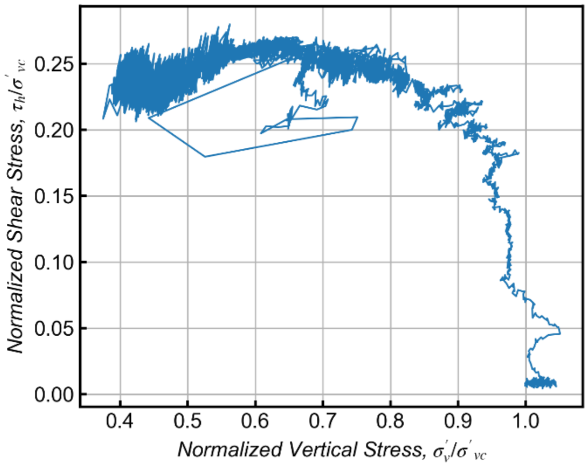

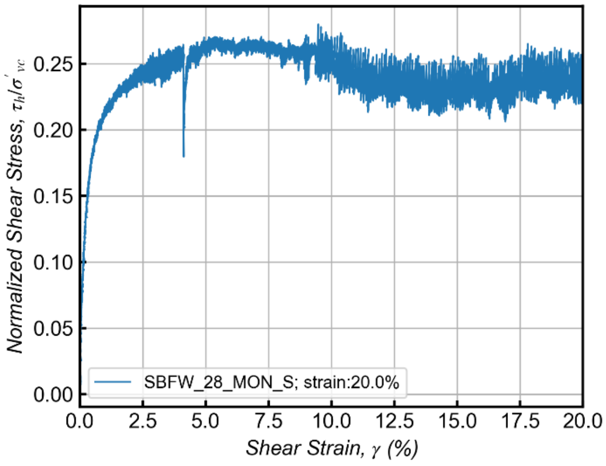

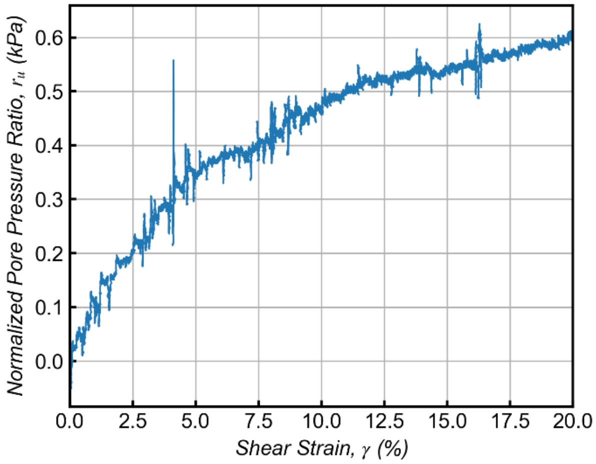

SBFW-Test # 50

Stage 1: Consolidation

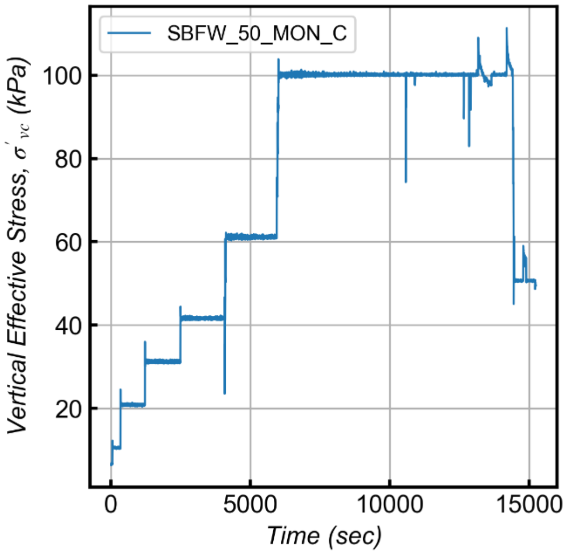

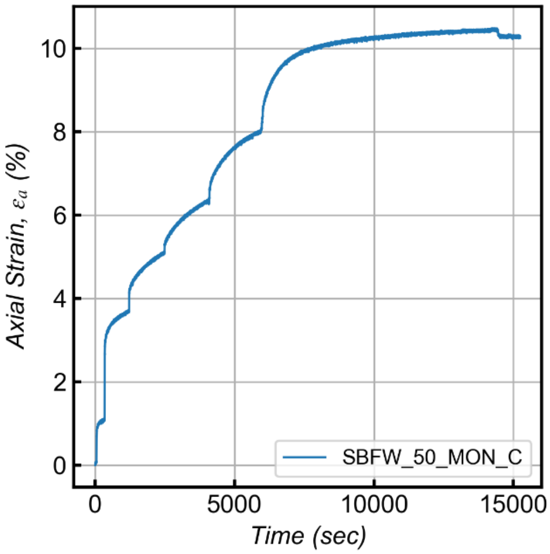

Stage 2: Monotonic Shear

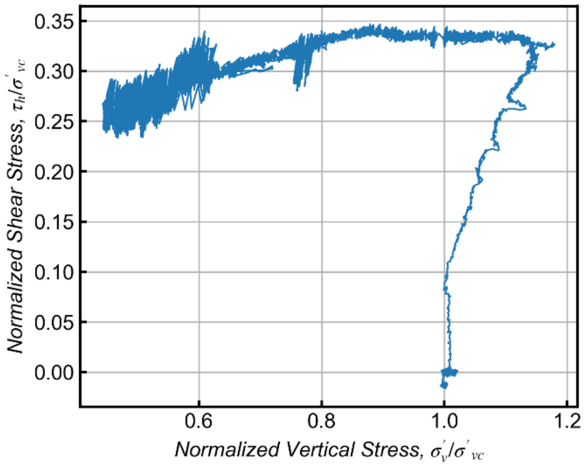

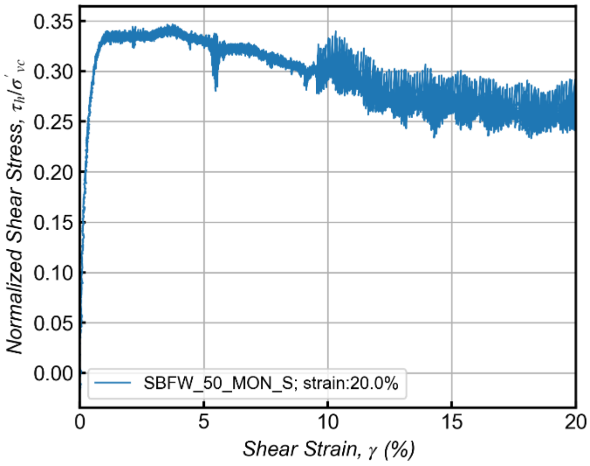

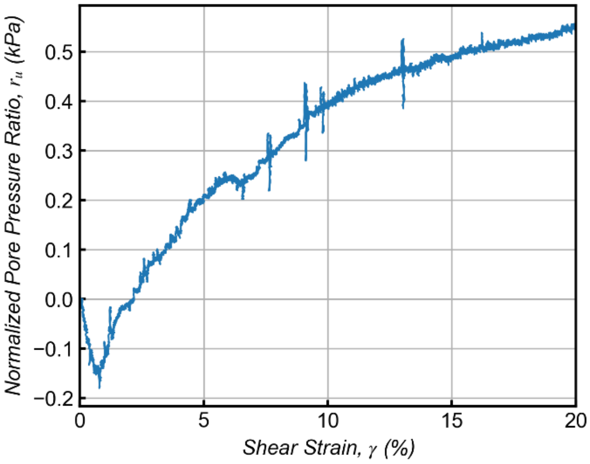

SBFW-Test # 51

Stage 1: Consolidation

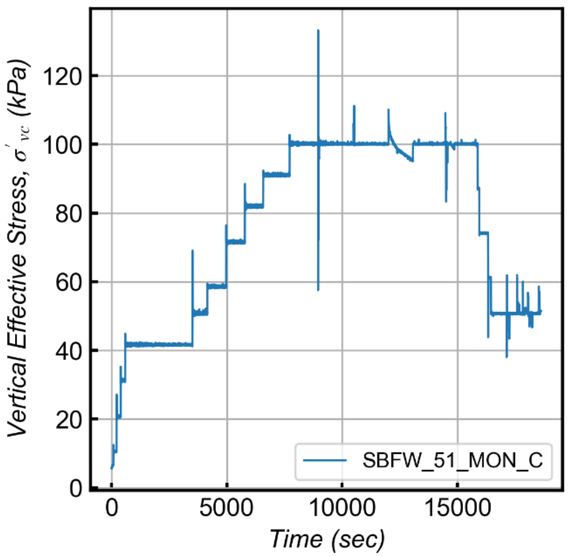

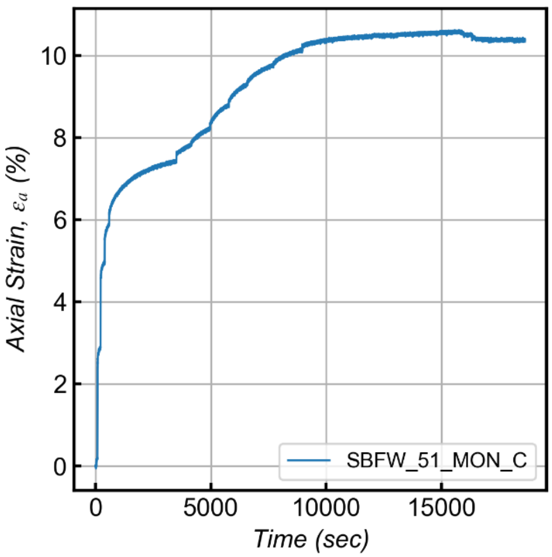

Stage 2: Monotonic Shear

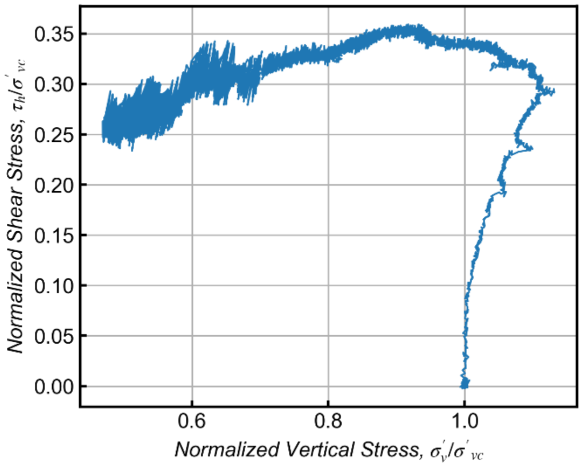

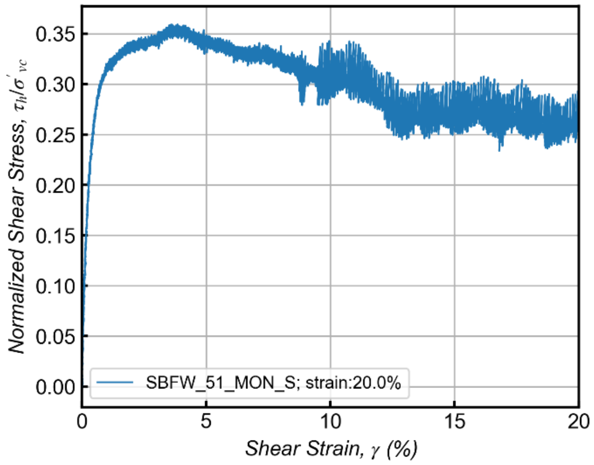

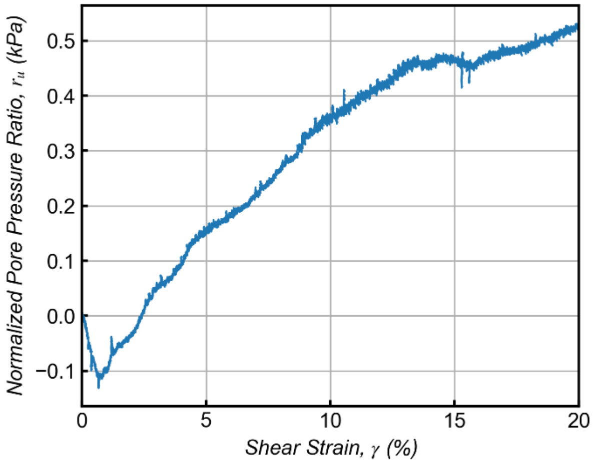

SBFW-Test # 55

Stage 1: Consolidation

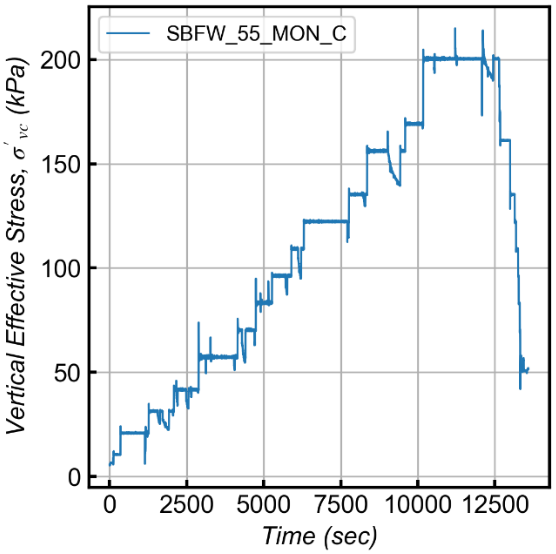

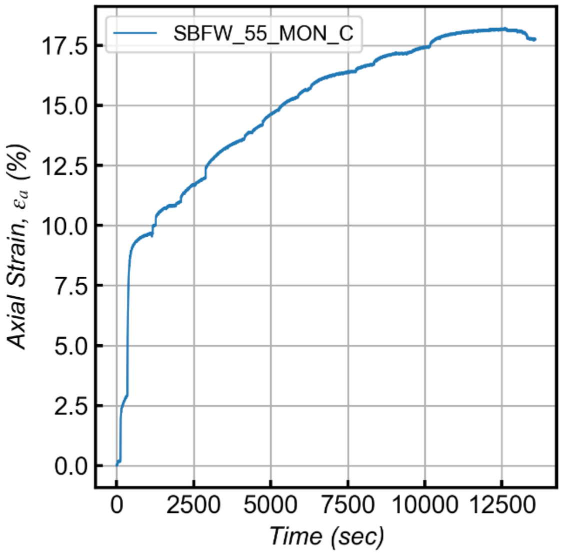

Stage 2: Monotonic Shear

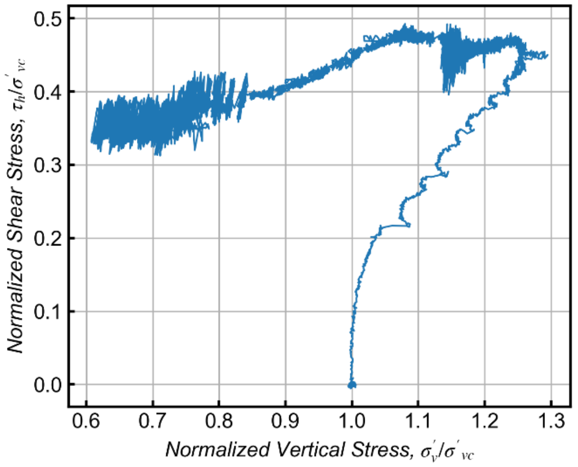

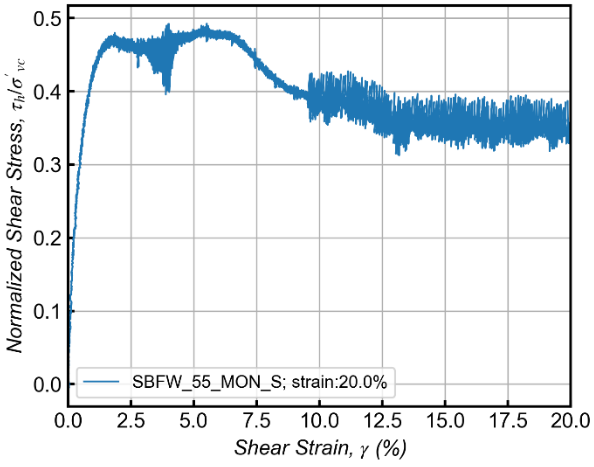

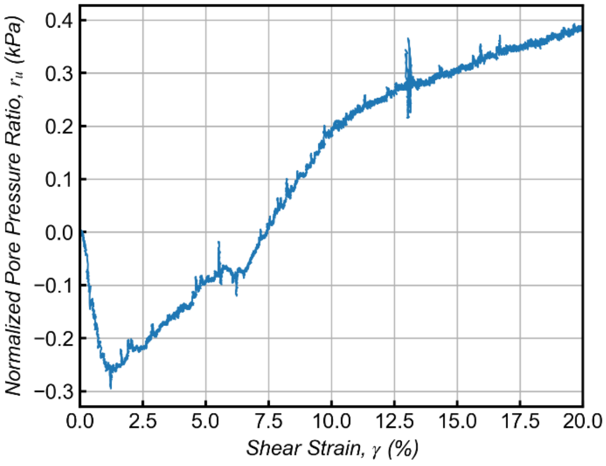

SBFW-Test # 85

Stage 1: Consolidation

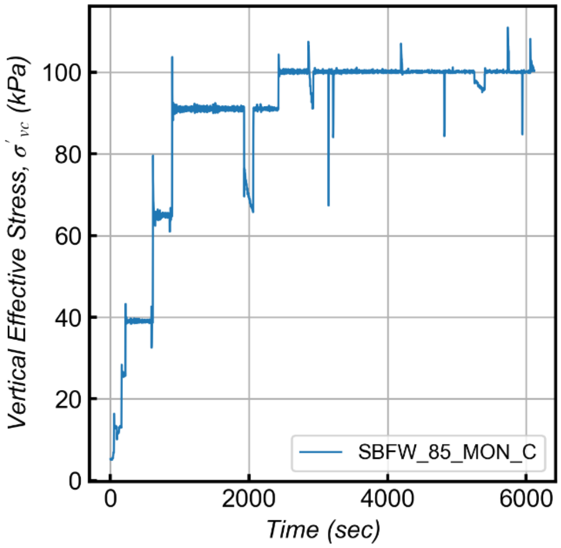

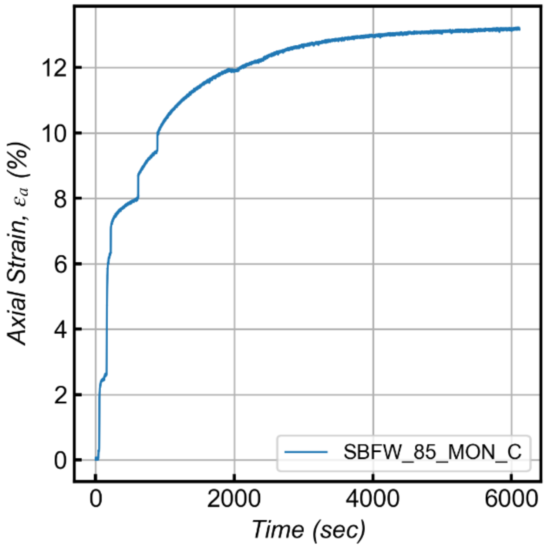

Stage 2: Monotonic Shear

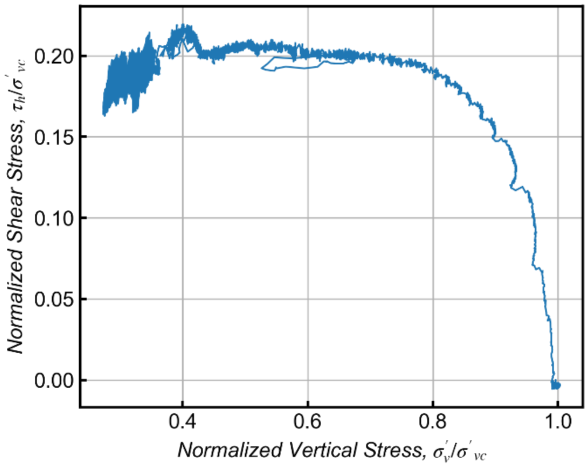

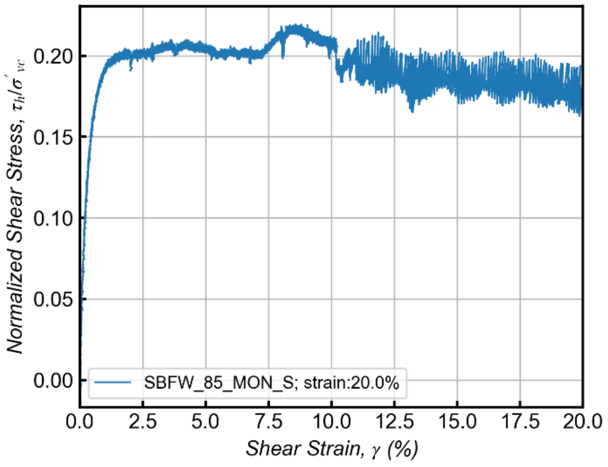

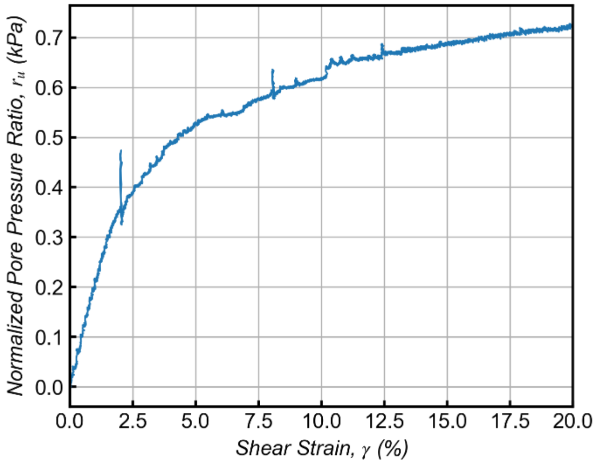

SBSW-Test # 23

Stage 1: Consolidation

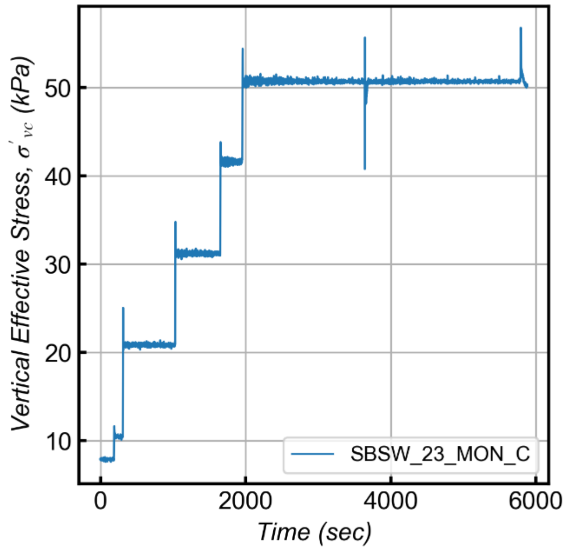

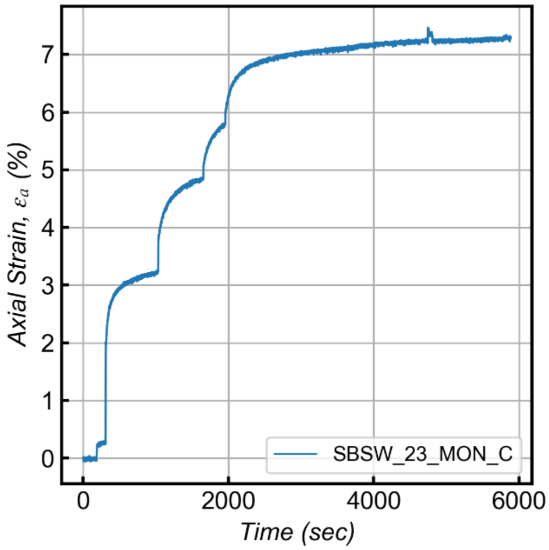

Stage 2: Monotonic Shear

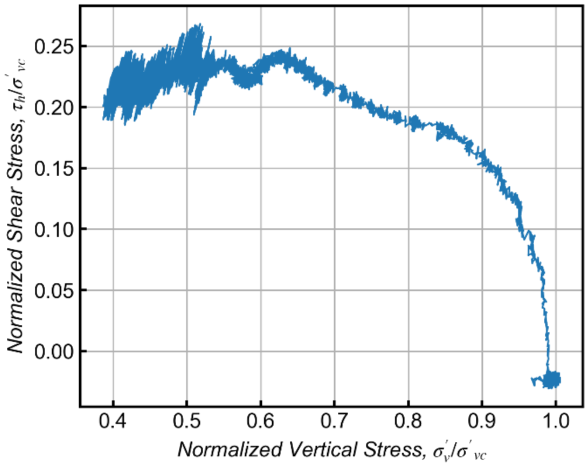

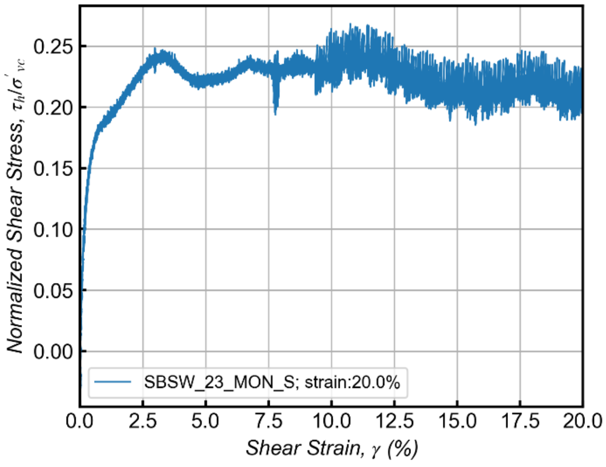

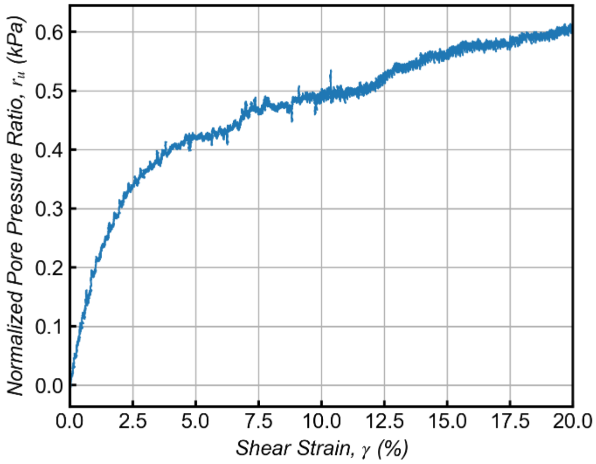

SBSW-Test # 24

Stage 1: Consolidation

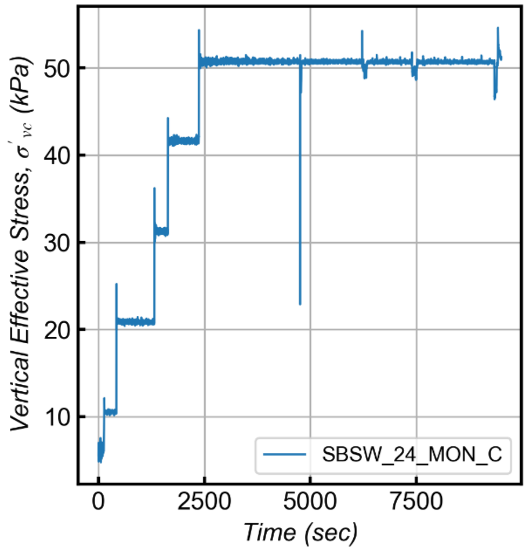

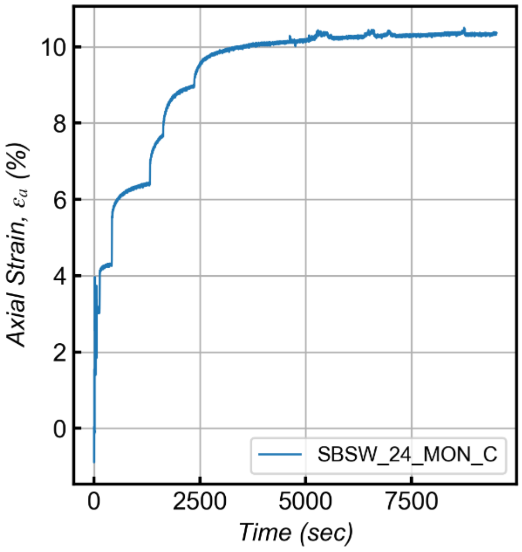

Stage 2: Monotonic Shear

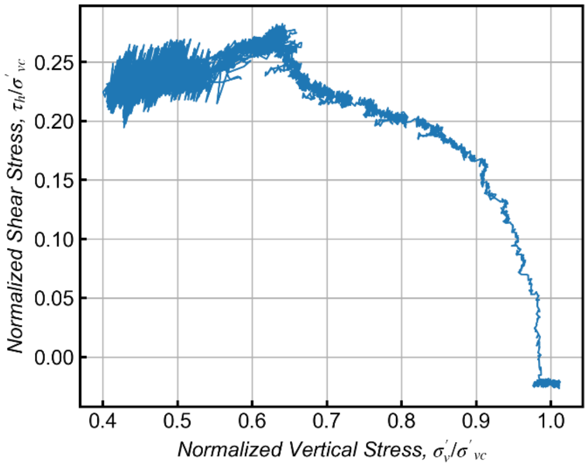

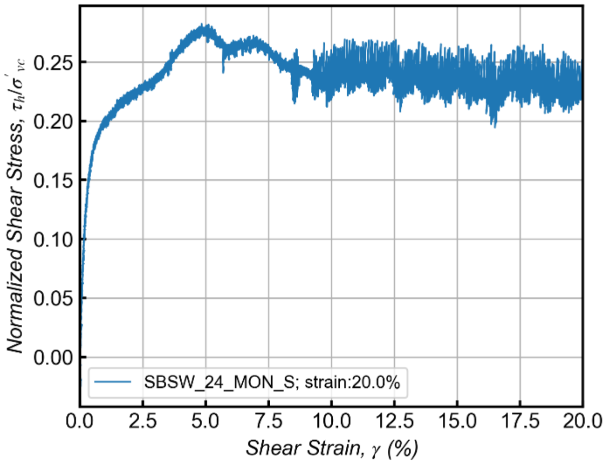

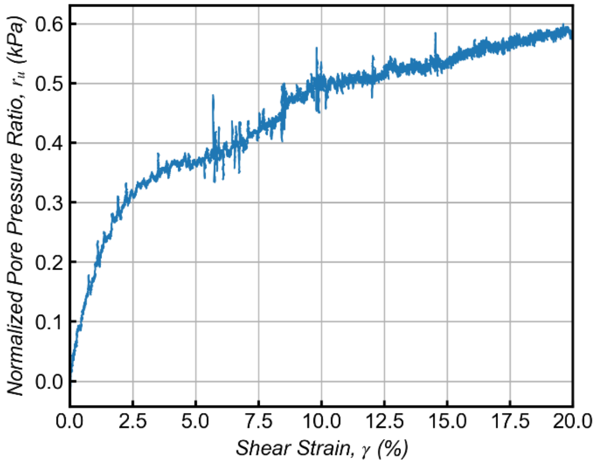

SBSW-Test # 25

Stage 1: Consolidation

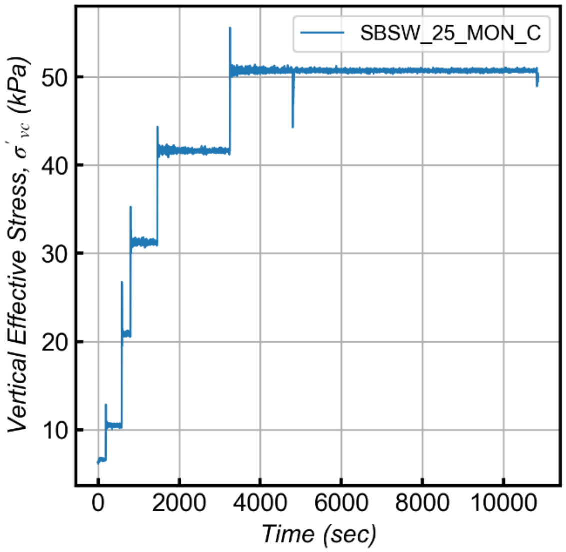

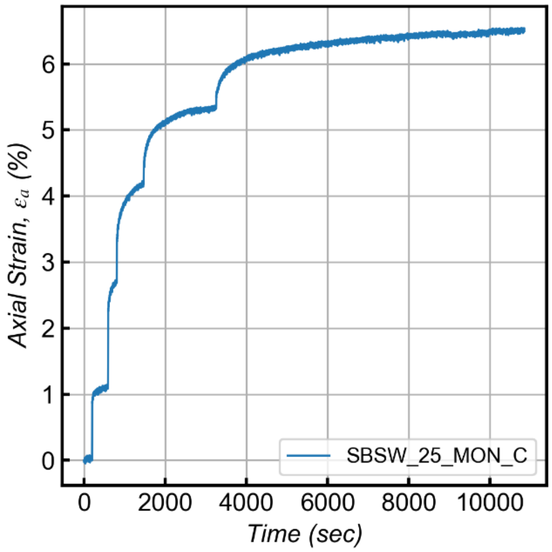

Stage 2: Monotonic Shear

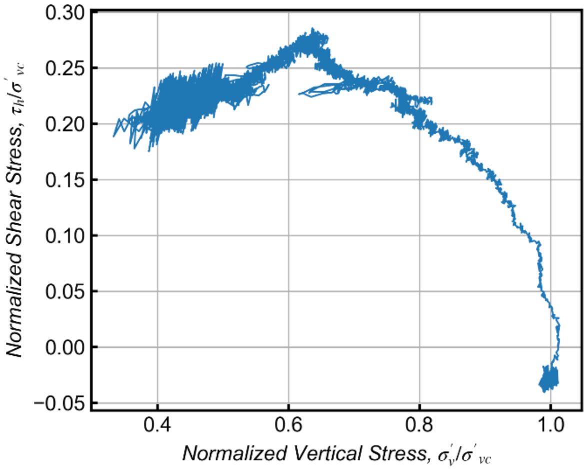

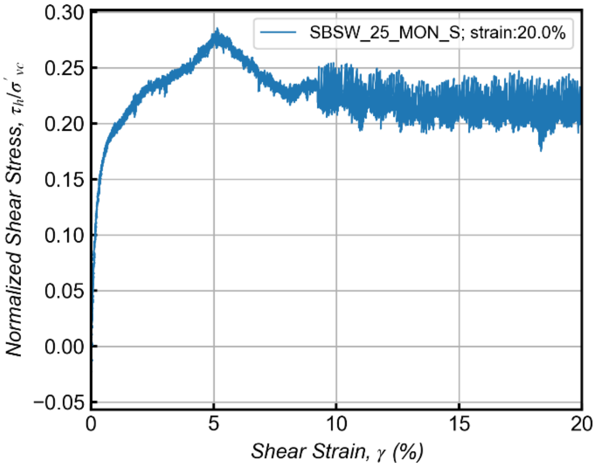

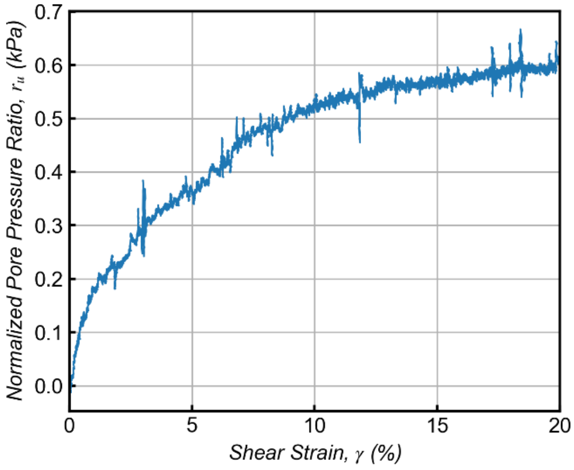

SBSW-Test # 49

Stage 1: Consolidation

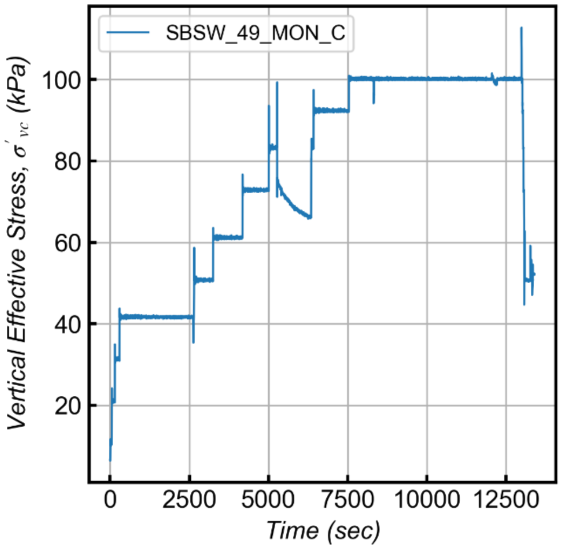

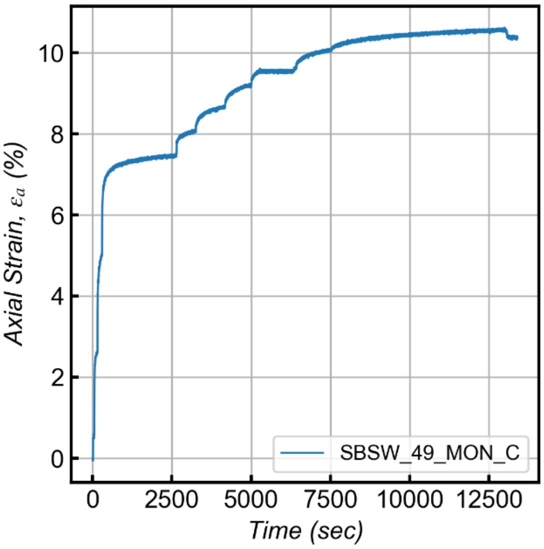

Stage 2: Monotonic Shear

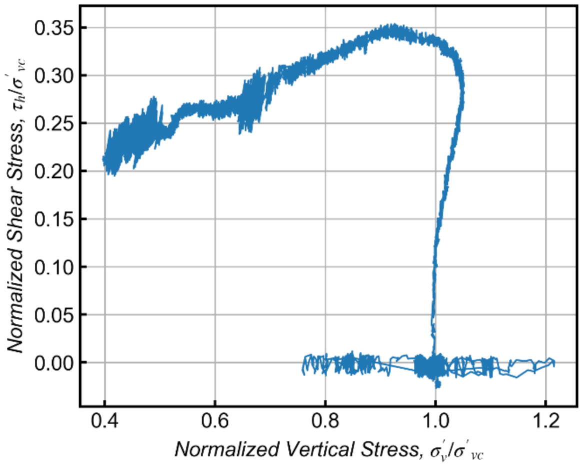

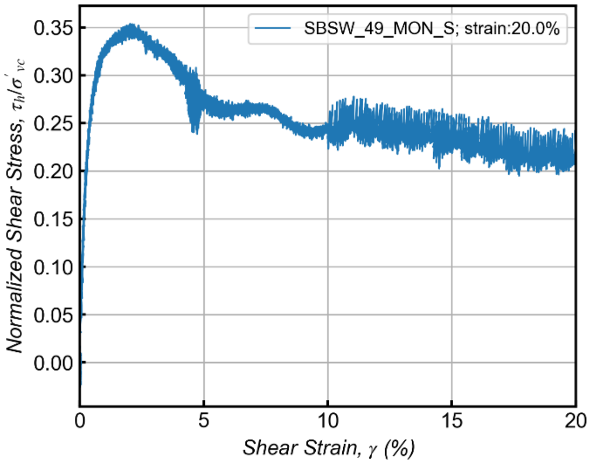

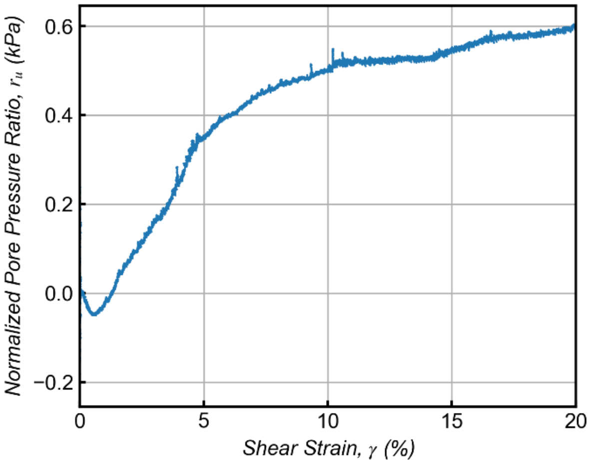

SBSW-Test # 52

Stage 1: Consolidation

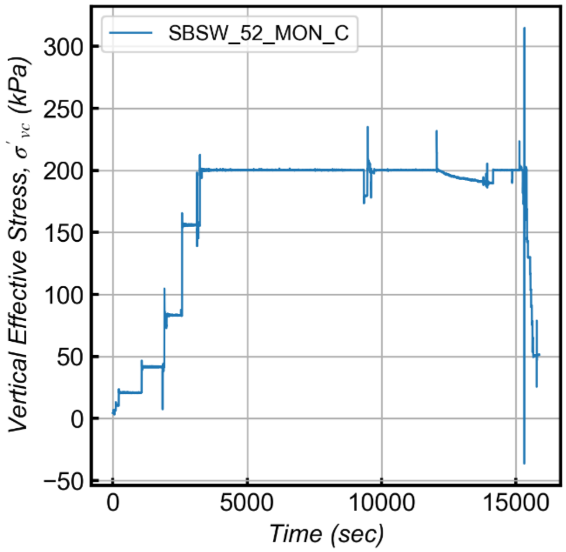

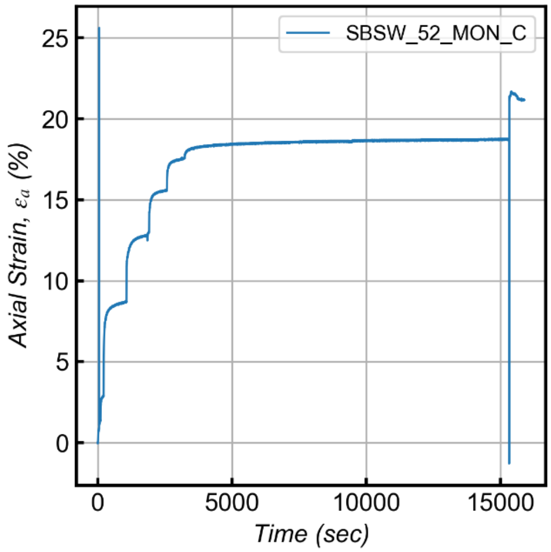

Stage 2: Monotonic Shear

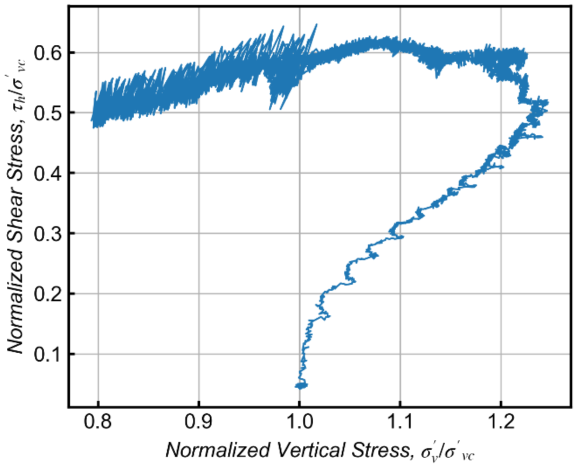

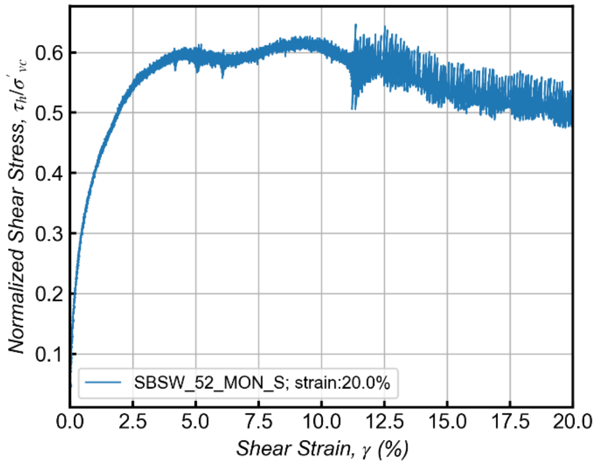

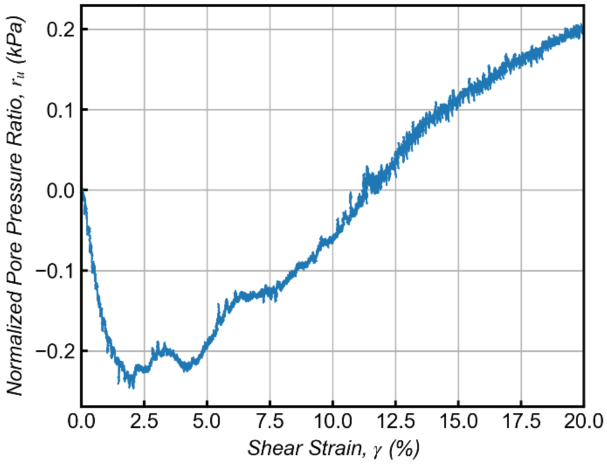

SBSW-Test # 53

Stage 1: Consolidation

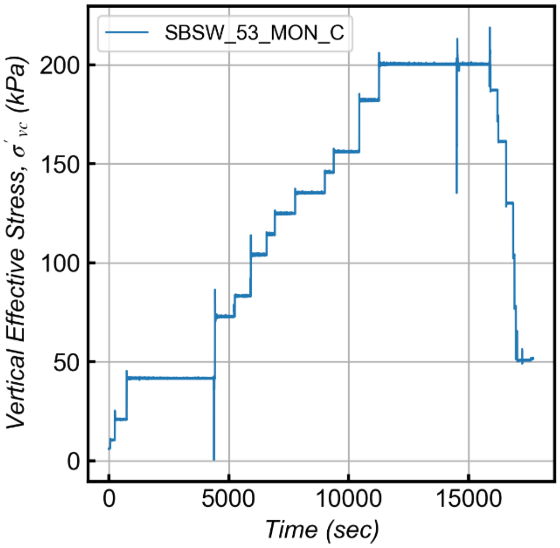

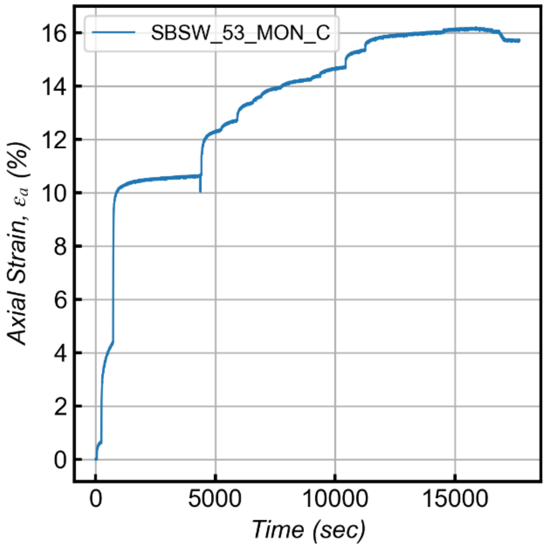

Stage 2: Monotonic Shear

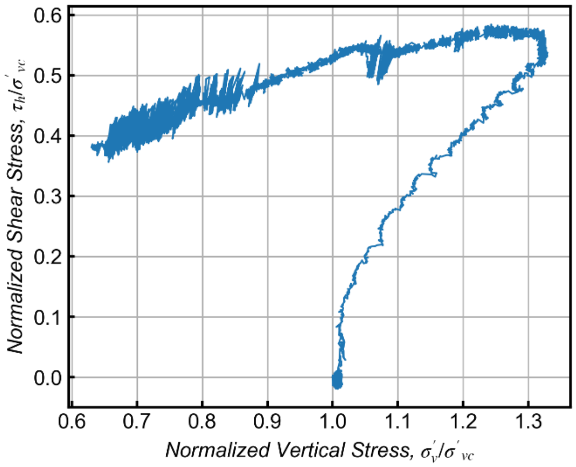

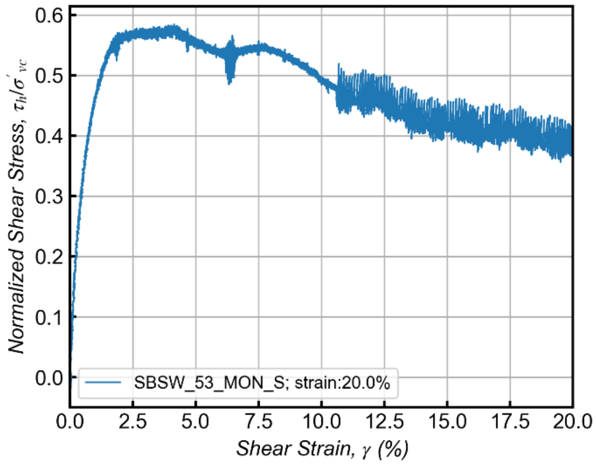

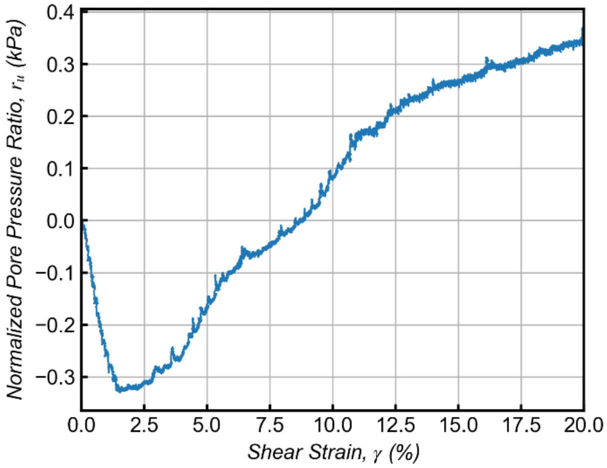

SBSW-Test # 54

Stage 1: Consolidation

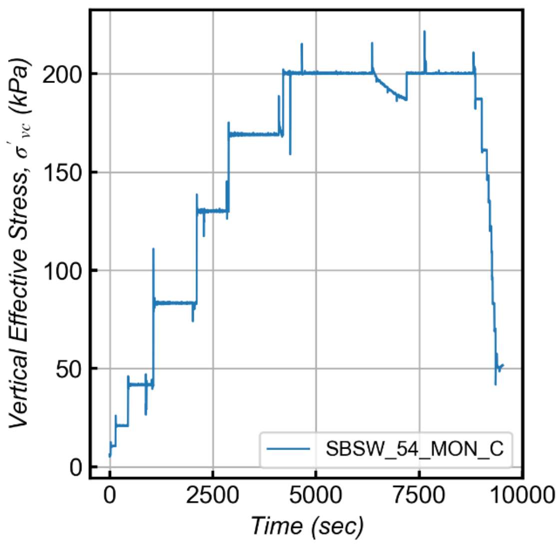

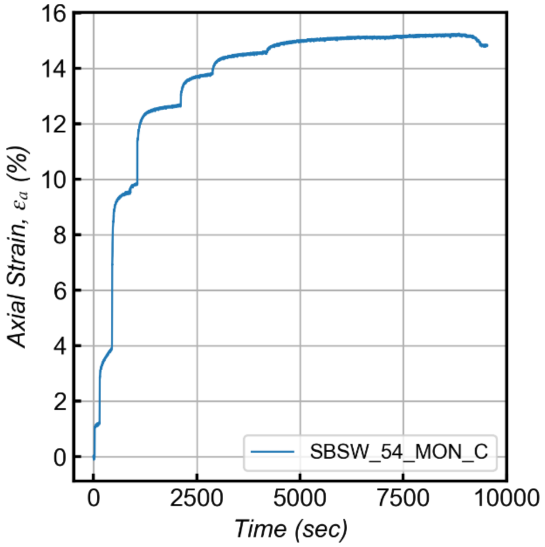

Stage 2: Monotonic Shear

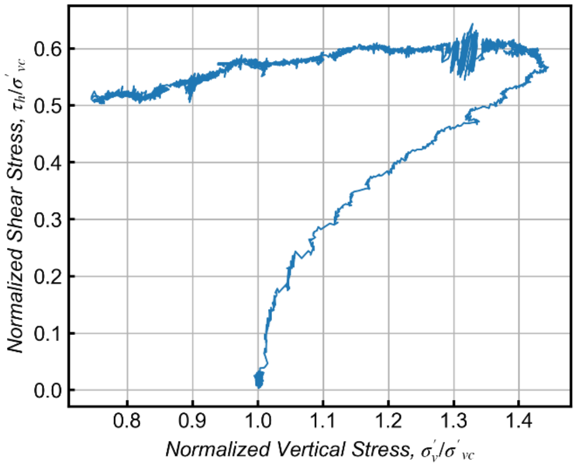

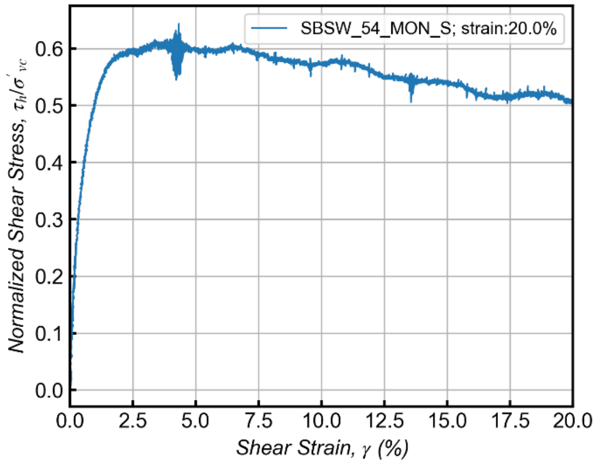

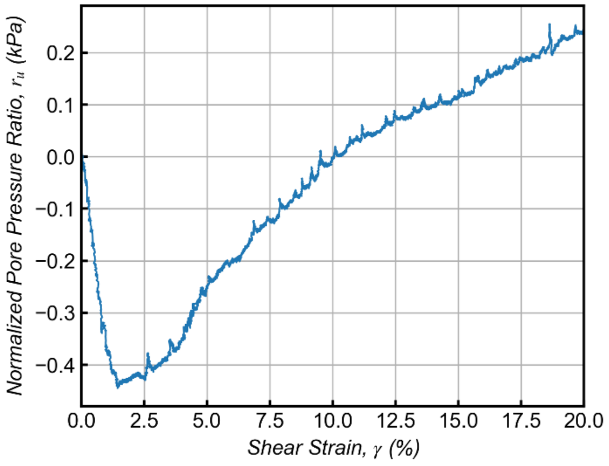

SBSW-Test # 87

Stage 1: Consolidation

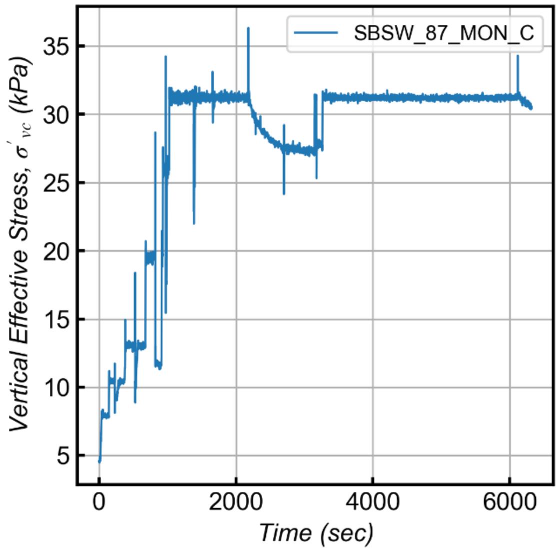

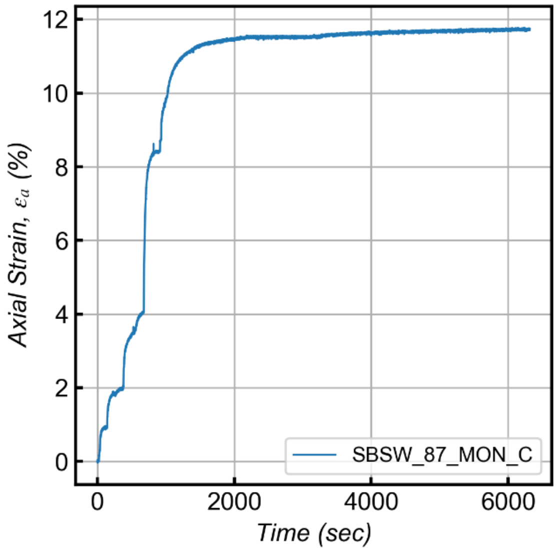

Stage 2: Monotonic Shear

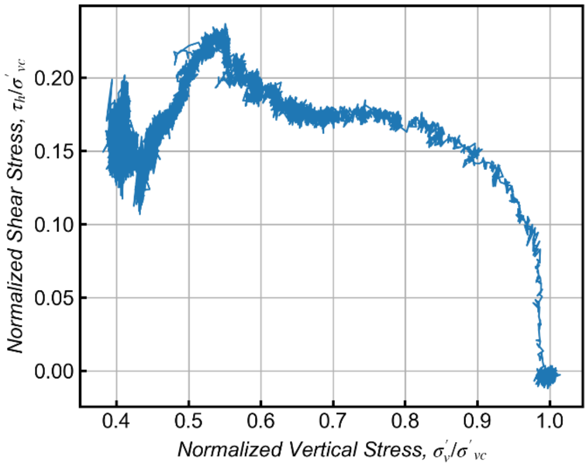

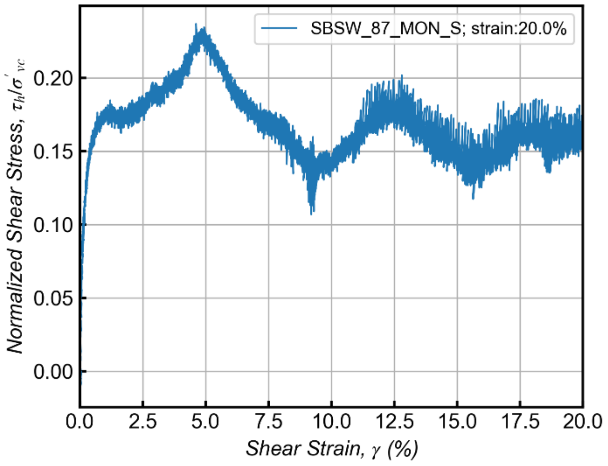

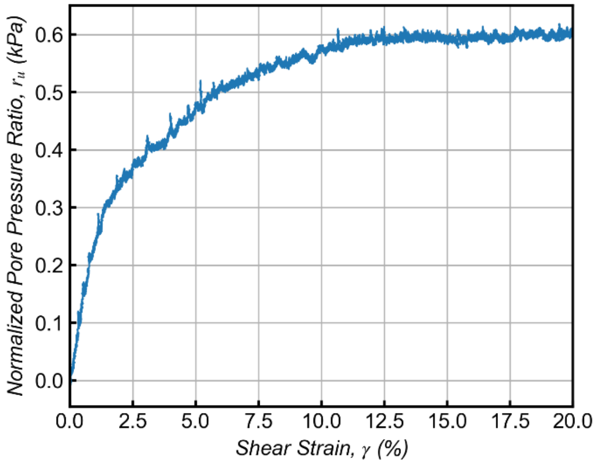

SBSW-Test # 88

Stage 1: Consolidation

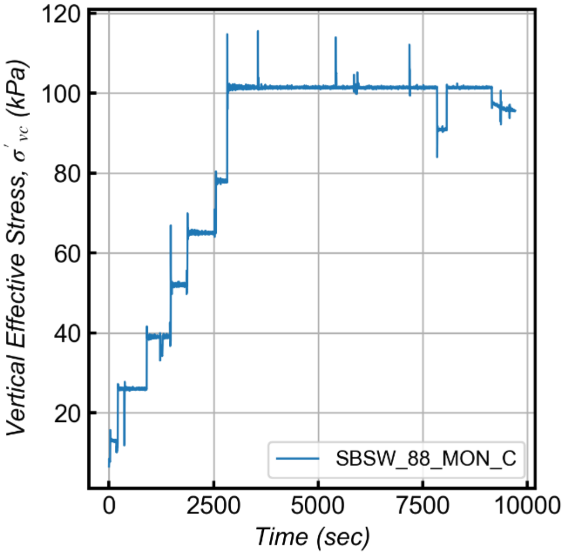

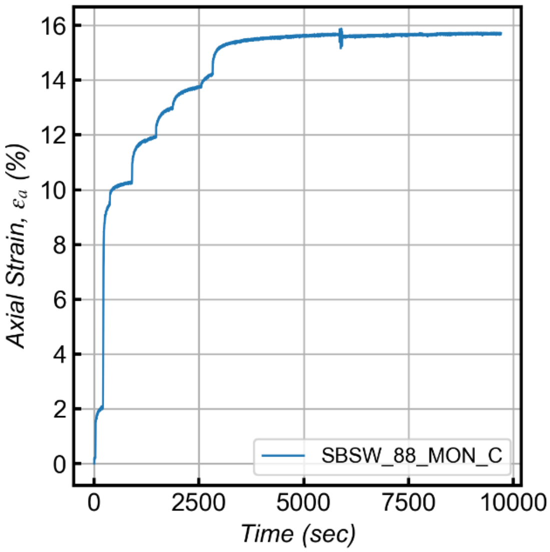

Stage 2: Monotonic Shear

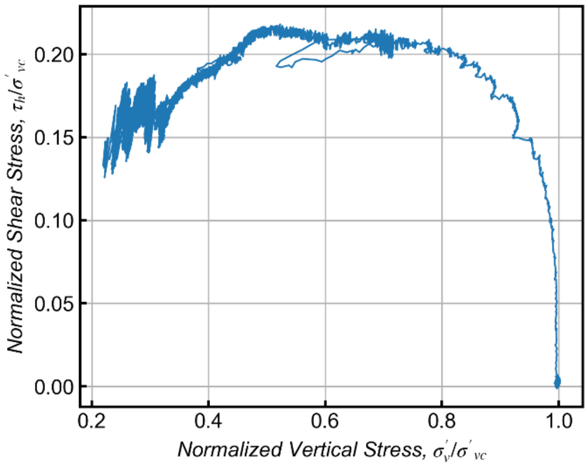

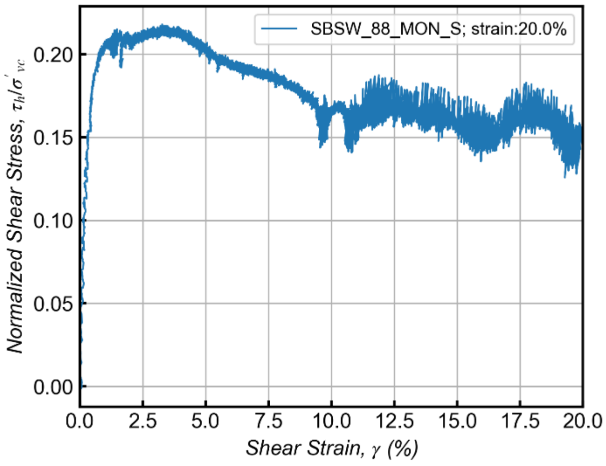

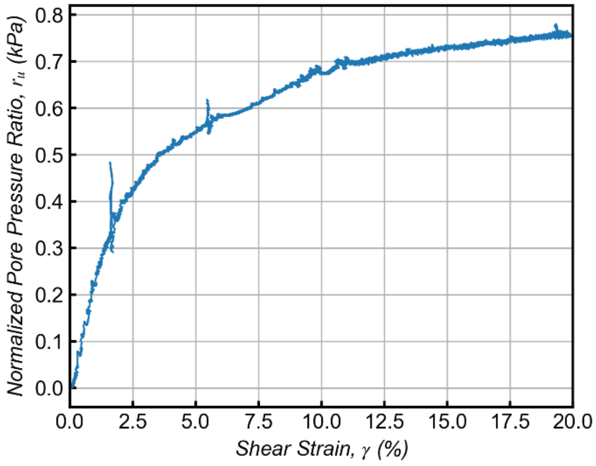

SBSW-Test # 89

Stage 1: Consolidation

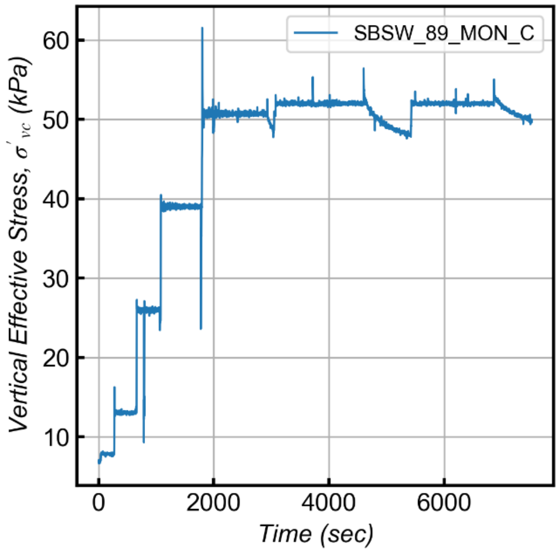

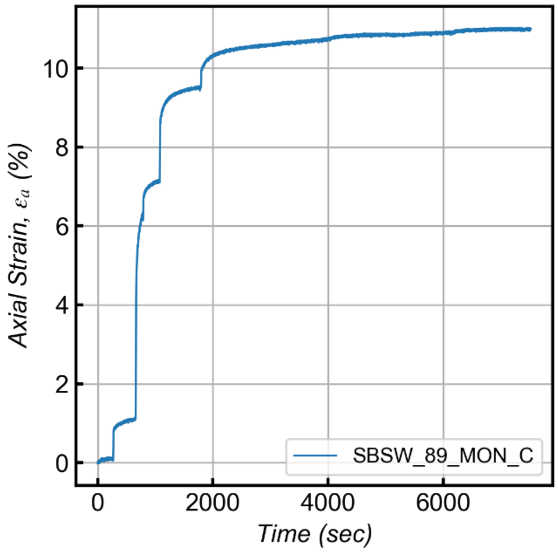

Stage 2: Monotonic Shear

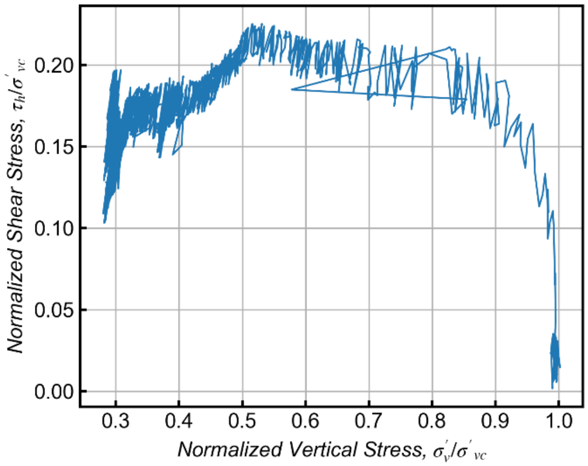

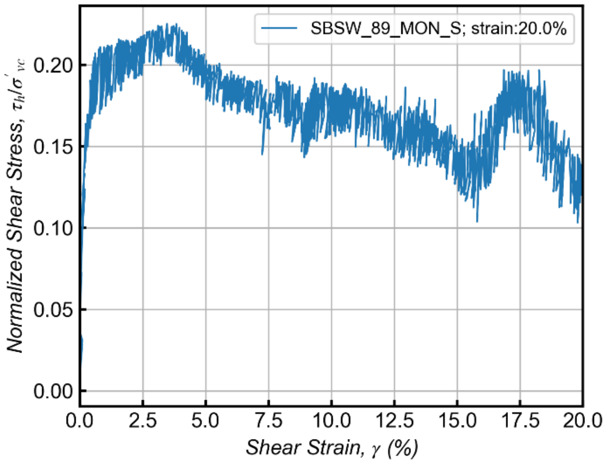

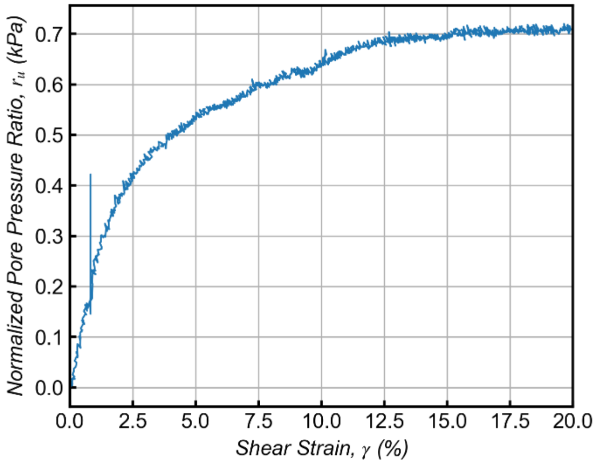

SKFW-Test # 68

Stage 1: Consolidation

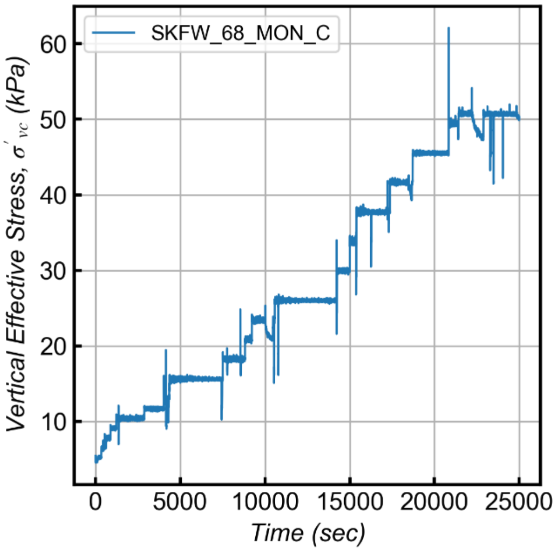

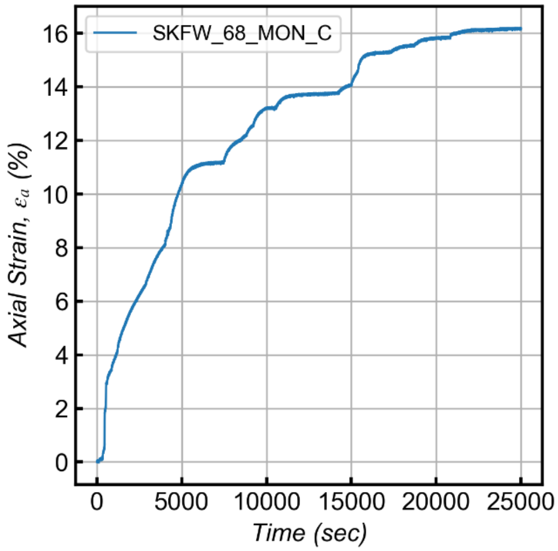

Stage 2: Monotonic Shear

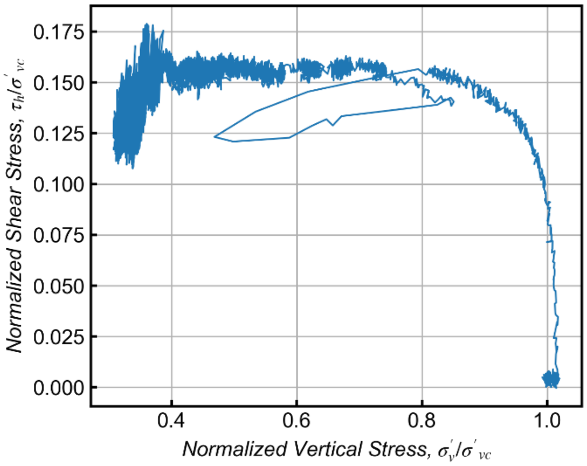

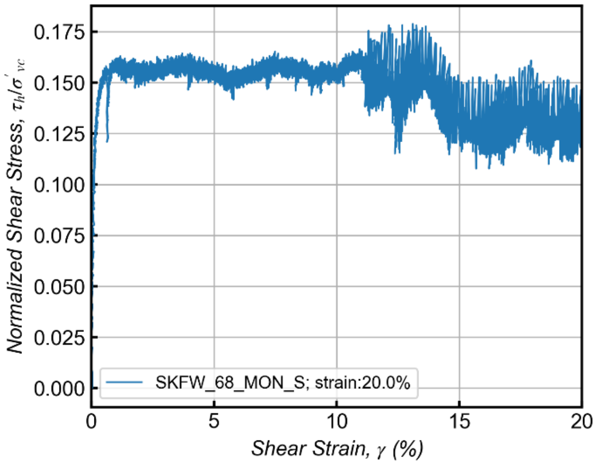

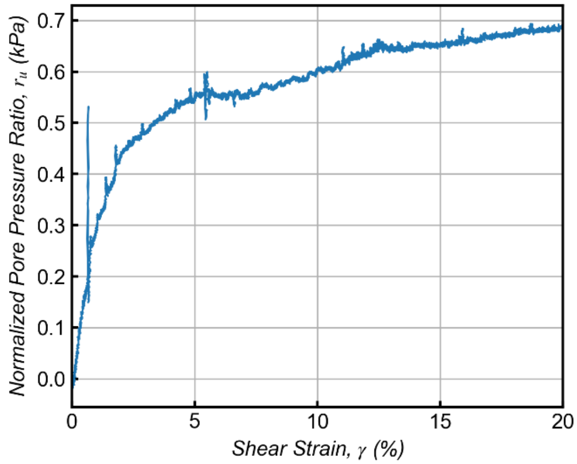

SKFW-Test # 69

Stage 1: Consolidation

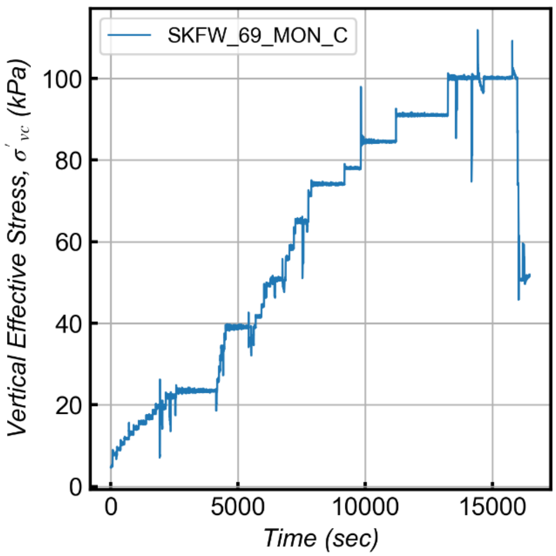

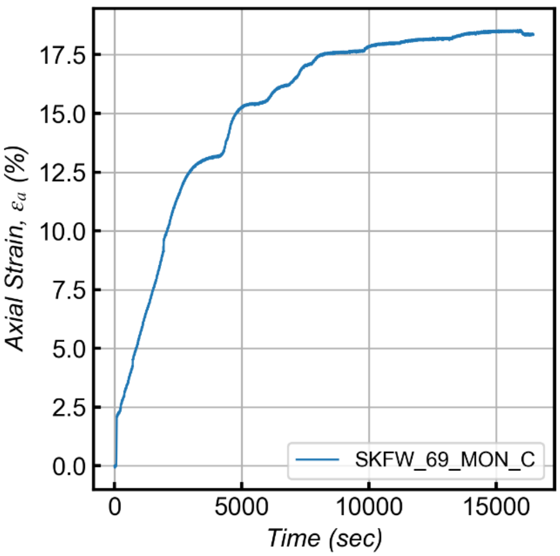

Stage 2: Monotonic Shear

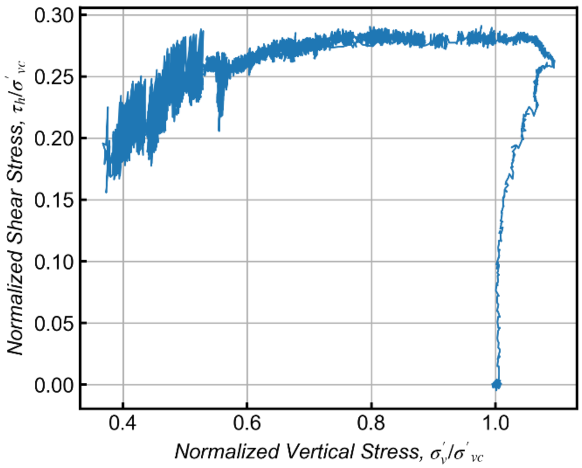

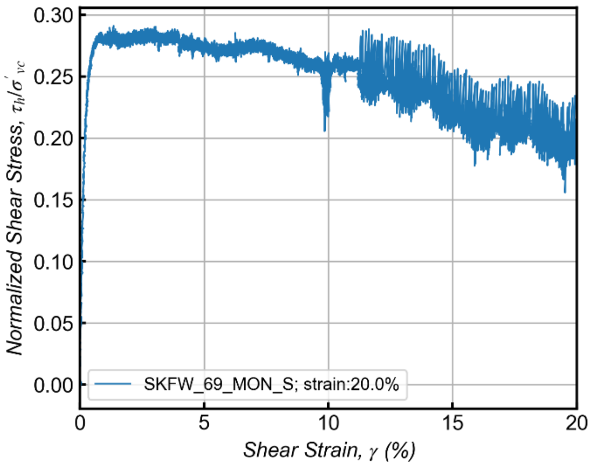

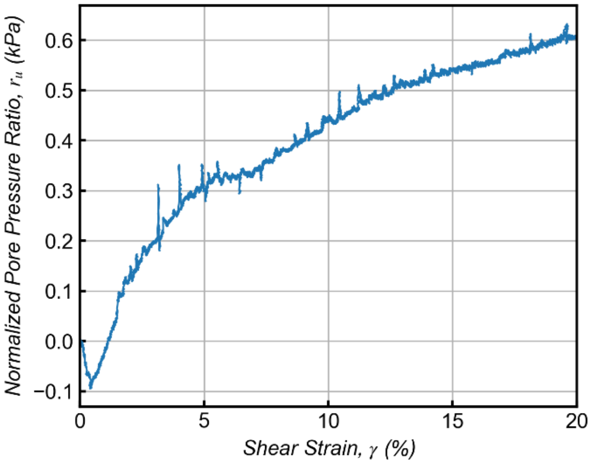

SKFW-Test # 70

Stage 1: Consolidation

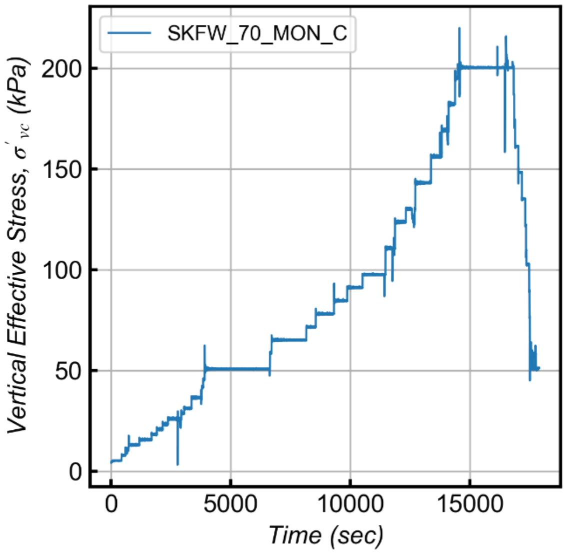

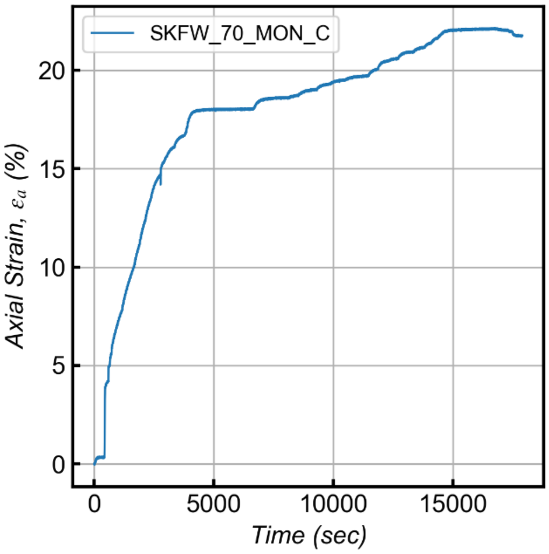

Stage 2: Monotonic Shear

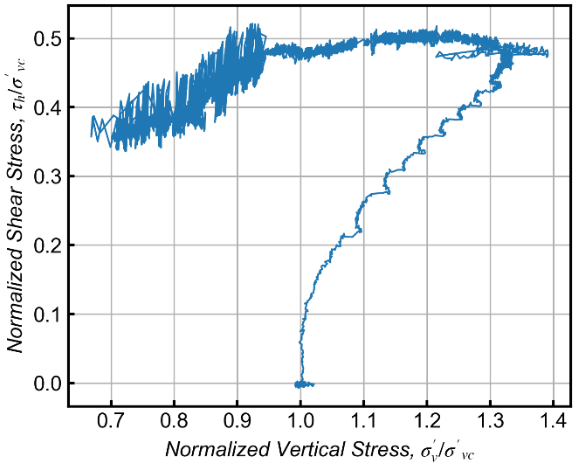

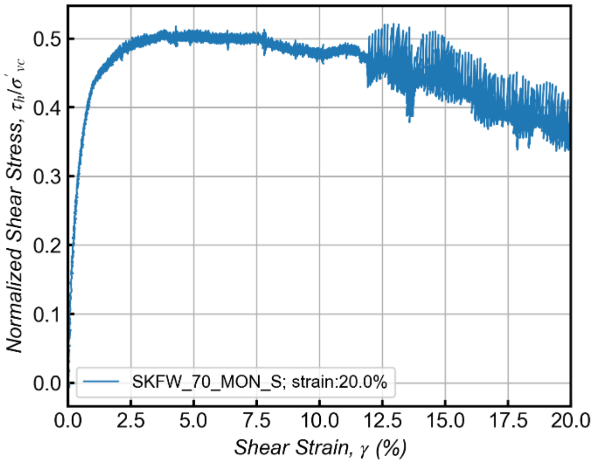

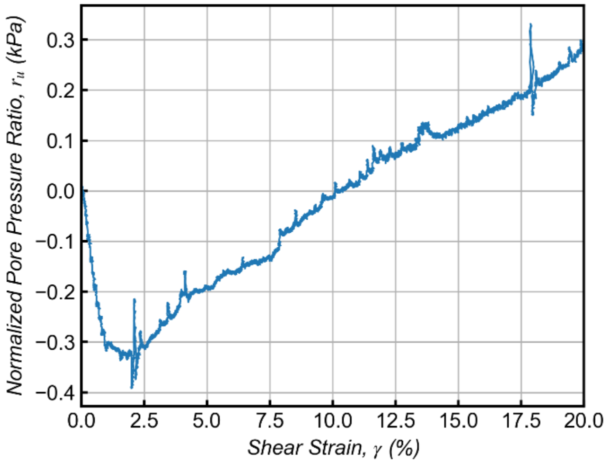

SKFW-Test # 71

Stage 1: Consolidation

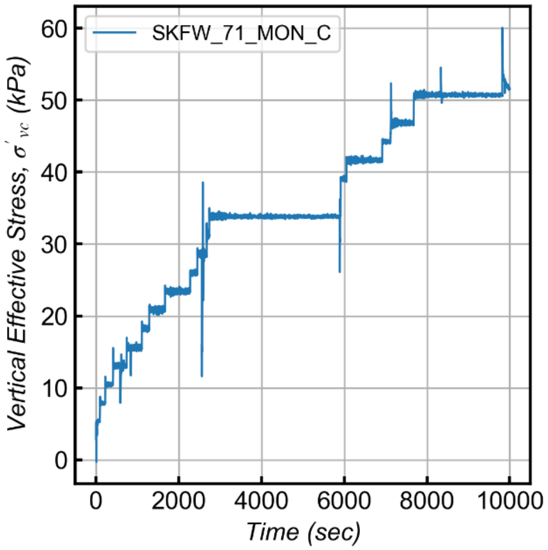

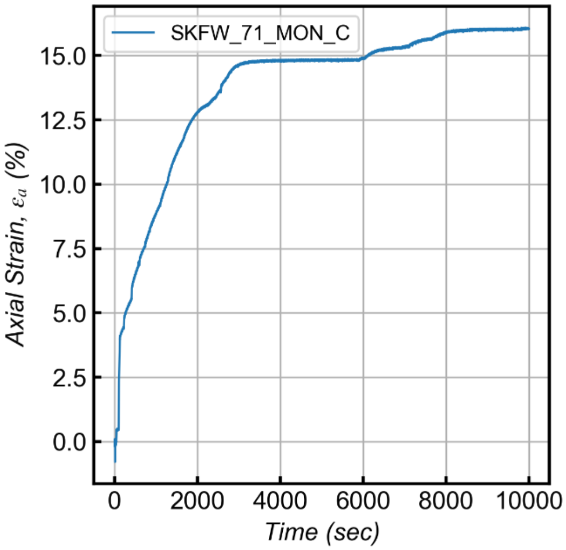

Stage 2: Monotonic Shear

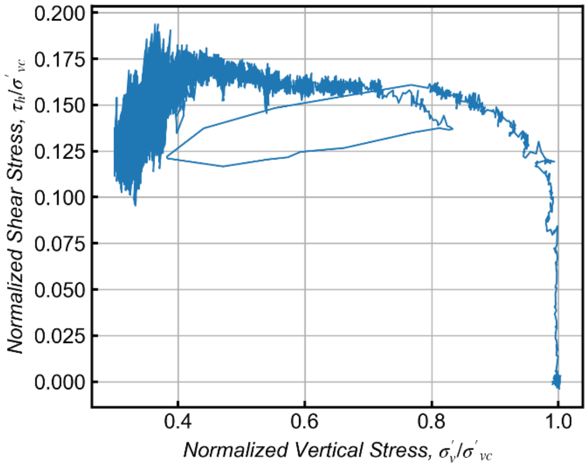

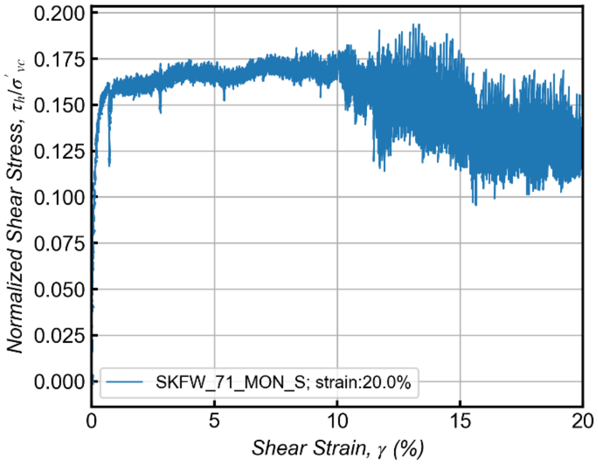

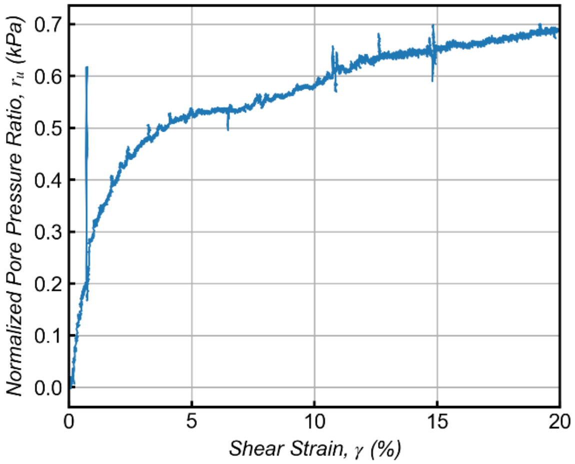

SKFW-Test # 81

Stage 1: Consolidation

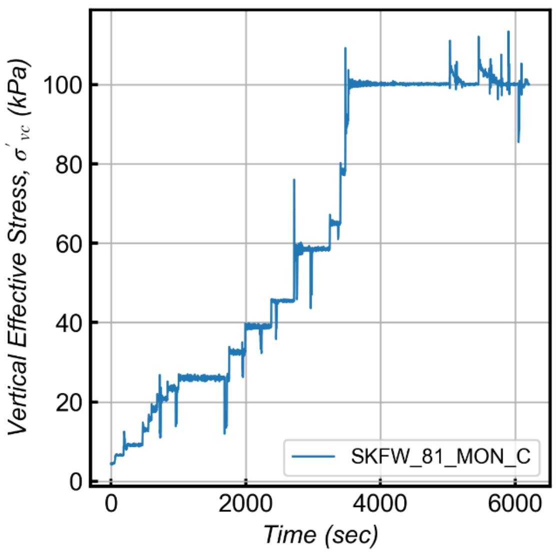

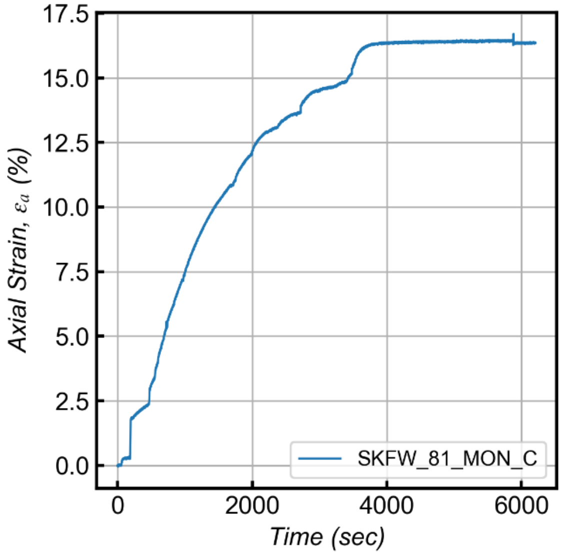

Stage 2: Monotonic Shear

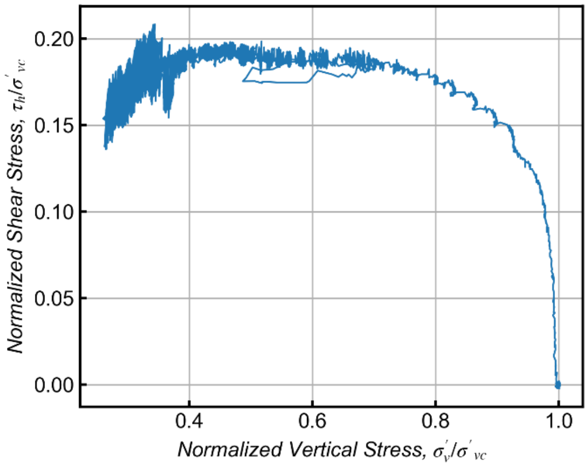

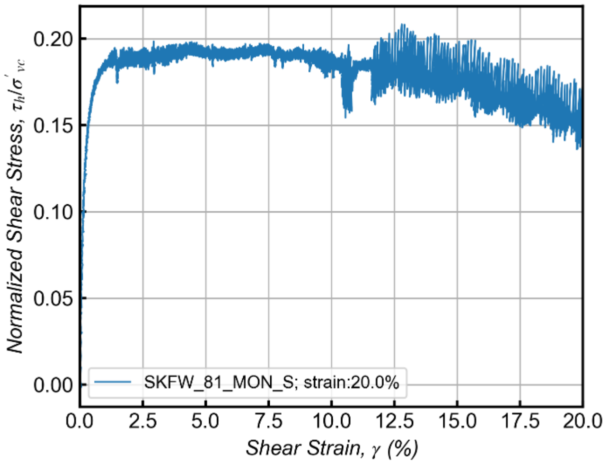

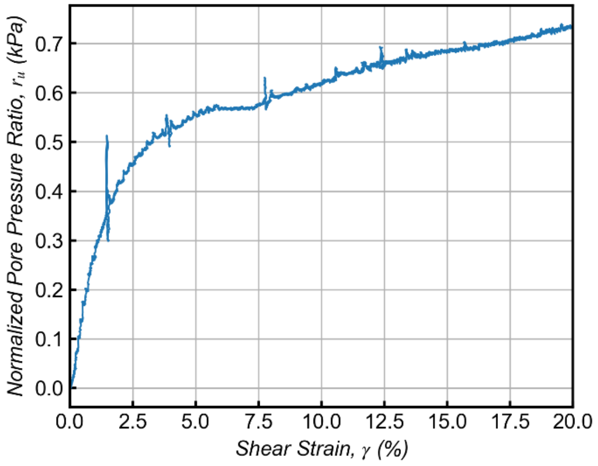

SKFW-Test # 82

Stage 1: Consolidation

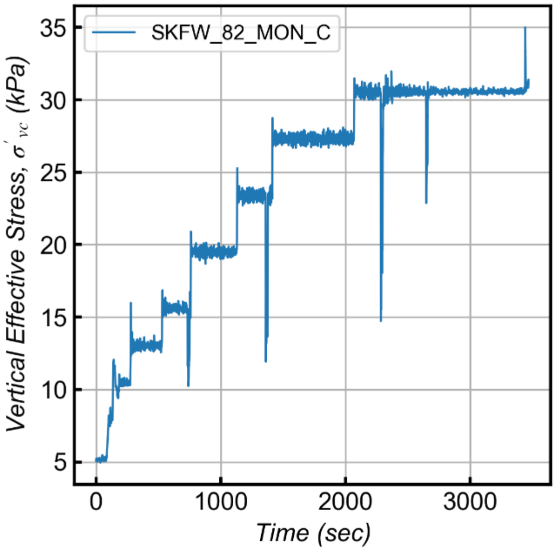

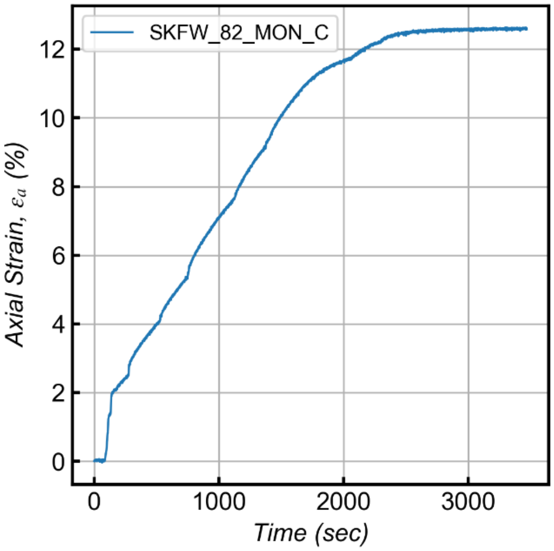

Stage 2: Monotonic Shear

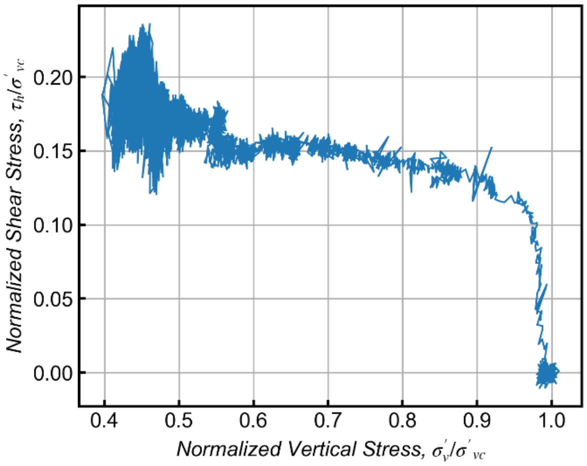

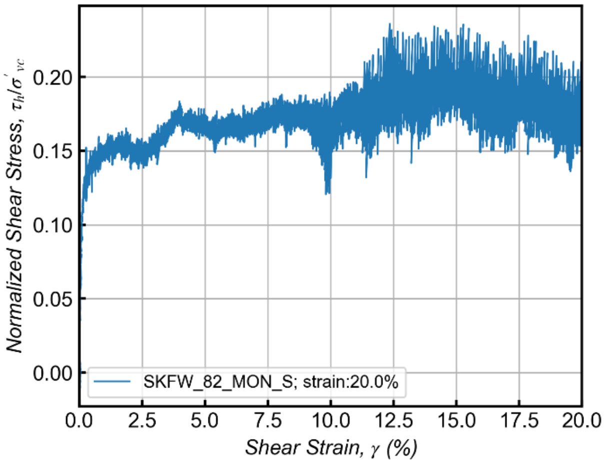

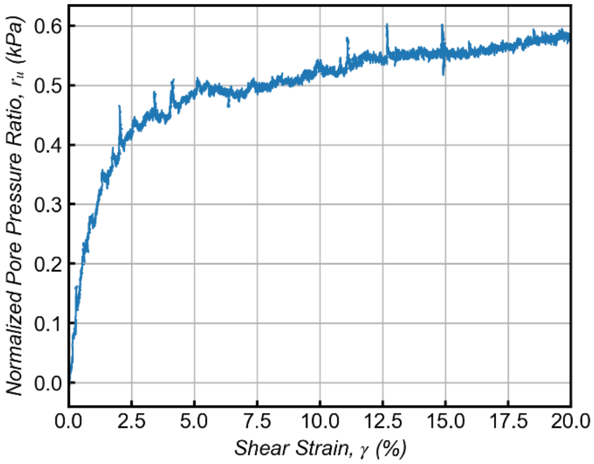

SKFW-Test # 83

Stage 1: Consolidation

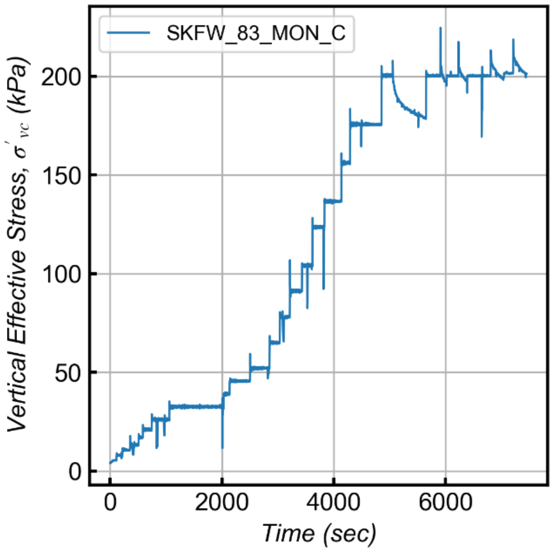

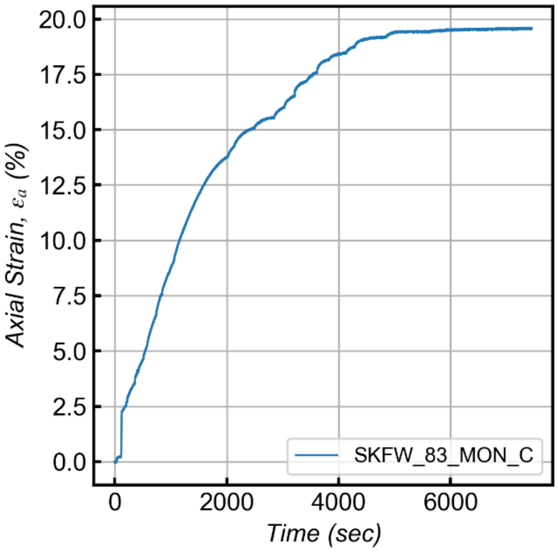

Stage 2: Monotonic Shear

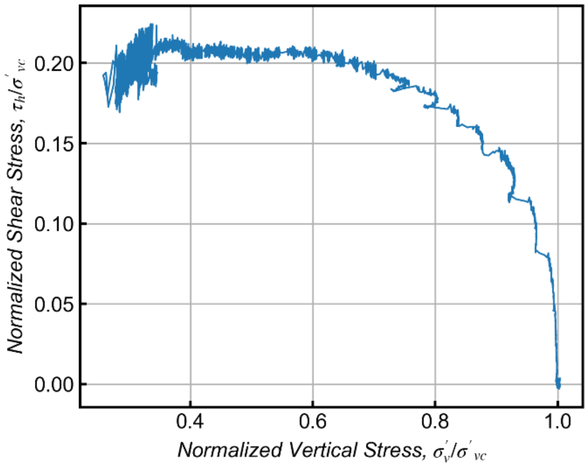

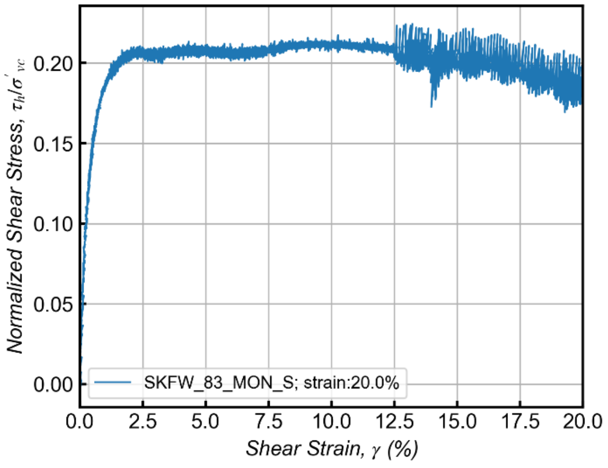

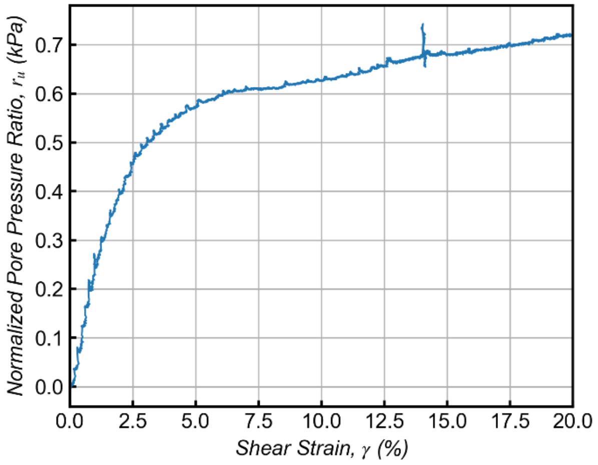

Appendix C: Cyclic Direct Simple Shear Test Results

The Table below provides metadata about the stress-controlled constant-height cyclic shear tests that were performed in this dissertation. The following pages in this Appendix provide measurements of stresses and strains for both consolidation and shearing stages of each experiment. The stress-strain curves, stress paths, as well as equivalent excess pore pressure ratio and shear strain versus number of uniform cycles are provided for each test and up to a shear strain of about 6%. All values are plotted in ratios normalized by the effective consolidation stress.

Note that the test results are presented in the order of the mixtures with SBFW first, followed by SBSW, and lastly SKFW mixtures.

Mixture	*Test ID*	*σ'_{vc} (kPa)*	*OCR*	*e_c**	*CSR*	*N***	*τ_{cyc}/s_u*
SBFW	Test36	50	1	0.915	0.149	13.3	0.700
	Test37	50	1	0.904	0.161	8.3	0.756
	Test38	50	1	0.896	0.18	3.6	0.845
	Test39	50	1	0.88	0.186	2.6	0.873
	Test40	50	1	0.875	0.137	17.1	0.643
	Test44	50	1	0.915	0.126	20.8	0.592
	Test45	50	1	0.904	0.115	67.1	0.540
	Test46	50	1	0.889	0.161	4.7	0.756
	Test56	50	2	0.832	0.174	76.7	0.497
	Test61	50	2	0.815	0.185	63.1	0.528
	Test62	50	2	0.801	0.199	33.7	0.568
	Test63	50	2	0.833	0.228	11.8	0.651
SBSW	Test33	50	1	0.85	0.213	3.5	0.930
	Test41	50	1	0.864	0.187	4.6	0.817
	Test42	50	1	0.856	0.161	8.4	0.703
	Test43	50	1	0.84	0.136	51.8	0.594
	Test48	50	1	0.855	0.141	13.1	0.616
	Test57	50	2	0.826	0.219	22.8	0.565
	Test58	50	2	0.83	0.201	33.8	0.519
	Test59	50	2	0.813	0.233	16	0.602
	Test60	50	2	0.794	0.279	3.7	0.720
SKFW	Test64	50	1	0.7	0.116	11.3	0.586
	Test65	50	1	0.682	0.098	38.2	0.495
	Test66	50	1	0.717	0.124	9.8	0.626
	Test67	50	1	0.699	0.141	3.3	0.712
	Test72	50	2	0.674	0.17	51.7	0.569
	Test74	50	2	0.65	0.192	17.3	0.642
	Test75	50	2	0.638	0.214	13.7	0.716
	Test76	50	2	0.628	0.249	7.4	0.833
	Test78	50	2	0.661	0.26	4.1	0.870

**e_c: post-consolidation void ratio*

***N: number of uniform cycles to reach 3% peak shear strain*

SBFW-Test # 36

Stage 1: Consolidation

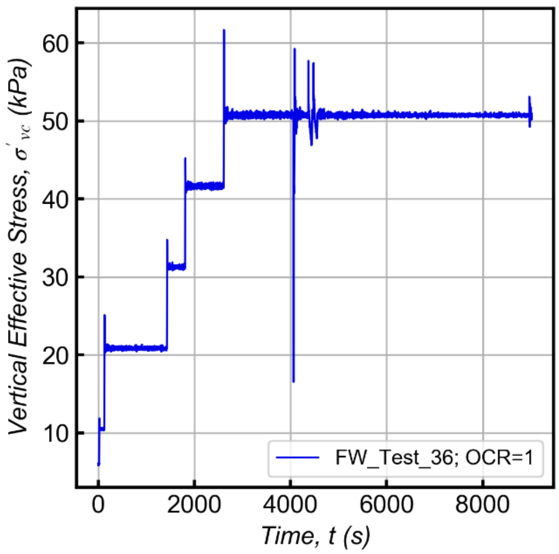

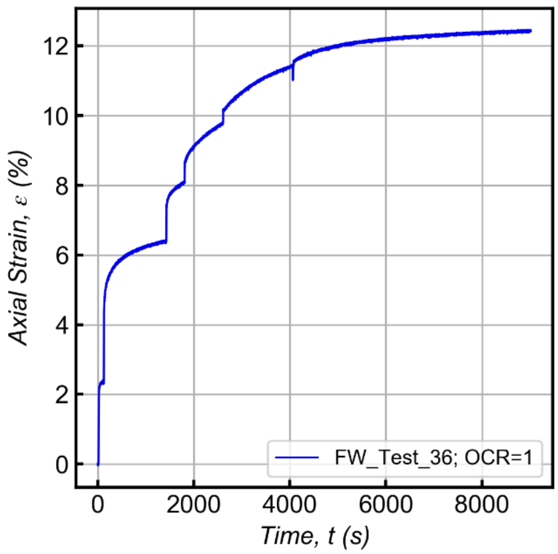

Stage 2: Cyclic Shear

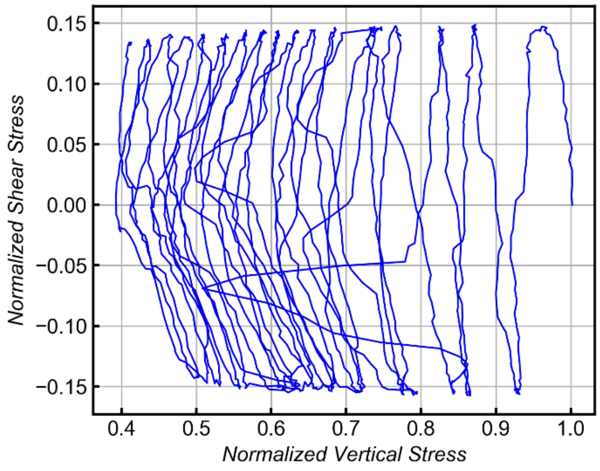

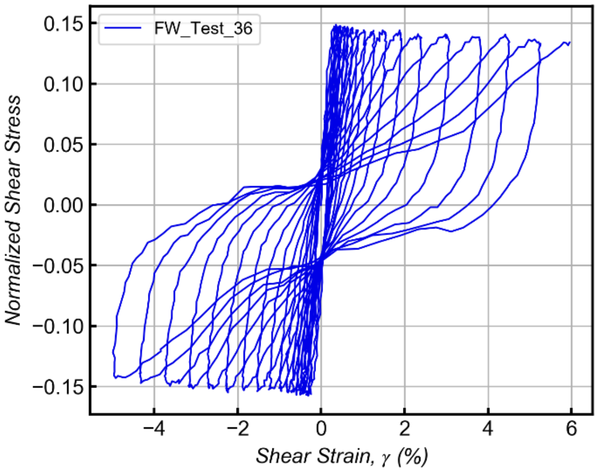

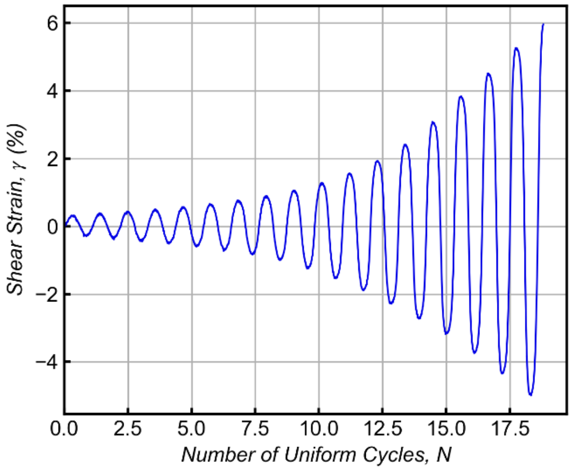

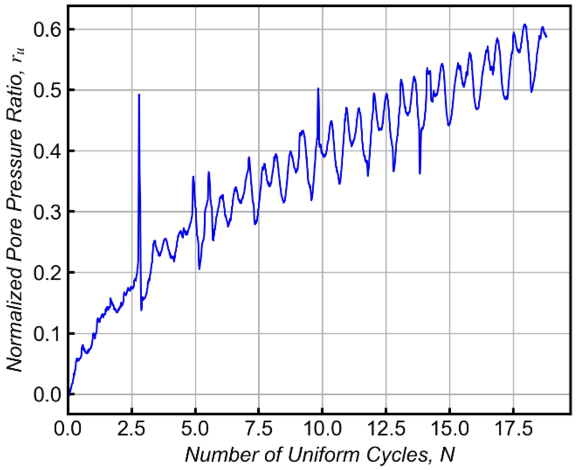

SBFW-Test # 37

Stage 1: Consolidation

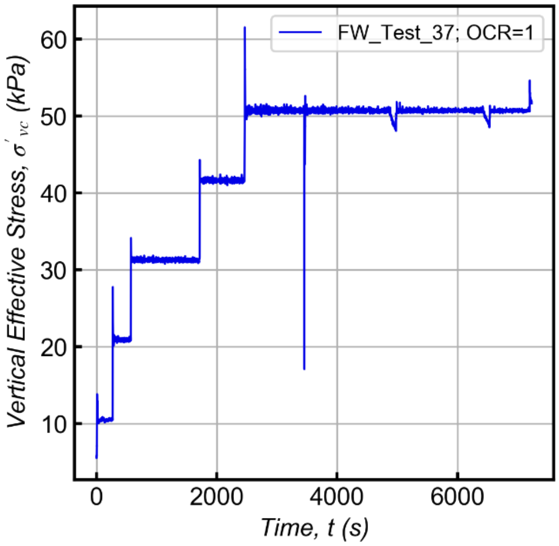

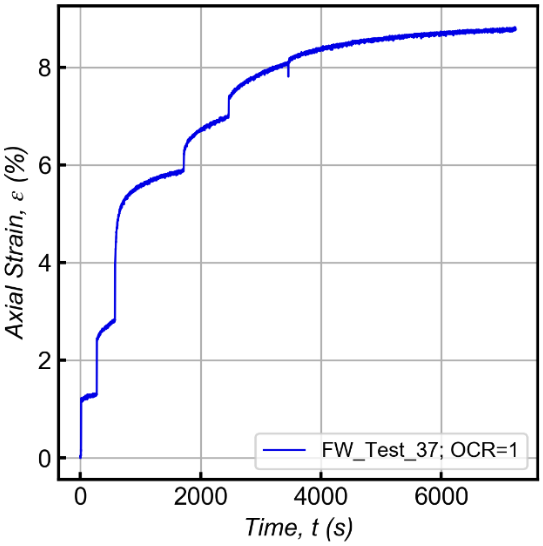

Stage 2: Cyclic Shear

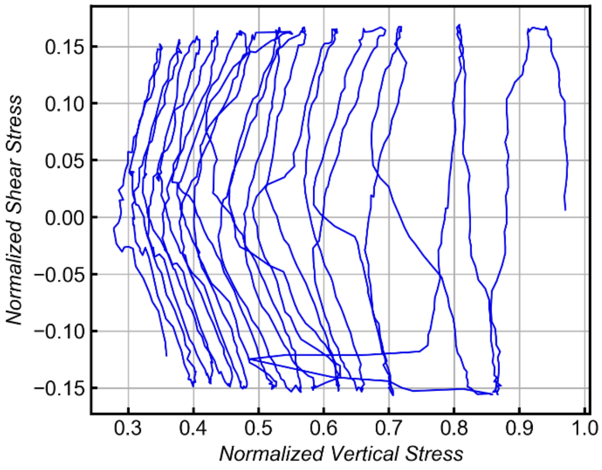

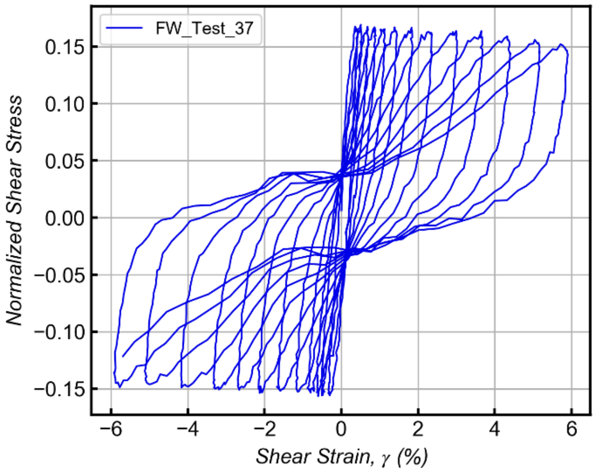

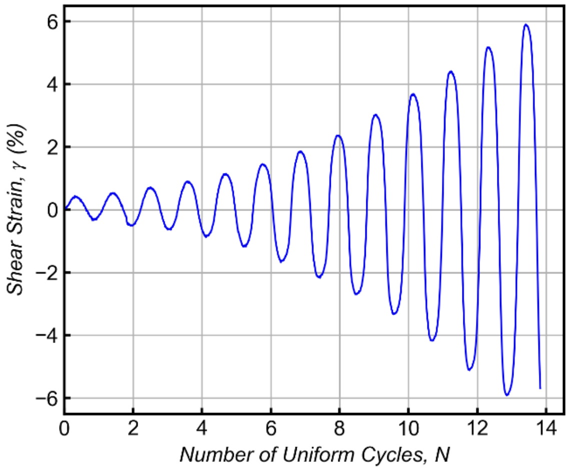

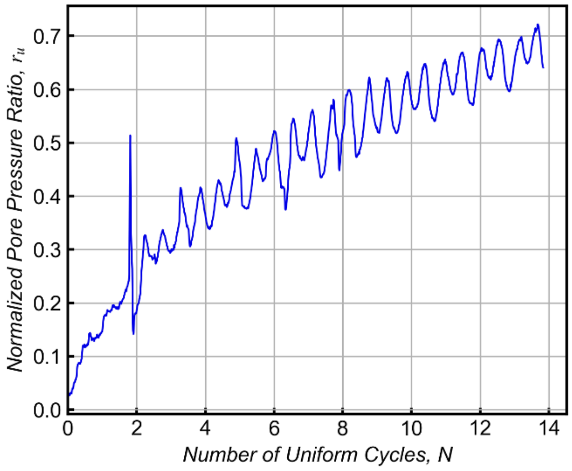

SBFW-Test # 38

Stage 1: Consolidation

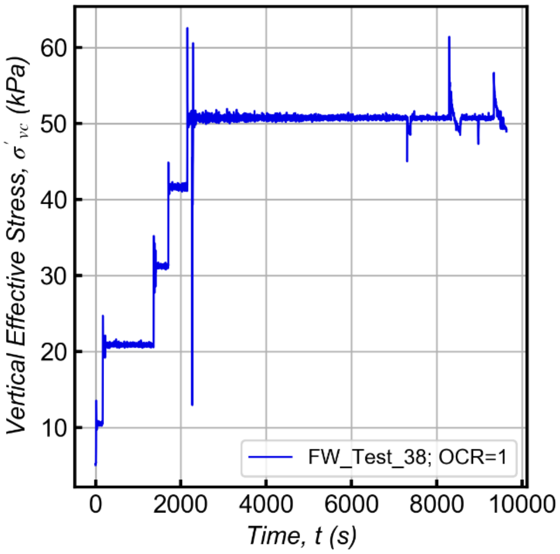

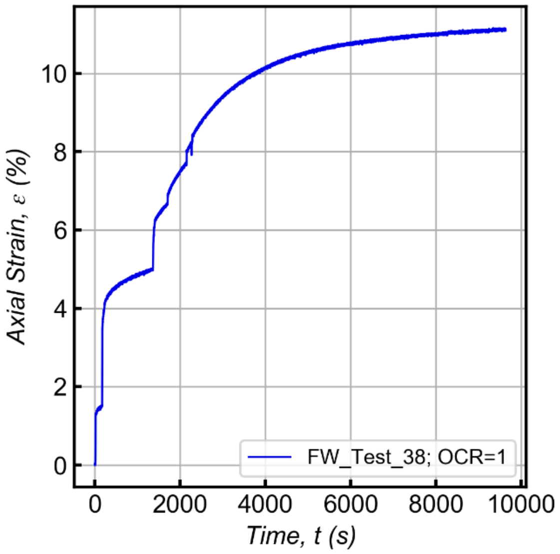

Stage 2: Cyclic Shear

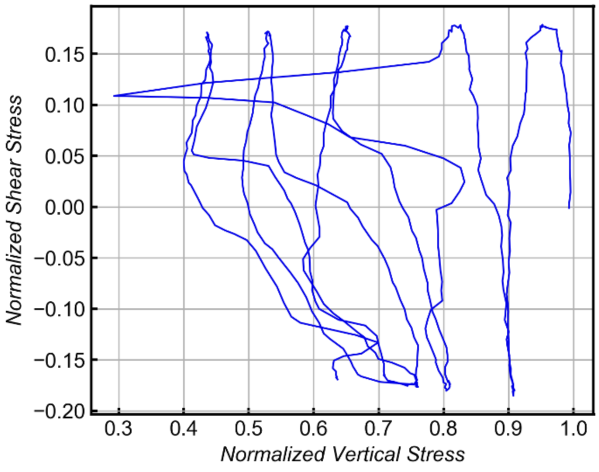

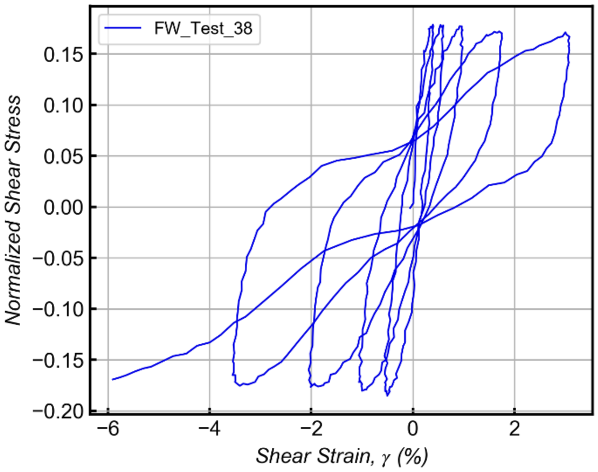

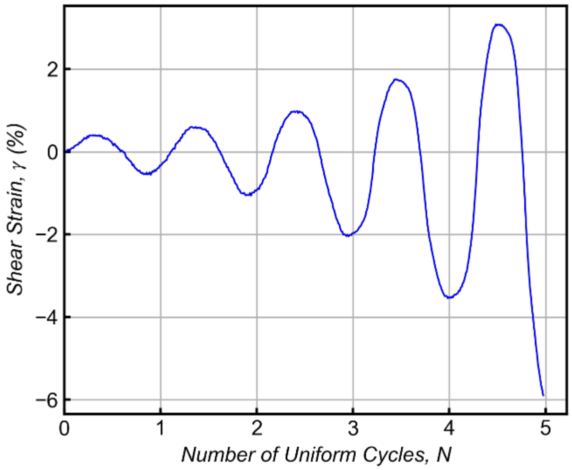

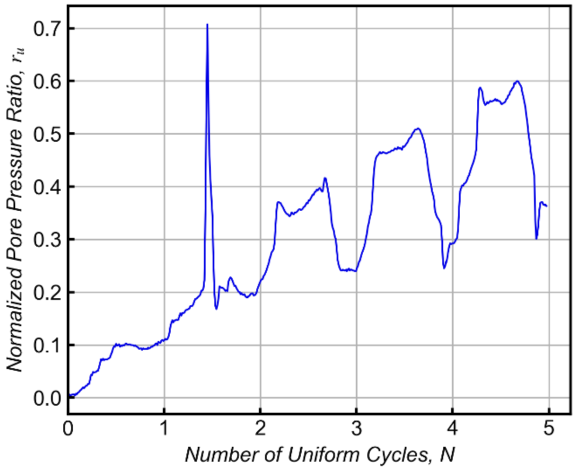

SBFW-Test # 39

Stage 1: Consolidation

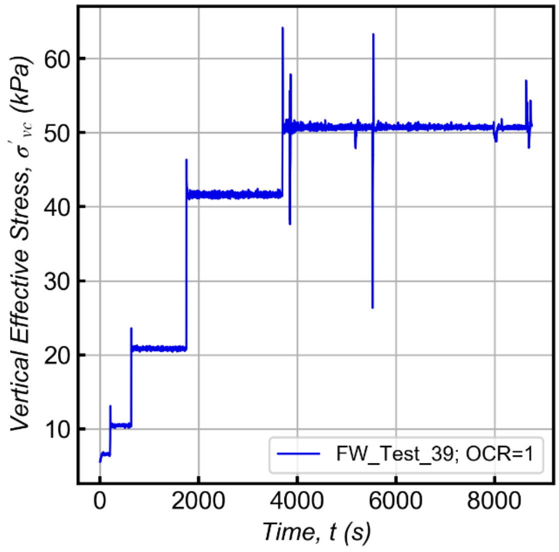

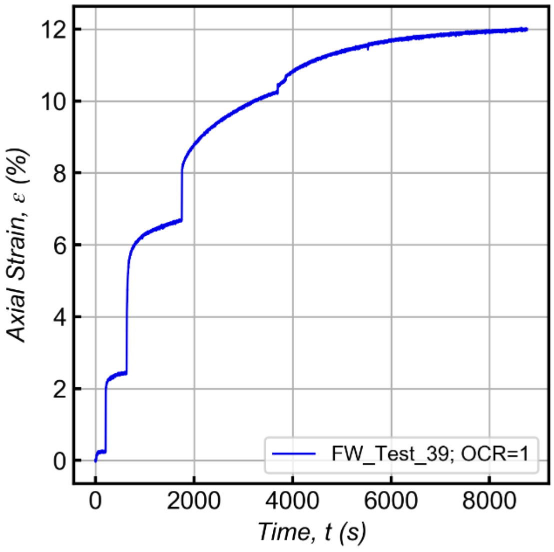

Stage 2: Cyclic Shear

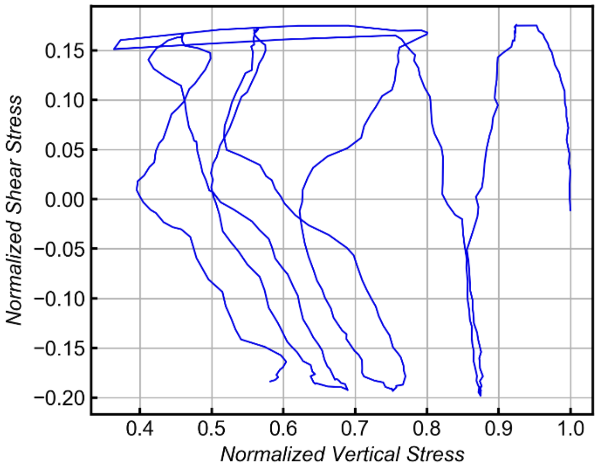

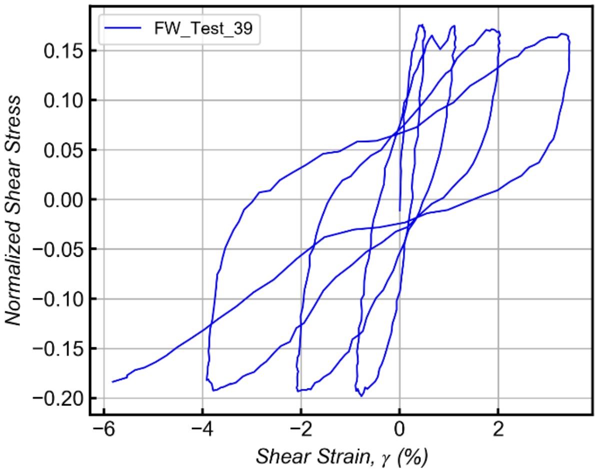

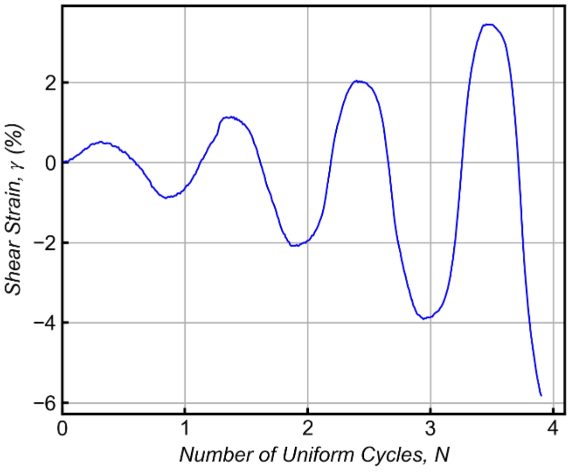

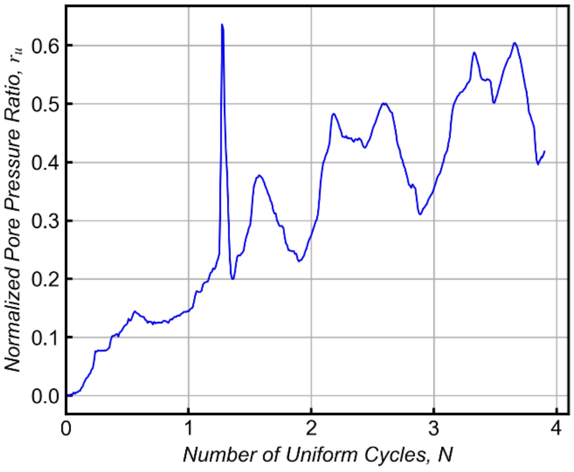

SBFW-Test # 40

Stage 1: Consolidation

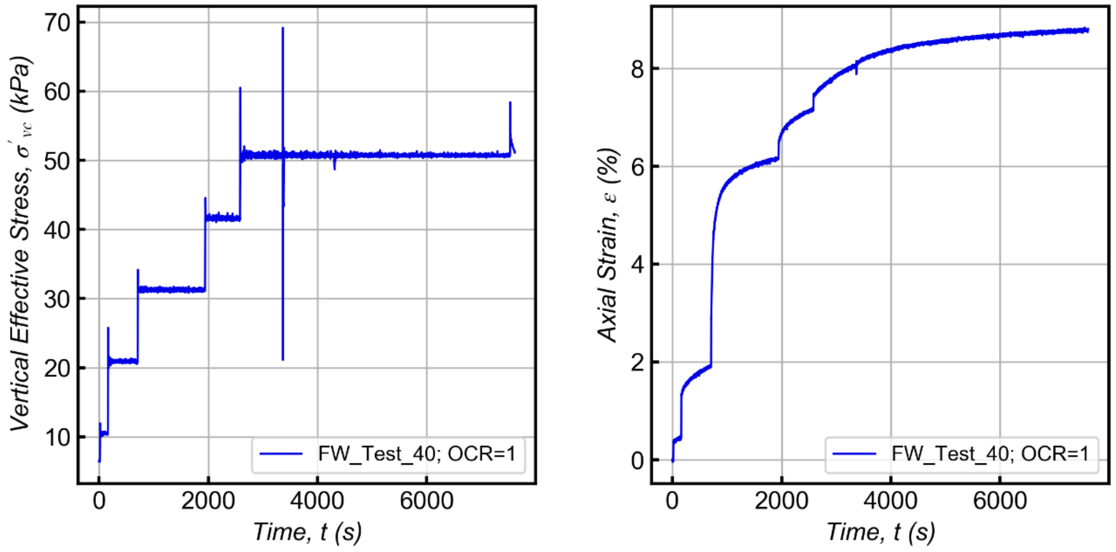

Stage 2: Cyclic Shear

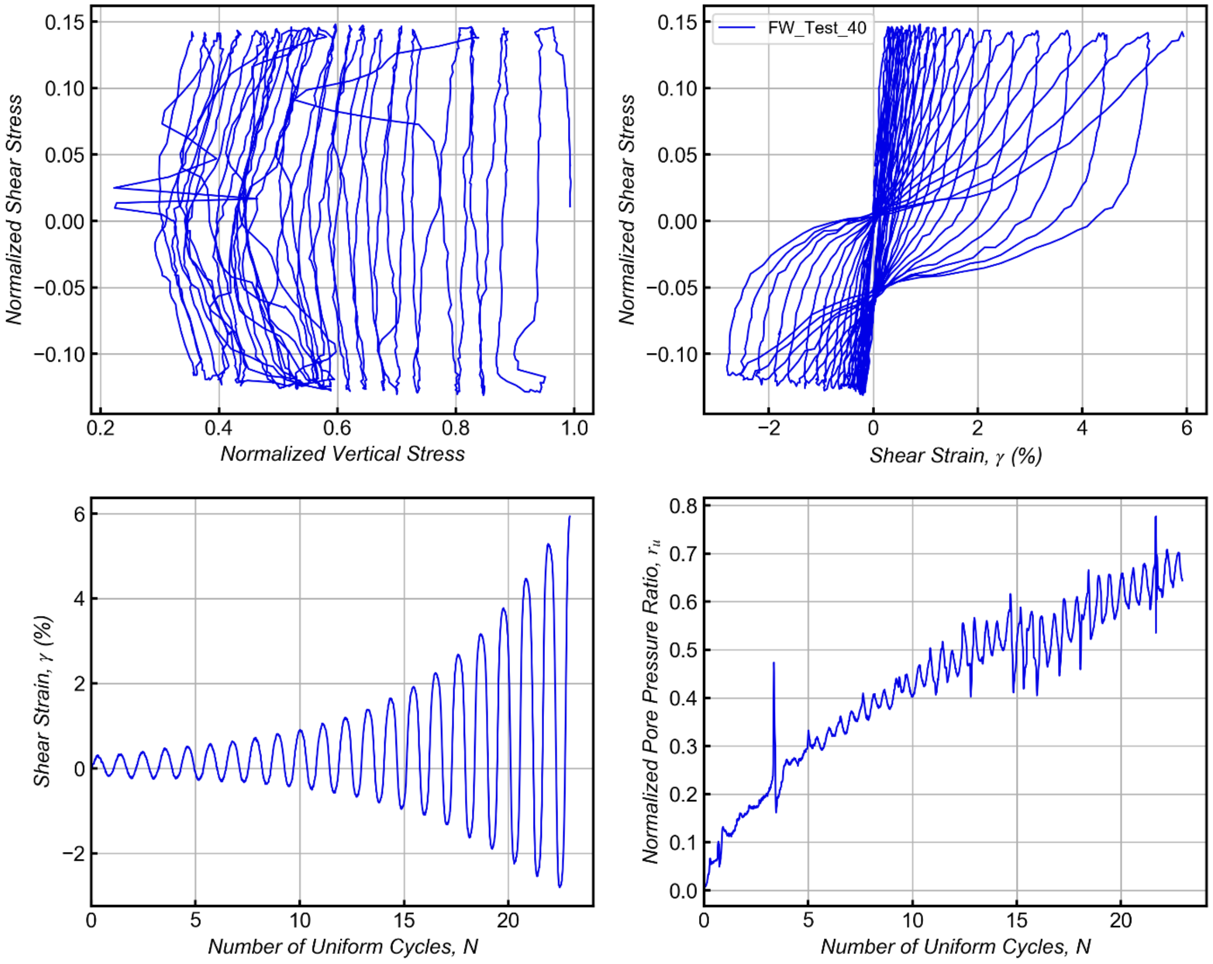

SBFW-Test # 44

Stage 1: Consolidation

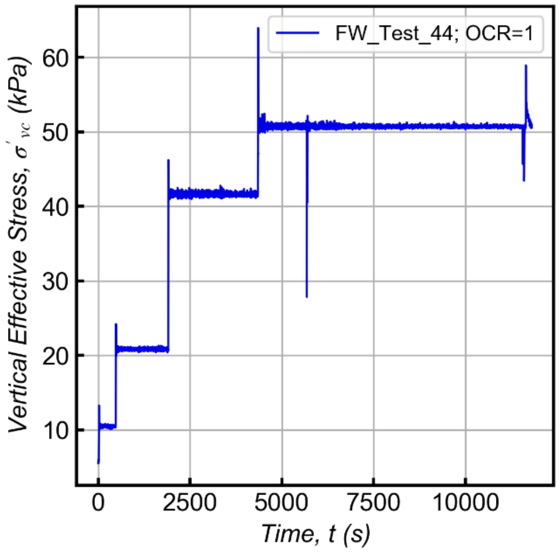

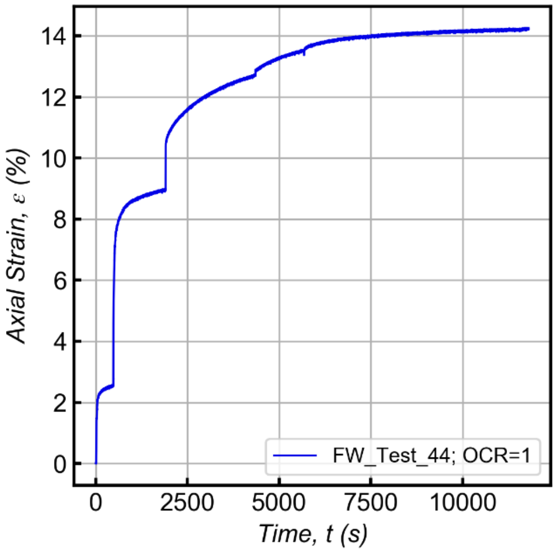

Stage 2: Cyclic Shear

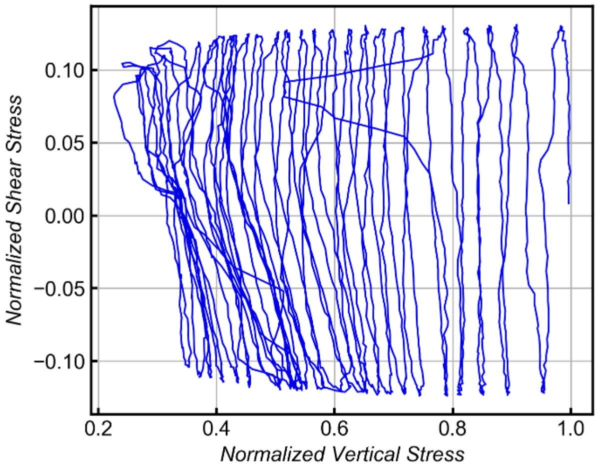

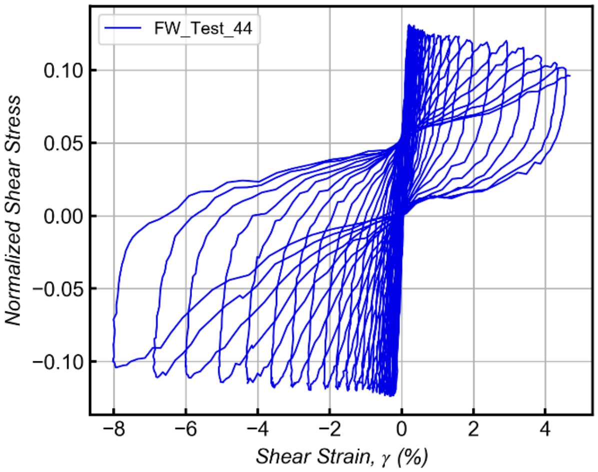

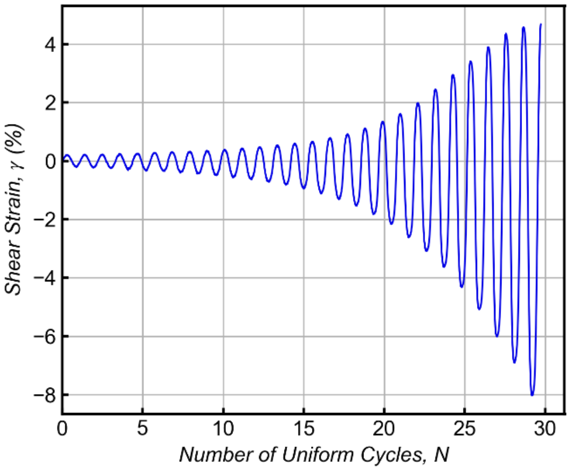

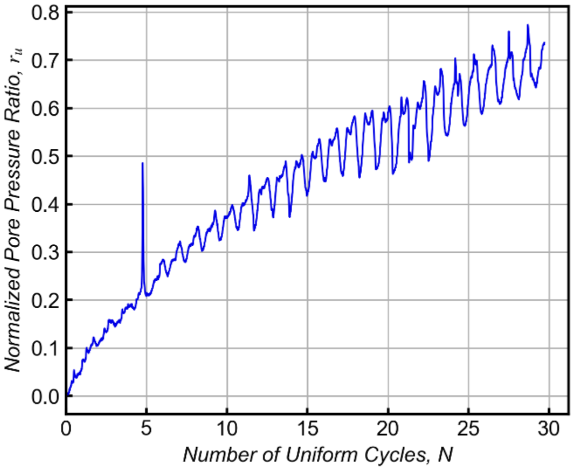

SBFW-Test # 45

Stage 1: Consolidation

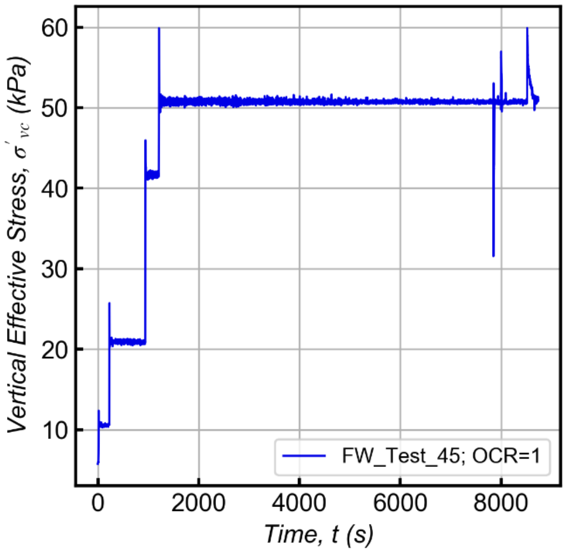

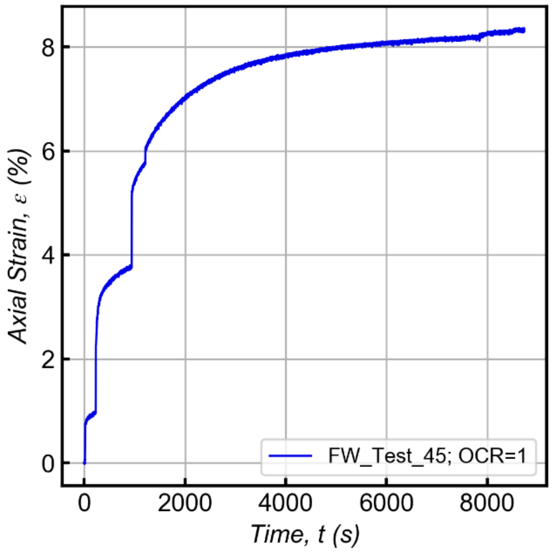

Stage 2: Cyclic Shear

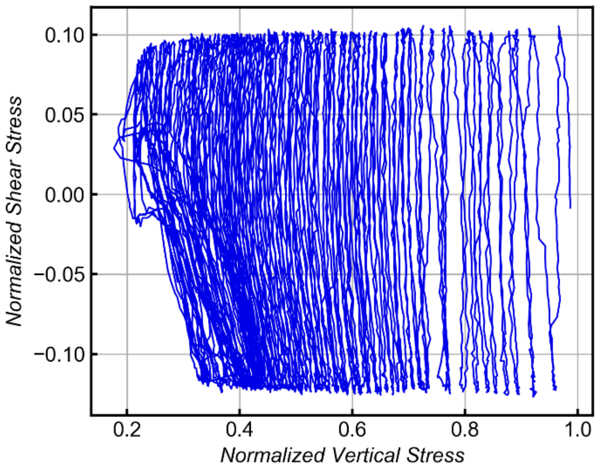

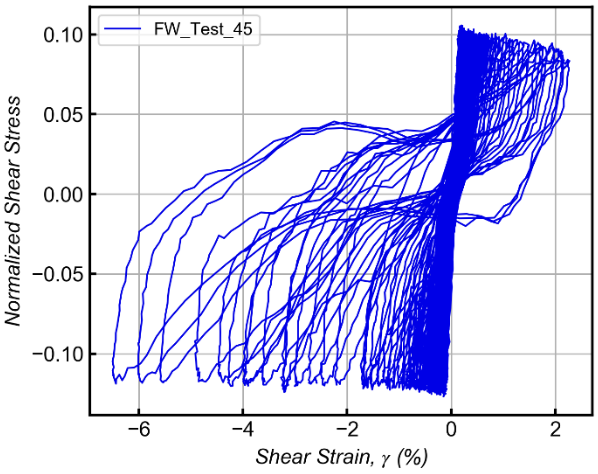

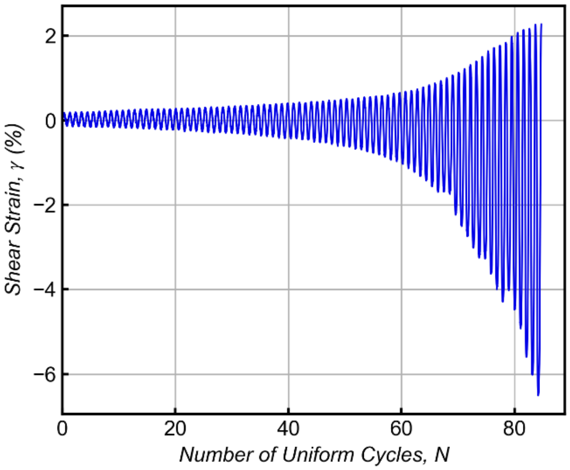

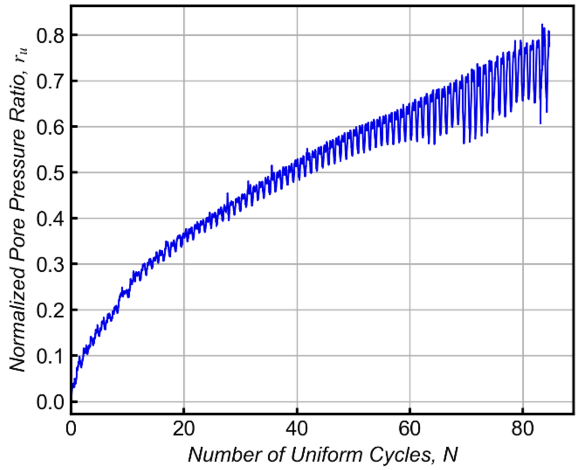

SBFW-Test # 46

Stage 1: Consolidation

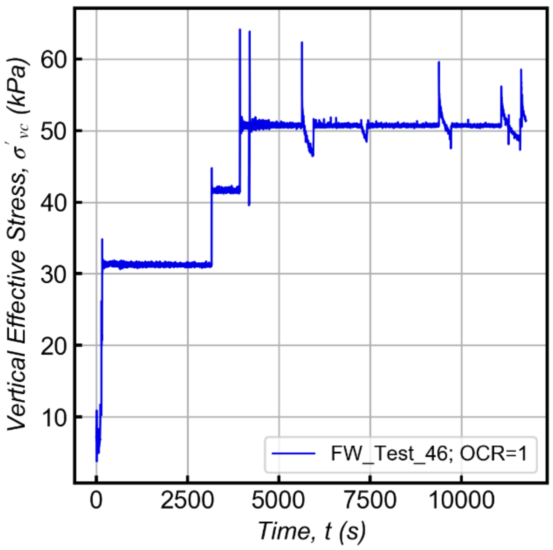

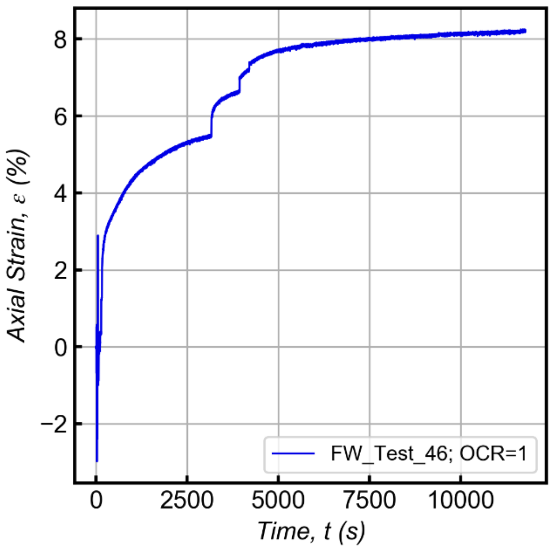

Stage 2: Cyclic Shear

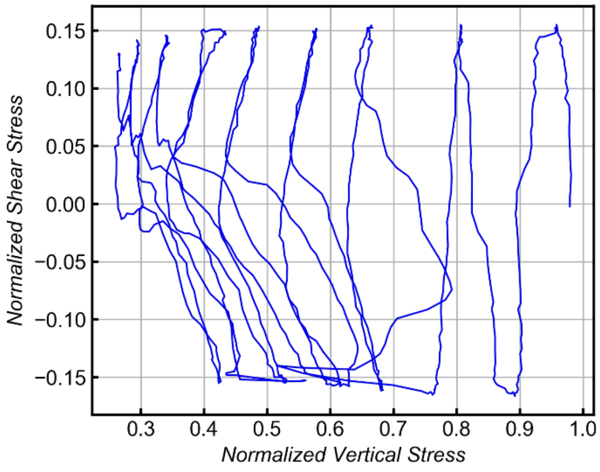

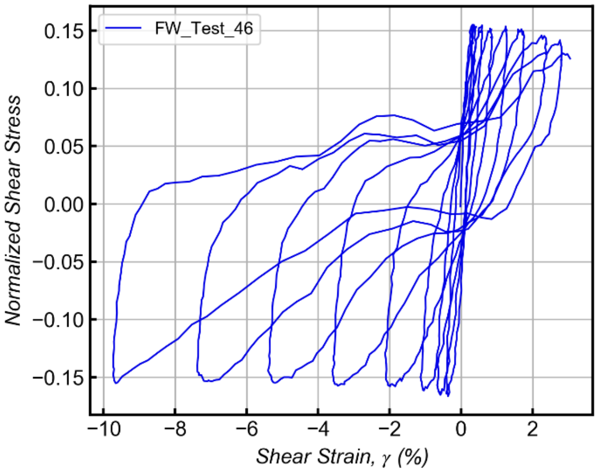

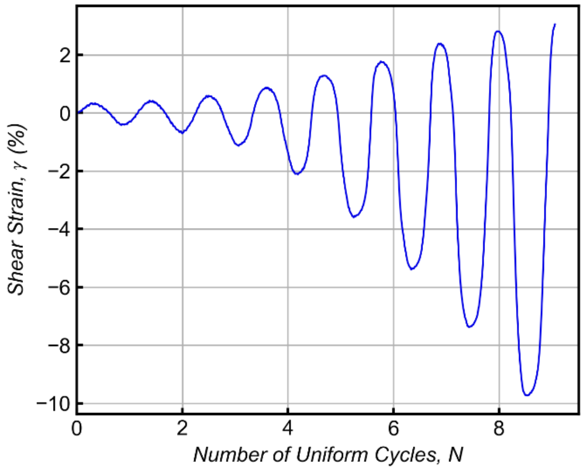

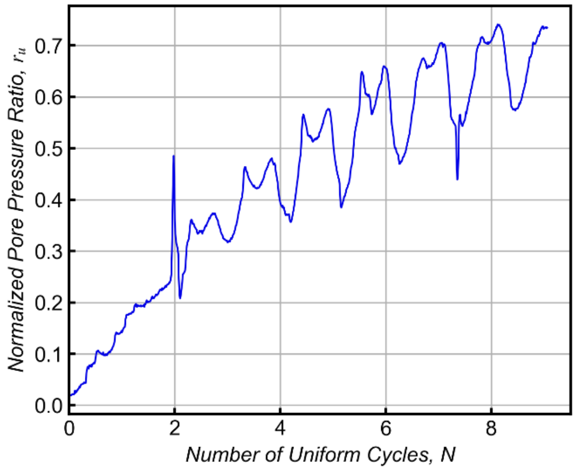

SBFW-Test # 56

Stage 1: Consolidation

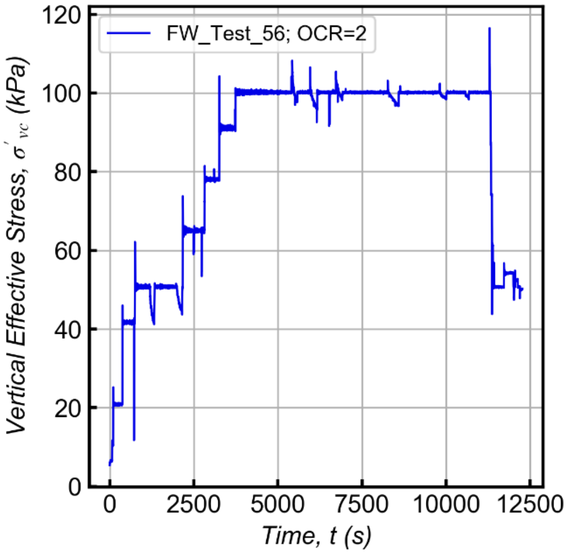

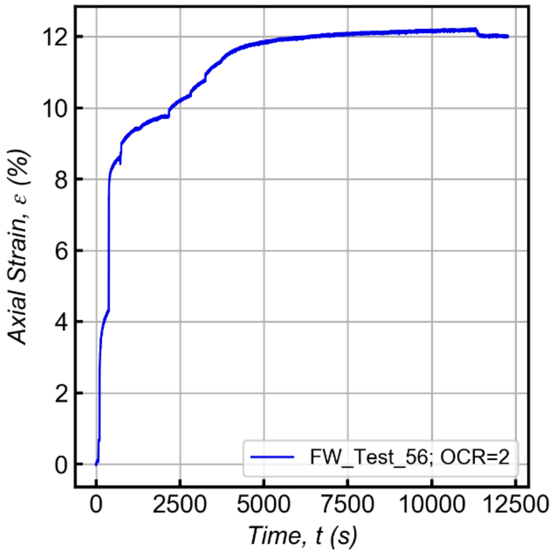

Stage 2: Cyclic Shear

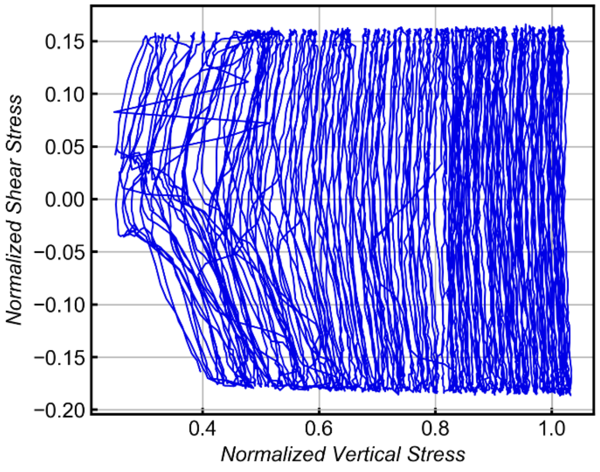

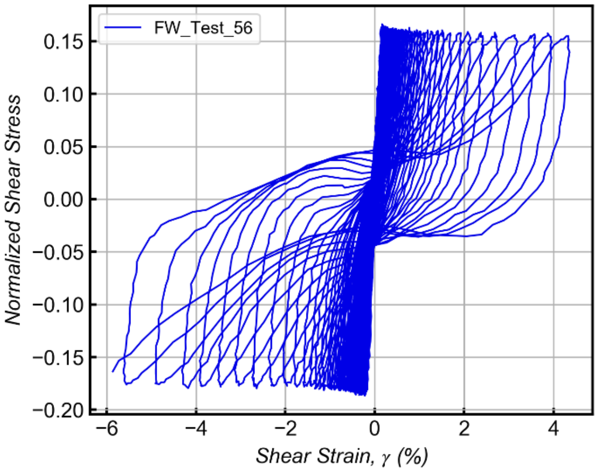

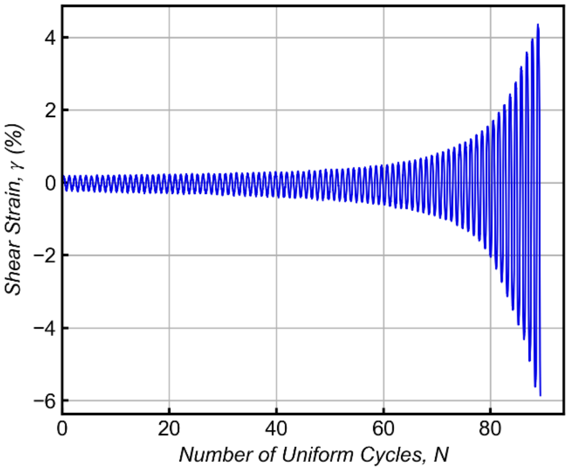

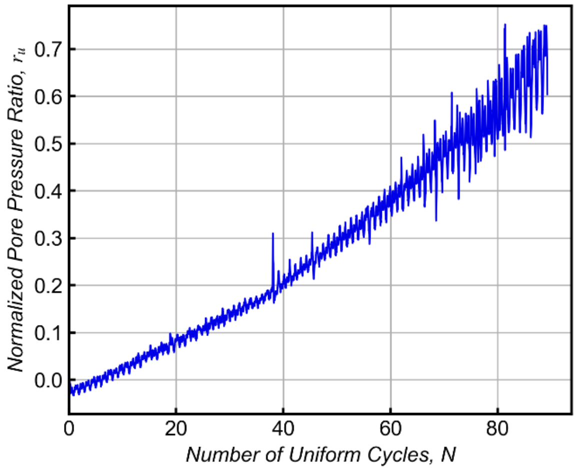

<u>SBFW-Test # 61</u>

Stage 1: Consolidation

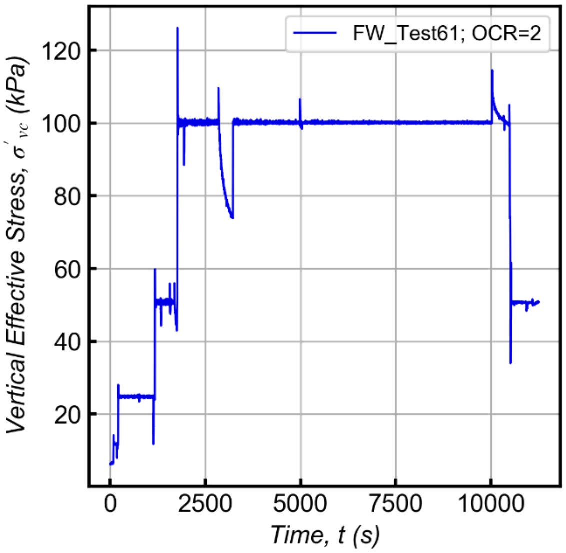

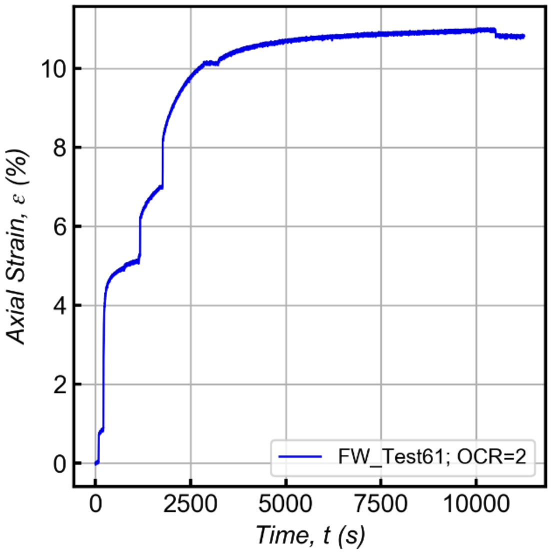

Stage 2: Cyclic Shear

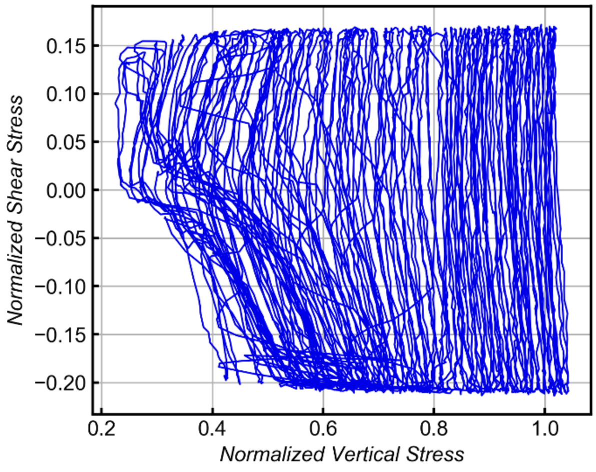

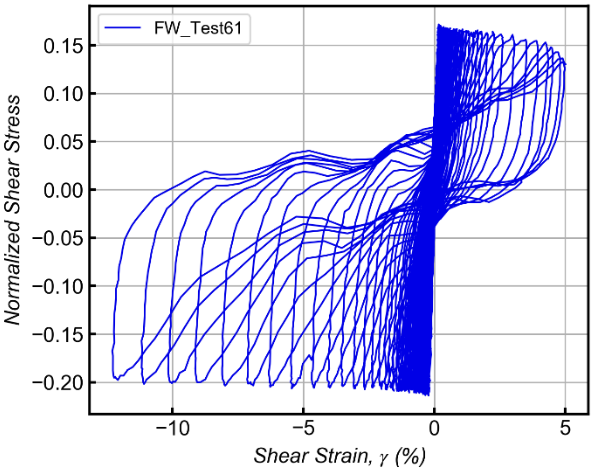

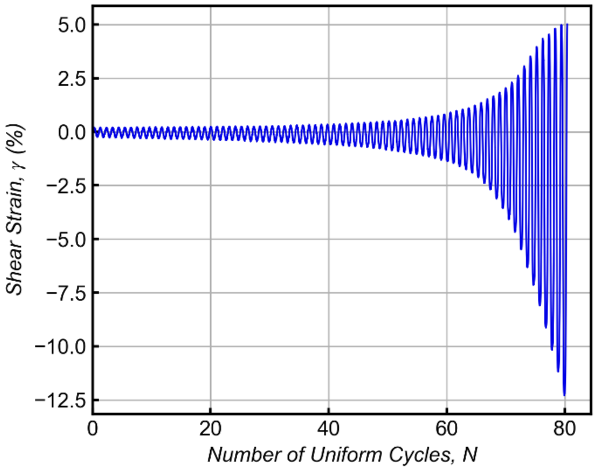

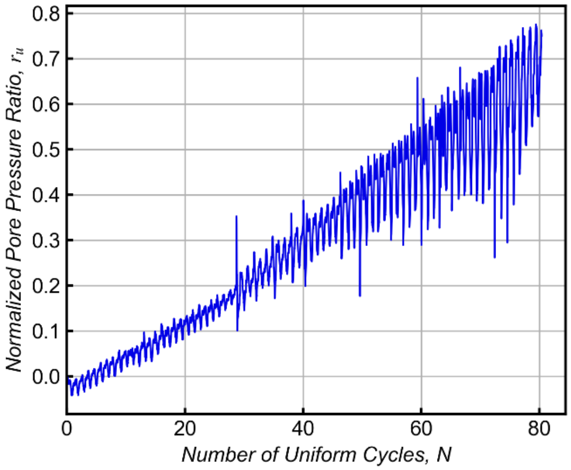

SBFW-Test # 62

Stage 1: Consolidation

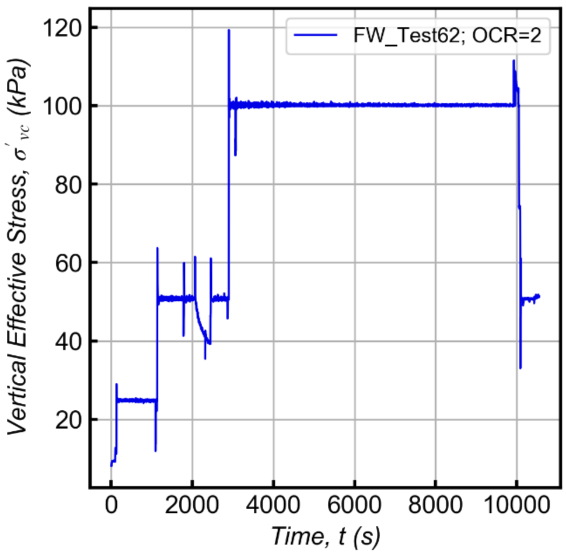

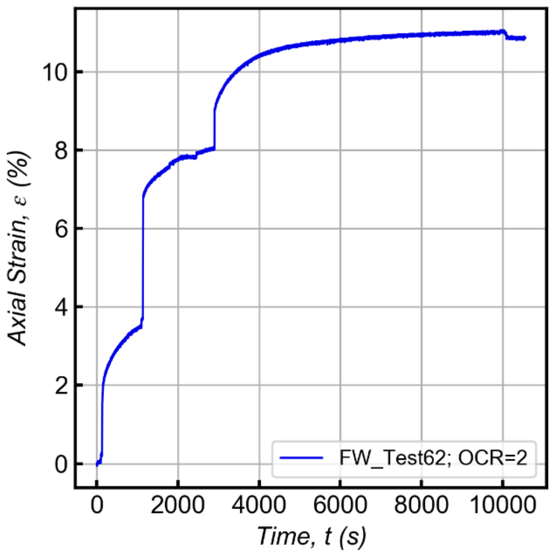

Stage 2: Cyclic Shear

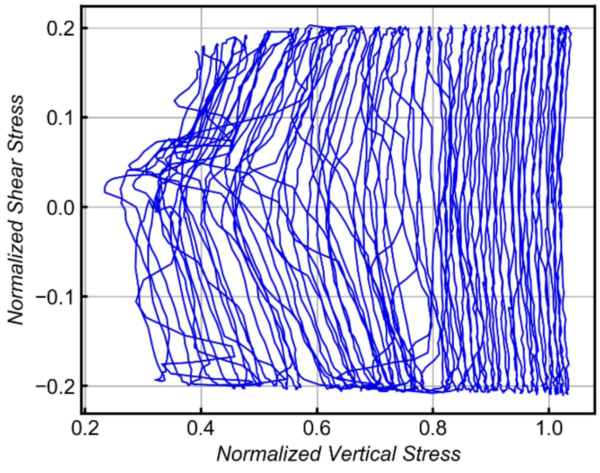

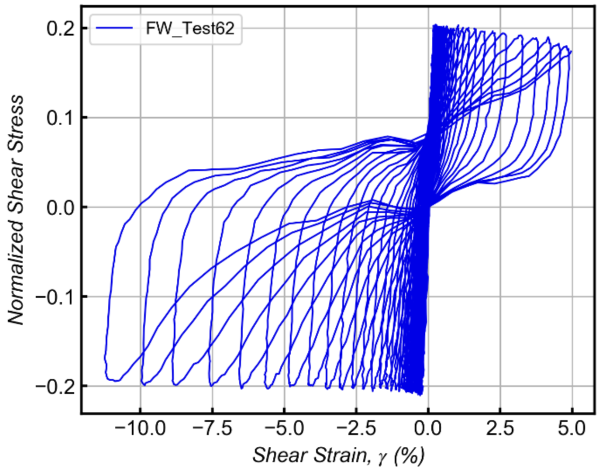

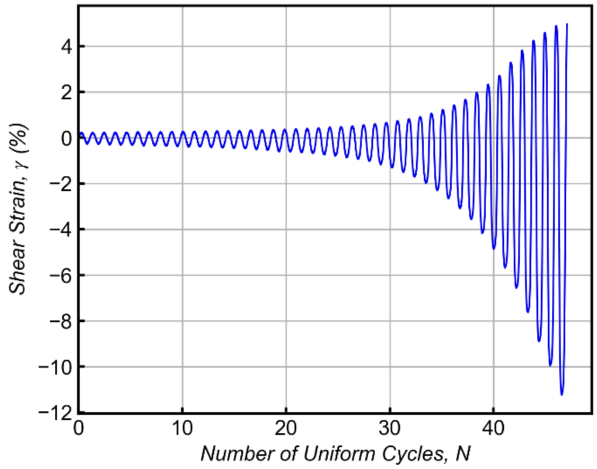

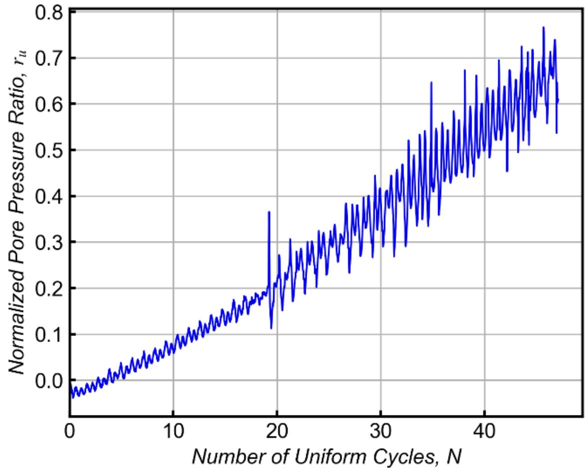

SBFW-Test # 63

Stage 1: Consolidation

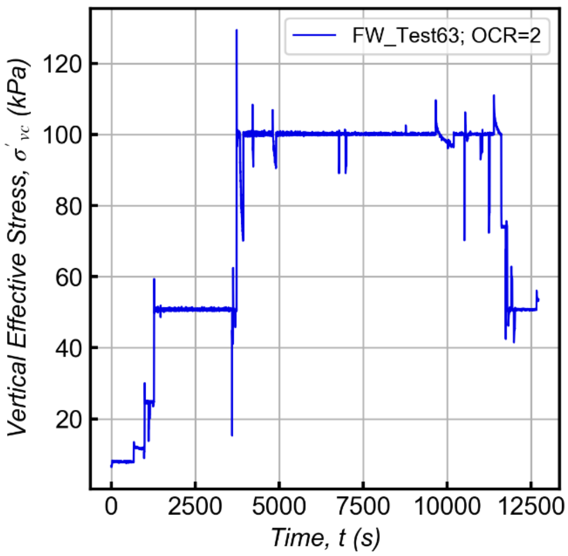

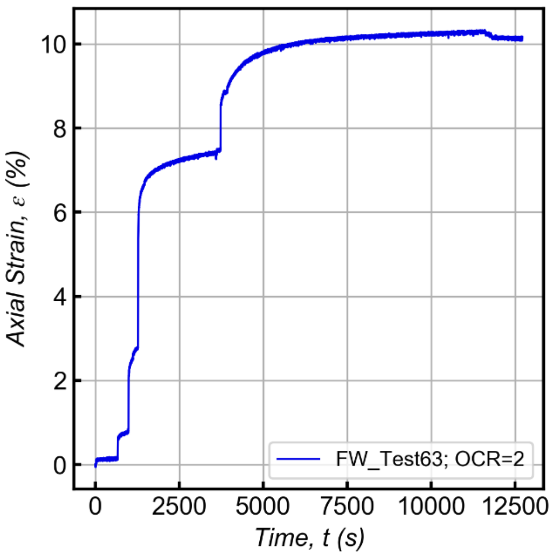

Stage 2: Cyclic Shear

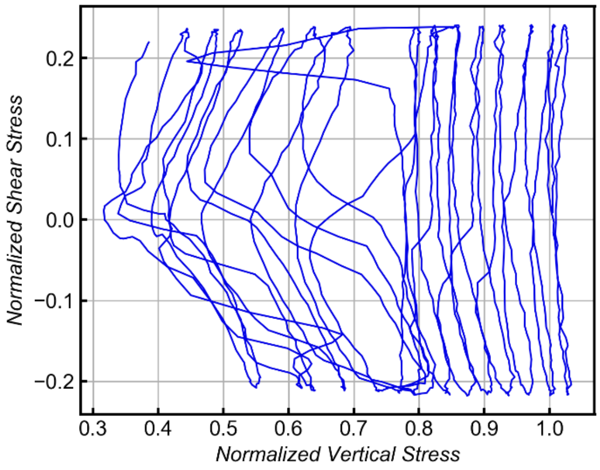

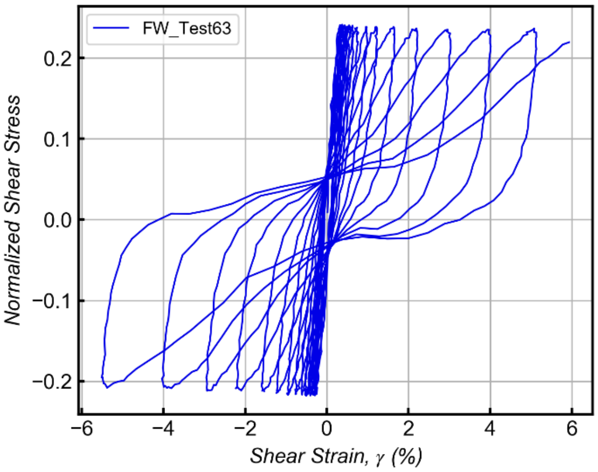

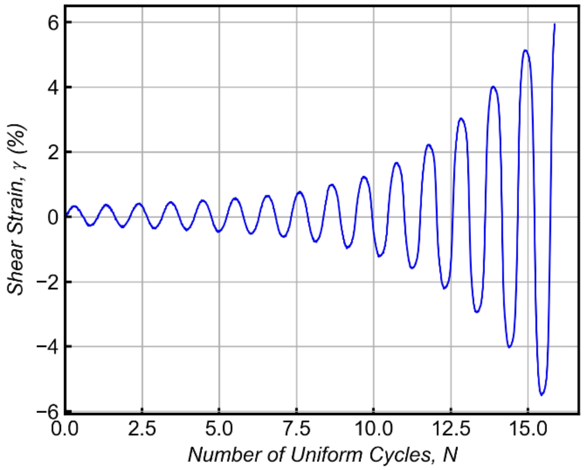

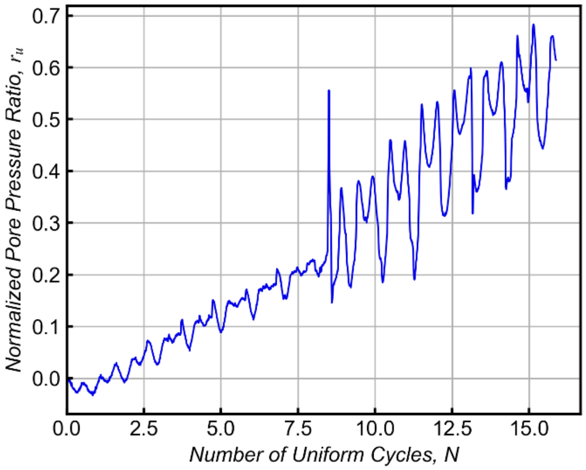

SBSW-Test # 33

Stage 1: Consolidation

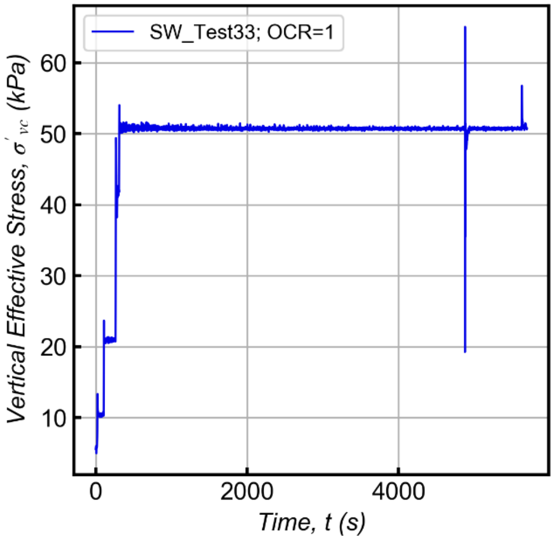

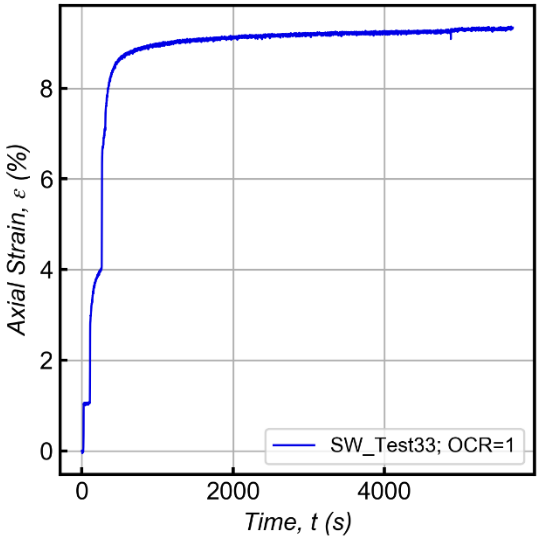

Stage 2: Cyclic Shear

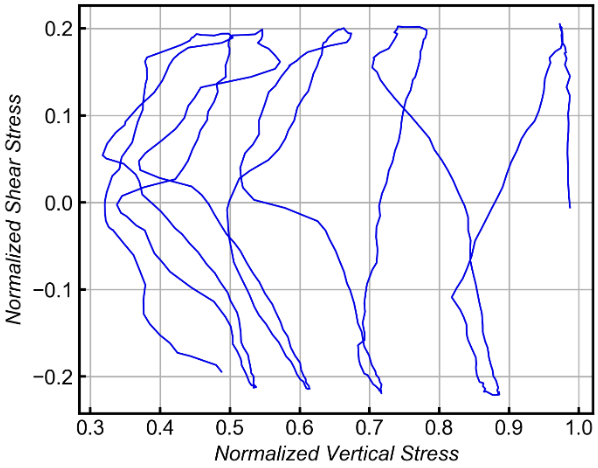

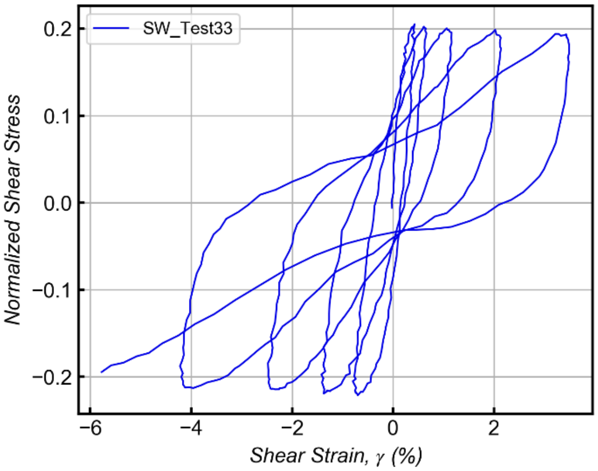

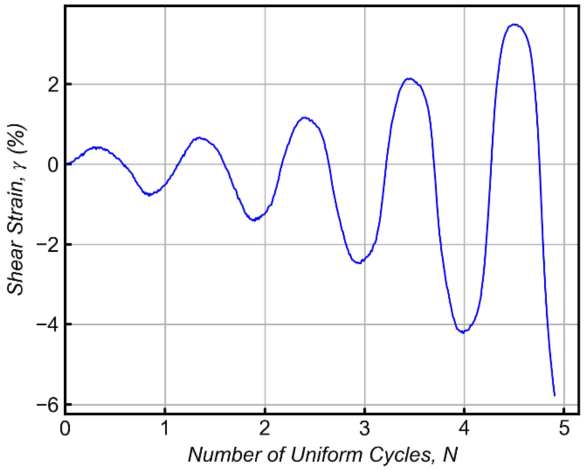

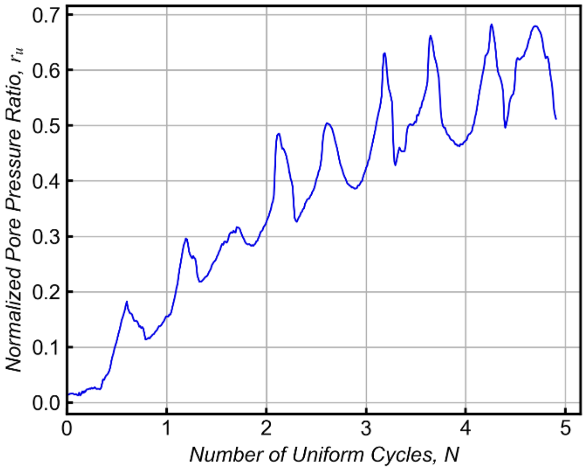

SBSW-Test # 41

Stage 1: Consolidation

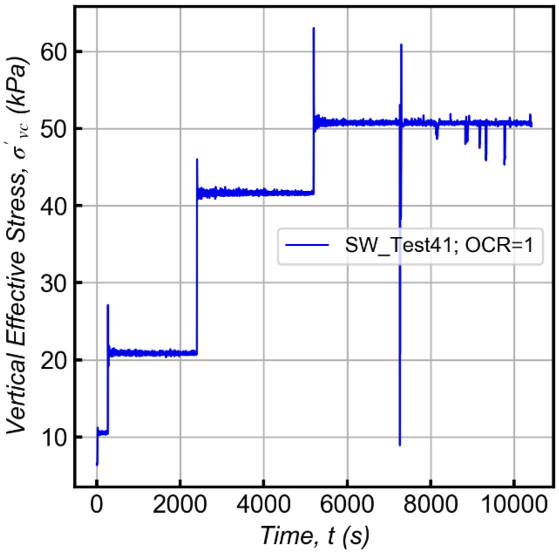

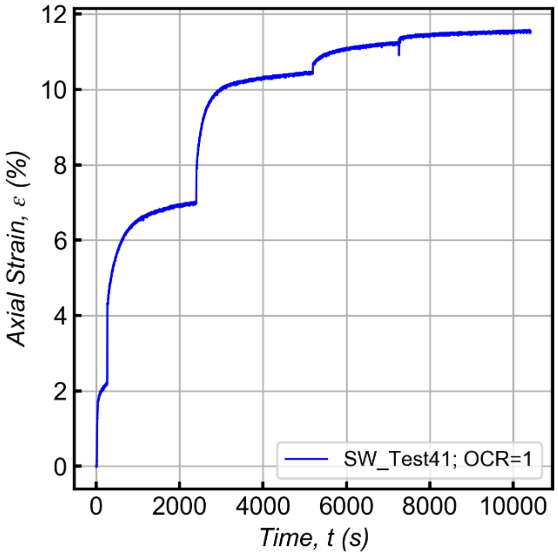

Stage 2: Cyclic Shear

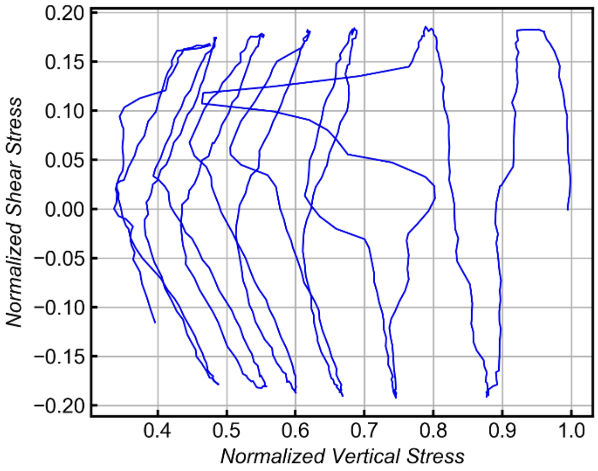

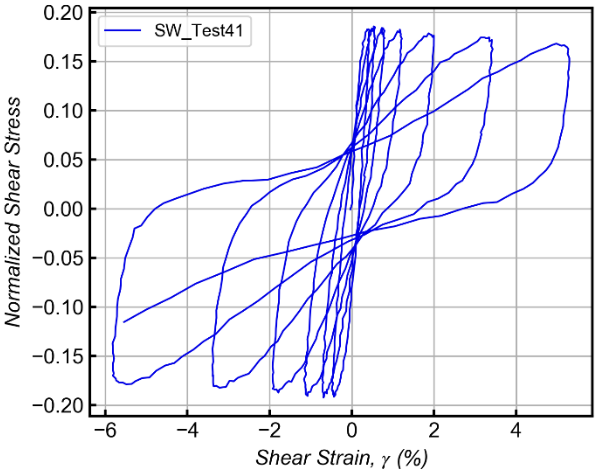

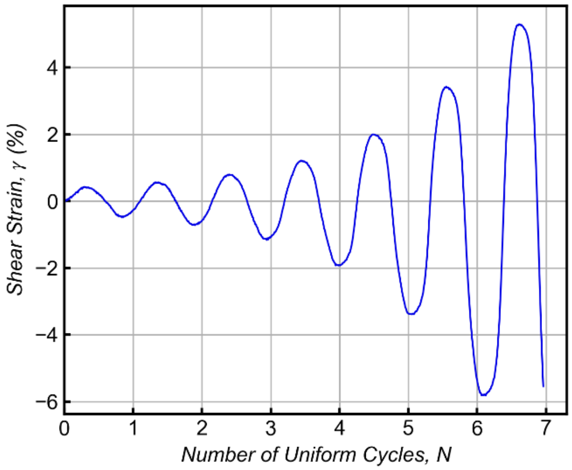

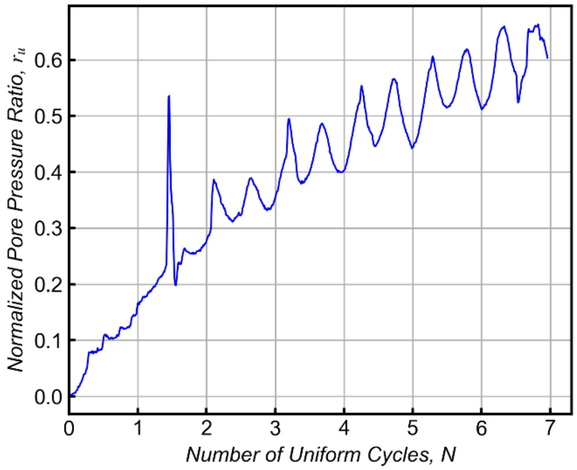

SBSW-Test # 42

Stage 1: Consolidation

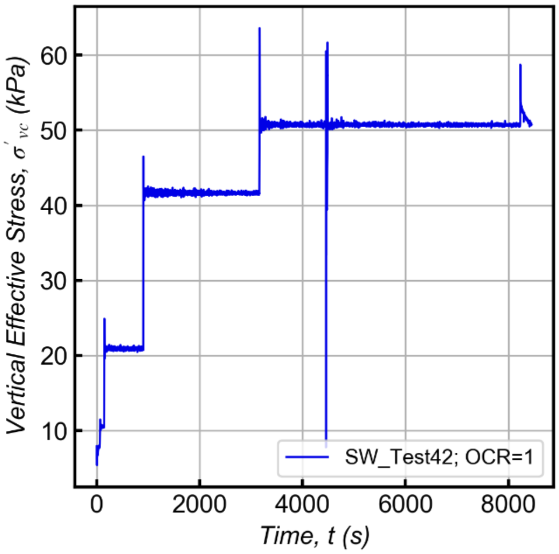

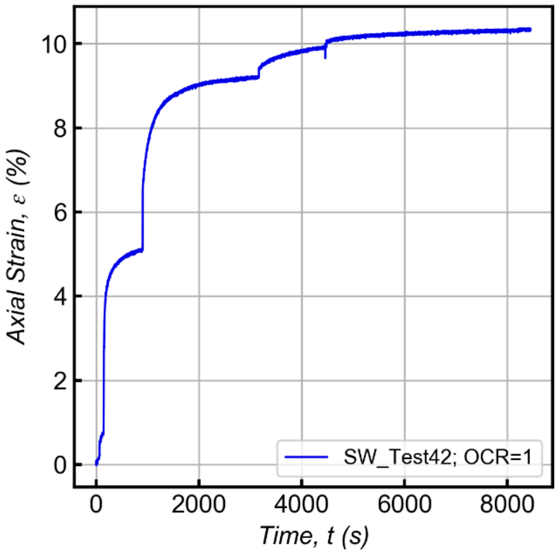

Stage 2: Cyclic Shear

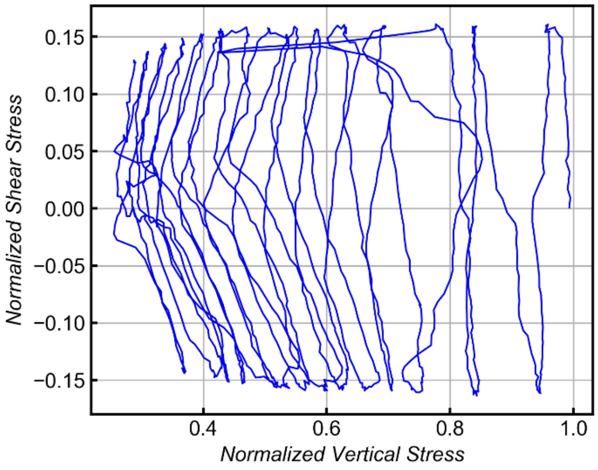

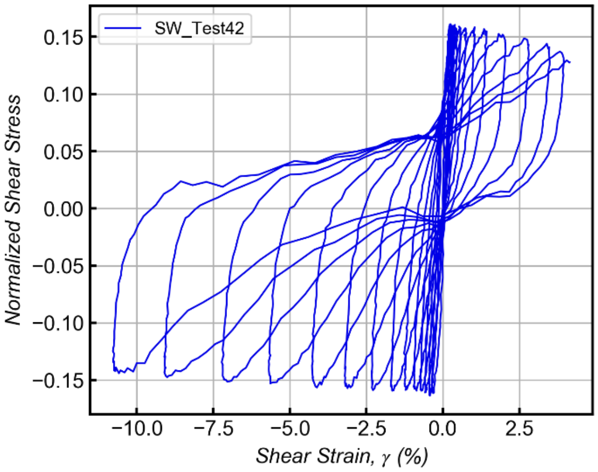

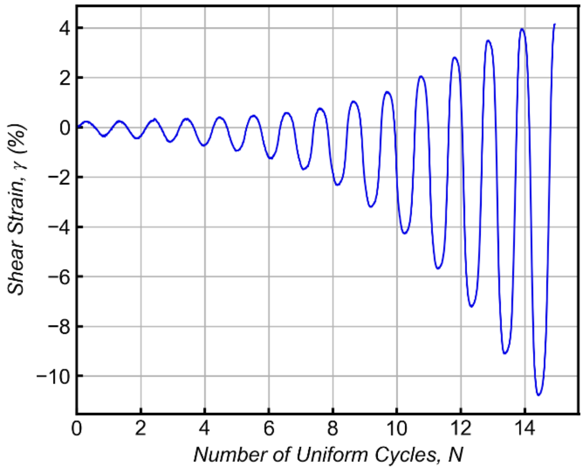

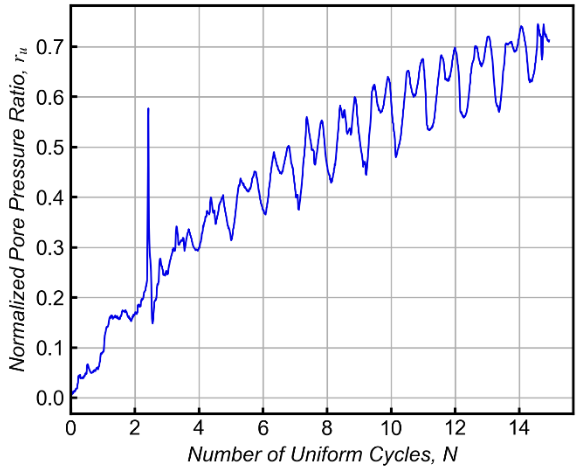

SBSW-Test # 43

Stage 1: Consolidation

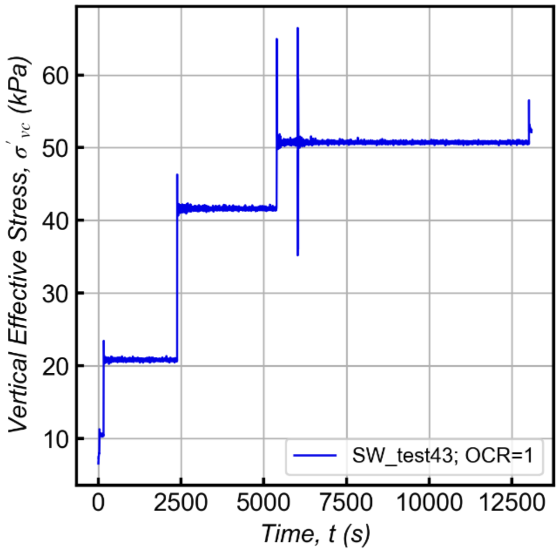

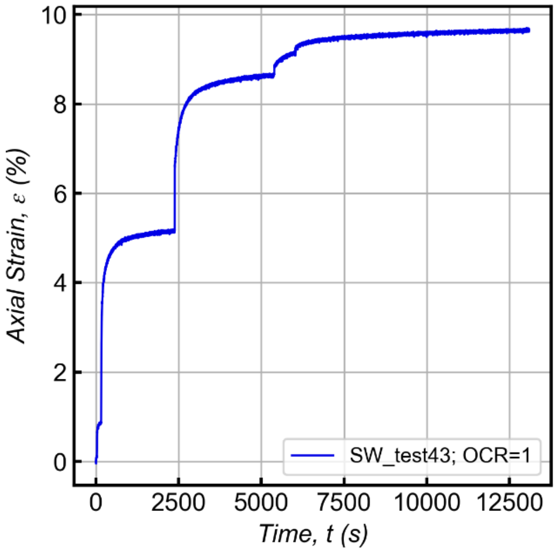

Stage 2: Cyclic Shear

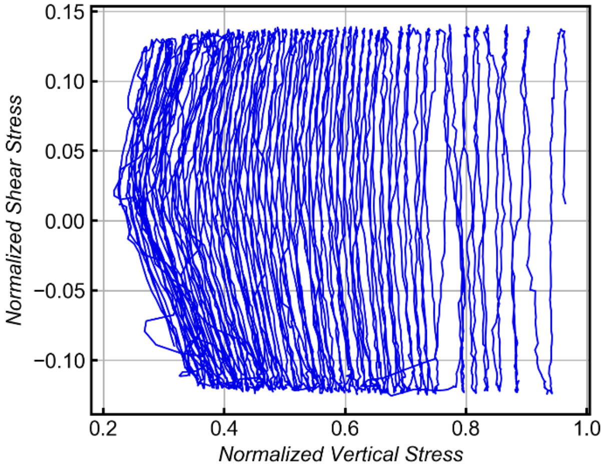

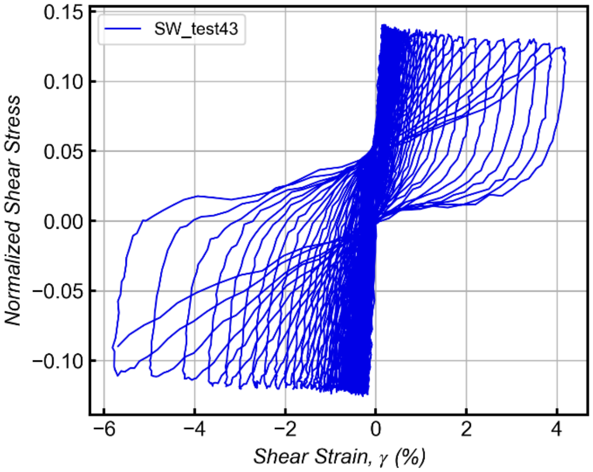

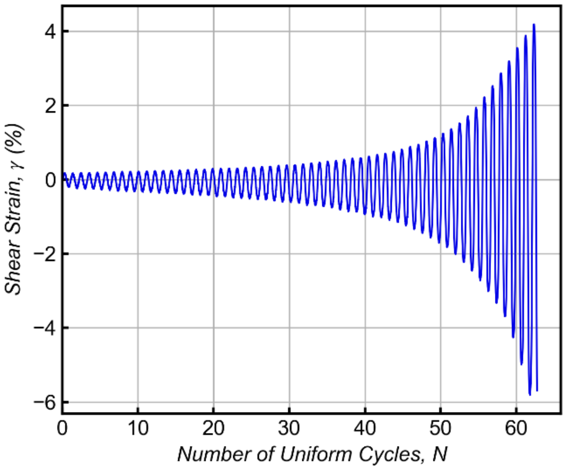

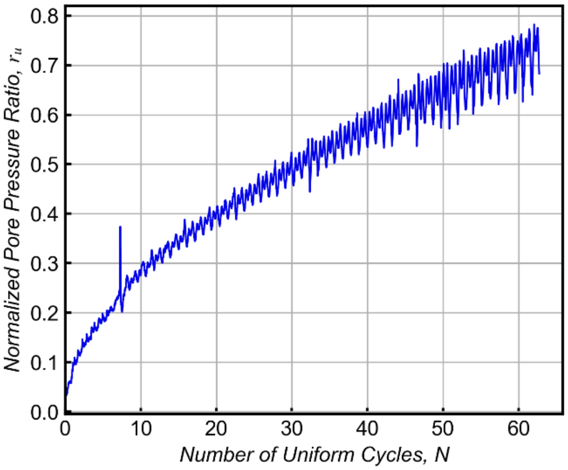

SBSW-Test # 48

Stage 1: Consolidation

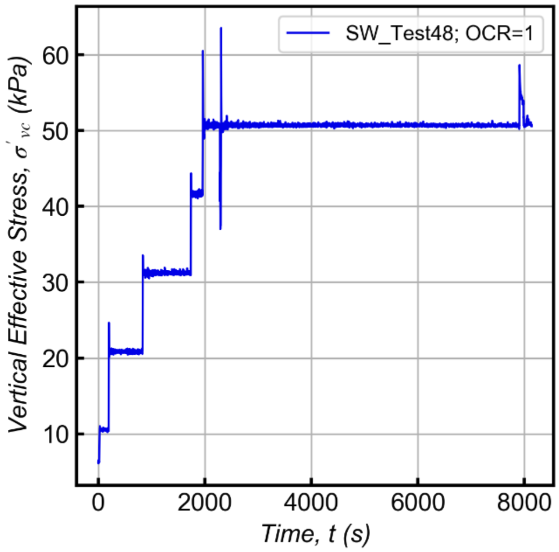

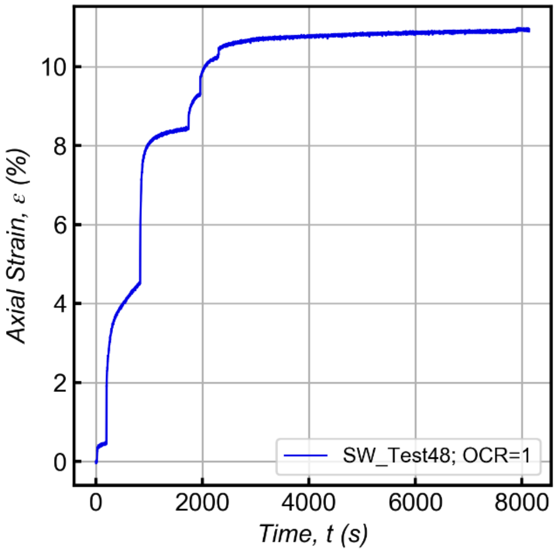

Stage 2: Cyclic Shear

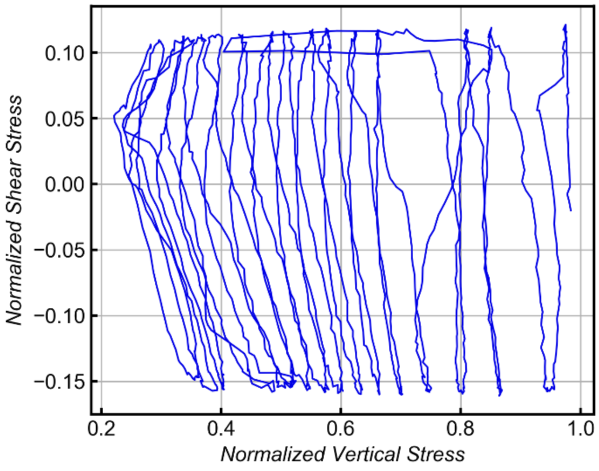

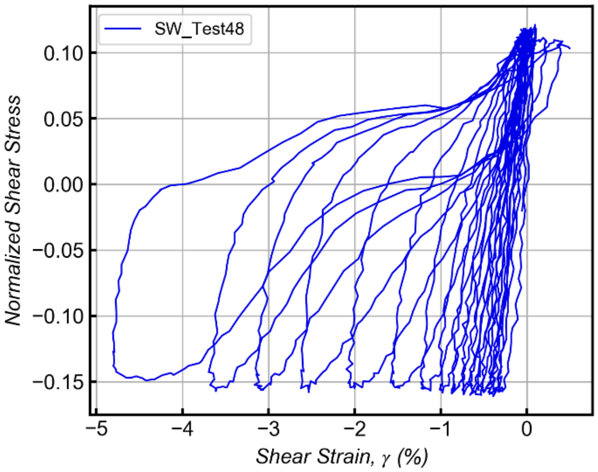

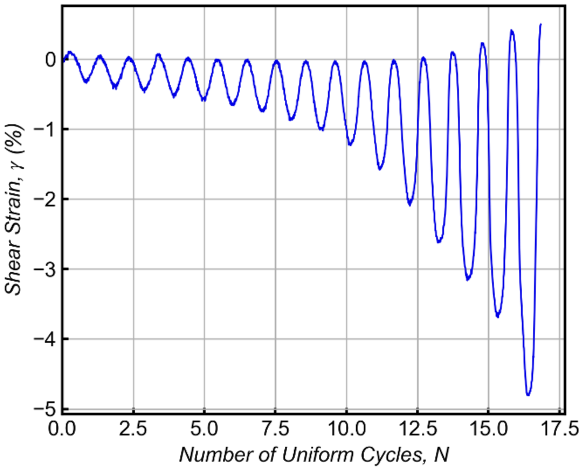

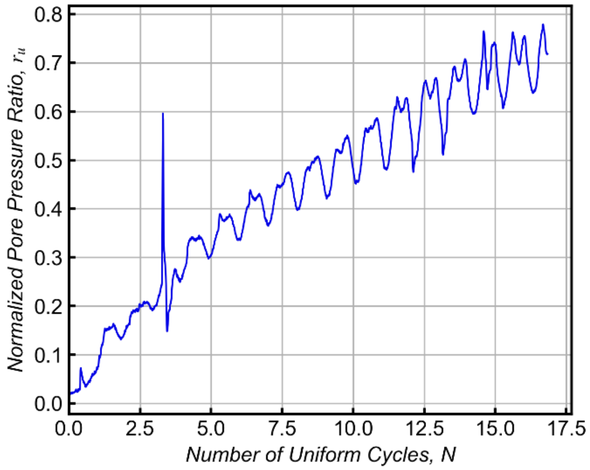

SBSW-Test # 57

Stage 1: Consolidation

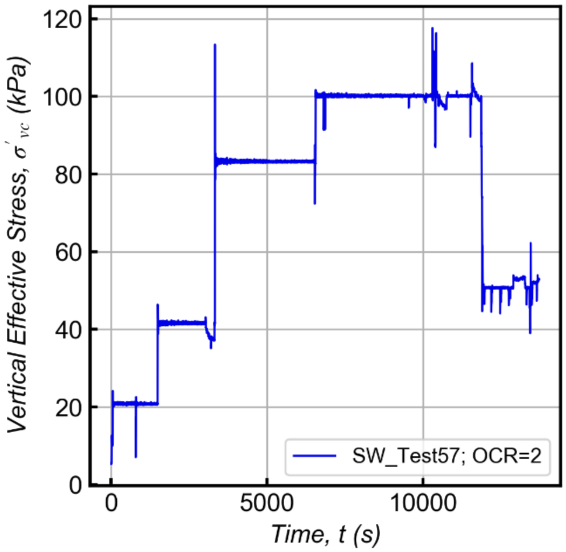

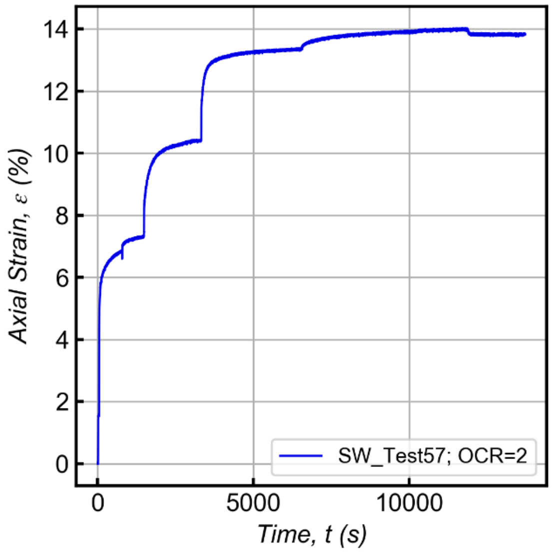

Stage 2: Cyclic Shear

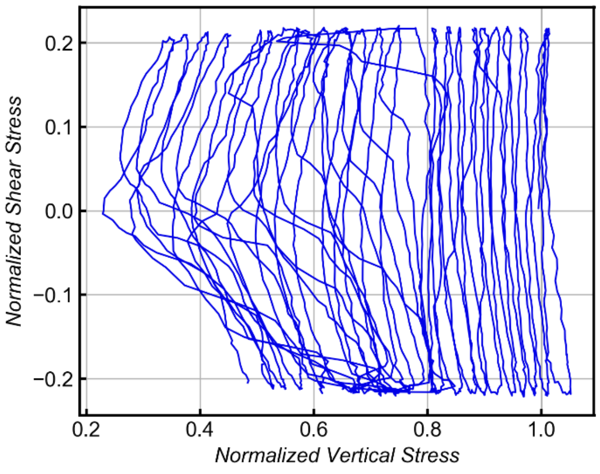

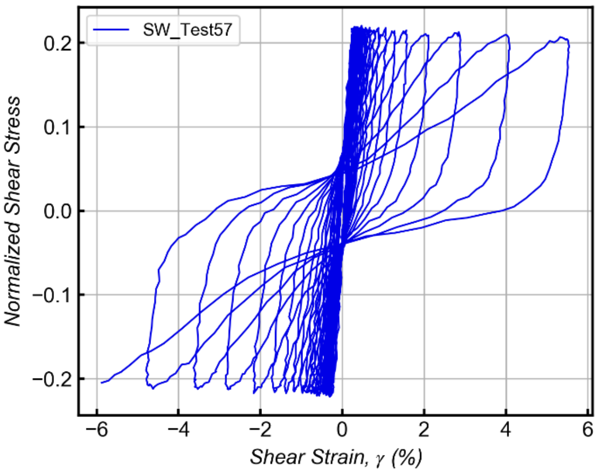

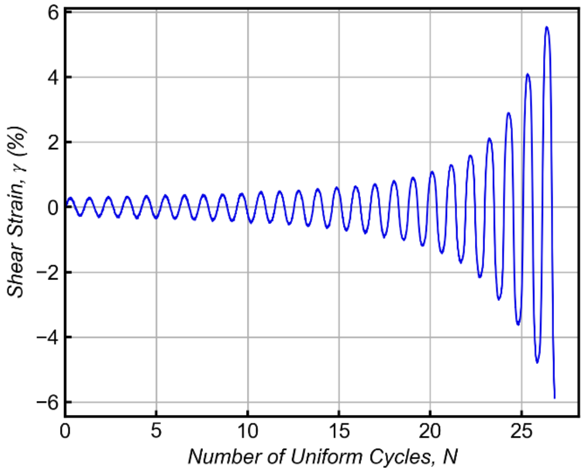

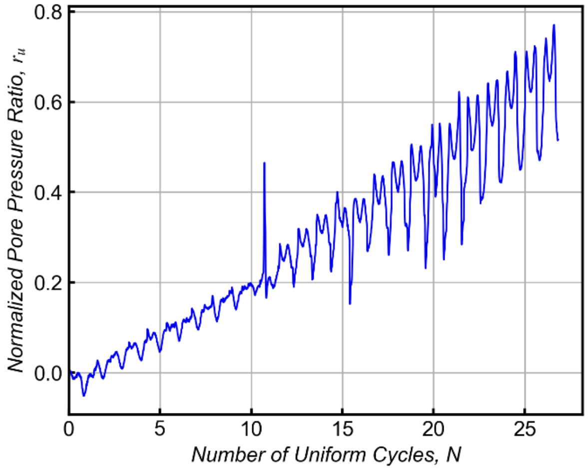

SBSW-Test # 58

Stage 1: Consolidation

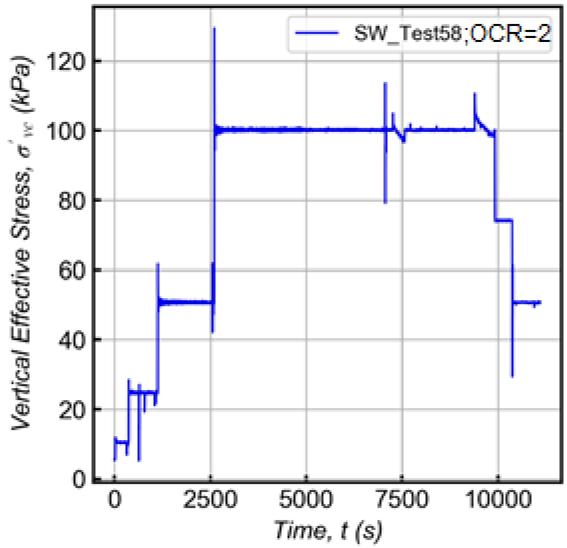

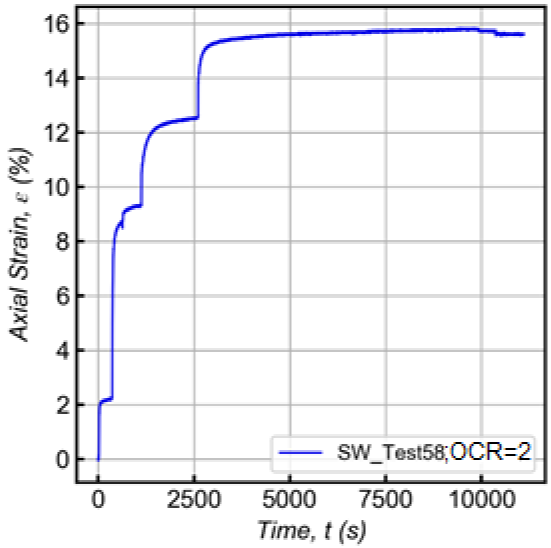

Stage 2: Cyclic Shear

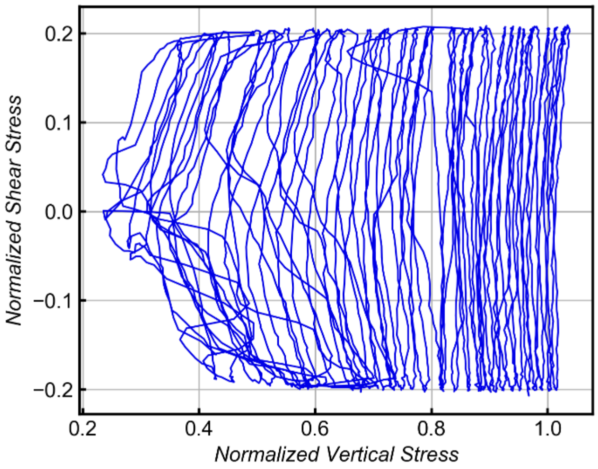

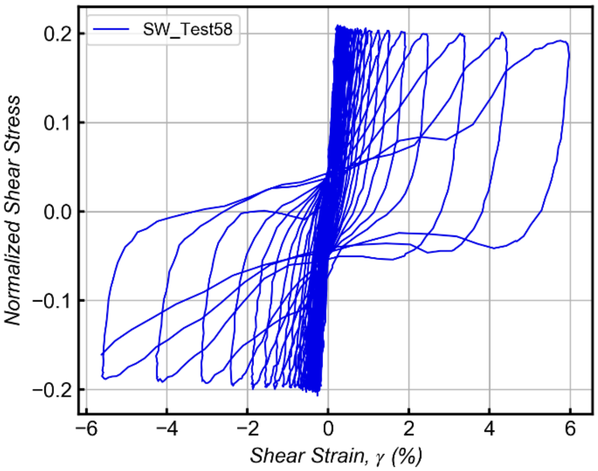

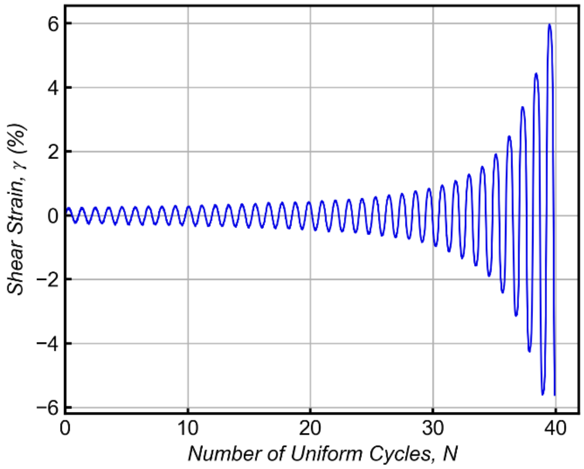

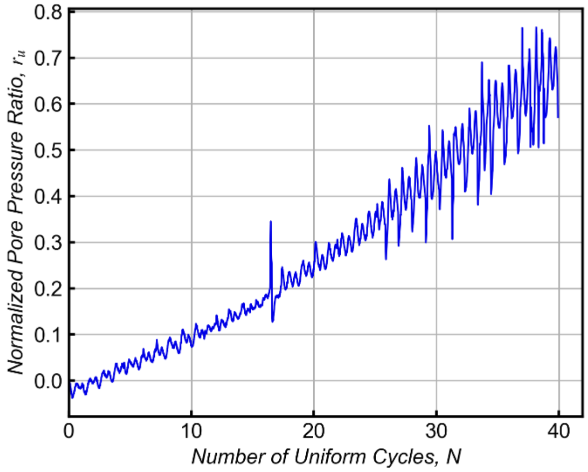

SBSW-Test # 59

Stage 1: Consolidation

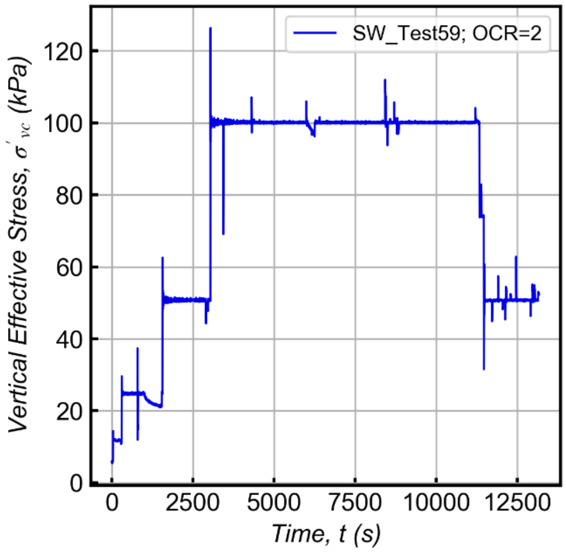

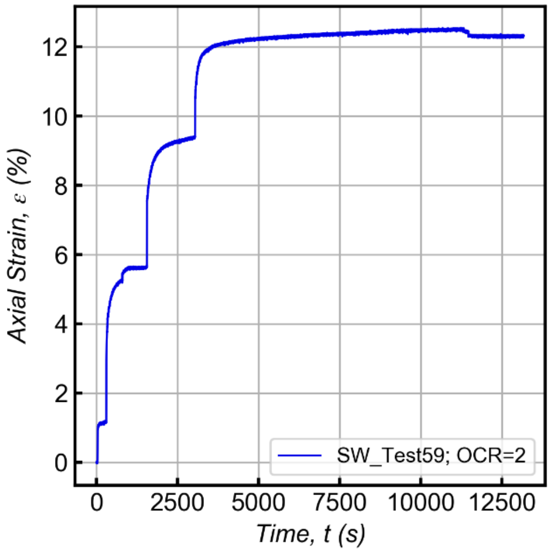

Stage 2: Cyclic Shear

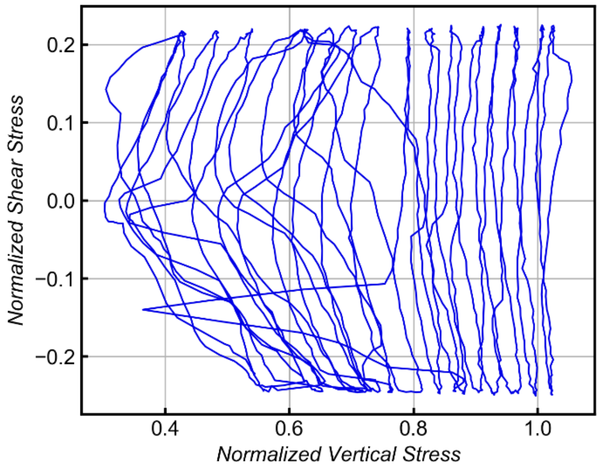

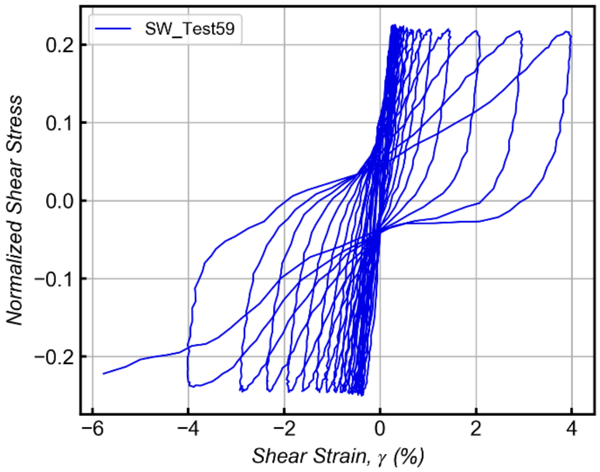

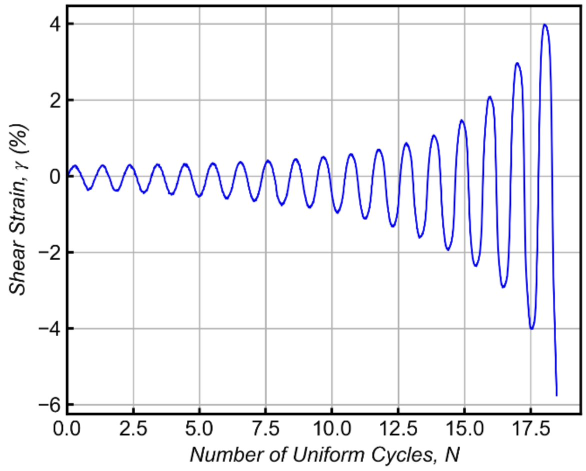

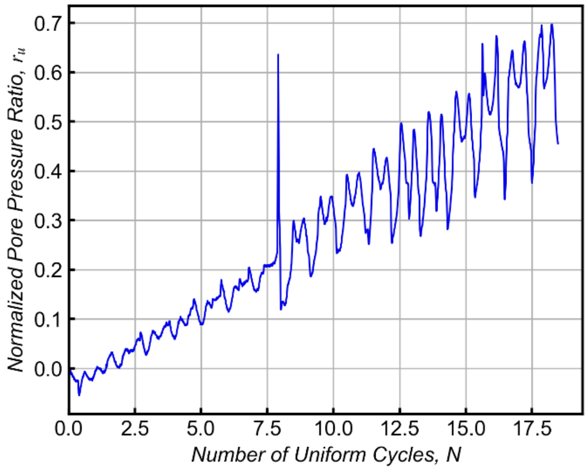

SBSW-Test # 60

Stage 1: Consolidation

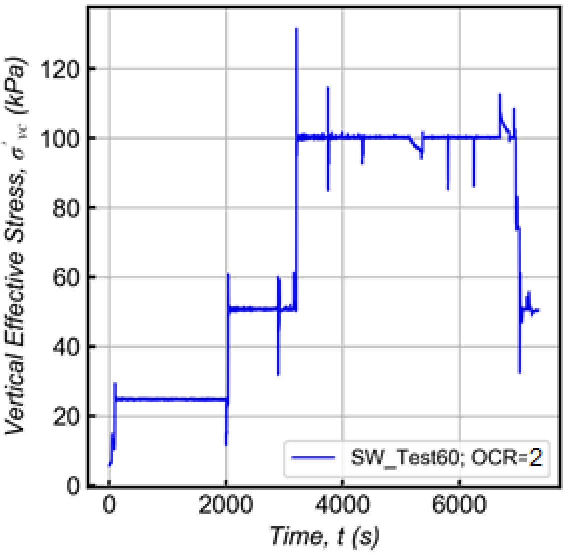

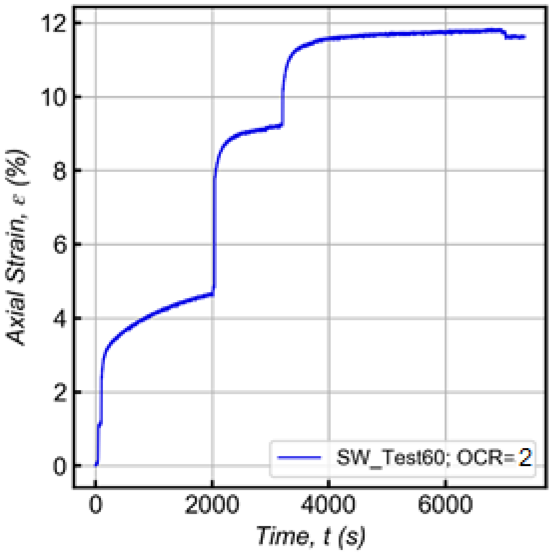

Stage 2: Cyclic Shear

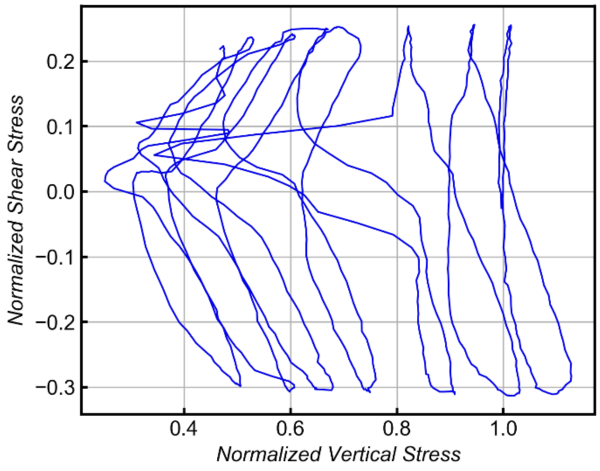

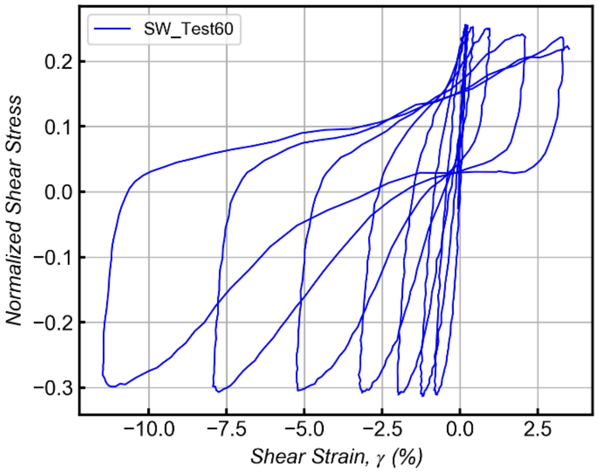

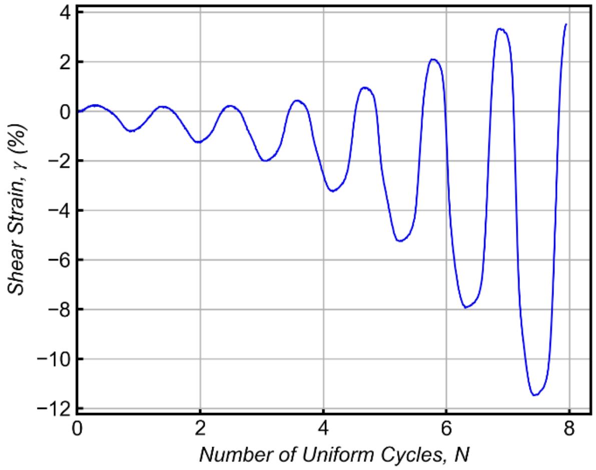

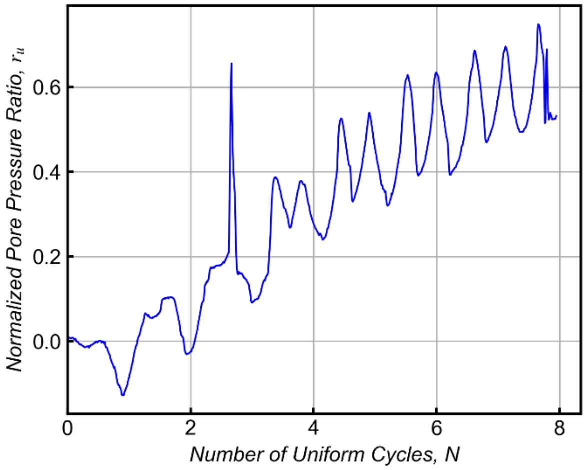

SKFW-Test # 64

Stage 1: Consolidation

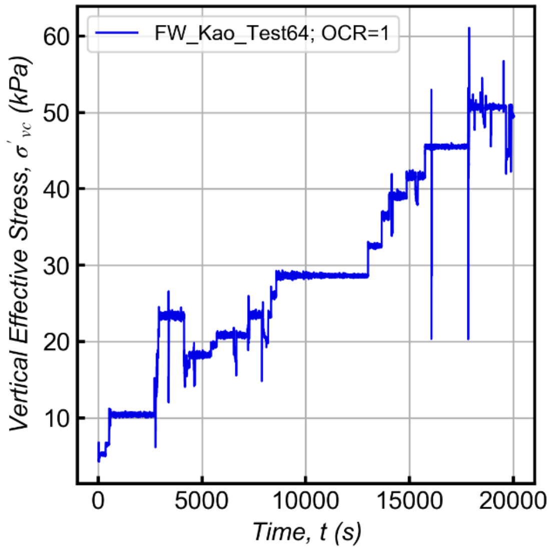

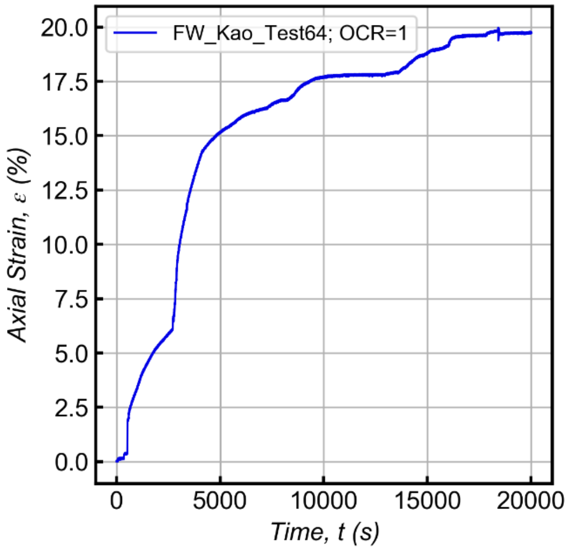

Stage 2: Cyclic Shear

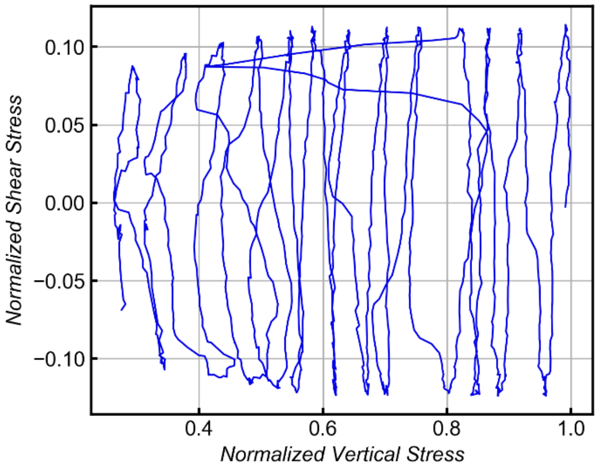

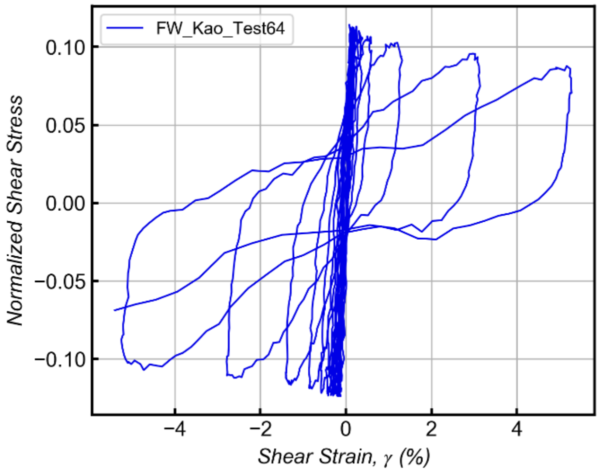

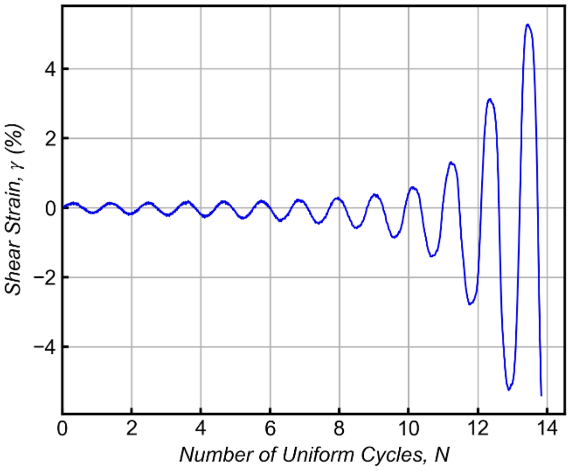

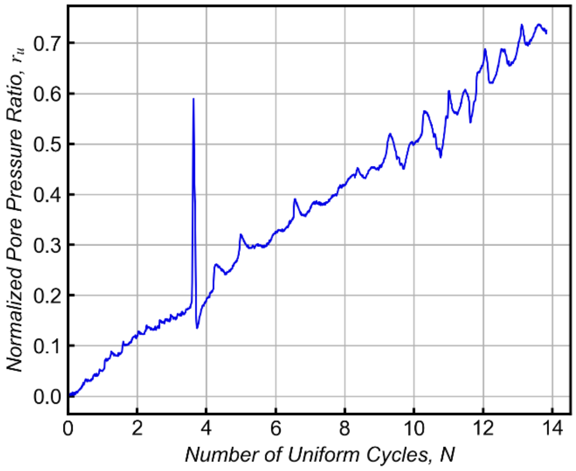

SKFW-Test # 65

Stage 1: Consolidation

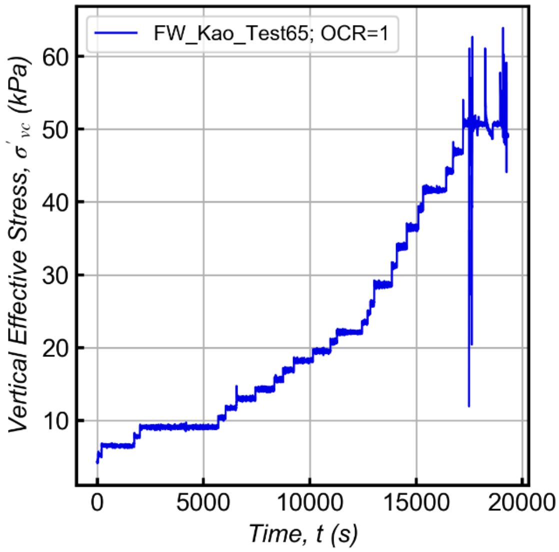

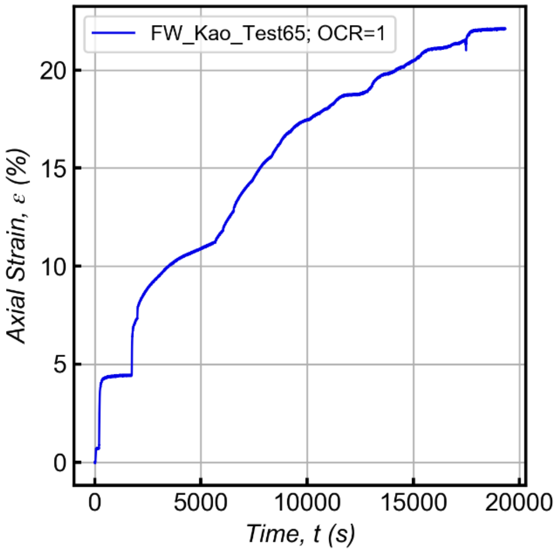

Stage 2: Cyclic Shear

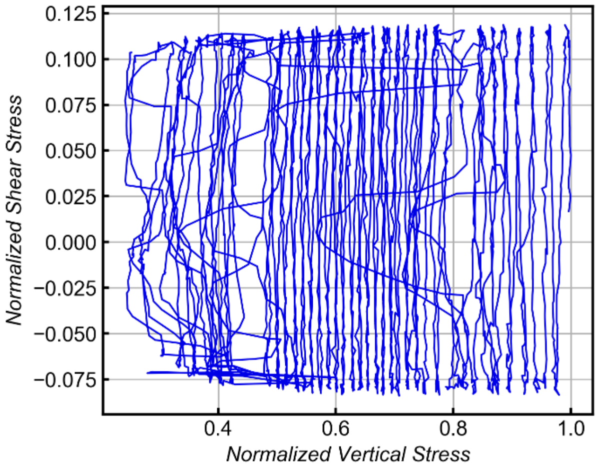

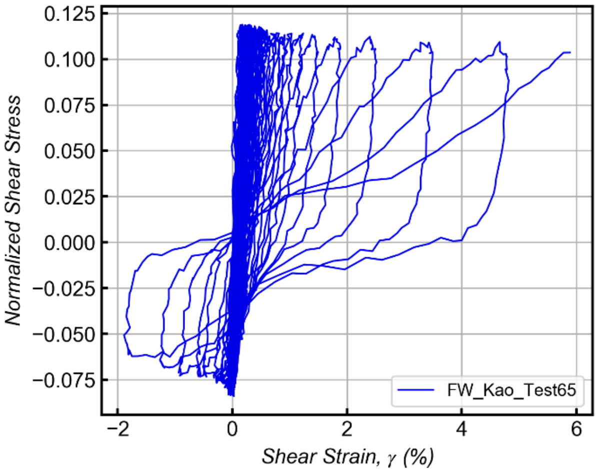

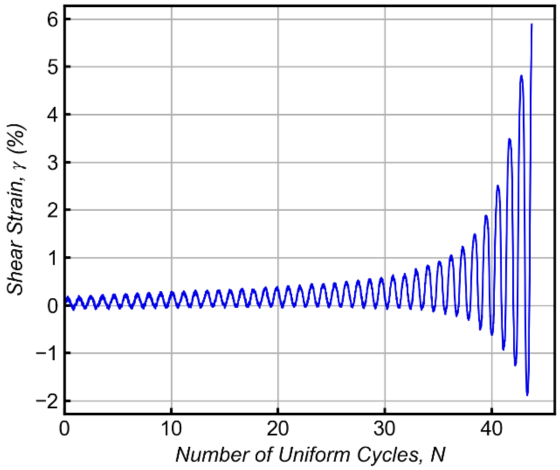

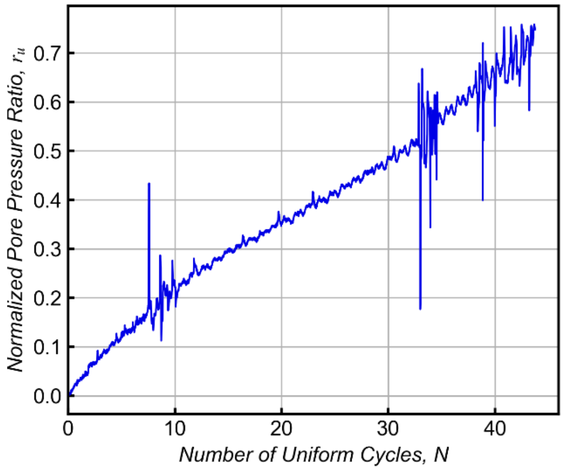

SKFW-Test # 66

Stage 1: Consolidation

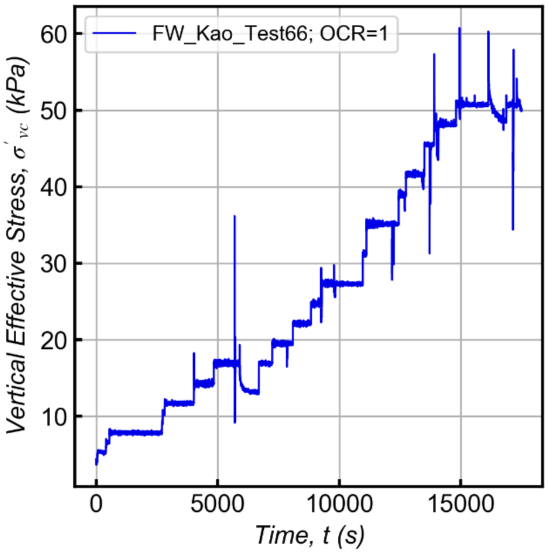

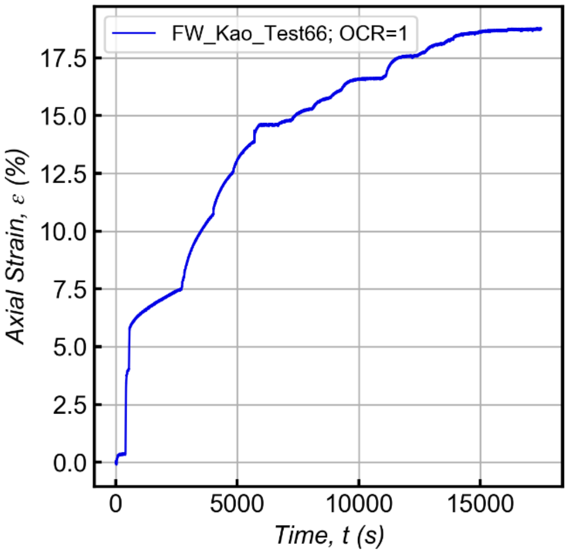

Stage 2: Cyclic Shear

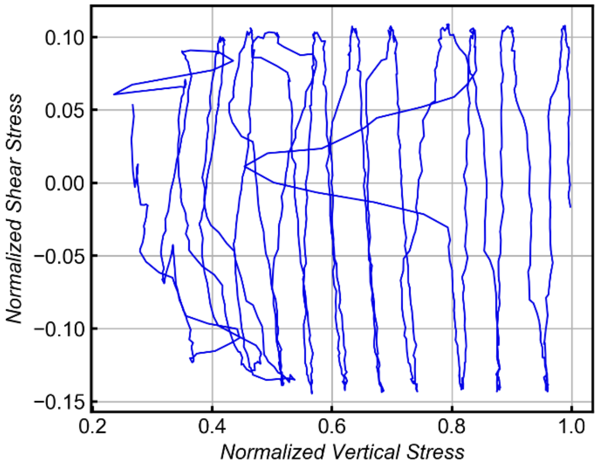

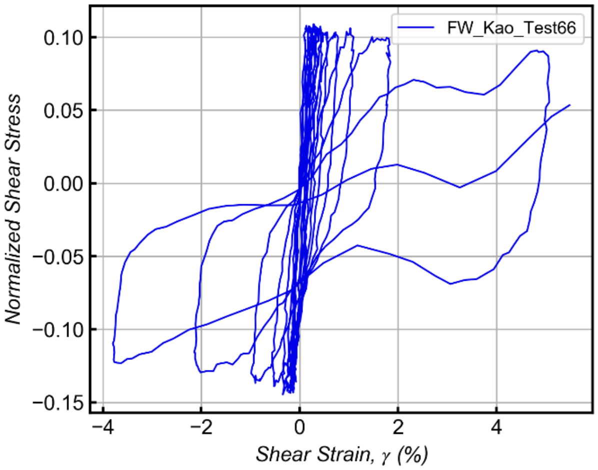

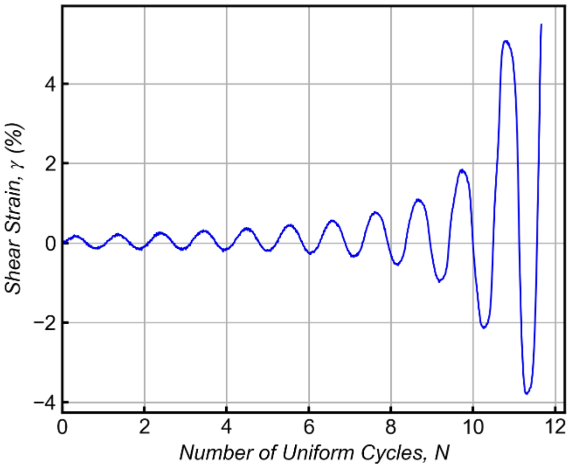

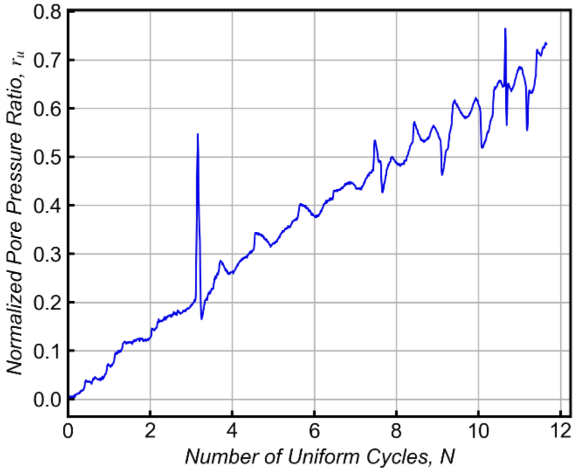

SKFW-Test # 67

Stage 1: Consolidation

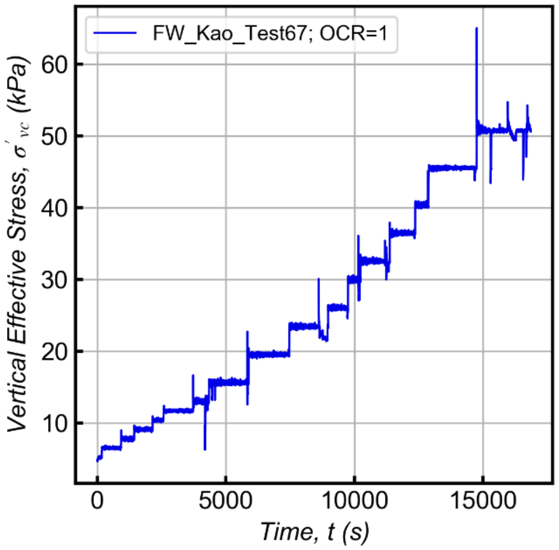

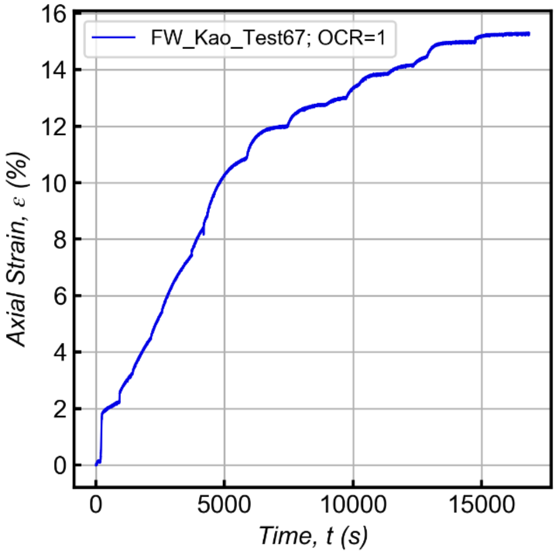

Stage 2: Cyclic Shear

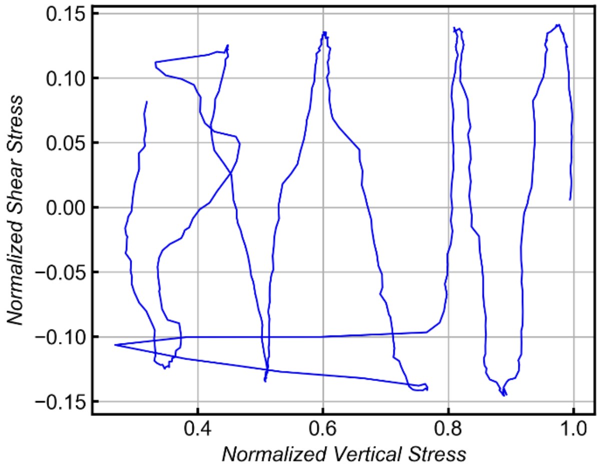

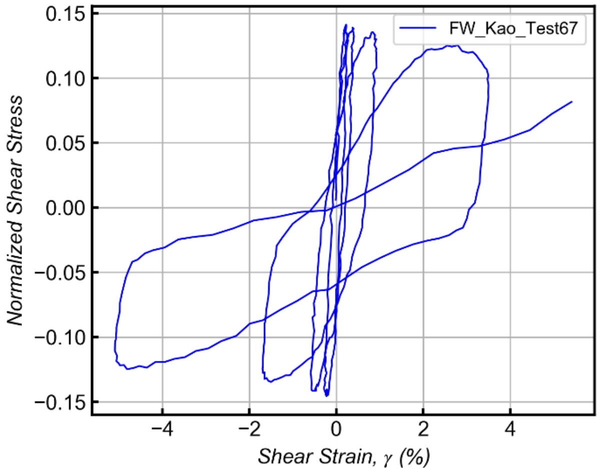

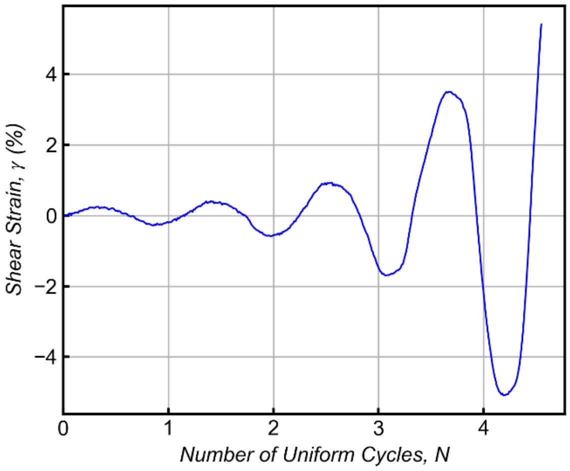

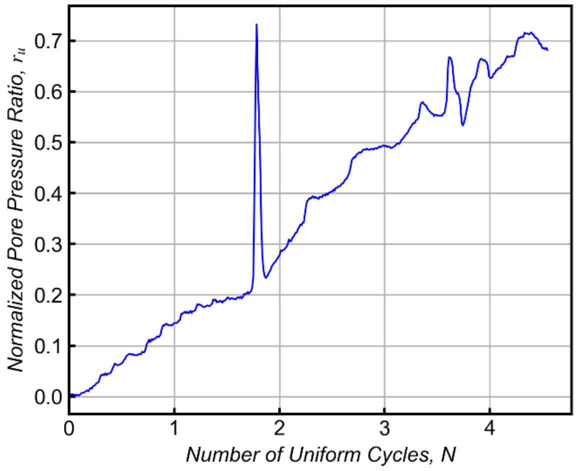

SKFW-Test # 72

Stage 1: Consolidation

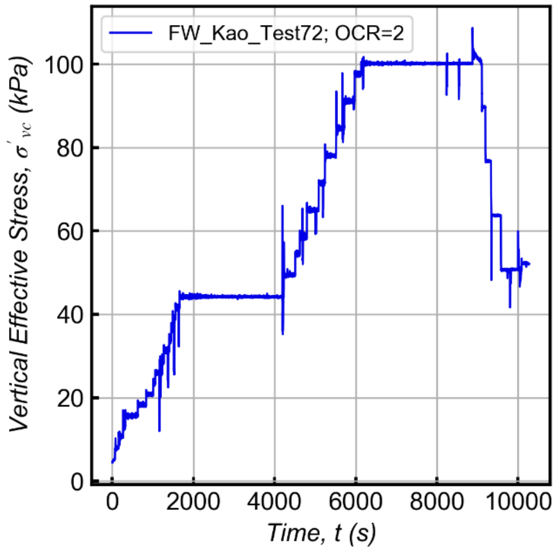

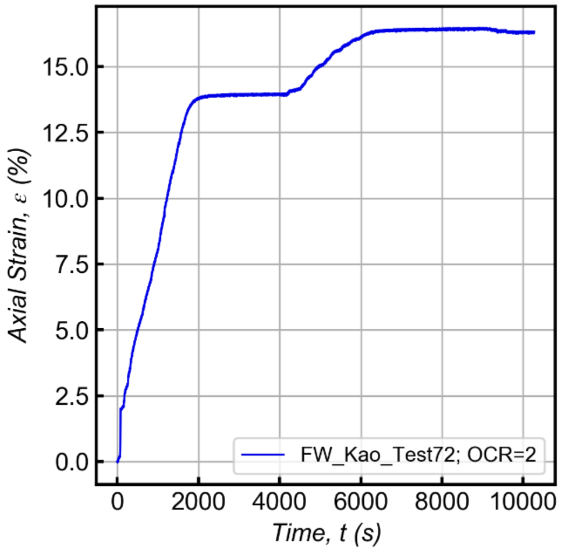

Stage 2: Cyclic Shear

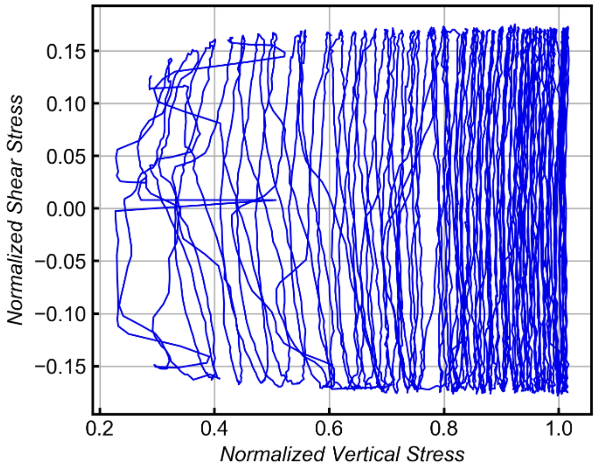

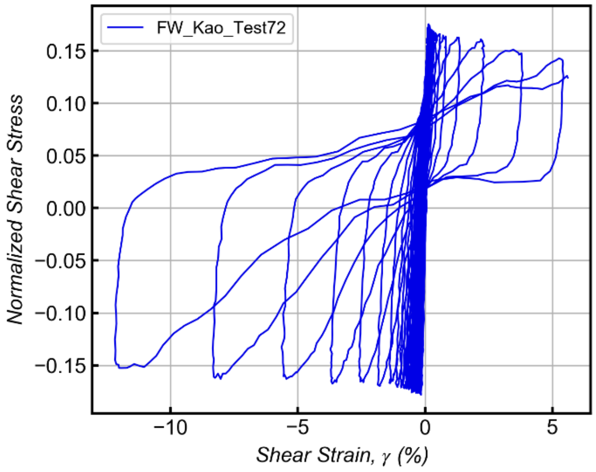

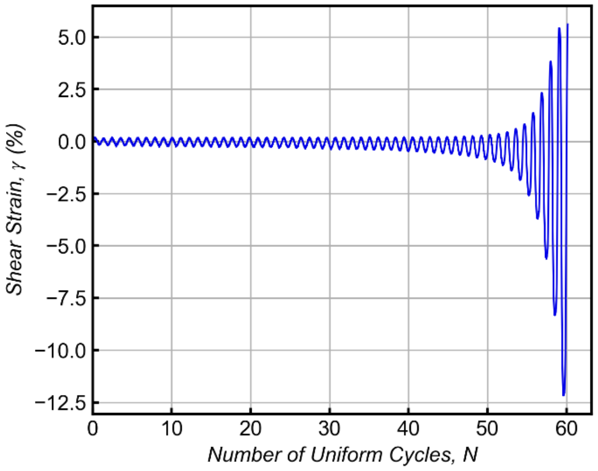

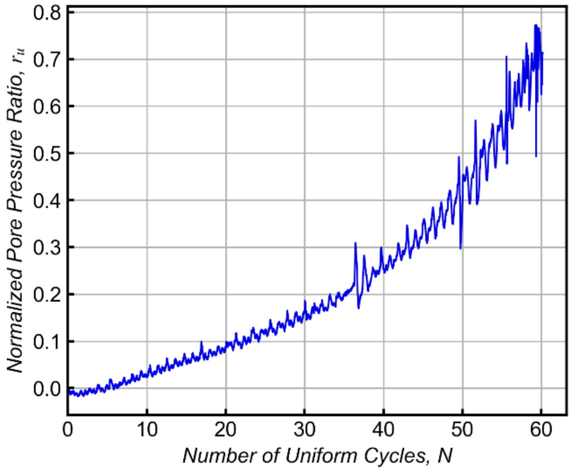

SKFW-Test # 74

Stage 1: Consolidation

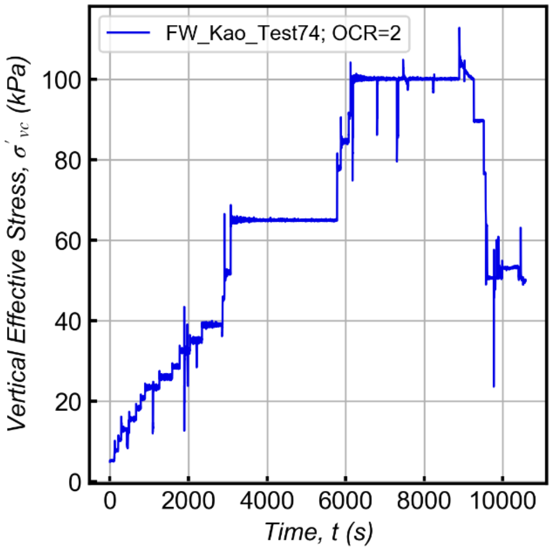

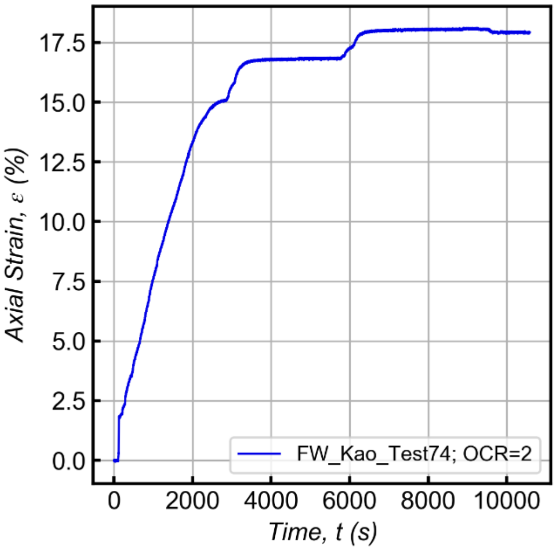

Stage 2: Cyclic Shear

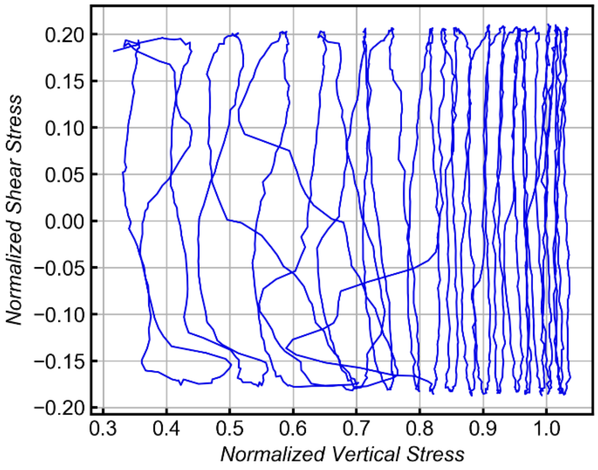

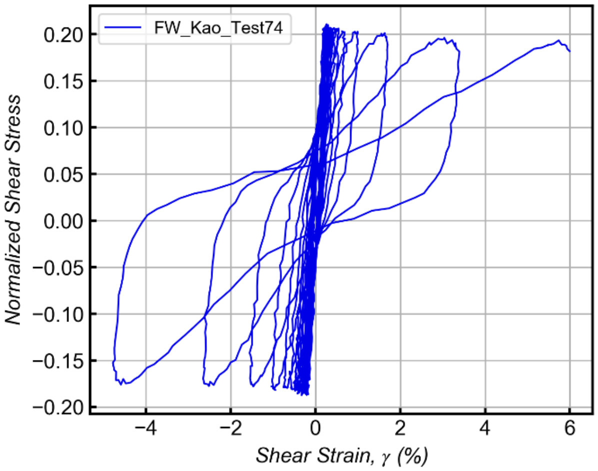

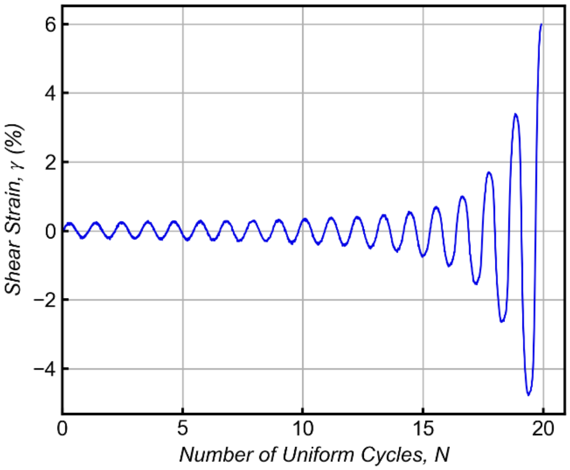

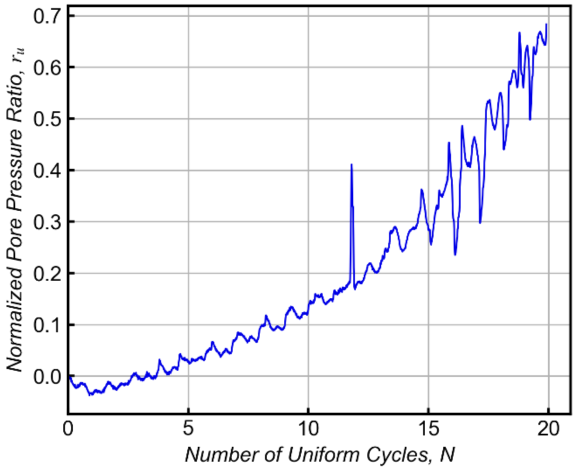

SKFW-Test # 75

Stage 1: Consolidation

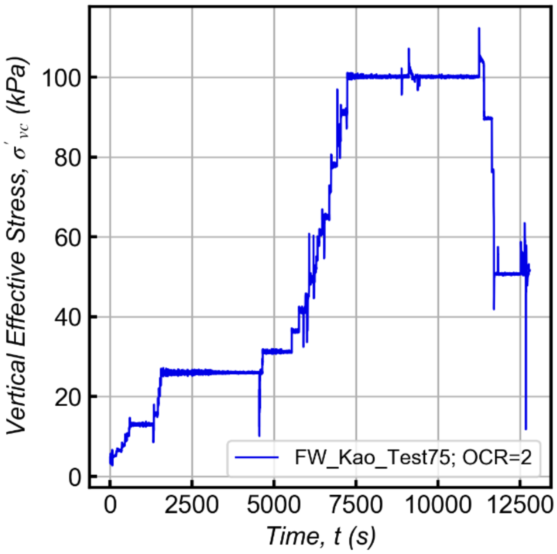

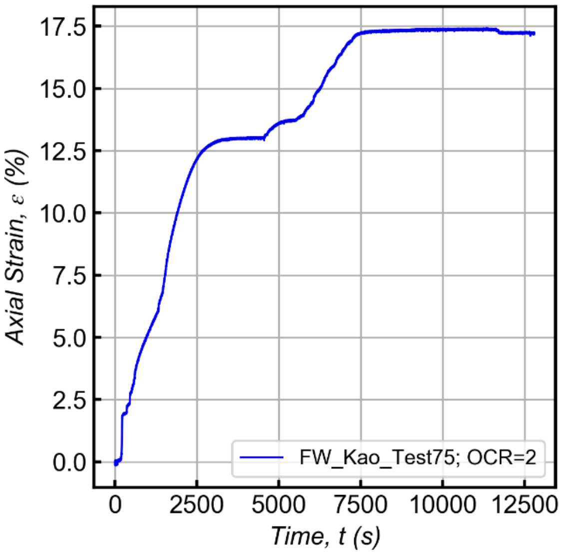

Stage 2: Cyclic Shear

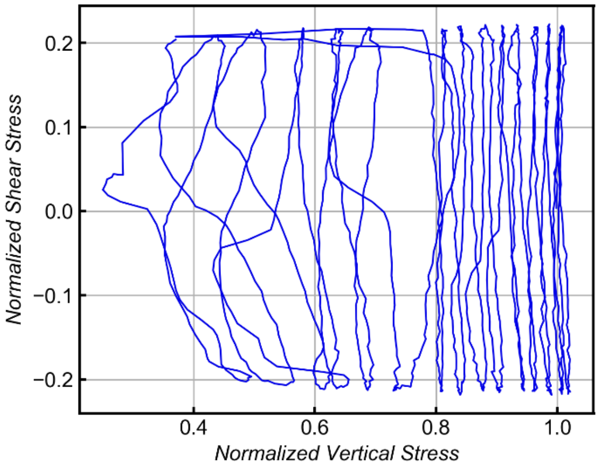

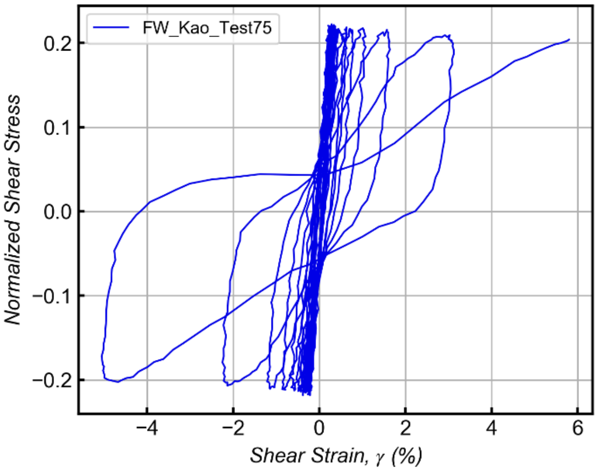

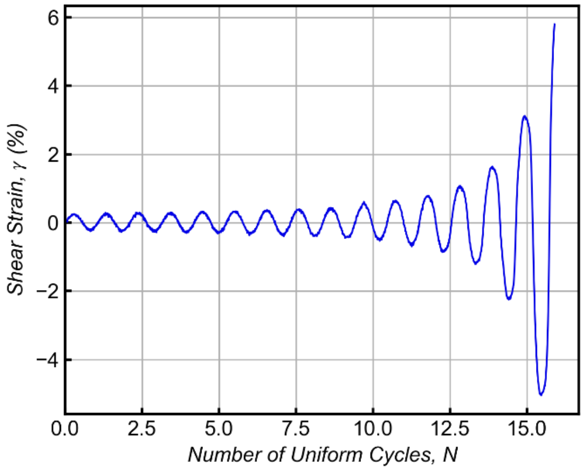

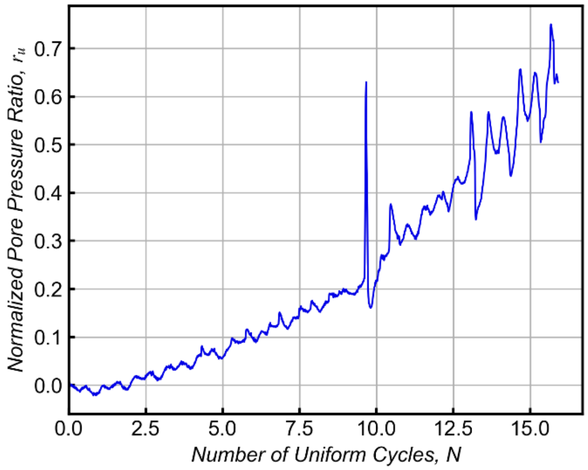

SKFW-Test # 76

Stage 1: Consolidation

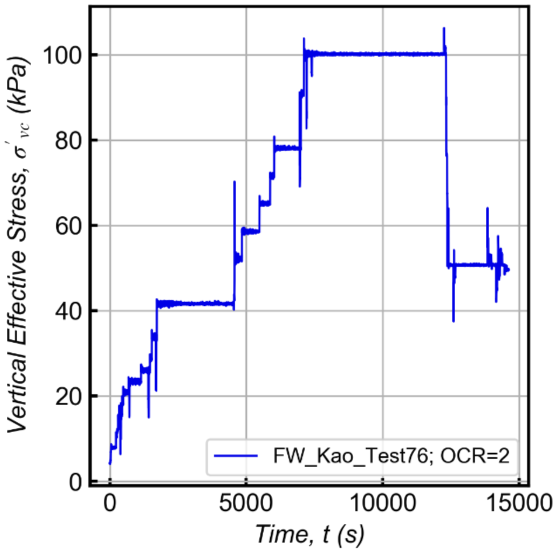

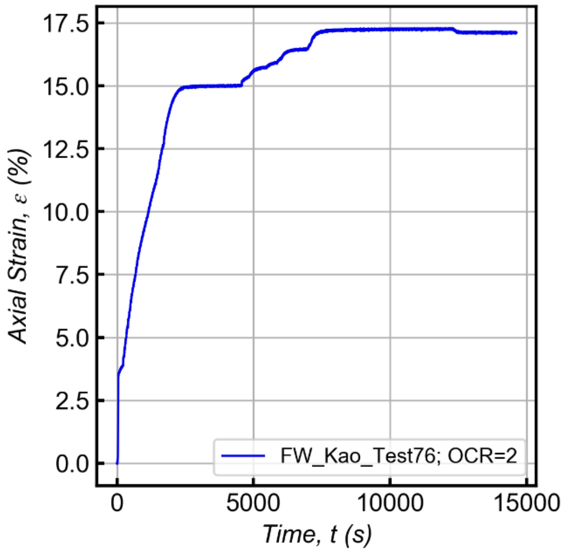

Stage 2: Cyclic Shear

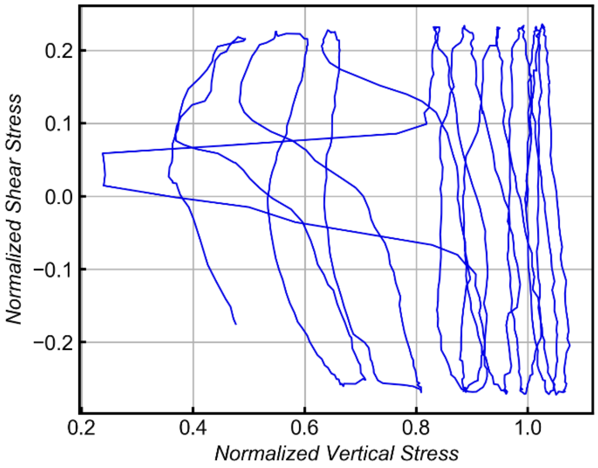

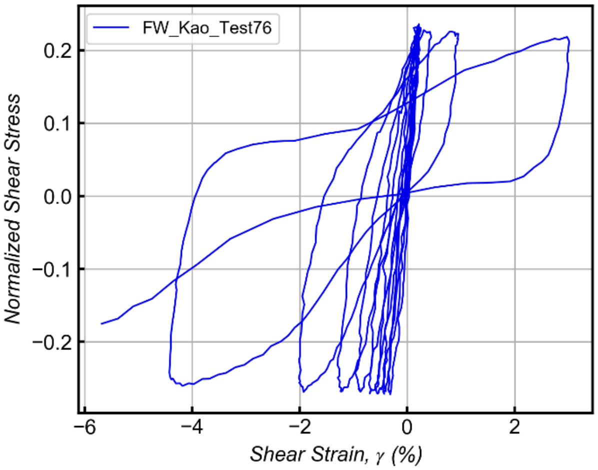

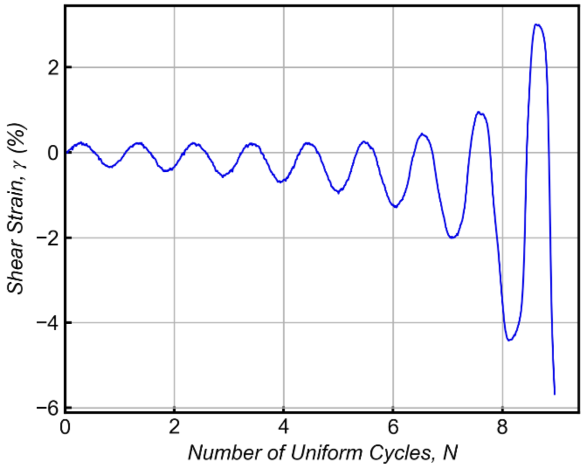

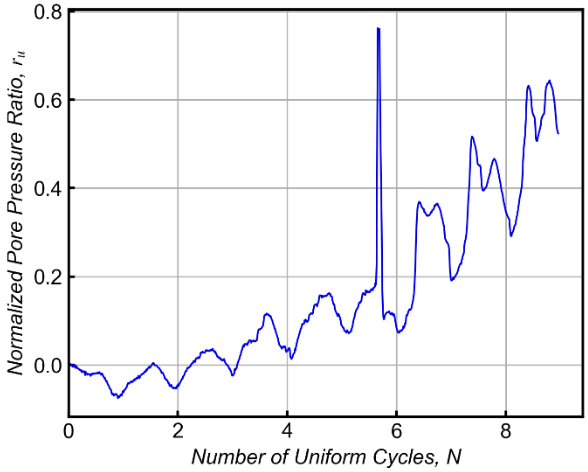

SKFW-Test # 78

Stage 1: Consolidation

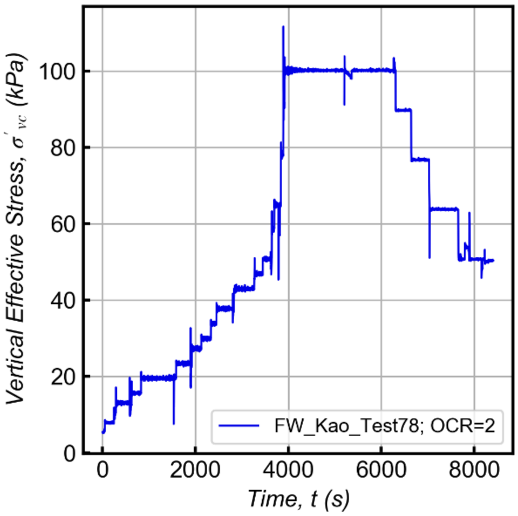

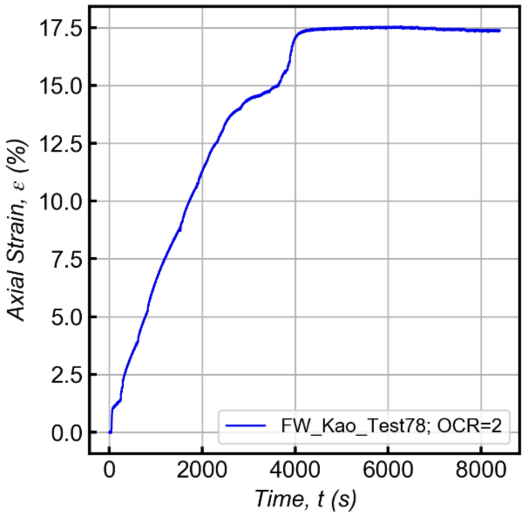

Stage 2: Cyclic Shear

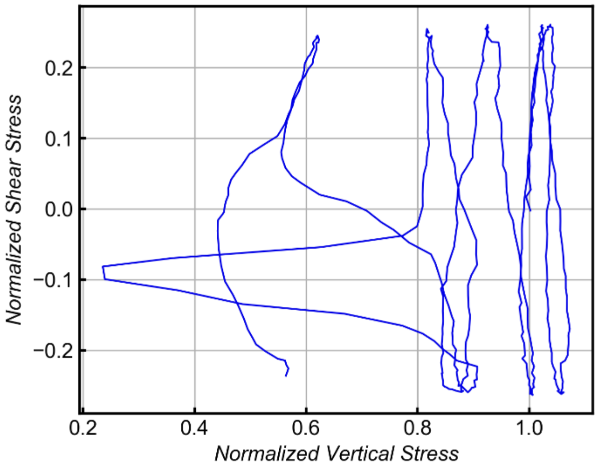

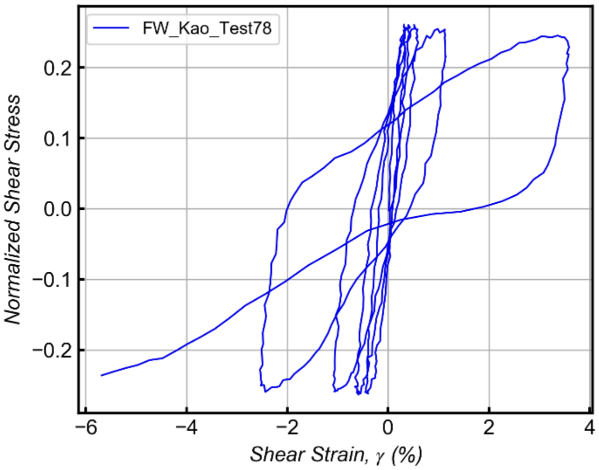

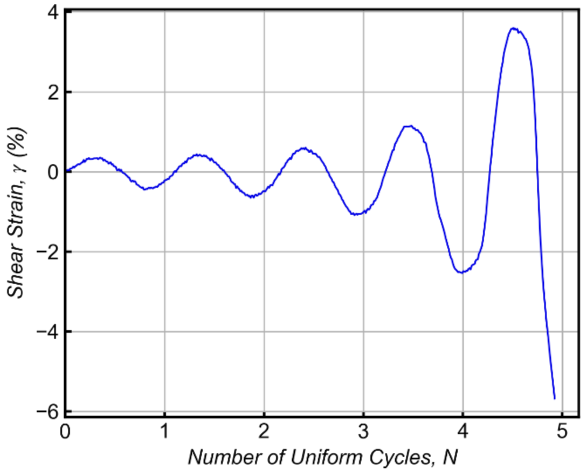

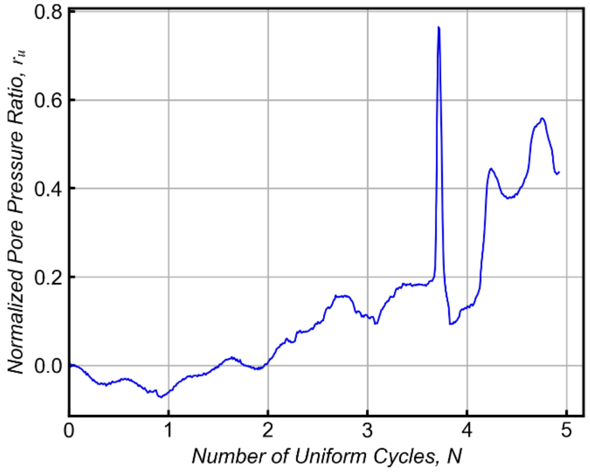

References for Part I

Al-Tabbaa, A. and Wood, D. M., (1989), “An experimentally based "bubble' model for clay”, Numerical models in geomechanics. NUMOG III. pp. 91-99

ASCE (2010), “GeoFlorida 2010: Advances in Analyses, Modeling & Design”, Geotechnical Special Publication No.199 (GSP199), D.O. Fratta, A.J. Puppala, and B. Muhunthan (editors.), West Palm Beach, FL.

Baladi G. Y. and Rohani B. (1979), "Elastic-Plastic Model for Saturated Sand," Journal of Geotechnical Engineering, ASCE, 105, p. 465-477.

Beagrie, N. (2004), “The Digital Curation Centre” Learned Publishing 17, No. 1: 7-9

Been, K., and Jefferies, M. G. (1985). ‘‘A state parameter for sands”, Geotechnique, 35(2), 99-112.

Bolton, M. D., (1986), “The strength and dilatancy of sands”, Geotechnique, Vol. 36 (1), 65–78

Brandenberg, S. J., Kutter, B. L., and Wilson, D.W. (2008). “Fast Stacking and Phase Corrections of Shear Wave Signals in a Noisy Environment.”, Journal of Geotechnical and Geoenvironmental Engineering, 134(8), 1154-1165.

Dafalias, Y. F. (1986), “Bounding surface plasticity. I: mathematical foundation and hypoplasticity,” Journal of Engineering Mechanics, ASCE, 112(9), 966-987.

Dafalias, Y. F. and Manzari M. T. (2004), “Simple plasticity sand model accounting for fabric change effects”, Journal of Engineering mechanics, 130(6), 622-634.

Desai, C.S., and Siriwardane, H.J. (1984), “Constitutive laws for engineering materials. With emphasis on geologic materials”, Prentice Hall, Inc., Englewood Cliffs, NJ

DiMaggio, F.L. and Sandler, I.S., (1971), “Material models for granular soils”, J. Eng. Mech., ASCE, Vol. 97, 935-950

Drucker, D. C. and Prager, W., (1952), “Soil mechanics and plastic analysis for limit design”, Quart. Appl. Math., Vol. 10, 157-165

Duncan, J. M. and Chang, C. Y., (1970), “Nonlinear analysis of stress and strain in soils”, Journal of the soil mechanics and foundations division, ASCE, 96(SM5), 1629-1653

Elgamal. A., Yang, Z., Parra, E., Ragheb, A., (2003), “Modeling of cyclic mobility in saturated cohesionless soils”, International journal of plasticity, 19, 883-905

Eslami, M.; Brandenberg, S. J.; Zhong, A.; Pradel, D., (2017). “Triaxial Tests on Sand for Yield Surface Mapping.” DesignSafe-CI [publisher], Dataset, DOI: https://doi.org/10.17603/DS23T00

Esteva, M., Brandenberg, S. J., Eslami, M., Adair, A., Kulasekaran, S., (2016), “Modelling Natural Hazards Engineering Data to Cyberinfrastructure.” Proceedings of the SciDataCon 2016. 11-13 September 2016, Denver, Colorado. Available online at: http://www.scidatacon.org/2016/sessions/104/paper/282/

Itasca Consulting Group (2011), “Computer Program FLAC 7.0”, Minneapolis, MN. www.itascacg.com.

Jones, R. M. (2009), “Deformation Theory of Plasticity”, Bull Ridge Publishing

Khoei, A. R., (2005), “Computational Plasticity in Powder Forming Processes”, Elsevier Science Publications

Kuwano, R., and Jardine, R. J. (2007), “A triaxial investigation of kinematic yielding in sand”, Geotechnique, 57(7), 563-580.

Lade, P. V. (1977), “Elasto-plastic stress-strain theory for cohesionless soil with curved yield surfaces”, Int. Journal of Solids and Structures, 13(11), 1019-1035.

Lade, P. V., and Kim, M. K. (1988), “Single hardening constitutive model for frictional materials II. Yield criterion and plastic work contours”, Computers and Geotechnics, 6(1), 13-29.

Lade, P. V., and Pradel, D., (1989). “Comparison of Single and Double Hardening Constitutive Models for Frictional Materials.” 3rd International Symposium on Numerical Models In Geomechanics (NUMOG3), Niagara Falls, Canada.

Masing, G. (1926, September), “Eigenspannungen und verfestigung beim messing”, Proceedings of the 2nd Int. Congress of Applied Mechanics (Vol. 100, 332-5).

Menq, F-Y., (2003), “Dynamic properties of sandy and gravelly soils”, Dissertation at the University of Texas, Austin

Mróz, Z., Norris, V. A., and Zienkiewicz, O. C. (1979). “Application of an anisotropic hardening model in the analysis of elasto-plastic deformation of soil”, Géotechnique 29, No. 1, 1–34

Nawir, H., Tatsuoka, F. and Kuwano, R. (2003), “Viscous effects on the shear yielding characteristics of sand”, Soils and Foundations, Vol. 43, No. 6, pp. 33-50

Pestana, J. M., and Whittle, A. J. (1999). ‘‘Formulation of a unified constitutive model for clays and sands.’’ Int. J. Numer. Analyt. Meth. Geomech. 23(12), 1215-1243.

Plaxis BV (2015), “Computer Program PLAXIS 2015”, Delft, Netherlands. www.plaxis.nl.

Poorooshasb, H. B., (1971), “Deformation of sand in triaxial compression”, Proc. 4th Asian Regional Conf. on Soil Mechanics and Foundation Engineering, Bangkok, Vol. 1, pp. 63-66

Poorooshasb, H. B., and Pietruszczak, S. (1985), “On yielding and flow of sand; a generalized two-surface model”, Computers and Geotechnics, 1(1), 33-58.

Poorooshasb, H. B., Holubec, I., and Sherbourne, A. N. (1966) “Yielding and flow of sand in triaxial compression: Part I”, Canadian Geotechnical Journal, 3(4), 179-190.

Poorooshasb, H. B., Holubec, I., and Sherbourne, A. N. (1967), “Yielding and flow of sand in triaxial compression: Parts II and III”, Canadian Geotechnical Journal, 4(4), 376-397.

Pradel D., Ishihara K., and Gutierrez M. (1990), “Yielding and Flow of Sand under Principal Stress Axes Rotation”, Soils and Foundations, Vol. 30, No. 1, 87-99.

Pradel, D., and Lade, P. V. (1990), “Instability and plastic flow of soils. II: Analytical investigation”, Journal of Engineering Mechanics, ASCE, 116(11), 2551-2566.

Prevost, J. H., (1985), “A simple plasticity theory for frictional cohesionless soils”, Soil Dynamics and Earthquake Engineering, Vol. 4, 9-17

Rathje, E., Dawson, C. Padgett, J.E., Pinelli, J.-P., Stanzione, D., Adair, A., Arduino, P., Brandenberg, S.J., Cockerill, T., Dey, C., Esteva, M., Haan, Jr., F.L., Hanlon, M., Kareem, A., Lowes, L., Mock, S., and Mosqueda, G. (2017), “DesignSafe: A New Cyberinfrastructure for Natural Hazards Engineering,” ASCE Natural Hazards Review, DOI: 10.1061/(ASCE)NH.1527-6996.0000246

Roscoe K. H., and J. B. Burland (1968), “On the Generalised Stress-Strain Behavior of ‘Wet Clay’”, in Engineering Plasticity, pp. 535-609. J. Heyman and F. A. Leckie, Eds. Cambridge University Press.

Roscoe, K. H. and Schofield, A. N. (1963), “Mechanical Behaviour of an Idealised ‘Wet’ Clay”, Proc. 2nd European Conf. on Soil Mechanics and Foundation Engineering, Wiesbaden, vol. 1, pp. 47-54

Schofield and Wroth (1968), “Critical State Soil Mechanics”, McGraw-Hill.

Simo, J. C. and Hughes, T. R. J., (1998), “Computational Inelasticity”, Springer, New York

Taiebat, M., and Dafalias, Y. F. (2008), "SANISAND: Simple anisotropic sand plasticity model", Int. Journal for Numerical and Analytical Methods in Geomechanics, 32(8), 915-948.

Tanimoto, K., and Tanaka, Y. (1986), "Yielding of soil as determined by acoustic emission", Soils and Foundations, 26(3), 69-80.

Tatsuoka, F., (2006), "Inelastic Deformation Characteristics of Geomaterial", Soil Stress-Strain Behavior: Measurement, Modeling and Analysis, A collection of papers of the Geotechnical Symposium in Rome, March 16 & 17, 2006, Springer

Tatsuoka, F., and Ishihara, K. (1974), "Yielding of sand in triaxial compression", Soils and Foundations, 14(2), 63-76.

Tatsuoka, F., and Molenkamp, F. (1983), "Discussion on yield loci for sands", Mechanics of Granular Materials: New Models and Constitutive Relations, Elsevier Science Publisher B.V., pp.75-87.

Vermeer, P. A. (1978), "A double hardening model for sand", Geotechnique, 28(4), 413-433.

Wood, D. M. (1990), "Soil Behaviour and Critical State Soil Mechanics", Cambridge University Press.

Yasufuku, N., Murata, H., and Hyodo, M., (1991), "Yield characteristics of anisotropically consolidated sand under low and high stresses", Soils and Foundations, Vol. 31, No. 1, 95-109

Yu, S. H., (2006), "Plasticity and Geotechnics", University of Nottingham, UK, Springer publications

References for Part II

Ajmera, B., Brandon, T., Tiwari, B. (2015). “Cyclic strength of clay-like materials.” *Proc. Of the 6th International Conference on Earthquake Geotechnical Engineering*, Christchurch, New Zealand.

Ajmera, B., Tiwari, B., Brandon, T. (2016). “Influence of mineralogy and plasticity on the cyclic and post-cyclic behavior of normally consolidated soils.” *Geotechnical and Structural Congress 2016*, ASCE, Phoenix, Arizona.

Andrews, D. C. A., and Martin, G. R. (2000). “Criteria for liquefaction of silty soils.” Proc., 12th World Conference on Earthquake Engineering, Auckland, New Zealand.

Andrus, R. D., and Stokoe, K. H. (2000). “Liquefaction resistance of soils from shear wave velocity.” *Journal of Geotechnical and Geoenvironmental Engineering*, ASCE, 126 (11), 1015-1025.

ASTM (2007). “Annual Book of Standards,” Vol. 4.08, Soil and Rock (I): D420 -D5611, and Soil and Rock (II): D5714-latest, ASTM International, West Conshohocken, PA, USA.

Beroya, M. A. A., Aydin, A., Katzenbach, R. (2009). “Insight into the effects of clay mineralogy on the cyclic behavior of silt-clay Mixtures. *Engineering Geology Journal*, 106: 154-162.

Bjerrum, L., and Landva, A., (1966). “Direct Simple Shear Tests on a Norwegian Quick Clay,” Geotechnique, Vol. 16, No. 1, pp. 1–20.

Boulanger, R. W., and Idriss, I. M. (2004). “Evaluating the potential for liquefaction or cyclic failure of silts and clays.” Report No. UCD/CGM-04/01, Center for Geotechnical Modeling, Department of Civil & Environmental Engineering, College of Engineering, University of California, Davis, California.

Boulanger, R. W., and Idriss, I. M. (2006). “Liquefaction susceptibility criteria for silts and clays.” Journal of Geotechnical and Geoenvironmental Engineering, ASCE, 132(11), 1413-1426.

Boulanger, R. W., and Idriss, I. M. (2007). “Evaluation of cyclic softening in silts and clays.” Journal of Geotechnical and Geoenvironmental Engineering, ASCE, 133(6), 641-652.

Boulanger, R. W., Meyers, M. W., Mejia, L. H., and Idriss, I. M. (1998). “Behavior of a fine-grained soil during Loma Prieta earthquake.” *Canadian Geotechnical Journal*, 35, 146-158.

Brandenberg, S.J., Stewart, J.P., Shafiee, A., (2016). “Post-Cyclic Settlement Potential of Sherman Island Peat.” Final project report for California Department of Water Resources for research performed under contract No. 4600010406.

Bray, J. D., and Sancio, R. B. (2006). "Assessment of the liquefaction susceptibility of fine-grained soils." *Journal of Geotechnical and Geoenvironmental Engineering*, ASCE, 132 (9), 1165-1177.

Bray, J. D., Sancio, R. B., Durgunoglu, T., Onalp, A., Youd, T. L., Stewart, J. P., Seed, R. B., Cetin, O. K., Bol, E., Baturay, M. B., Christensen, C., and Karadayilar, T. (2004). "Subsurface characterization at ground failure sites in Adapazari, Turkey." J. Geotechnical and Geoenvironmental Engineering, ASCE, 130(7), 673-685.

Cubrinovski, Green, R.A., and Wotherspoon, L., Eds. (2011). "Geotechnical Reconnaissance of the 2011 Christchurch (New Zealand) Earthquake," GEER Report No. GEER-024, (http://www.geerassociation.org/GEER_Post%20EQ%20Reports/Christchurch_2011/Cover_Christchurch_2011.html)

Dahl, K. R., DeJong, J. T., Boulanger, R. W., Pyke, R., and Wahl, D. (2014). "Characterization of an alluvial silt and clay deposit for monotonic, cyclic, and post-cyclic behavior." Canadian Geotechnical Journal, 51 (4), 432–440.

Dahl, K.R. (2011). "Evaluation of seismic behavior of intermediate and fine-grained soils." Doctoral thesis, University of California, Davis.

DeGroot, D. J., Germaine, J. T., and Ladd, C.C. (1994). "Effect of nonuniform stresses on measured DSS stress-strain behavior." Journal of Geotechnical and Geoenvironmental Engineering, ASCE, 120(5), 892-912.

Duku, P.M., Stewart, J.P., Whang, D.H., and Venugopal, R., 2007, "Digitally Controlled Simple Shear Apparatus for Dynamic Soil Testing," Geotechnical Testing J., Vol. 30, No. 5, pp. 1-10.

Gratchev, I. B. and Sassa, K., (2009). "Cyclic Behavior of Fine-Grained Soils at Different pH Values." Journal of Geotechnical and Geoenvironmental Engineering, ASCE, 135 (2), 271-279.

Gratchev, I. B. and Sassa, K., (2013). "Cyclic Shear Strength of Soil with Different pore Fluid." Journal of Geotechnical and Geoenvironmental Engineering, ASCE, 139 (10), 1817-1821.

Gratchev, I. B., Sassa, K., and Fukuoka, H. (2006a). "How reliable is the plasticity index for estimating the liquefaction potential of clayey sands?" Journal of Geotechnical and Geoenvironmental Engineering, ASCE, 132 (1), 124-127.

Gratchev, I. B., Sassa, K., Osipov, V.I., and Sokolov, V.N. (2006b). "The Liquefaction of Clayey Soils under Cyclic Loading." Engineering Geology, 86 (2006) 70-84.

Guo, T., and Prakash, S. (1999). "Liquefaction of silts and silt-clay mixtures." Journal of Geotechnical and Geoenvironmental Engineering, ASCE, 125 (8) 706-710.

Guo, T., and Prakash, S. (2000). "Liquefaction of Silt-Clay Mixtures." Proceedings of the 12th World Conference on Earthquake Engineering, Paper 0561, Auckland, New Zealand.

Idriss, I. M., and Boulanger, R. W. (2008). "Soil liquefaction during earthquakes." Monograph MNO-12, Earthquake Engineering Research Institute, Oakland, CA, 261 pp.

Jang, J., and Santamarina, J. C. (2016). “Fines classification based on sensitivity to pore-fluid chemistry.” *Journal of Geotechnical and Geoenvironmental Engineering*, ASCE, 142 (4).

Koester, J. P., (1992). “The influence of test procedure on correlation of Atterberg limits with liquefaction in fine-grained soils.” Journal of Geotechnical Testing, ASTM, 15(4), 352-360.

Ladd, C. C. (1991). “Stability evaluation during staged construction.” Journal of Geotechnical Engineering, ASCE, 117 (4), 540-615.

Mitchell, J. K. and Soga, K. (2005). “Fundamentals of Soil Behavior,” 3rd Edition, John Wiley and Sons, Inc.

Prakash, S. and Sandoval, J.A., (1992) “Liquefaction of low plasticity silts,” Journal of Soil Dynamics and Earthquake Engineering, Vol. 11 No. 7, pp. 373-397.

Price, A. B., Boulanger, R. W., DeJong, J. T., Parra Bastidas, A. M., Moug, D. (2015). “Cyclic strengths and simulated CPT penetration resistances in intermediate soils.” *Proc. Of the 6th International Conference on Earthquake Geotechnical Engineering*, Christchurch, New Zealand.

Puri, V.K., (1984) “Liquefaction behavior and dynamic properties of loessial (silty) soils,” Ph.D. Thesis, University of Missouri-Rolla, MO.

Reid, D., and Fourie, A. (2017). “Effects of polymer treatment on undrained strengths and cyclic behavior of a low-plasticity slurry.” *Journal of Geotechnical and Geoenvironmental Engineering*, ASCE, 143 (6).

Robertson, P. K., and Wride, C. E. (1998). "Evaluating cyclic liquefaction potential using the cone penetration test." *Canadian Geotechnical Journal*, 35 (3), 442-459.

Sancio, R. B. (2003). "Ground failure and building performance in Adapazari, Turkey." Ph.D. thesis, University of California, Berkeley, 790 pp.

Sancio, R. B., Bray, J. D., Stewart, J. P., Youd, T. L., Durgunoglu, H. T., Onalp, A., Seed, R. B., Christensen, C., Baturay, M. B., Karadayilar, T. (2002). "Correlation between ground failure and soil conditions in Adapazari, Turley." *Soil Dynamics and Earthquake Engineering Journal*, 22 (2002) 1093-1102.

Seed, H. B., and Idriss, I. M. (1982). *Ground motions and soil liquefaction during earthquakes*, Earthquake Engineering Research Institute, Berkeley, CA,134.

Seed, R. B., Cetin, K. O., Moss, R. E. S., Kammerer, A., Wu, J., Pestana, J., Riemer, M., Sancio, R. B., Bray, J. D., Kayen, R. E., and Raris, A. (2003). "Recent advances in soil liquefaction engineering: a unified and consistent framework." Keynote presentation, 26th Annual ASCE Los Angeles Geotechnical Spring Seminar, Long Beach, CA.

Shafiee, A., 2015, "Cyclic and Post-Cyclic Behavior of Sherman Island Peat," Ph.D. thesis, University of California, Los Angeles, Los Angeles, 303pp.

Shafiee, A., Stewart, J. P., Venugopal, R., and Brandenberg, S. J. (2017). "Adaptation of Broadband Simple Shear Device for Constant Volume and Stress-Controlled Testing," *Geotechnical Testing Journal*, Vol. 40, No. 1, pp. 15–28, http://dx.doi.org/10.1520/GTJ20150181. ISSN 0149-6115

Soysa, A., and Wijewickreme, D. (2017). “Comparison of cyclic shear response of three natural fine-grained soils having different plasticity.” *Proc. Of the 16th World Conference on Earthquake Engineering*, Santiago, Chile, paper No. 0550.

Stewart, J. P., Chu, D. B., Lee, S., Tsai, J. S., Lin, P. S., Chu, B. L., Moss, R. E. S., Seed, R. B., Hsu, S. C., Yu, M. S., and Wang, M. C. H. (2003). “Liquefaction and non-liquefaction from 1999 Chi-Chi, Taiwan, earthquake,” Advancing Mitigation Technologies and Disaster Response for Lifeline Systems, Technical Council on Lifeline Earthquake Engineering, Monograph No. 25, J. E. Beavers ed., 1021-1030.

Stewart, J.P., Kramer, S.L., Kwak, D.Y., Greenfield, M.W., Kayen, R.E., Tokimatsu, K., Bray, J.D., Beyzaei, C.Z., Cubrinovski, M., Sekiguchi, T., Nakai, S., Bozorgnia, Y., (2016). “PEER-NGL Project: Open Source Global Database and Model Development for the Next-Generation of Liquefaction Assessment Procedures.” Soil Dynamics and Earthquake Engineering, https://doi.org/10.1016/j.soildyn.2016.07.009

Taylor, D.W. (1948). “Fundamentals of Soil Mechanics,” *John Wiley and Sons*, Inc. New York.

Tom, J.G. (2011). “Numerical study of drainage effects on prediction of cone penetration resistance in a silty-clay.” *MS thesis*, University of California, Davis.

Wang, S., Luna, R., Honghua, Z. (2015). “Cyclic and post-cyclic behavior of low-plasticity silt with varying clay content.”, *Soil Dynamics and Earthquake Engineering Journal*, 75 (2015), 112-120.

Wang, W. S. (1979). *Some Findings in Soil Liquefaction*, Water Conservancy and Hydroelectric Power Scientific Research Institute, Beijing, China.

Yasuda, S., Harada, K., Ishikawa, K., and Kanemaru, Y., (2012). “Characteristics of Liquefaction in Tokyo Bay area by the 2011 Great East Japan Earthquake,” *Soils and Foundations*, 52(5): 793-810.

Yee, E., Stewart, J.P., and Schoenberg, R.P., 2011, “Characterization and Utilization of Noisy Displacement Signals from Simple Shear Device using Spectral, Linear, and Kernel Regression,” Soil Dynamics and Earthquake Engineering, Vol. 31, No. 1, pp. 25-32.

Youd, T. L., Idriss, I. M., Andrus, R. D., Arango, I., Castro, G., Christian, J. T., Dobry, R., Finn, W. D. L., Harder, L. F. Jr., Hynes, M. E., Ishihara, K., Koester, J. P., Liao, S. S. C., Marcuson, W. F., III, Martin, G. R., Mitchell, J. K., Moriwaki, Y., Power, M. S., Robertson, P. K., Seed, R. B., and Stokoe, K. H., II (2001). “Liquefaction resistance of soils: summary report from the 1996 NCEER and 1998 NCEER/NSF workshops on evaluation of liquefaction resistance of soils.” *Journal of Geotechnical and Geoenvironmental Engineering*, ASCE, 127 (10), 817-833.